Electrochemical Characterization for Improvement of PEM Electrolysers

Elsøe, Katrine

Publication date:
2018

Document Version
Publisher's PDF, also known as Version of record

Electrochemical Characterization for Improvement of PEM Electrolysers

Katrine Elsøe

June 2018

Electrochemical Characterization for Improvement of PEM Electrolysers

Author
Katrine Elsøe
Department of Energy Conversion and Storage
Technical University of Denmark
E-mail: katel@dtu.dk

Main Supervisor
Mogens B. Mogensen
Research Professor
Department of Energy Conversion and Storage
Technical University of Denmark

Co-supervisor
Johan Hjelm
Associate Professor
Department of Energy Conversion and Storage
Technical University of Denmark

External Supervisor
Günther G. Scherer
Professor

Technical University of Denmark
Department of Energy Conversion and Storage
Frederiksborgvej 399
DK - 4000 Roskilde
Denmark
www.energy.dtu.dk
Phone (+45) 46 77 58 00

Preface

This thesis is submitted in candidacy for the PhD degree from the Technical University of Denmark (DTU). The work presented was carried out at the Department of Energy Conversion and Storage from 15th June 2015 to 14th June 2018. The work was mainly supervised by research professor Mogens Bjerg Mogensen and co-supervised by associate professor Johan Hjelm.

The PhD project was part of the e-STORE project with contract number 4106-00025B funded by the Innovation Fund Denmark. The work included close collaboration with the project partner EWII Fuel Cells A/S, who supplied the majority of the PEMECs for testing in this work. The work included a two months research stay at Paul Scherrer Institute (PSI) in Switzerland. PSI benchmark PEMECs were prepared during the research stay and later electrochemically tested at DTU in Denmark.

Katrine Elsøe
Roskilde, Denmark, June 2018

Acknowledgements

I would like to thank everybody who helped me making this thesis possible. First and foremost, I would like to thank my main supervisor Mogens B. Mogensen for all the interesting discussions, your optimism and for always having time for questions and discussions. Thank you to my co-supervisor Johan Hjelm for inputs and introducing me to Python and thank you to my external supervisor Günther G. Scherer for all the challenging questions and discussions.

Thank you to Laila Grahl-Madsen from EWII Fuel Cells A/S for close collaboration and for supplying PEMECs for my electrochemical tests, and thank you to Thomas Justus Schmidt, Ugliesa Babic and Alexandra Patru at the Paul Scherrer Institute in Switzerland for hosting me during my external research stay.

Thank you to Søren Koch and Martin Nørby Nielsen for introduction to and help with the softwares Labsystem and Elchemea, with the Solartron and with designing and constructing the electrochemical test rigs. Thank you to Søren Koch for help with Unix and to Martin Nørby Nielsen for help with the Oscilloscope. Thank you to Christopher R. Graves for help with the EIS software RAVDAV. Thank you to Henrik Henriksen, Jens F. S. Borchsenius, Jens Østergaard and Ole Hansen for help in the laboratory whenever needed and with ordering things from suppliers. Thank you to Søren Højgaard Jensen for interesting discussions and help with the cabling of the test rig and making EIS measurements on the test rig possible. Thank you to Larisa Seerup, Ebtisam Abdellahi, Karl Tor Sune Thydén and Peter Stanley Jørgensen for help with the microscopes and thank you to Anne Heglingegård for help with administrative things.

Thank you to Filippo, Jette, Mathias, Doris, Daniel, Kosova, Simon, Salvatore, Steven and the other PhDs in the PhD group for all the lunches together and gatherings outside working hours.

Last but not least, I want to thank my boyfriend Kåre and my family and friends for all the support and encouragement during these three PhD student years.

Abstract

These years the interest in electrical energy from renewable energy sources such as e.g. wind power is increasing. However, the demand of society for electrical energy does not always correspond to the production rate, and a method to store the electrical energy is needed. Electrolysis of water into hydrogen is one such method. It converts electrical energy into chemical energy bound in hydrogen molecules, which can then be stored.

Knowing of performance limiting processes in operating PEMECs should enable engineering of improved electrolysis cells with a better performance allowing for economic storage of a bigger fraction of the renewable electrical energy. In this thesis polymer electrolyte membrane electrolysis cells (PEMECs) are investigated electrochemically in order to gain knowledge of the processes limiting the performance of PEMECs by contributing to the differential cell resistance. Three different PEMEC types from EWII A/S and Paul Scherrer Institute (PSI) were investigated with cyclic voltammetry (CV) combined with current density - voltage (i,V) curves and electrochemical impedance spectroscopy (EIS) measured at three different temperatures (approximately 54, 61 and 69 °C, but the exact temperature varied a bit between the cells) and at four to six different current densities (0.07, 0.35, 0.69, 1.00, 2.00, 3.00 A cm^{-2}) for the EIS measurements. The influence of platinum coating of the titanium current collector was also investigated. The electrochemical results were supplemented with some scanning electron microscopy.

Based on the experimental results a new hypothesis for the internal resistance of PEMECs was suggested. It was found that the performance of PEMECs are limited by proton conduction resistance of Nafion in the electrolyte and in the anode and by constrictions of the current path at the electrolyte/electrode interfaces. An optimized structure of the PEMECs has been suggested, which includes a thinner Nafion membrane that still prevents H_2 cross over. It also includes IrO_x anode catalyst particles as small as possible, but still being able to form triple phase boundaries with the Nafion binder and the water and produced gas in the electrode. This in combination with a titanium current collector with smaller pores than the titanium felt applied in the experiments in this thesis, but still very porous to prevent mass transport limitations, will decrease the current constrictions in the PEMECs. By applying smaller IrO_x particles the thickness of the anode catalyst layer can be decreased, though still obtaining the same proton conduction from the same amount of Nafion binder in the anode catalyst layer, and this will further decrease the differential cell resistance and increase the performance of the PEMECs.

The presented hypothesis is new and discovered from the combination of EIS, CV and iV-curves. Only limited amounts of EIS on PEMECs is reported in literature, probably due to frequent observations of noise in the EIS measurements. This phenomenon has been investigated in this thesis. Based on EIS measurements a hypothesis has been presented, which suggests that the noise originates from the unstable gas bubble release at the electrodes caused by the AC perturbation and that the noise is dependent on the microstructure of the particular PEMEC.

Resumé

I disse år, stiger interessen for elektrisk energi produceret fra bæredygtige energi kilder som fx. vindkraft. Det er dog ikke altid, at efterspørgslen fra samfundet på elektrisk energi svarer til den producerede mængde elektrisk energi, og der er derfor brug for en metode til at gemme elektrisk energi. Elektrolyse af vand til brint er sådan en metode. Den omdanner elektrisk energi til kemisk energi bunder i brintmolekyler, som kan gemmes.

Kendskab til hvilke processer, der begrænser ydeevnen af polymer membran elektrolyt elektrolyse celler (PEMECs), kan gøre det muligt at designe forbedrede elektrolyseceller med en højere ydeevne, som vil gøre det muligt at gemme en større del af den bæredygtige elektriske energi. I denne afhandling er PEMECs undersøgt med elektrokemiske metoder, for at opnå kendskab til, hvilke processer, der begrænser ydeevnen af cellerne ved at medvirke til cellens differentielle modstand. Tre forskellige PEMEC typer fra EWII Fuel Cells A/S og Paul Scherrer Instituttet (PSI) er blevet undersøgt med cyklisk voltammetri (CV) kombineret med strømtæthed – potential (i,V) kurver og elektrokemisk impedans spektroskopi (EIS) målt ved tre forskellige temperaturer (ca. 54, 61 and 69 °C, men temperaturen varierede lidt for de enkelte celler) og ved fire til seks forskellige strøm tætheder (0.07, 0.35, 0.69, 1.00, 2.00, 3.00 A cm^{-2}) under EIS målingerne. Det blev også undersøgt, hvordan en platin belægning af strømopsamleren, som var lavet af titanium, påvirkede cellens ydeevne. De elektrokemiske resultater blev suppleret med skanning elektron mikroskopi (SEM).

En ny hypotese er foreslået i afhandlingen baseret på den eksperimentelle resultater. Det er opdaget, at ydeevnen af PEMEC'erne var begrænset af proton ledningsevne modstand i elektrolytten og i anoden. Derudover var ydeevnen også begrænset af indsnævringer af strømvejen ved elektrolyt/elektrode grænsefladen. En optimeret struktur for PEMEC'erne er blevet foreslået, som inkluderer en tyndere Nafion membran, som stadig er tyk nok til at forhindre brintovergang fra katoden til anoden. De optimerede struktur inkluderer også at IrO_x anode katalysator partiklerne bliver så små som muligt, hvor de stadig kan forme trefasegrænser med Nafion binderen, vand og produceret gas i anoden. Hvis dette implementeres i kombination med en titanium strømopsamler med mindre porer end den titan filt, som er brugt i eksperimenterne i denne afhandling, men som stadig har en meget porøs struktur for at forhindre masse-transport-begrænsninger, vil indsnævringer af strømvejen mindskes. Ved at anvende mindre IrO_x partikler vil tykkelsen på anode-katalysator-laget kunne mindskes, selvom den samme protonledningsevne opretholdes ved at anvende den samme mængde Nafion binder i anode-katalysator-laget, og dermed til den differentielle celle modstand blive yderligere sænket, hvilket vil forbedre ydeevnen af PEMEC'erne.

Den foreslåede hypotese er ny og opdaget ved at kombinere EIS, CV og iV-kurver. I litteraturen findes kun begrænsede publiceringer med EIS målt på PEMEC'er, sandsynligvis fordi der ofte observeres støj i EIS målinger på PEMEC'er. Dette støjfænomen er også undersøgt i afhandlingen. Endnu en hypotese er præsenteret, som foreslår, at EIS støjen skyldes en ustabil gas boble frigivelse på elektroderne, når der måles EIS, hvilket tilskrives AC påvirkningen af den pågældende PEMEC under EIS målingerne. Det foreslås yderligere, at EIS støjen er afhængig af mikrostrukturen af den pågældende PEMEC.

List of Publications

The thesis is based on the following two articles, additional experiments, and data analysis, which is not yet published. Two more articles are expected published after the PhD project based on this thesis.

Article 1: K. Elsøe, L. Grahl-Madsen, G. G. Scherer, J. Hjelm, M. B. Mogensen, Electrochemical Characterization of a PEMEC Using Impedance Spectroscopy, J. Electrochem. Soc., **164**, F1419 (2017).

Contribution: All literature review, experimental work, analysis and interpretation of data and writing.

Erratum: In article 1 it was stated that the Ir metal layer is not electrochemically active, but later CV measurements of an EWII cell without IrO_x catalyst layer, but only Ir metal layer contradicted this statement. There will as soon as possible be send an erratum to article 1 to the journal making aware of the correction. In the article is was also stated the mQ water was applied for the measurements, but as stated in this thesis, milli-DI water was supplied to the PEMECs during operation. This will also be corrected in the erratum.

Article 2: K. Elsøe, M. R. Kraglund, L. Grahl-Madsen, G. G. Scherer, J. Hjelm, S. H. Jensen, T. Jacobsen, M. B. Mogensen, Noise Phenomena in Electrochemical Impedance Spectroscopy of Polymer Electrolyte Membrane Electrolysis Cells, manuscript accepted for publication in Fuel Cells – From Fundamentals to Applied Systems.

Contribution: Experimental work on the acidic PEMECs. All literature review, analysis and interpretation of data. Most of the writing except the experimental section on alkaline PEMECs.

Abbreviations

AC	Alternating current
CCM	Catalyst coated membrane
OCV	Open circuit voltage
CNLS	Complex non-linear least squares
CV	Cyclic voltammetry/voltammogram
DC	Direct current
DTU	Technical University of Denmark
ECSA	Electrochemical surface area
EIS	Electrochemical impedance spectroscopy
EMF	Electro motoric force
FFT	Fast Fourier transform
FIB	Focused ion beam
GDL	Gas diffusion layer
HER	Hydrogen evolution reaction
MEA	Membrane electrode assembly
OER	Oxygen evolution reaction
PEMEC	Polymer electrolyte membrane electrolysis cell
PSI	Paul Scherrer Institute
SEM	Scanning electron microscopy
SHE	Standard hydrogen electrode
XPS	X-ray photoelectron spectroscopy

Contents

1. Introduction

These years the interest in renewable energy is increasing, since EU has a goal of decreasing the emissions of greenhouse gases 80-95 % by 2050. The aim in Denmark is by 2050 to be a low emission society independent on fossil fuels. Today 30 % of the energy production in Denmark comes from renewable energy sources, and this number should be increased to 50 % by 2030 in order to reach the target of 100 % in 2050. (1)

However, renewable energy sources are intermittent, which means that the production rate not always correspond to the production rate, and a method to store excess sustainable energy is needed (2). Electrolysis of water into hydrogen is one such method. At times with low energy production compared to the demand, the produced hydrogen can be reconverted into electrical energy. Furthermore, the hydrogen produced by electrolysis has a very high purity, which makes it attractive in the chemical industry. (3) (4)

The overall electrolytic reaction is given by equation (1). Practically the overall electrolytic reaction is divided into two half-cell reactions taking place on each electrode and separated by an electrolyte. Electrolysis cells are distinguished by their electrolyte and operating temperature, because the choice of materials is depending on these properties. (5) Three main types of water electrolysis cells exist, which are alkaline, solid oxide and polymer electrolyte membrane water electrolysis cells.

$$H_2O \rightarrow H_2 + \frac{1}{2}O_2 \tag{1}$$

1.1 Alkaline Water Electrolysis

The first electrolysis cells from 1789 had an alkaline electrolyte, and these cells are nowadays commercially available. Most often the electrolyte of alkaline electrolysis cells consists of 20-30 % KOH, and the two electrodes are separated by a diaphragm, which is permeable to hydroxide ions and water molecules, but separates the produced gases. The cathodic and anodic half-cell reactions in alkaline electrolysis is shown in equation (2) and (3), respectively. Due to the low electrode potentials vs. SHE and alkaline electrolyte in this electrolysis type, cheap materials can be used as catalysts and flow fields. The alkaline water electrolysis cells suffer from limited current densities, which is caused by high ohmic losses across the electrolyte and diaphragm. High operating pressure would be advantageous, since it would make directly pressurized hydrogen storage possible. (3) (5)

$$4e^- + 4H_2O \rightarrow 4OH^- + 2H_2 \tag{2}$$

$$4OH^- \rightarrow 2H_2O + 4e^- + O_2 \tag{3}$$

1.2 Solid Oxide Water Electrolysis

Electrolysis with a solid oxide electrolyte was introduced in the 1980s, and in these cells the electrolyte conduct oxide ions. The cathodic and anodic half-cell reactions in alkaline electrolysis are shown in equation (4) and (5), respectively. Solid oxide cells have a high efficiency and a lot of research at universities, research institutions and in companies are taking place at the moment. The issues to be solved for solid oxide electrolysis cells are the durability of the ceramic materials at elevated temperatures and long term operation. (3) (6)

$$4e^- + O_2 \rightarrow 2O^{2-} \tag{4}$$

$$2O^{2-} + 2H_2 \rightarrow 2H_2O + 4e^- \quad (5)$$

1.3 Polymer Electrolyte Membrane Water Electrolysis

The electrolyte in polymer electrolyte membrane electrolysis cells consists of a polymer membrane such as e.g. a Nafion® or a Fumapem® membrane. The electrolyte is most often proton conducting (some researchers have tried with alkaline membranes), and the cathodic and anodic half-cell reactions are shown in equation (6) and (7), respectively. (3) (5)

$$4e^- + 4H^+ \rightarrow 2H_2 \quad (6)$$

$$2H_2O \rightarrow 4H^+ + 4e^- + O_2 \quad (7)$$

The working principle of a PEMEC is shown in figure 1.3.1. The polymer membrane enable a compact system design and high pressure operation. The cells experience low ohmic losses and high current densities, which lowers the operation costs. A drawback of the PEM electrolysis cell is the acidic environment, which requires usage of certain materials, which can withstand the corrosive environment, and furthermore they have to be stable at a high overpotential. These materials are often rare and very expensive such as e.g. the IrO_2 anode catalyst and titanium anode support material. (3) (5)

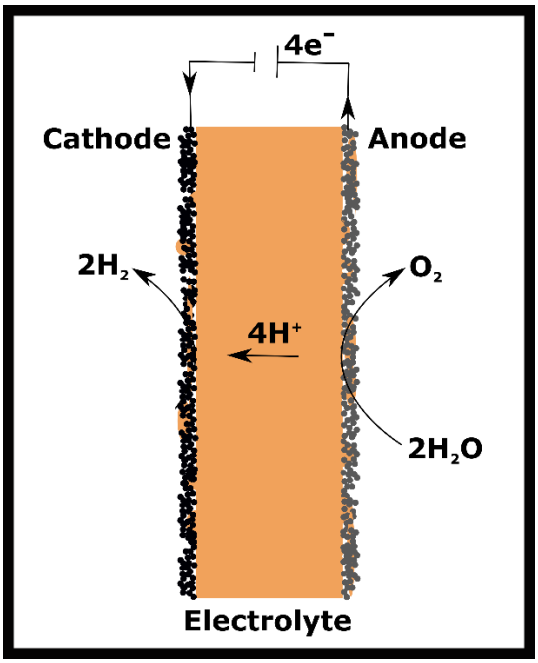

Figure 1.3.1 Working principle of a PEMEC.

1.3.1 The Scope of this Thesis

The hydrogen production rate of an electrolysis cell is determined by the current density during operation. The higher the current density the more hydrogen is produced per time unit and the lower the cost of the produced hydrogen. The highest possible operation current density at a given potential is dependent on the internal cell resistance. This means that as low an internal cell resistance as possible is preferred. The total cell resistance is given by the slope of the current density – voltage (i,V) curve of the cell, but multiple processes may contribute to the total

cell resistance. In order to identify these performance limiting processes, electrochemical impedance spectroscopy (EIS) in combination with other characterisation techniques have to be applied.

In this thesis the performance limiting processes contributing to the total cell resistance of operating PEMECs have been investigated with EIS in combination with iV-curves, cyclic voltammetry (CV) and some scanning electron microscopy (SEM). By knowing of the performance limiting processes it should be possible to engineer better performing PEMECs able to operate at higher current densities and with a lower internal cell resistance.

2. Development of the PEMEC Technology

The first electrolyser with a solid polymer as electrolyte was demonstrated by General Electric in the 1960s, and the Nafion membrane, which was developed by DuPont in the early 1960s, were applied as electrolyte. The Nafion membrane is a perfluorinated sulfonic acid membrane, which is ionic conducting due to the mobility of hydrated protons. The protons are transported between the sulfonic acid groups, which are bound in the Nafion membrane. (7) (8) (9)

2.1 Materials

The very acidic polymer membrane limits the amount of materials applicable as catalysts and components in the PEMECs. The exact pH of Nafion is not well-known, but it is expected to be 2-3. (10) (11) (3) Platinum is usually used as cathode catalyst. Carbon is often used as cathode current collector. At the anode the very acidic environment is combined with a very high oxidizing potential above 1.4 V during OER, which further limits the amount of materials applicable as catalysts at the anode, and iridium oxides or iridium-ruthenium oxide is the most promising catalysts for the OER at the anode. RuO_2 is a more active catalyst with a lower faradaic overpotential than the iridium based catalyst, however, IrO_x is more stable. Mixing RuO_x with IrO_x improves the stability of RuO_x, while keeping the good catalytic activity (12). Due to the high potentials titanium is often used as current collector at the anode. (4) (3) (5) The anode materials are expensive, especially the IrO_x, which is also scarce in case of an increase PEMEC production, because it is obtained as a byproduct of the platinum production (13). Therefore, extended research in ways to lower the IrO_x loading or to substitute the IrO_x catalyst is taking place (5). An approach has been to mix noble-metal and transition-metal oxides or to use noble-metal free oxides as catalyst materials. Another approach is to apply a corrosion-resistance support material, on which the catalyst IrO_x is dispersed, and thereby increase the specific surface area and durability of the catalyst. (14)

2.2 The IrO_x Anode Catalyst

The most used catalyst in PEMEC is still IrO_x. The catalytic cycle of the IrO_x during OER in 1 N H_2SO_4 have been investigated with X-ray photoelectron spectroscopy (XPS) by Kötz et al. (15). The found iridium in the oxidations states Ir^{4+}, Ir^{5+} and Ir^{6+} and suggested the catalytic reaction cycle shown in figure 2.2.2. Lettenmeier et al. (16) have investigated the oxidation states of an iridium nanoparticle catalyst with XPS in a PEMEC operating at potentials up to 1.4 V. They report the maximum oxidation state of the iridium to be Ir^{4+}, but mention in the conclusion that the iridium may be found in higher oxidation states, but at very short time scales, which they were not able to detect. Furthermore, the maximum potential at which they measured XPS was 1.4 V, while OER of PEMECs starts to take place at 1.4 V, and therefor PEMECs are normally operated at potentials above 1.8 V. At these high potentials (1.8 V) it may be reasonable to assume that the iridium will be present in oxidation states higher than 4+.

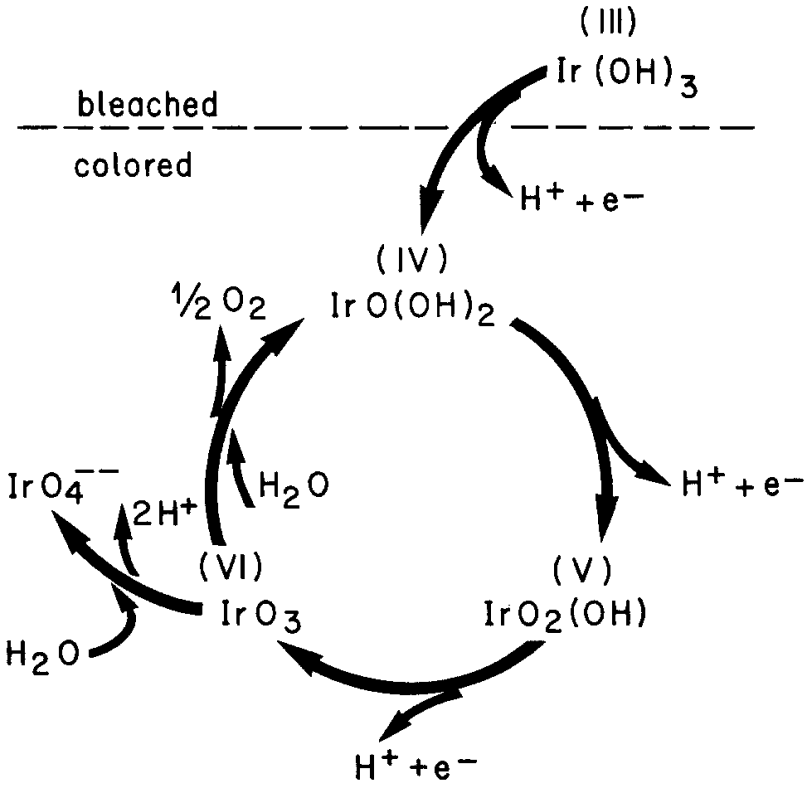

Figure 2.2.2 Model for charge storage and oxygen evolution on IrO_x electrodes (15).

2.3 EIS of PEMECs

EIS have primarily been used to determine the electrolyte resistance for iR-correction of iV-curves (17) (18) (19) (20) (21) (22) (23) (24) (25). Within the last few years, the interest of examining PEMECs with EIS have increased, and full EIS spectra have been interpreted. Some research groups have studied EIS of PEMECs in details such as Rozain et al. (26) (27), Lettenmeier et al. (28) and Siracusano et al. (23) (29). Often EIS of PEMECs is studied at low current densities in the activation region of the iV-curve, where the OER current density is very low (23) (22) (21) (30) (27) (26) (29) (31). Only a few research groups report EIS measured in the linear region of the iV-curves during OER (22) (21) (30) (20). The EIS spectra are often fitted to an equivalent circuit consisting of a serial resistance and one or two RQ elements originating from the anode or from the anode and the cathode. Sometimes diffusion elements are added as well. (21) (30) (26) (28) (29) In this thesis a new hypothesis for the interpretation and equivalent circuit of EIS spectra measured at PEMECs during OER is presented.

3. Methods

3.1 Cyclic Voltammetry

Cyclic voltammetry is a potential sweep technique, where the potential is cycled between E_1 and E_2 by sweeping the potential first between E_1 and E_2, then reversed and swept from E_2 to E_1, and then the cycle is repeated for several times cf. figure 3.1.3 b). From this procedure a cyclic voltammogram is obtained (see figure 3.1.3 a)), which shows the measured current or current density as function of the swept potential, and from this the potentials at which the electrochemical processes occur, can be read off. It is a valuable technique for qualitative investigation of electrochemical systems. (32) (33)

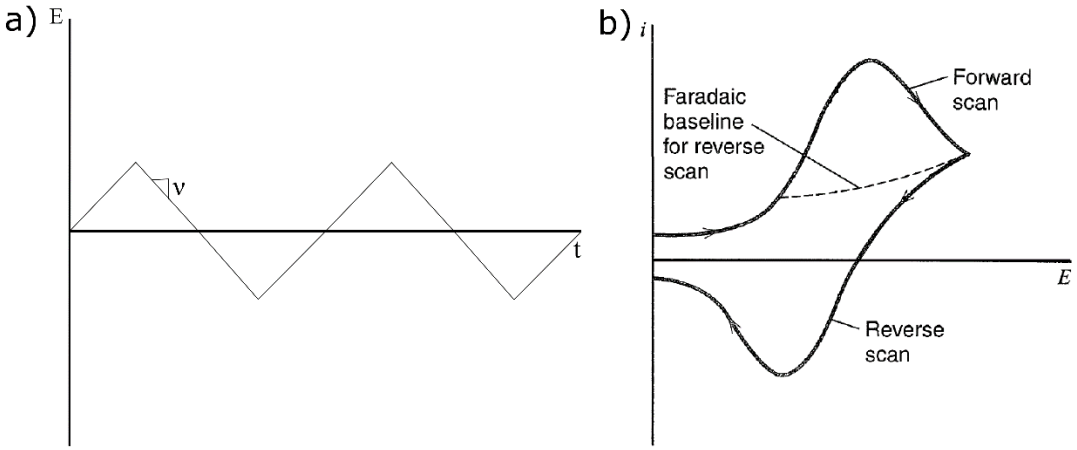

Figure 3.1.3 a) Potential-time profiles for cyclic voltammetry. b) Cyclic voltammogram. Figure a) is adapted from reference (33).

3.2 Electrochemical Impedance Spectroscopy

In electrochemical impedance measurements the electrochemical system under investigation is perturbed with an alternating current or voltage signal, while monitoring the responding voltage or current signal, respectively. Now consider an electrochemical system, which is perturbed with the sinusoidal voltage signal, e, given in equation (8) and responds with the sinusoidal current signal, i, given in equation (9). E is the voltage amplitude, I is the current amplitude, ω is the angular frequency and φ is the phase angle with which the two sinus signals are separated. (33)

$$e = E \cdot \sin(\omega t) \tag{8}$$

$$i = I \cdot \sin(\omega t + \varphi) \tag{9}$$

Another way of describing the sinusoidal voltage and current signals is as phasors (rotating vectors) in a coordinate system rotating around origo at the same frequency, ω, and separated by the phase angle, φ. The two sinus signals and the corresponding phasors are seen in figure 3.2.4.

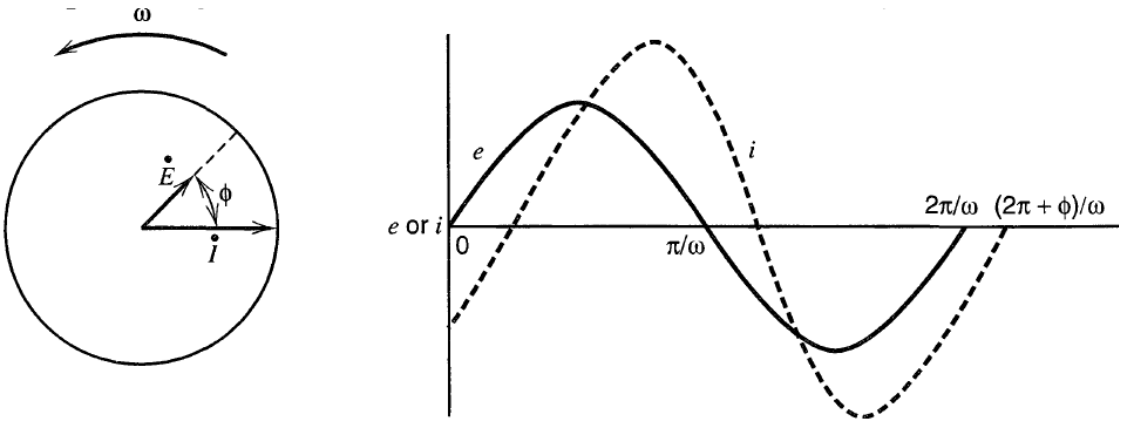

Figure 3.2.4 Phasor diagram showing the relationship between alternating current and voltage signals at frequency ω. The figure is adapted from reference (33).

For a pure resistor the voltage and current phasors will be in phase with a phase angle equal to zero and the phasor diagram will be a straight line. For a pure capacitor the phase angle is $\frac{\pi}{2}$ and the phasor diagram is a plane. Most processes are not purely resistive or capacitive in nature, but is a mix of the two and the resulting phasor is called the impedance, $Z(\omega)$. The impedance is in general given by equation (10), in which Z_{re} is the real part of the impedance, which is the resistance part of the impedance, and Z_{im} is the imaginary part of the impedance, which is the capacitive part of the impedance. This means that impedance is a generalized resistance, which links voltage and current. (33)

$$Z(\omega) = Z_{Re} - jZ_{Im} \tag{10}$$

3.2.1 Graphical Representation Forms

Impedance is often represented graphically in Nyquist or Bode plots, and visual inspection of these plots is often the first method used in EIS data treatment. The Nyquist (or Argand) plots is a complex plane plot showing the real impedance on the x-axis and the imaginary impedance multiplied with -1 on the y-axis. The unit length on the two axis in the complex plane plot should be equal in order to prevent distortions in the plot and in order to be able to identify semicircles and Warburg diffusion having a 45 ° slope. These plots may indicate types of mechanisms contributing to the overall impedance, but do not indicate at what time scales the various processes are taking place unless frequencies are noted at some of the measurements points in the plot. Bode plots, on the other hand, contains information about the timescale of the processes contributing to the impedance, since these plots either show the logarithm of the magnitude of the impedance (modulus), the real part of the impedance, the imaginary part of the impedance or the phase angle as function of the logarithm of the frequency. (33) (34)

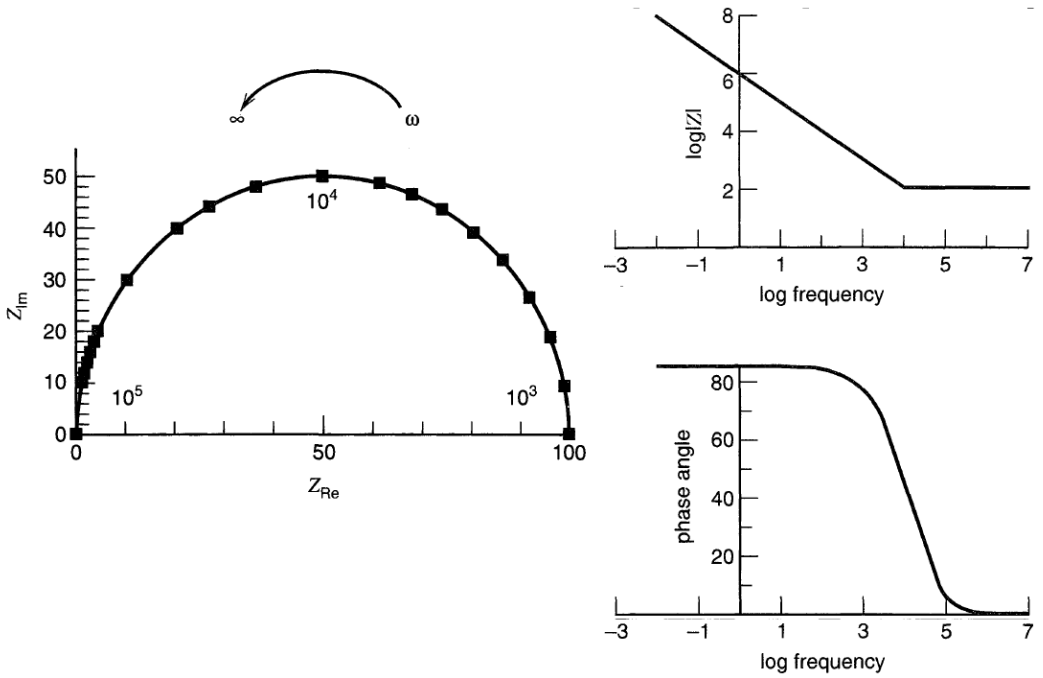

Figure 3.2.1.5 Nyquist plot (left) and Bode plots (right) for a parallel RC circuit. The figure is adapted from reference (33).

Figure 3.2.1.5 depicts a Nyquist plot and Bode plots of a parallel RC circuit. It should be noted that the visual inspection is only an introductive examination and should be complemented by complex nonlinear least square fit of the impedance data to an equivalent circuit in order to quantify the various impedance contributions. (33)

3.2.2 Equivalent Circuit Model

In order to be able to quantify the measured EIS, the data have to be fitted by complex non-linear least squares fitting to an appropriate equivalent circuit. The equivalent circuit should be physically explainable, since multiple equivalent circuits may be able to fit the EIS data, and therefore the EIS technique can never be used on its own, but have to be accompanied by other techniques such as e.g. CV, iV-curves, SEM etc. (35) (36)

3.2.3 Kramers-Kronig Compliance Test

Experimental EIS data can be validated or checked for how good the data is by applying the Kramers-Kronig compliance test. This is possible due to the Cauchy's integral theorem, which cause the real part of the impedance and the imaginary part of the impedance to be interdependent. The Kramers-Kronig relations describe this relation through integral equations. The system have to fulfill four requirements in order for the EIS data measured on the system, to obey the Kramers-Kronig relations. (35) (34) (36) These four requirements are:

1. **Linearity.** The system show linearity if the response signal of the system is a linear function of the perturbation signal. This imply that the impedance is independent of the magnitude of the perturbation. (35) (34) (36)

2. **Causality.** Causality implies that the response of the system only must originate from the perturbation of the system. (35) (34) (36)

3. **Stability.** The system is stable, it returns to its original state after the perturbation has been applied. (35) (34) (36)

4. **Finiteness.** The real and imaginary parts of the impedance must be finite in the full frequency range $0 < \omega < \infty$. The real part of the impedance should approach real values for $\omega \to 0$ and $\omega \to \infty$. (35) (34) (36)

If the four Kramers-Kronig requirements are fulfilled by the EIS examined system, the real part of the impedance can be calculated from the imaginary part of the impedance and vice versa by applying the Kramers-Kronig relations given in equation (11) and (12), in which ω is the angular frequency and Z_{re} and Z_{im} are the real and the imaginary part of the impedance, respectively. (35) (34)

$$Z_{re}(\omega) = Z_{re}(\infty) + \frac{2}{\pi}\int_0^{\infty} \frac{xZ_{im}(x) - \omega Z_{im}(\omega)}{x^2 + \omega^2} dx \tag{11}$$

$$Z_{im}(\omega) = \frac{-2\omega}{\pi}\int_0^{\infty} \frac{Z_{re}(x) - Z_{re}(\omega)}{x^2 + \omega^2} dx \tag{12}$$

From equation (11) and (12) it is seen that according to the Kramers-Kronig relations frequencies should be measured from 0 to ∞ Hz, which is experimentally impossible. Therefore various methods have been developed to apply Kramers-Kronig transforms on experimental EIS data, by which the method described by Boukamp (37) is widely applied. (34)

Boukamp suggested to model the EIS data with multiple Voigt elements (parallel R-C circuits) in series. The idea behind was that since each Voigt element is Kramers-Kronig transformable, the series of Voight elements consequently will be Kramers-Kronig transformable. With this approach the frequencies do not have to be extrapolated to 0 and ∞, but the EIS data have to be fitted to the equivalent circuit of multiple Voigt elements, which requires some starting values for the fit. The imaginary part of the fitting function suggested by Boukamp is then given by equation (13) and the real part of the fitting function is given by equation (14). (37)

$$Z_{im}(\omega_i) = -\sum_{k=1}^{M} \frac{\omega_i \cdot {R_k}^2 \cdot C_k}{1 + (\omega_i \cdot R_k \cdot C_k)^2} \tag{13}$$

$$Z_{re}(\omega_i) = R_{\infty} + \sum_{k=1}^{M} \frac{R_k}{1 + (\omega_i \cdot R_k \cdot C_k)^2} \tag{14}$$

After fitting the EIS data to multiple Voigt elements cf. equation (13) and (14), the relative Kramers-Kronig residuals are calculated as the difference between the fitted values and the measured impedance values at each frequency according to equation (15). $Z_{re,i}$ and $Z_{im,i}$ the real and imaginary parts of the *i*th data set impedance, and $Z_{re}(\omega_i)$ and $Z_{im}(\omega_i)$ are the fitted value of the real and the imaginary parts of the impedance for ω_i. $|Z(\omega_i)|$ is the absolute length or the modulus of the modelling function. These Kramers-Kronig relative residuals give an estimate of how

well the EIS data obey the Kramers-Kronig relations and therefore how valid the EIS data are. (37) (34)

$$\Delta_{re,i}= \frac{Z_{re,i} - Z_{re}(\omega_i)}{|Z(\omega_i)|} \; and \; \Delta_{im,i}= \frac{Z_{im,i} - Z_{im}(\omega_i)}{|Z(\omega_i)|} \tag{15}$$

4. Test Setup and Membrane Electrode Assemblies

4.1 Cell Test House from EWII

The cell test house from EWII is depicted in figure 4.1.6 assembled with an EWII benchmark cell in a) and assembled with a PSI benchmark cell in b). The cell test house consists on the cathode of a carbon flow plate equipped with a EPDM O-ring and on the anode of a titanium plate, and on both electrodes were placed a gold coated copper current collector with nitrile O-rings and a stainless steel end plate. The active electrode area was 2.9 cm^2.

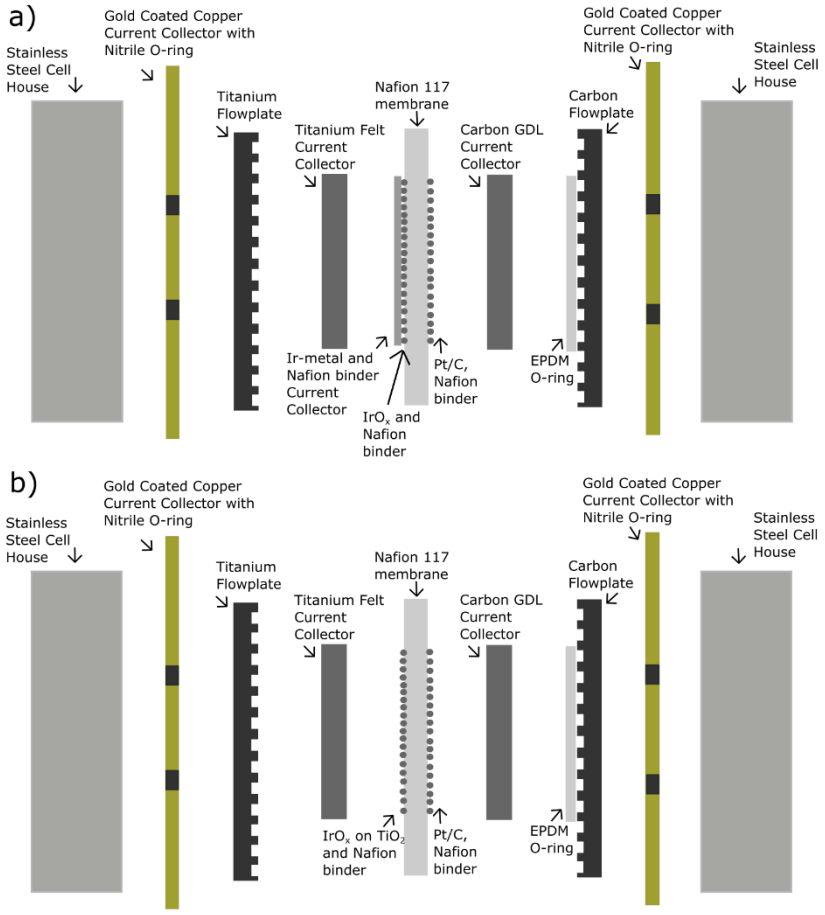

Figure 4.1.6 Schematic drawings of a) the PEMEC test setup provided by EWII Fuel Cells A/S assembled with an EWII benchmark PEMEC MEA (this drawing is similar to the drawing in article 1) and b) the same PEMEC test setup assembled with a PSI benchmark cell.

4.2 PEMECs from EWII vs. from PSI

Different types and constellations of PEMECs have been tested. Common to all the tested PEMEC MEAs was the Nafion 117 membrane, the titanium felt used as current collector at the anode and the carbon GDL used as current collector at the cathode. The different PEMEC MEAs tested, which were;

1. **EWII benchmark cells.** The EWII benchmark cells have been supplied by EWII. They contained 0.3 mg cm^{-2} IrO_x catalyst mixed with Nafion binder in the anode catalyst layer, which were applied to the Nafion membrane by spray coating. On top of the anode catalyst layer, 2.7 mg cm^{-2} iridium metal mixed with Nafion binder had been applicated by the decal method, and which should function as current collector and improve contact between the coarse IrO_x layer and the titanium felt, which contains large pores cf. figure 5.1.4.16. The cathode consisted of 0.5 mg cm^{-2} platinum (60 wt. % Pt/C), and the carbon GDL (Sigracet 35 DC) is hotpressed onto the CCM simultaneously with the decal of the Ir metal layer at 150 °C.

2. **PSI benchmark cells.** The PSI benchmark were prepared at PSI during the author's external stay. A Nafion 117 membrane was pretreated prior to catalyst coating by placing the membrane in a 32.5 % nitric acid solution at 80 °C for one hour followed by washing the membrane one time at room temperature and three times at 80 °C for 1 hr each time. The cathode consisted of 0.5 mg cm^{-2} platinum (platinum supported on carbon catalyst from Tanaka, 47 %) and was spray coated onto the membrane by hand. The anode contained 10.1 mg cm^{-2} IrO_x (IrO_x supported on TiO_2 from Umicore, wt. 90 %) spray coated onto the membrane by hand as well. The catalyst loadings of the PSI benchmark cells are determined from the concentrations of the prepared inks and the amount of ink loaded into the spray gun for application on the MEA. The real loading of the PSI cells may be smaller, but it was not possible to determine the exact loading due to difficulties with weighing due to the hygroscopic Nafion membrane absorbing water from the ink and not enough time to dry the membrane between the measurements due to the demand of the equipment. According to PSI a loading of 0.1 mg cm^{-1} Pt on the cathode and 3.4 mg cm^{-2} IrO_x on the anode is obtained, when applying this amount of ink in the spray gun.

3. **EWII cell without IrO_x layer.** This cell have been supplied by EWII and contains no IrO_x catalyst layer, but does contain 2.2 mg cm^{-2} iridium metal with Nafion binder at the anode and 0.5 mg cm^{-2} platinum (60 wt. % Pt/C) with Nafion binder as cathode. A carbon GDL (35 DC Sigracet) was hotpressed onto the CCM simultaneously with the decal of the Ir metal layer at 150 °C. The iridium metal surface will oxidise to IrO_x immediately at the beginning of the test.

4. **EWII benchmark cell tested with platinum coated Ti felt.** An EWII benchmark cell similar to the benchmark cells described above (bullet 1) was assembled in the cell housing with a platinized titanium felt instead of a pure titanium felt, which were applied for the other cells. It should be noted that there might be in-homogeneities in the platinum coating the Ti felt, causing platinum-free spots.

The primary differences between the PEMEC types and constellations tested are observed at the anode, and drawings of these different anode microstructures can be seen in figure 4.2.7. a) depicts the microstructure of the EWII benchmark cells, b) depicts the microstructure of the PSI benchmark cells, c) depicts the microstructure of the EWII cell without IrO_x and d) depicts the microstructure of the EWII benchmark cell tested with platinized titanium felt. It should be noted that the drawings are not to scale. When assembling the MEAs in the cell test house from EWII, a pressure of 60 kg onto the top of the cell house while tightening the screws by hand.

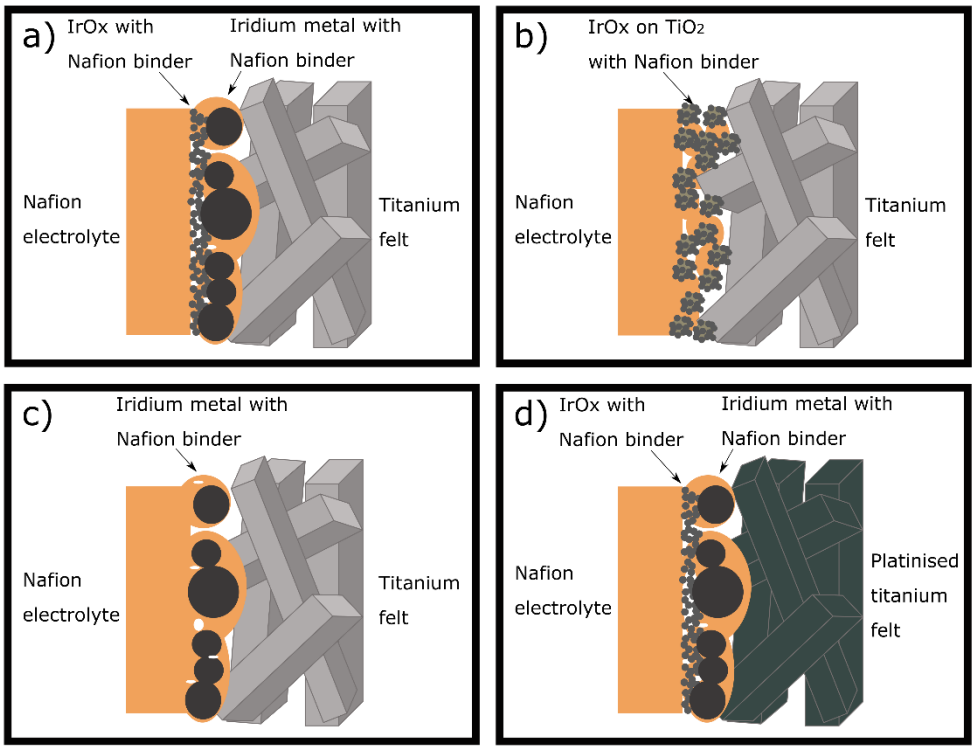

Figure 4.2.7 Schematic drawings of microstructures of the anodes of an EWII benchmark cell (a), of a PSI cells (b), of an EWII cell without IrO_x anode catalyst layer, but only iridium metal layer (c), and of a EWII benchmark cell operated with platinized titanium felt instead of uncoated titanium felt (d), which is usually applied during testing. It should be noted that the drawings are not to scale.

4.2.1 Scanning Electron Microscopy of PEMECs

The microstructure of the EWII benchmark cells was examined with scanning electron microscopy. Different cross section preparation methods have been tried, which were;

1. Cutting the MEA with scalpel
2. Freezing the MEA in liquid nitrogen followed by cutting with scalpel
3. Cutting the MEA with scalpel followed by ion milling with argon atoms for 18 hours in an E-3500 ion milling system from Hitachi with an acceleration voltage of 6 kV.
4. Cutting the MEA with laser done by the company Laser Tech.
5. Cutting the MEA with a FIB probe with an acceleration voltage of 30 kV and a 50 pA current.

Ti felt applied for all the electrolysis tests in this thesis and Ir metal and IrO_x catalyst from EWII, equivalent to the Ir metal and IrO_x catalyst in the EWII cells were also examined with SEM.

The SEM samples were examined with five different SEM microscopes; a Zeiss Supra 35 with a field emission gun and backscatter detector, a Zeiss Merlin SEM microscope with a field emission gun and backscatter detector, a Zeiss EVO MA 10 with a field emission gun and backscatter detector, a TM3000 microscope from Hitachi and with a CrossBeamTM 1540 XB (Carl Zeiss AG). Acceleration voltage, detector type and microscope is specified in the figure text for each of the SEM images shown in section 5.1.

4.3 Solartron 1287 vs. Solartron 1260+Delta

The electrochemical tests of the PEMECs (CV, iV-curves and EIS) have been measured in two different test setups. Common for the two test setups have been the gas supply, water supply and the heating of the water. The water was heated with a heat mantle controlled by a 2216e oven controller from Eurotherm. The water temperature and cell temperature were measured with Pt100 thermoresistors mounted in the water flask and in the stainless steel cell housing close to the water inlet, respectively. Micro diaphragm liquid pumps from KNF (NF 25 KPDC-M) was used to pump the water. The computer software Labsystem developed at DTU Energy combined with a Keithley and ICP modules, were used for communication to the oven controllers and pumps and for monitoring temperatures. The software Elchemea developed at DTU Energy were used for communication with the Solartron 1287 and the Solartron 1260.

CV measurements were conducted with a Solartron 1287. For further details on the CV measurements see section 4.3.1. The maximum current supplied by the Solartron 1287 is 2 A, which for the PEMECs tested in the cell housing from EWII described in section 4.1 (with an active electrode area of 2.9 cm^2) implies that the maximum obtained current density of the PEMECs when using the Solartron 1287 is 0.69 A cm^{-2} (38). The aim in the e-STORE project is to operate PEMECs at current densities up to 5 A cm^{-2}, and therefore another test setup, which could supply up to 15 A, has to be build.

Two test setups were built for electrochemical characterization at high current densities. A Delta Elektronika ES 015-10 or a Delta Electronika SM 18-50 were applied for cell polarization and a Solartron 1260 impedance analyser was used for EIS measurements. DC current determination was done by measuring the potential over a 50 mΩ shunt resistance serially connected with the PEMEC. The Solartron 1260 was connected in parallel to the PEMEC and to the shunt resistance. The Solartron 1260 was supplied with DC cancellation boxes build at DTU Energy for improved AC signal resolution. Though it has been possible to polarise the PEMECs up to 5 A cm^{-2} with the setup, iV-curves and EIS have only been measured up to 3 A cm^{-2}. The reason for this was that the only cooling of the PEMECs was by the heated water supplied to the anode as fuel, and at high current densities (ca. above 1.5 A cm^{-2}) increasing temperatures, due to the high effect of the PEMEC, was influencing the measurements. The water pumps were operating at maximum speed, so further cooling was not possible by increasing the water flowrate and therefore it was chosen to operate at lower current densities.

4.3.1 Cyclic Voltammetry of PEMECs (Solartron 1287)

An EWII benchmark cell, ALIP, a PSI benchmark cell, PSI_s5_3, and an EWII cell without IrO_x were characterized with cyclic voltammetry at 61, 66 and 64 °C, respectively. The cathodes of the cells were flushed with 10 mL min^{-1} hydrogen with 3 vol. % humidity over-night prior to the CV measurements. As described in article 1 the potential of the cathode is assumed to be 0 V vs. SHE at OCV, due to the flushing of the cathode with humidified hydrogen, the acidic environment of the Nafion binder and membrane and that the cathode consists of pure platinum. The exact potential of the cathode is hard to determine, since the pH of the Nafion in the cathode is bot well-known (3) (11) (10). On the other hand it is known that the kinetics of the Pt/H_2

electrode is very fast compared to the kinetics of OER on IrO_x, implying that the primary part of the resistance of the PEMEC originate from the anode and not the cathode (39) (40) (41). Approximately 300 - 500 mL min^{-1} Milli-DI water from Millipore was supplied to the anode during the CV measurements. The cathode was applied as counter and reference electrode and the anode was applied as working electrode, and the potential range were from 0.00 to 1.40 V. Seven cycles were recorded at a potential sweep rate of 50 mV s^{-1}. The data acquisition were conducted with a Solartron 1287.

4.3.2 iV-curves and EIS of PEMECs Measured During OER (Solartron 1260 + Delta)

Experimental conditions during iV-curve measurements such as cell temperature, step size, time between steps, current density range of the iV-curves and whether or not the cathode was flushed with 10 mL min^{-1} hydrogen with 3 vol.% humidity are given in table 4.3.2.1 for each of the examined PEMECs.

Table 4.3.2.1 Experimental parameters during iV-curves measurement on a variety of tested PEMECs.

	Cell 0	**ALIP**	**ATMJ**	**PSI_s5_2**	**PSI_s5_3**	**Pt coated Ti felt cell**
Cell T [°C]	53, 61, 69	55-56, 63, 70-71	56, 64, 70-71	57-60, 66-68, 73-76	58, 66, 74	54-55, 62, 69
i range [A cm^{-2}]	0-1	0-1	0-1	0-3	0-1	0-1
Step size [mA]	50	50	50	i < 0.35 A cm^{-2}: 50 i > 0.35 A cm^{-2}: 500	50	50
Time between steps [s]	20	60	60	120	60	60
H_2 on cathode?	No	Yes	Yes	Yes	Yes	Yes

Experimental parameters during EIS measurements are given in table 4.3.2.2 for the examined PEMECs. EIS was measured galvanostatically at three different temperatures and four to six different current densities. With galvanostatically EIS measurements are meant that the DC load and the AC perturbation are both current controlled. The exact temperatures and current densities are given in table 4.3.2.2.

Table 4.3.2.2 Experimental parameters during EIS measurement on a variety of tested PEMECs.

	Cell 0	**ALIP**	**ATMJ**	**PSI_s5_2**	**PSI_s5_3**	**Pt coated Ti felt cell**
i measurement order [A cm^{-2}]	1.00, 0.69, 0.35, 0.07	0.07, 0.35, 0.69, 1.00	0.07, 0.35, 0.69, 1.00	0.07, 0.35, 0.69, 1.00, 2.00, 3.00	0.07, 0.35, 0.69, 1.00	0.07, 0.35, 0.69, 1.00
Cell T measurement order [°C]	61, 69, 53	63, 70-71, 55-56	64, 70-71, 56	66-68, 73-76, 57-60	66, 74, 58	62, 69, 54-55
Frequency range [Hz]	96,850-0.01	968,500-0.0117	968,500-0.0117	968,500-0.0117	968,500-0.0117	968,500-0.0117
Amplitude [mA cm^{-2}]	24.5	29.3	29.3	29.3	29.3	29.3
Points per decade	12	12	12	12	12	12
Time at particular i before EIS measurements [min]	20	20	20	20	20	20
Time to ramp T and reach steady state [min]	60	60	60	60	60	60

Table 4.3.2.3 shows potentials measured at the four current densities and three temperatures on the reference EWII benchmark cell, cell0. The potential change the last five minutes before each EIS measurement at the three temperatures and four current densities on the reference EWII benchmark cell, cell 0, is given in table 4.3.2.4. The potential change just before the EIS measurements is a measure of how steady the system was just before the EIS measurements. Tables similar to table 4.3.2.3 and 4.3.2.4 for all the other cells tested with EIS (the cells from table 4.3.2.2) can be found in appendix A.

Table 4.3.2.3 Potentials measured during EIS measurements at four different current densities and at three different temperatures on the reference EWII benchmark cell, cell 0.

		Current density [A cm^{-2}]			
		1.00	**0.69**	**0.35**	**0.07**
Tem-	**53**	1.87 V	1.76 V	1.64 V	1.52 V
pera-	**61**	1.80 V	1.72 V	1.61 V	1.50 V
ture [°C]	**69**	1.77 V	1.69 V	1.59 V	1.48 V

Table 4.3.2.4 Potential change the last 5 minutes before EIS measurements at four different current densities and three different temperatures on the reference EWII benchmark cell, cell 0.

		Current density [A cm^{-2}]			
		1.00	**0.69**	**0.35**	**0.07**
Tempera-	**61**	0.2 mV min^{-1}	0.0 mV min^{-1}	0.0 mV min^{-1}	0.0 mV min^{-1}
ture [°C]					

The EIS data was analyzed and plotted using the software Ravdav developed at DTU Energy (42). All other data treatment have been done using the software Python. Electrochemical test histories of iV-curve and EIS tests can be found for all cells the appendix B.

5. Results

5.1 Microstructure

In this section, the microstructure of the EWII cell is examined. SEM sample preparation of PEMECs is hard, and it has only been possible to obtain proper SEM images of one of the PEMEC types, which was the EWII benchmark cells.

5.1.1 Sample Preparation of PEMEC SEM Samples

Various methods of sample preparation have been done. Figure 5.1.1.8 show SEM images of an EWII benchmark PEMEC after electrochemical testing, where the SEM sample preparation consisted in cutting with a scalpel (left) and where the SEM sample preparation consisted in freezing the sample with liquid nitrogen followed by cutting with scalpel. Large flakes of the Nafion membrane can be observed in both images, and the amount of flakes in the Nafion membrane seem equal for the two preparation methods. This imply that cutting with scalpel introduce flakes in the Nafion membrane and cooling with liquid nitrogen prior to the cutting does not seem to influence the sample result.

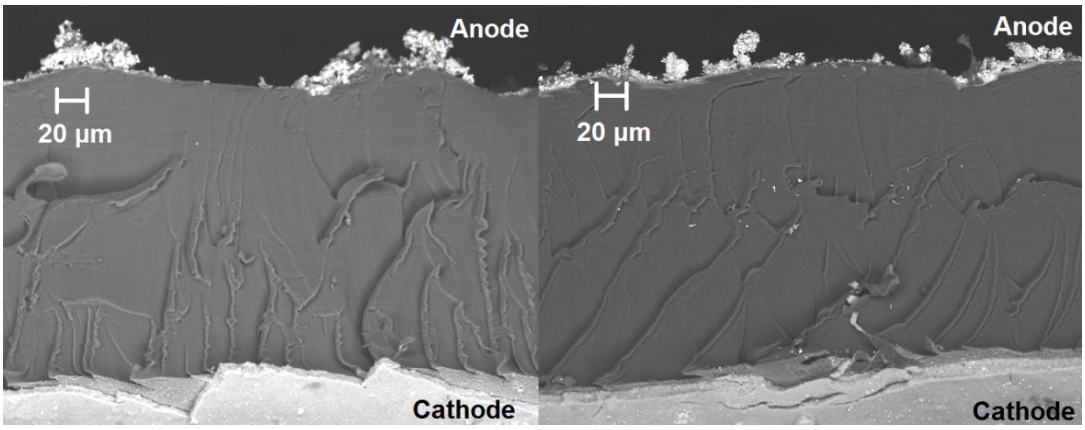

Figure 5.1.1.8 Backscattered electrons SEM images of cross sections of a used EWII benchmark cell, which has been cut with a scalpel (left) and which has been frozen with liquid nitrogen prior to cutting with scalpel (right). The left image is equivalent to the right image in figure 5.1.2.13. The images were obtained with a Zeiss Merlin microscope at an acceleration voltage of 15 kV.

Another sample preparation method tried, was ion milling of the EWII benchmark PEMECs, which is shown to the left in figure 5.1.2.13 and to the left in figure 5.1.2.12. Reasonable SEM images were obtained with this preparation method. However, it was furthermore tried to obtain better SEM images by additionally cutting the ion milled SEM sample with a FIB, and SEM images of this is shown to the right in figure 5.1.2.12. However, if the sample was cut with the FIB for too long time, the Nafion membrane started to degrade as observed in the white circle in figure 5.1.1.9.

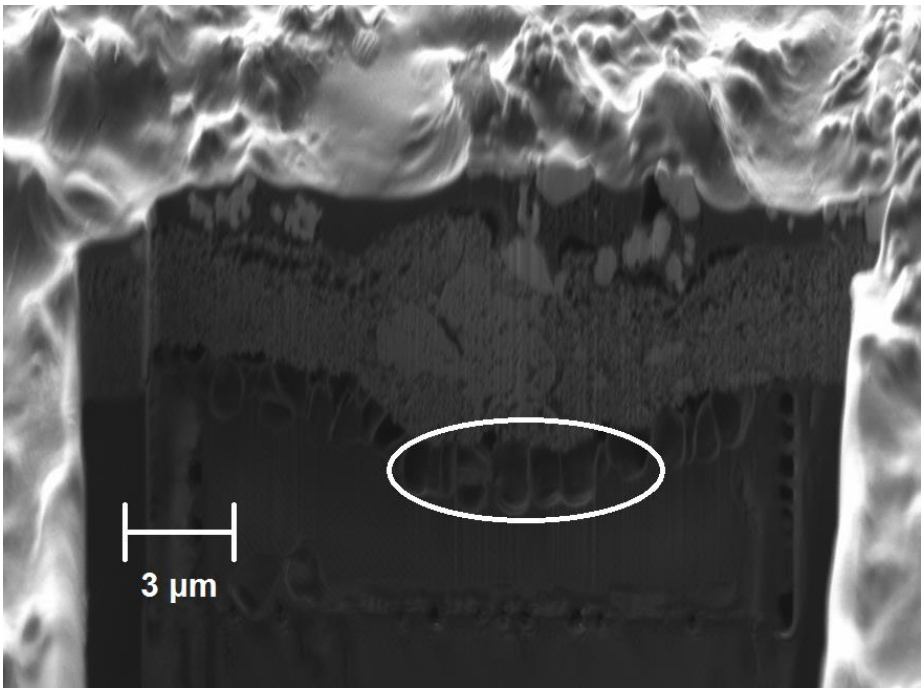

Figure 5.1.1.9 Secondary electrons SEM image of a cross section of the anode of a pristine EWII benchmark cell cut with FIB. Holes in the Nafion membrane caused by FIB for too extensive time is marked with the white circle. The image is obtained with a CrossBeamTM 1540 XB at an acceleration voltage of 2 kV.

Another sample preparation method tried was laser cutting the EWII benchmark PEMECs. This is shown in figure 5.1.1.10, where big holes are observed in the Nafion membrane caused by heating of the membrane during laser cutting. It was tried to remove the holes by ion milling the laser cut sample, which is shown in figure 5.1.1.11, however, it was not possible to remove the holes completely by ion milling the laser cut SEM sample.

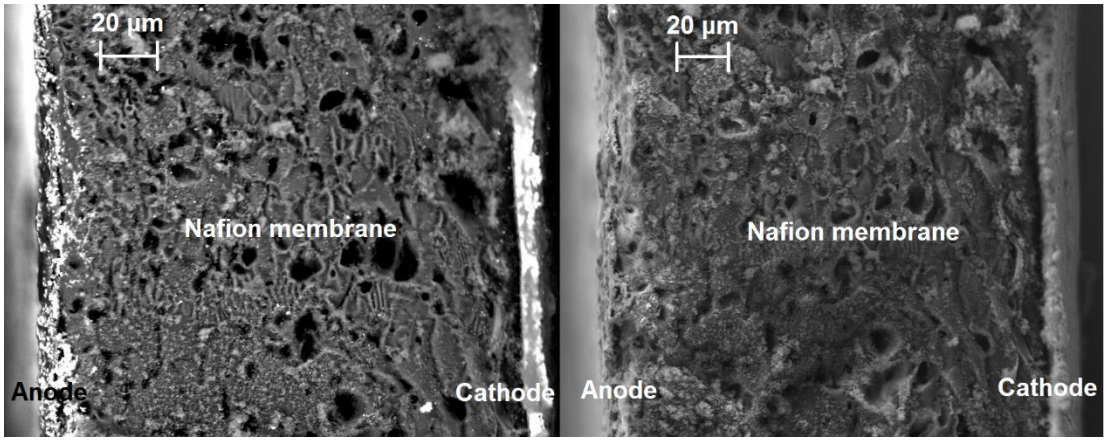

Figure 5.1.1.10 Backscattered electrons SEM images (left) and secondary electrons SEM image of a cross section of a pristine EWII benchmark cell, which has been laser cut prior to SEM examination. Big holes are seen in the Nafion membrane, which are caused by the laser, probably due to heating of the membrane. The images are obtained at a Zeiss EVO MA 10 microscope at an acceleration voltage of 15 kV.

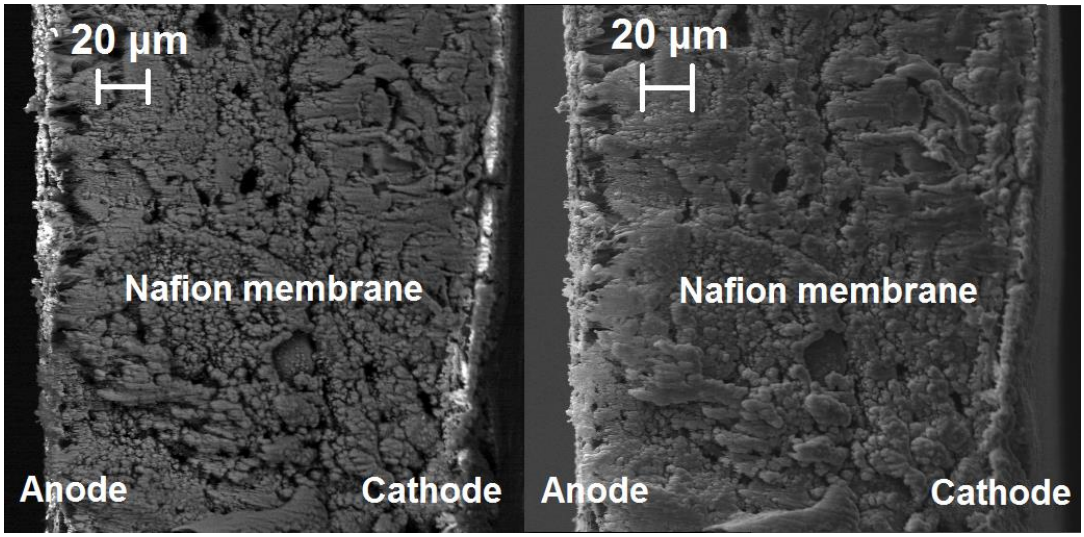

Figure 5.1.1.11 Backscattered electrons SEM images (left) and secondary electrons SEM image of a cross section of a pristine EWII benchmark cell, which has been laser cut and ion milled prior to SEM examination. Big holes are seen in the Nafion membrane, which are caused by the laser, probably due to heating of the membrane, and which have not been possible to remove with ion milling. The images are obtained at a Zeiss EVO MA 10 microscope at an acceleration voltage of 15 kV.

5.1.2 EWII Benchmark PEMEC MEA

As described in article 1, the EWII benchmark cells consist of a microporous IrO_x layer with Nafion binder with a porous Ir metal layer with Nafion binder on top, as seen in figure 5.1.2.12. According to EWII Fuel Cells A/S the size of the IrO_x particles is 9 nm, and from figure 5.1.2.12 the size of the Ir metal particle can be approximated to 1 µm.

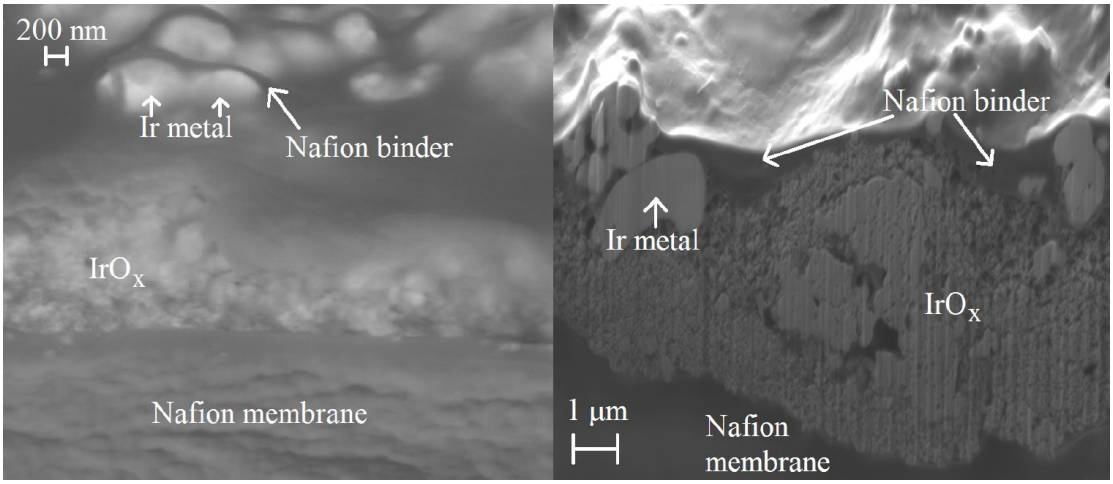

Figure 5.1.2.12 Backscattered electrons SEM image of a cross section of an ion milled anode of a pristine EWII benchmark cell (left) and secondary electrons SEM image of a cross section of the anode of a pristine EWII bench-

mark cell cut with FIB (right). The IrOx catalyst layer containing Nafion binder is observed on top of the Nafion membrane. Ir metal particles functioning as current collector are observed on top of the IrO_x layer. The Ir metal current collector layer does also contain Nafion binder, which is observed as black shadows between the Ir metal particles. The left image is obtained with a Zeiss Supra 35 microscope at an acceleration voltage of 10 kV and the right image is obtained with a CrossBeamTM 1540 XB at an acceleration voltage of 2 kV.

Figure 5.1.2.13 shows a pristine EWII benchmark cell to the left and an EWII benchmark cell after electrochemical testing to the right. As described in article 1, it can be observed that some of the Ir metal and IrO_x have been peeled off the Nafion membrane during detachment of Ti felt, which have been attached the anode during electrochemical testing. This may imply a bad contacting between the Nafion membrane and the IrOx and Ir metal layers, since the Ti felt easily removes it.

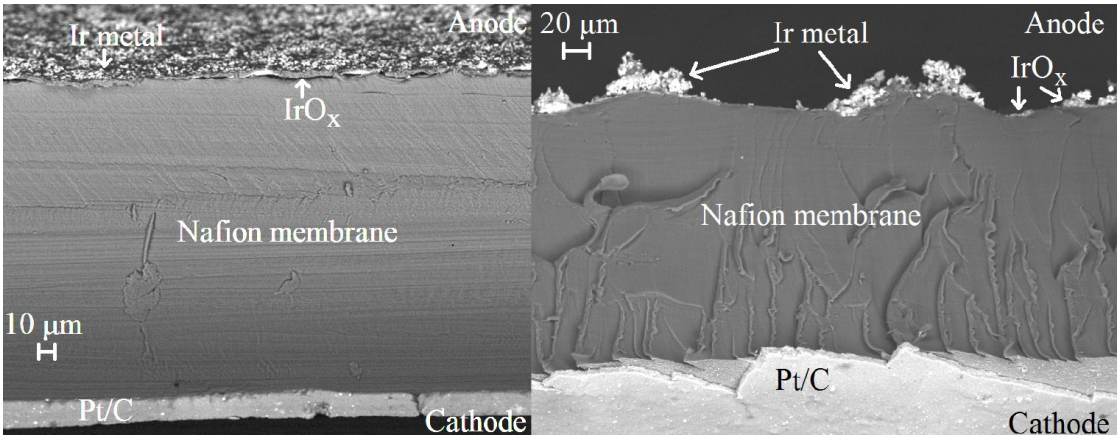

Figure 5.1.2.13 Backscattered electrons SEM images of cross sections of an ion milled pristine EWII benchmark cell (left) and a used EWII benchmark cell cut with a scalpel (right). A fine IrO_x catalyst layer is seen on the Nafion membrane of the pristine sample and the IrO_x layer is in contact with a well dispersed Ir metal current collector layer, whereas the IrO_x catalyst layer and the Ir metal current collector has been peeled off the used EWII benchmark cell during detachment of titanium felt after operation. The left image was obtained with a Zeiss Supra 35 microscope at an acceleration voltage of 10 kV, and the right image was obtained with a Zeiss Merlin microscope at an acceleration voltage of 15 kV.

5.1.3 Iridium Metal

SEM images of the Ir metal applied in the EWII cells are shown in figure 5.1.3.14. Agglomerates of Ir metal particles of two different sizes are observed, and the particle size of the big Ir metal particles are approximately 1 µm cf. figure 5.1.2.12 showing the Ir metal particles in the PEMEC.

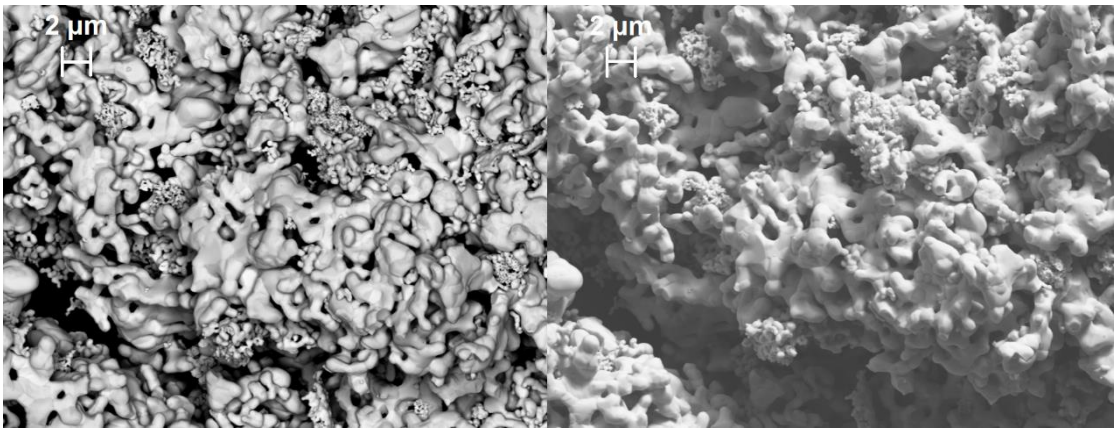

Figure 5.1.3.14 Backscattered electrons SEM image (left) and secondary electrons SEM image (right) of the iridium metal from EWII. The images were obtained with a Zeiss Supra 35 microscope at an acceleration voltage of 15 kV.

5.1.4 Iridium Oxide

SEM images of the IrO_x catalyst applied in the EWII cells are shown in figure 5.1.4.15. A very porous structure of the IrO_x is observed, and it is not possible to determine particle size of the IrO_x from the SEM images.

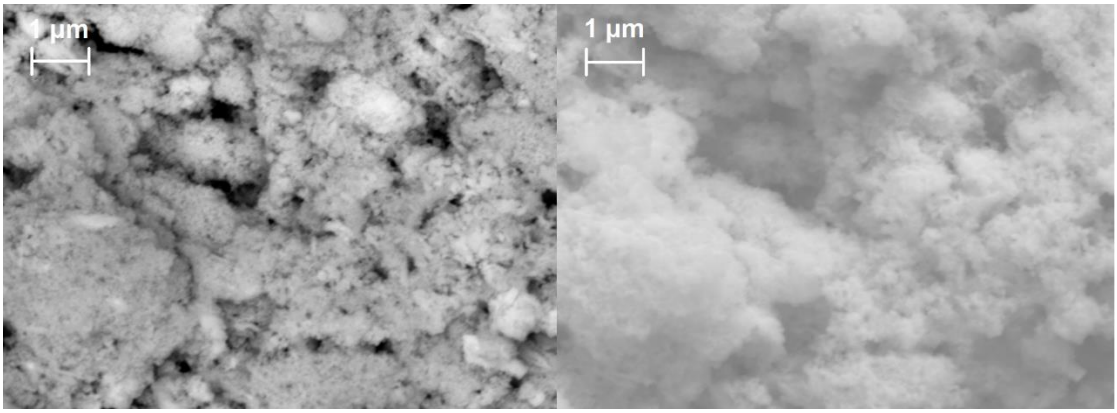

Figure 5.1.4.15 Backscattered electrons SEM image (left) and secondary electrons SEM image (right) of the IrO_x catalyst from EWII. The images were obtained with a Zeiss Supra 35 microscope at an acceleration voltage of 15 kV.

5.1.5 Titanium Felt

SEM images of the Ti felt applied in all the electrolysis tests in this thesis are seen in figure *5.1.4.16*. Large pores (100 µm range) are observed between the squared Ti fibers, which are approximately 25 µm on each side.

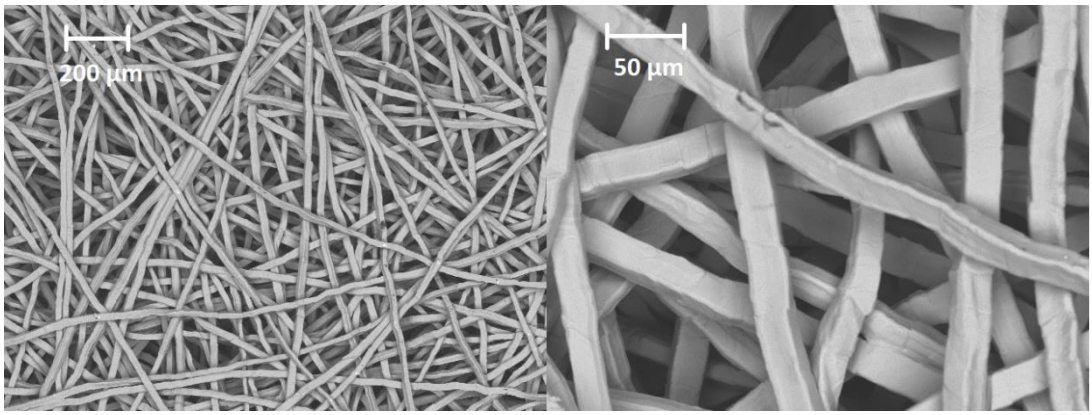

Figure 5.1.4.16 Backscattered electrons SEM images of the Ti felt applied for electrolysis testing. The images were obtained with a TM3000 microscope from Hitachi at an acceleration voltage of 15 kV.

5.2 Cyclic Voltammograms

Cyclic voltammetry have been measured on a variety of PEMECs with a scan rate of 50 mV s^{-1}, in the potential region 0.0 - 1.4 V and with the cathode flushed with 10 mL min^{-1} moisturized hydrogen with 3 vol. % humidity. As described in article 1 these experimental conditions imply that primarily the redox properties of the anode is seen in the CVs, since the potential of the cathode is close to 0 V vs. SHE due to the nature of the cathode consisting of platinum in an acidic environment due to the Nafion membrane flushed with moisturized hydrogen. Though the pH of Nafion in the cathode is not well-know, it is known that the kinetics of the Pt/H_2 cathode of a PEMEC is much faster than the IrO_x/O_2 anode meaning that the primary contributor to the total cell polarization resistance arise from the anode implying the potential of the cathode to be close to 0V vs. SHE. (3) (11) (10) (39) (40) (41). CVs measured on three different EWII benchmark cells with nitrogen-saturated water supplied to the anode are shown in figure 5.1.5.17. These CVs were measured after EIS measurements at potentials up to 1.4 V meaning that the Ir-metal layers in the cells were oxidized to some extent. In figure 5.1.5.17 it is noticed that the peak currents of the redox peaks seen in the CVs are slightly varying between the three cells, however, the shape of all three CVs are similar and show redox peaks at 0.77 and 1.23 V and an increase in anodic current density at 1.4 V due to oxygen evolution as described in article 1. The redox peak at 0.77 V is due to oxidation of Ir^{3+} to Ir^{4+}, and the redox peak at 1.23 V is due to oxidation of Ir^{4+} to Ir^{5+}. (18) (43) (27) A list of iridium redox peaks reported by various references can be found in article 1. Furthermore, the CVs almost have no slope in the potential region 0.07 – 0.40 V, which suggests that no faradaic reactions are taking place at these potentials in the EWII benchmark cells. Negative current densities are observed at 0.00 V to approximately 0.07 V in all three CVs, which originate from hydrogen evolution on the IrO_x anode catalyst. Positive potentials are observed due to concentration differences of the hydrogen gas at the anode and cathode cf. Nernst equation given in equation (16). E is the cell potential, $E^{0'}$ is the formal potential of the electrode, R is the gas constant, T is the temperature, n is the number of electrons involved in the reaction, F is Faradays constant, C_O^* is the concentration of the oxidized specie at the surface of the electrode and C_R^* is the concentration of the reduced specie at the surface of the electrode. The equation can both be used when considering a full cell or a half-cell.

$$E = E^{0\prime} + \frac{RT}{nF} ln \frac{C_O^*}{C_R^*} \quad (16)$$

When considering the cathode of the PEMECs during CV measurements, the electrode is flushed with hydrogen, which means that the activity of hydrogen is 1. The concentration of protons at the cathode is determined by the Nafion membrane, which is acidic and $E^{0'}$ of the hydrogen evolution reaction is 0 V. Considering the anode of the same PEMECs during CV measurements, $E^{0'}$ is 0 V, as at the cathode, since it is the same electrochemical reaction taking place, the concentration of protons is the same as at the cathode, since the two electrodes are in contact with the same acidic Nafion membrane, but the concentration of hydrogen on the anode is much lower than the concentration of hydrogen at the cathode since the anode is not flushed with hydrogen and only small amounts of hydrogen are produced due to the reduction of protons. These considerations imply that the last term of the Nernst equation must be 0.0 V for the cathode, but slightly positive for the anode due to the very small hydrogen concentration in the denominator of the last term of the Nernst equation for the anode.

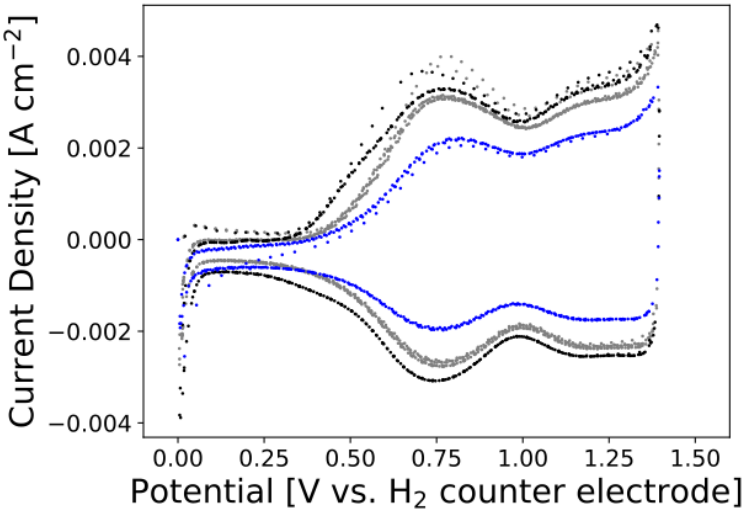

Figure 5.1.5.17 CVs measured on three EWII benchmark cells with a sweep rate of 50 mV s^{-1} at 61-63 °C and ambient pressure. The CVs were measured after EIS had been measured at potentials up to 1.4 V, meaning that the cells are slightly initiated. The cathode consisted of platinum flushed with 10 mL min^{-1} moisturized hydrogen with 3 vol. % humidity. The anode was flushed with nitrogen saturated milli-DI water. These experimental conditions imply that only the redox properties of the anode catalyst are displayed in the CV.

Figure 5.1.5.18 depicts CVs measured on various PEMEC types at 63-66 °C; the EWII benchmark cell, ALIP (figure 5.1.5.18 a)), the PSI benchmark cell, PSI_s5_3 (figure 5.1.5.18 b)) and the EWII cell without IrO_x catalyst (figure 5.1.5.18 c)). In all three subfigures, CVs measured on the pristine PEMECs are shown in gray (when just assembled in the cell house and the cathode has been flushed with moisturized hydrogen with 3 vol. % humidity and nitrogen saturated water has been supplied to the anode overnight) CVs of the initiated PEMECs are shown in black (when the cell has been operated at 1 A cm^{-2} overnight with moisturized hydrogen with 3 vol. % humidity supplied to the cathode and oxygen saturated water supplied to the anode) and a CV

measured on the partly oxidized EWII benchmark cell, ALIP, after EIS measurements up to 1.4 V is shown in blue in figure 5.1.5.18 a). In figure 5.1.5.18 a) it is seen that the same redox peaks are observed for the pristine, the partly oxidized and the initiated EWII benchmark cell, and these are observed at 0.77 and 1.23 V as earlier described, however, the peak current of the two redox peaks increase when the EWII benchmark cell is oxidized during initiation. This increase in peak current is due to the oxidation of the Ir metal layer at the anode of the EWII benchmark cell cf. figure 4.2.7 in section 4.2. Furthermore, it is noticed that the CV in the potential region 0.00-0.30 V is shifted to more negative current densities leading to negative current densities even in the anodic sweep, when the cell has been initiated. The CVs measured on the pristine and initiated PSI benchmark cell, PSI_s5_3, shown in figure 5.1.5.18 b) are overlapping, which imply that the catalyst material is not activated further by oxidation during initiation of the PSI benchmark cell, which is according to the microstructure, which consists of IrO_x and no Ir-metal cf. figure 4.2.7 in section 4.2 meaning that all the iridium is oxidized prior to initiation. Large hysteresis is observed in the CVs of the PSI benchmark cell in the full potential range, which is due to a large double layer capacitance in the anode catalyst layer due to the insolating TiO_2 phase cf. figure 4.2.7 in section 4.2. In figure 5.1.5.18 c) a very flat CV with no redox peaks but only a small double layer capacitance is observed for the pristine EWII cell without IrO_x, but with Ir-metal (gray graph). However, when the EWII cell without IrO_x has been activated (black graph) over-night at 1.00 A cm-2, the CV shows a clear redox peak at 0.77 V, which originate from the oxidation of Ir^{3+} to Ir^{4+}, and a small redox peak at 0.50 V, which may be a pre-oxidation peak originating from the oxidation of the Ir-metal to Ir^{3+} (43) (18). This major increase in redox activities of the Ir-metal upon initiation implies that the Ir-metal in the EWII cells is electrochemically active after the formation of an IrO_x layer on the surface of the Ir-metal particles, which are formed during oxidation at higher potentials, also called the initiation (1 A cm^{-2}, 2.6-2.1 V).

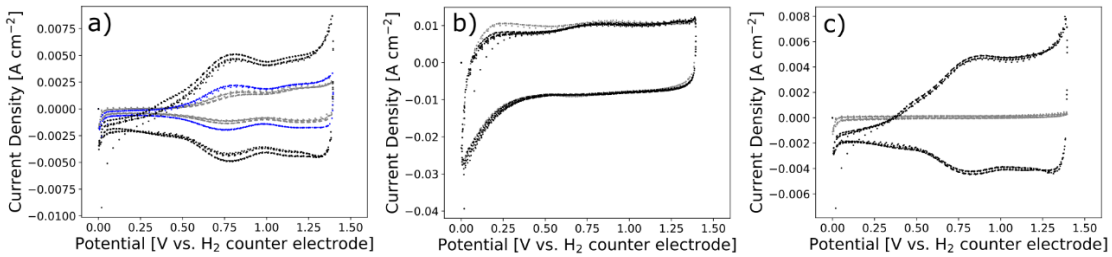

Figure 5.1.5.18 CVs measured on the EWII benchmark cell, ALIP, (a), on the PSI cell, PSI_s5_3 (b) and on the EWII cell without IrO_x catalyst (c) with a sweep rate of 50 mV s^{-1} at 63-66 °C and ambient pressure. Gray CVs were measured on pristine samples prior to initialization, the blue CV of the EWII benchmark cell, ALIP, was measured after EIS had been measured at potentials up to 1.4 V, meaning that the cell was slightly initiated, and black CVs were measured after initialization with oxygen saturated water supplied to the anode. The cathode consisted of platinum flushed with 10 mL min^{-1} moisturized hydrogen with 3 vol. % humidity. The anode was flushed with nitrogen saturated milli-DI water before the initialization and with oxygen saturated water after the initialization.

The CVs in figure 5.1.5.18 are compared in figure 5.1.5.19, in which figure 5.1.5.19 a) compares CVs measured on the various pristine PEMECs and figure 5.1.5.19 b) compares CVs measured on the various PEMECs initiated over-night at 1 A cm^{-2}. In figure 5.1.5.19 b) it is noted that the CVs of the initiated EWII benchmark cell and of the EWII cell without IrO_x catalyst is equal, which implies that the amount of activated IrO_x functioning as catalyst after initiation is the same for the two different EWII cells. This is a bit surprising, since the EWII benchmark cell, ALIP,

contains more Ir-metal current collector and additionally IrO_x catalyst than the EWII cell without IrO_x, ATMJ, and one would therefor expect the redox activity of the EWII benchmark cell to be slightly higher than for the EWII cell without IrO_x. From figure 5.1.5.19 a) and 5.1.5.19 b) it is seen that the current densities of the CV of the PSI benchmark cell, PSI_s5_3, is much larger than the current densities measured for the two EWII cells.

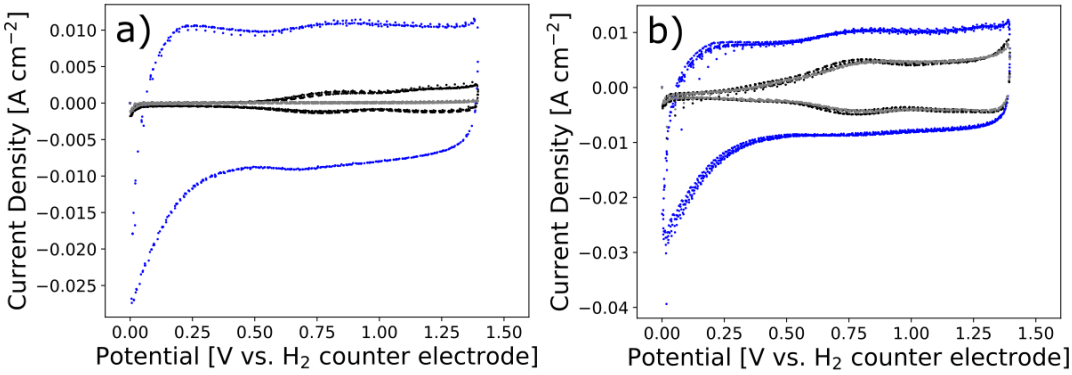

Figure 5.1.5.19 CVs measured with a sweep rate of 50 mV s^{-1} at 63-66 °C and ambient pressure on various pristine PEMECs of various types (a) and CVs measured on the same PEMECs after initialization at 1 A cm-2 over night with oxygen-saturated water. Black curves were CVs measured on the EWII benchmark cell, ALIP, blue curves were measured on the PSI cell, PSI_s5_3 and gray curves were measured on the EWII cell without IrO_x catalyst. The cathode consisted of platinum flushed with 10 mL min^{-1} moisturized hydrogen with 3 vol. % humidity. The anode was flushed with nitrogen saturated milli-DI water before the initialization and with oxygen saturated water after the initialization.

Table 5.1.5.5 IrO_x content, Ir-metal current collector content and total Ir content for the three PEMEC tested with CV.

	IrO_2 [mg cm^{-2}]	**Ir metal current collector [mg cm^{-2}]**	**Total Ir content [mg cm^{-2}]**
EWII benchmark cell, ALIP	0.3	2.7	2.95
PSI benchmark cell, PSI_s5_3	3.4	0	2.8
EWII cell without IrO_x catalyst, ATMJ	0	2.2	2.2

5.2.1 Calculation of IrO_x Surface Charge from CV Curves

The charge associated with an anodic or cathodic scan of a CV can be determined from equation (17) in which Q is the charge in C, E_1 and E_2 is the lower and upper boundaries of the potential range at which i, the current density in A cm^{-2}, as function of E, the potential in V, is integrated, A is the electrode area and ν is the scan rate of the CV.

$$Q = \frac{\int_{E_1}^{E_2} i(E) \cdot A}{\nu} \tag{17}$$

The charge of the anodic scan of the second cycle of the CVs shown in figure 5.1.5.19 of the three different PEMEC types have been calculated and are listed in table 5.1.5.6. From the obtained charge the electrochemical surface area, ECSA, can be calculated from equation (18), in which Q is the charge calculated from equation (17), $6.24150934 \cdot 10^{18}\ \frac{e}{C}$ is the amount of elementary particle charges per coulomb, q is the number of electrons transferred during oxidation of an iridium atom, which is set to one, when considering the oxidation of Ir^{3+} to Ir^{4+}, and $A_{Per\ Ir\ surface\ atom}$ is the surface area per iridium atom in IrO_x, which is calculated from the unit cell of IrO_x. This imply that the charge of the surface (further on denoted the surface charge) is not the charge of the double layer, as often seen in literature, but the charge associated with the electron transfers in the surface iridium atoms during redox reactions. According to Brewer et al. (44) the unit cell of IrO_2 has a rutile structure, and the lattice parameters are a=b=4.5051 Å and c=3.1586 Å. If it is assumed that the $a \cdot b$ side of the unit cell is the electrochemically active side, which contains 1 Ir atom, then $A_{Per\ Ir\ surface\ atom} = (4.5051\text{Å})^2 = 20.2959\text{Å}^2$.

$$ECSA = \frac{Q \cdot 6.24150934 \cdot 10^{18} \frac{e}{C} \cdot A_{Per\ Ir\ surface\ atom}}{q} \tag{18}$$

ECSA has been calculated for all three PEMEC types based on Q calculated from the CVs in figure 5.1.5.19 and are listed in table 5.1.5.6.

Table 5.1.5.6 Charge, Q, and electrochemical surface area, ECSA, calculated for the three different PEMEC types from the anodic scan of the second cycle of the CVs in figure 5.1.5.19.

	Q [mC]		**ECSA [m²]**	
	Pristine	**Initialized**	**Pristine**	**Initialized**
EWII benchmark cell, ALIP	60.4	239.9	$7.66 \cdot 10^{-2}$	$3.040 \cdot 10^{-1}$
EWII cell without IrO_x, ATMJ	7.4	220.7	$9.4 \cdot 10^{-3}$	$2.796 \cdot 10^{-1}$
PSI benchmark cell, PSI_s5_3	701.3	646.3	$8.884 \cdot 10^{-1}$	$8.188 \cdot 10^{-1}$

According to table 5.1.5.6 the charge calculated from the CV of the PSI benchmark cell is decreasing 55 mC corresponding to 7.8 %, which means that the charge of the electrochemical active surface of the PSI benchmark cell, PSI_s5_3, is almost constant before and after initiation. This suggest that no further oxidation is taking place upon initiation, which is in accordance with the fact that the PSI benchmark cells only consists of IrO_x cf. figure 4.2.7. On the other hand the charge of the EWII cell without IrO_x, ATMJ, has increased with 213.3 mC upon initiation, which is a charge increase of 2882 % corresponding to 29 times the original charge. This suggest that the Ir metal is oxidized during initiation. The charge of the EWII benchmark cell, ALIP, increases 179.5 mC corresponding to 297 % or approximately 3 times the original charge during initiation. It is interesting that the charge increase of the EWII cell without IrO_x is bigger than the charge increase of the EWII benchmark cell upon initiation, even though the Ir metal loading is slightly higher for the EWII benchmark cell than the EWII cell without IrO_x cf. table 5.1.5.5., which compares the total Ir content in the three PEMECs tested with CV.

5.2.2 Calculation of Maximum Surface Charge from Ir Loading and Particle Geometry

It was unexpected that the CV derived surface charge of the Ir-metal layer is bigger for the EWII cell without IrO_x, since this cell contains less Ir-metal than the EWII benchmark cell cf. table 5.1.5.5 and the particle size of the Ir-metal particles are bigger than the particle size of the IrO_x particles (approximately 1 µm cf. section 5.1 compared to approximately 10 nm according to EWII) meaning that the ECSA of the EWII cell without IrO_x is supposed to be lower than the ECSA of the EWII benchmark cell. The ECSA is therefore calculated based on the loading given in table 5.1.5.5 for the three cells and the particle sizes determined from the SEM images in section 5.1. First the total volume of the Ir and IrO_x particles, $V_{total\ Ir\ or\ IrO_x}$, are calculated from equation (19), where $m_{Ir\ or\ IrO_x}$ is the loading of Ir metal or IrO_x catalyst found in table 5.1.5.5, $A_{electrode}$ is the geometrical electrodearea, which is 2.9 cm^2 and $\rho_{Ir\ or\ IrO_x}$ is the density of Ir metal or IrO_x, which is 22.56 g cm^{-3} for Ir and 11.66 g cm^{-3} for IrO_x.

$$V_{Total\ Ir\ or\ IrO_x} = \frac{m_{Ir\ or\ IrO_x} \cdot A_{electrode}}{\rho_{Ir\ or\ IrO_x}} \tag{19}$$

The total amount of Ir or IrO_x particles, $n_{Ir\ or\ IrO_x\ particles}$, is calculated from equation (20), in which $V_{Ir\ or\ IrO_x\ particle}$ is the volume of a Ir metal or IrO_x particle calculated from equation (21), in which it is assumed that the particles are spherical with the particlediameter, d (1 µm for Ir and 10 nm for IrO_x).

$$n_{Ir\ or\ IrO_x\ particles} = \frac{V_{Total\ Ir\ or\ IrO_x}}{V_{Ir\ or\ IrO_x\ particle}} \tag{20}$$

$$V_{Ir\ or\ IrO_x\ particle} = \frac{4}{3} \cdot \pi \cdot \left(\frac{d}{2}\right)^3 \tag{21}$$

In order to calculate the ECSA of the PEMECs the surface area of a spherical Ir or IrO_x particle is calculated from equation (22).

$$A_{Ir\ or\ IrO_x\ particle} = 4 \cdot \pi \cdot \left(\frac{d}{2}\right)^2 \tag{22}$$

Now ECSA is calculated from equation (23).

$$ECSA = A_{Ir\ particle} \cdot n_{Ir\ particles} + A_{IrO_x\ particle} \cdot n_{IrO_x\ particles} \tag{23}$$

From ECSA can the total charge be calculated from equation (24). Again $A_{Per\ Ir\ surface\ atom} = 20.2959\ Å^2$, since it is assumed that the surface of the Ir metal particles are oxidized and covered with IrO_2. q is one, since it is assumed the surface iridium atoms are oxidized from 3+ to 4+ meaning that one electron is transferred per iridium atom.

$$Q = \frac{ECSA \cdot q}{A_{Per\ Ir\ surface\ atom} \cdot 6.24150934 \cdot 10^{18}\ \frac{e}{C}} \tag{24}$$

ECSA and Q given in table 5.1.5.7 are calculated as described above based on the loading of the PEMECs (found in table 5.1.5.5) and the particle sizes of the Ir metal and the IrO_x. By comparing table 5.1.5.7 to table 5.1.5.6 it is realized that ECSA and maximum Q calculated from the

Ir and IrO_x loading are similar to the ECSA and Q calculated from the CVs measured before initiation of the PEMECs. This implies that about one monolayer on the surface of the IrO_x and Ir metal particles are electrochemically active in the pristine PEMEC. The ECSA and Q calculated from the CVs measured after initiation is for the PSI benchmark cell similar to the ECSA and Q calculated from the CV measured before initiation and the ECSA and Q determined from the IrO_x loading. However, the ECSA and Q of the EWII benchmark cell, ALIP, and the EWII cell without IrO_x, ATMJ, calculated from the CVs measured after initiation of the cells are higher than the ECSA and Q calculated from the CVs of the pristine samples and ECSA and Q calculated from the Ir and IrO_x loading. This implies that either is the surface of the iridium atoms increased upon oxidation due to an increase in the surface porosity of the Ir metal particles or a deeper surface region than a monolayer of the big Ir metal particles are activated upon initiation.

Table 5.1.5.7 Charge, Q, and electrochemical surface area, ECSA, calculated for the three different PEMEC types based on the Ir metal and IrO_x catalyst loading given in table 5.1.5.5 and the assumption that only a surface monolayer of IrO_x on the Ir metal particles and IrO_x particles are electrochemically active.

	Q [mC]	**ECSA [m²]**
EWII benchmark cell, ALIP	36.9	$4.6689 \cdot 10^{-2}$
EWII cell without IrO_x, ATMJ	1.33	$1.690 \cdot 10^{-3}$
PSI benchmark cell, PSI_s5_3	399.1	$5.05626 \cdot 10^{-1}$

It is now examined, if all the Ir metal volume has been oxidized and are electrochemically active and all the IrO_x particle volume are electrochemically active. It is assumed that all Ir atoms are oxidized and electrochemically active. The amount of Ir atoms, $n_{It\ atoms}$ in mol, are calculated from equation (25), where $m_{Ir\ or\ IrO_x}$ is the loading of Ir metal or IrOx catalyst, $A_{electrode}$ is the geometrical area of the electrode and $M_{Ir\ or\ IrO_x}$ is the molecular weight of the Ir metal or IrO_x.

$$n_{Ir\ atoms\ from\ Ir\ or\ IrO_x} = \frac{m_{Ir\ or\ IrO_x} \cdot A_{electrode}}{M_{Ir\ or\ IrO_x}} \tag{25}$$

Now the charge, Q in C, can be calculated from the amount of Ir atoms according to equation (26), when assumed that all iridium in the Ir metal and the IrO_x is electrochemically active.

$$Q_{Ir\ atoms} = \frac{(n_{Ir\ atoms\ from\ ir} + n_{Ir\ atoms\ from\ IrO_x}) \cdot q \cdot N_A}{6.24150934 \cdot 10^{18}\ \frac{e}{C}} \tag{26}$$

Q based on the assumption that all iridium in the Ir metal particles are oxidized to IrO_2 and electrochemically active, is given in table 5.1.5.8. Actually Q in table 5.1.5.8 may even be a higher number, since the charge transferred per iridium atom, q, in these calculations have been set to 1 for the oxidation of Ir^{3+} to Ir^{4+}, but may actually be up to 4 for bulk Ir metal particles, which may be oxidized from Ir^0 to Ir^{4+} at 1.4 V. Comparison of Q in table 5.1.5.8 and Q after initiation in table 5.1.5.6 show a factor 10 difference between the two Q-values (which may be even higher, if q is set to e.g. 4), which imply that not all the Ir atoms in the Ir particles are oxidized and electrochemically available after initiation.

Table 5.1.5.8 Charge, Q, and electrochemical surface area, ECSA, calculated for the three different PEMEC types based on the Ir metal and IrO_x catalyst loading given in table 5.1.5.5 and the assumption that all Ir metal is oxidized to IrO_x and all IrO_x is electrochemically active.

	Q [mC]
EWII benchmark cell, ALIP	4290
EWII cell without IrO_x, ATMJ	3190
PSI benchmark cell, PSI_s5_3	4230

5.2.3 Initial Activation of the IrO_x Electrodes

A strong decrease in potential have been observed at the very beginning of the initiation at 1.00 A cm^{-2} for all three PEMECs; the EWII benchmark cell, the PSI benchmark cell and the EWII cell without IrO_x. This is shown in figure 5.1.5.20. This strong potential decrease in the very beginning of the initiation of the cells may be explained by the activation of the Ir metal particles as described above based on the ECSA and Q calculations. It has been speculated if this decrease in potential during the initiation of the PEMECs can be explained by reaction between crossover hydrogen (the cathode is flushed with pure humidified hydrogen over-night prior to initiation) and oxygen produced at the anode, but reaction between crossover hydrogen and produced oxygen at the anode, would cause a potential increase at the beginning of the initiation cf. Nernst equation given in equation (16) instead of a potential decrease as observed. Therefore, the potential decrease during the initiation of the PEMECs is ascribed to activation of the IrO_x electrodes by oxidation.

Table 5.3.9 Initial potential, local potential minimum and constant potential value for an EWII benchmark cell, ALIP, a PSI benchmark cell, PSI_s5_3, and an EWII cell without IrO_x catalyst, ATMJ, during initialization of the cells. All the values are read of the graphs in figure 5.1.5.20.

	$E_{initial}$ [V]	**$E_{local\ minimum}$ [V]**	**$E_{constant}$ [V]**	**$E_{initial} - E_{local\ minimum}$ [V]**	**$E_{initial} - E_{constant}$ [V]**	**$E_{constant} - E_{local\ minimum}$ [V]**	**$t_{local\ minimum} - t_{initial}$ [Hr]**	**$t_{constant} - t_{initial}$ [Hr]**
EWII benchmark cell, ALIP	2.27	1.90	1.99	0.37	0.28	0.09	3.7	16.9
PSI benchmark cell, PSI_s5_3	2.38	2.00	2.06	0.38	0.32	0.06	3.2	15.5
EWII cell without IrO_x catalyst, ATMJ	2.62	2.13	2.14 (NB: Decreasing)	0.49	0.48	0.01	4.2	13.5

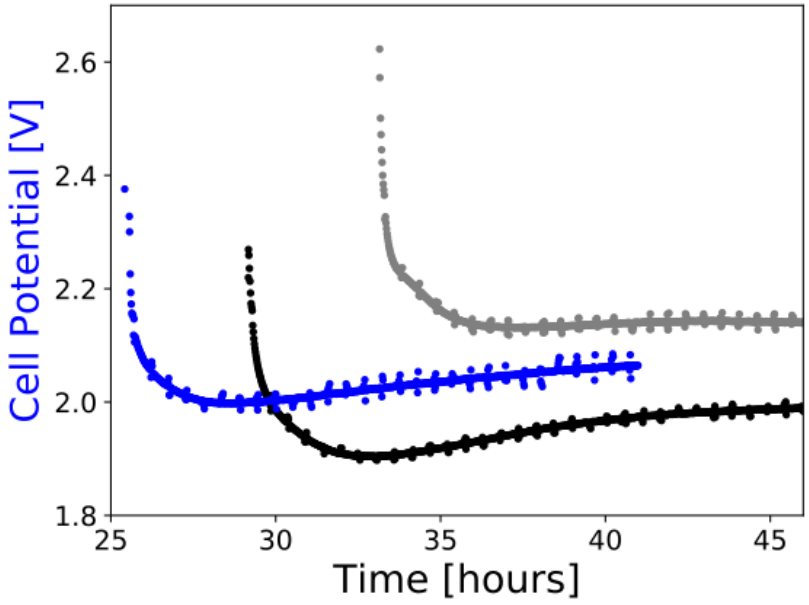

Figure 5.1.5.20 Initializations of various types of PEMECs; the EWII benchmark cell, ALIP (black), the PSI cell, PSI_s5_3 (blue) and the EWII cell without IrO_x catalyst, ATMJ (gray).

From table 5.1.5.5 it is seen that the total Ir content of the EWII benchmark cell and the PSI benchmark cell are similar; 2.95 and 2.8 mg cm^{-2}, respectively. However, according to the CVs in figure 5.1.5.19 the catalyst of the PSI benchmark cell is much more electrochemical accessible than the catalyst in the EWII cells, which is seen from the larger current densities of the CV of the PSI cell than the EWII cells. According to the iV-curve measurements on the exact same cells shown in section 5.3.1, 5.3.2 and 5.3.3 according to the potentiometric measurements during initiation of the same three cells over-night at 1.00 A cm^{-2} shown in figure 5.1.5.20., the best total performance of the PEMECs is the EWII benchmark cell, followed by the PSI benchmark cell and the least well performing cell is the EWII cell without IrO_x. This trend is contradicting the catalyst availability trend from the CV measurements, which support our hypothesis presented and discussed in section 6 that the catalyst activity is not limiting the performance of PEMECs, but other processes such as proton conductivity of the Nafion membrane, current constrictions at the electrode/electrolyte interphase and proton conductivity of the Nafion binder in the catalyst layers are limiting the PEMEC performance.

Another interesting observation in figure 5.1.5.19 a) and 5.1.5.19 b) is that the cathodic currents originating from hydrogen evolution at the anode observed at slightly positive potentials are much more negative for the PSI benchmark cell compared to the EWII benchmark cell and the EWII cell without IrO_x. This means that a larger amount of hydrogen is produced at the anode in the PSI benchmark cell probably due to large ECSA of the IrO_x catalyst cf. figure 4.2.7 in section 4.2, which catalyses the reduction of hydrogen protons to hydrogen gas. Furthermore, the HER takes place at higher potentials for the PSI cell (0 - ca. 0.3 V) compared to the EWII cells (0 – 0.07 V), which may be due to the more porous structure of the IrO_x/TiO_2 anode in the PSI cells cf. figure 4.2.7, which allow the produced hydrogen to escape the electrode easier than in the less porous structure of the EWII cells, which contains a fairly dense Ir-metal layer cf. figure 4.2.7, which may trap more hydrogen molecules at the electrode surface. This means that the denominator in the Nernst equation (equation (16)) is lower for the PSI benchmark cells compared to the EWII cells, which cause the potential of the anode of the PSI benchmark cell to be higher than the potential of the anode of the EWII cells.

5.3 Further Electrochemical Characterization of PEMECs

The three different types of PEMECs have been further electrochemically characterized with iV-curves and electrochemical impedance spectroscopy, and the results of these characterization techniques are shown for the EWII benchmark cells in section 5.3.1, for the EWII cell without IrO_x in section 5.3.2, for the PSI cells in section 5.3.3 and for EWII benchmark cells tested with Pt coated Ti felt in section 5.3.4.

5.3.1 EWII Benchmark Cells

iV-curves

5.3.1.1.1 Linearity

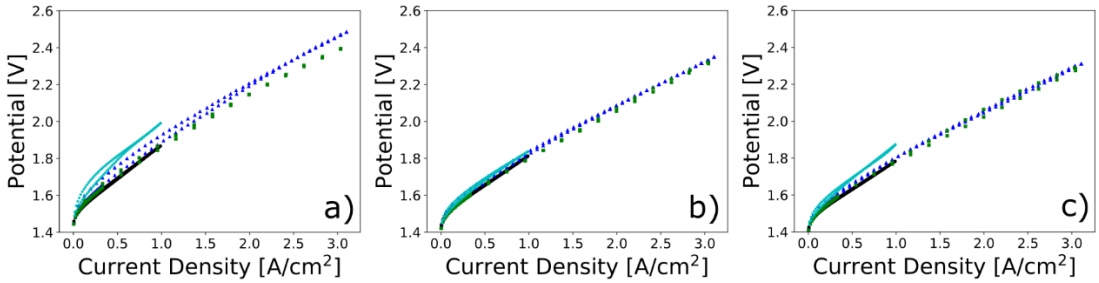

Figure 5.3.1.21 iV-curves measured on various benchmark EWII cells after EIS at 53-50 °C (a), at 61-68 °C (b) and at 69-75 °C (c). The four cells were Cell 0 (black circles), cell X (blue triangles), cell Y (green squares) and ALIP (cyan circles).

iV-curves measured on four different EWII benchmark cells are depicted in figure 5.3.1.21 and are very similar for the four cells. IV-curves of the EWII benchmark cell named cell 0 is shown with black circles, and since this iV-curve is representative for all four EWII benchmark cells, iV-curves of this EWII benchmark cell is chosen as reference in the following. All the iV-curves in figure 5.3.1.21 are very linear at current densities above 0.35 A cm^{-2}, and only a very limited amount of hysteresis is observed, even in the iV-curves measured up to 3 A cm^{-2}. The slope of the iV-curve is the total differential cell resistance, which is constant above 0.35 A cm^{-2}, when the iV-curve is linear as described in article 1. Table 5.3.1.10 gives an overview of the slopes of the iV-curves of the EWII benchmark cells shown in figure 5.3.1.21. All the linear regressions in table 5.3.1.10 are obtained for the linear regions of the iV-curves at 0.35-0.98 A cm^{-2}. The slope of the two iV-curves measured up to 3 A cm^{-2} is decreasing a bit at high current densities, due to an increase in cell temperature. This is due to insufficient cooling of the cell, when operating at hight current densities and therefor at higher effects. The temperatures given for each of the iV-curves in table 5.3.1.10 are intervals for the cells, where iV-curves were measured up to 3 A cm^{-2}, and this interval denotes the temperature increase during the iV-curve measurements. Linear regressions have been made in the current density interval 0.35-0.98 A cm^{-2} for all four cells, since at these low current densities, the cell temperature is stable cf. figure 5.3.1.22. In table 5.3.1.10 it is noted that for all four EWII benchmark cells, the total differential cell resistance

determined as the slope of the linear part of the iV-curves at 0.35-0.98 A cm^{-2} decrease with increasing cell temperature.

Table 5.3.1.10 Linear regressions from 0.35-0.98 A cm^{-2} of iV-curves measured on EWII benchmark cells shown in figure 5.3.1.21.

Cell	Cell Temperature, T	Linear slope of iV-curve before EIS at the given T [Ω cm^{-2}]	Linear slope of iV-curve after EIS at the given T [Ω cm^{-2}]
Cell 0 EWII reference	**53 °C**	0.366	0.365
	61 °C	0.311	0.321
	69 °C	0.301	0.309
ALIP EWII	**55-56 °C**	0.458	0.389
	63 °C	0.308	0.314
	70-71 °C	0.377	0.362
Cell x	**57-60 °C**	0.361	0.344
	65-68 °C	0.306	0.303
	71-75/73-76 °C	0.290	0.296
Cell y	**56-57 °C**	0.325	0.313
	65-66 °C	0.320	0.285
	73-75 °C	0.278	0.282

5.3.1.1.2 Hysteresis

Figure 5.3.1.22 shows iV-curves and temperatures measured on the reference EWII benchmark cell, cell 0, before EIS measurements (a, b and c) and after EIS measurements (d, e and f) at 53 °C (a and d), 61 °C (b and e) and 69 °C (c and f). In figure 5.3.1.22 it is noted that the small hysteresis of the iV-curve of the reference EWII benchmark cell is most pronounced at low current densities, before the iV-curve becomes linear. It is furthermore noted that during the anodic scan of the iV-curves, when the current density is increasing, the measured potentials are slightly lower than observed at the same current density during the following cathodic scan of the iV-curve in the region with slight hysteresis. This trend is the same at all three temperatures and both before and after the EIS measurements. The temperature plot in each graph shows that the temperature of the cell is almost constant and varies up to 0.5 °C, when the iV-curve is

recorded up to 1 A cm^{-2}. Since the cell temperature is almost constant during the measurement of the iV-curve, the small hysteresis cannot be ascribed to a temperature effect.

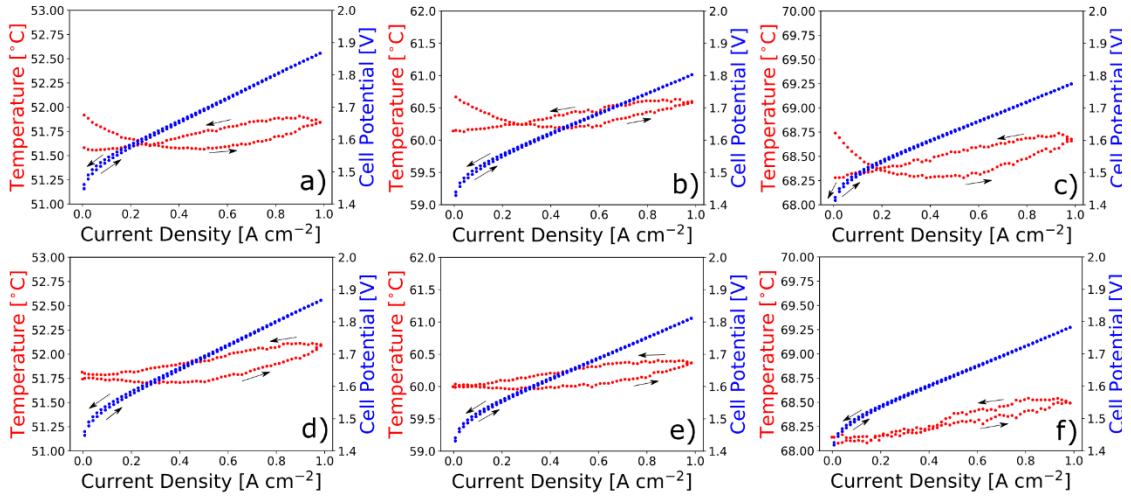

Figure 5.3.1.22 iV-curves with temperature measured on the benchmark EWII cell, Cell 0, at 53 °C (a) ,61 °C (b) and 69 °C(c) before EIS and at 53 °C (d), 61 °C (e) and 69 °C (f) after EIS measurements. The arrows express the current density scan direction.

5.3.1.1.3 Stability during EIS Measurements – Comparison of iV-curves Measured Before and After EIS.

Figure 5.3.1.23 and 5.3.1.24 compares the iV-curves measured before and after EIS measurements at the three operating temperatures for the two EWII benchmark cell, which have been examined with EIS, cell 0 and ALIP, respectively. For both EWII benchmark cells, the iV-curves measured before and after EIS measurements at the three different cell temperatures are overlapping, indicating that the cell have been stable and not degrading during the EIS measurements at each temperature.

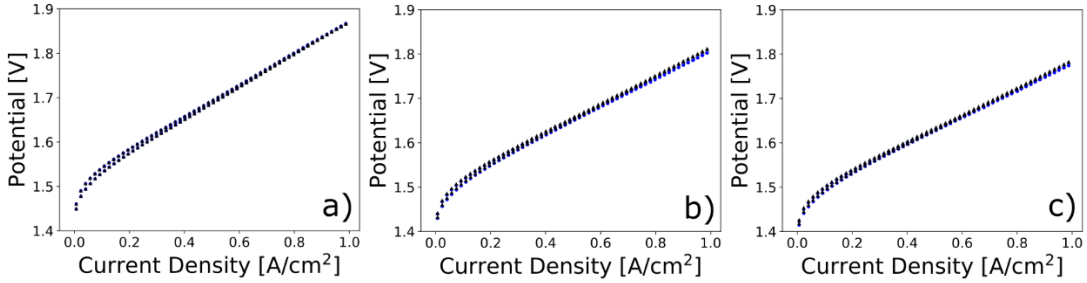

Figure 5.3.1.23 iV-curves measured before (blue dots) and after (black triangles) EIS measurements at 53 °C (a), 61 °C (b) and 69 °C (c) on a benchmark EWII cell, Cell 0. The iV-curves measured before and after the EIS measurement at each temperature is hardly distinguishable in each of the three plots meaning that the cell seem to be in the same state before and after the EIS measurements at each temperature.

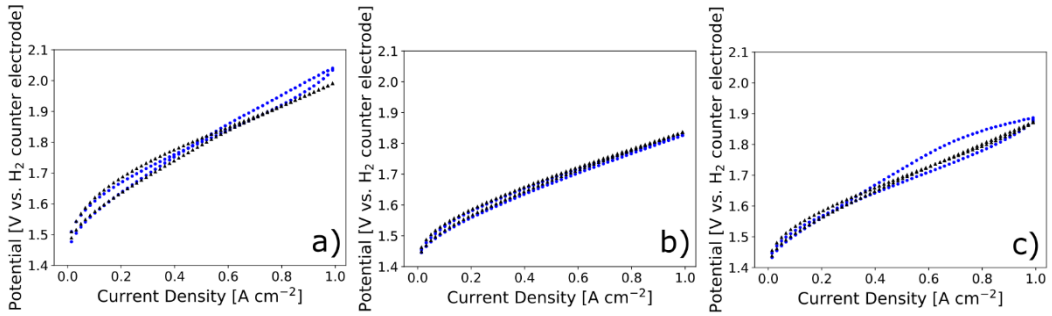

Figure 5.3.1.24 iV-curves measured before (blue dots) and after (black triangles) EIS measurements at 55-56 °C (a), 63 °C (b) and 70-71 °C (c) on a benchmark EWII cell, ALIP. The iV-curves measured before and after the EIS measurement at each temperature is fairly similar in each of the three plots meaning that the cell seem to be in the same state before and after the EIS measurements at each temperature.

Electrochemical Impedance Spectroscopy

5.3.1.1.4 Nyquist and Bode Plots of EIS Measured on EWII Benchmark Cells

Figure 5.3.1.25 depicts Nyquist plots of EIS measured on the reference EWII benchmark cell, cell 0, at various current densities (0.07, 0.35, 0.69 and 1.00 A cm^{-2}) and at cell temperatures of 53, 61 and 69 °C. Figure 5.3.1.26 shows Nyquist plots of EIS measured on another EWII benchmark cell, ALIP, at the same current densities and (0.07, 0.35, 0.69 and 1.00 A cm^{-2}) and at similar cell temperatures (55-56, 63 and 70-71 °C). In both figures two arcs, at low and middle frequencies, are clearly observed, and it is seen that the low frequency arc is increasing with increasing current density and that the middle frequency arc is decreasing with increasing current density. This trend is described and discussed in article 1 (45).

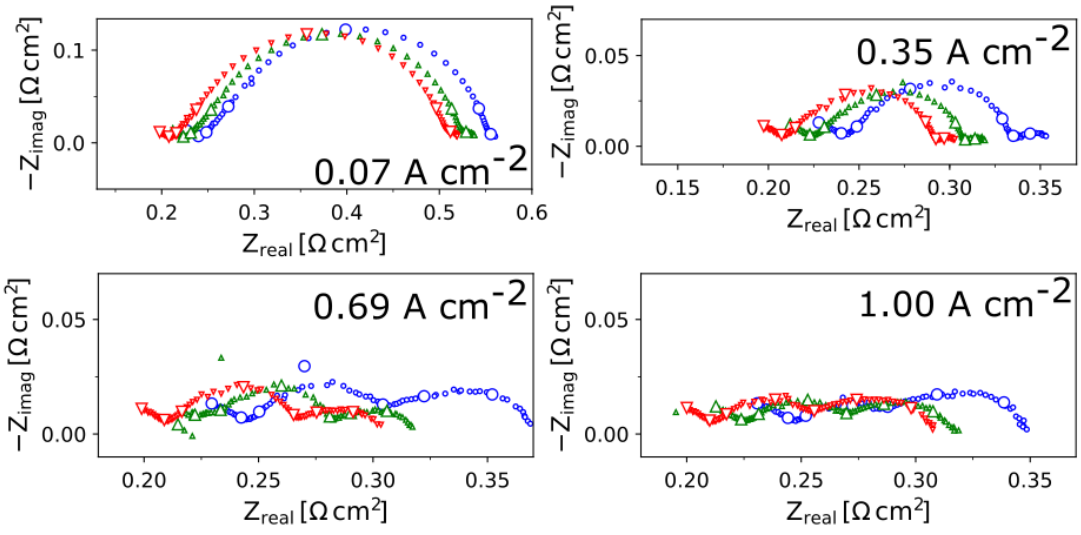

Figure 5.3.1.25 EIS measured at 53 °C (blue circles), 61 °C (green triangles) and 69 °C (red triangles) and at 0.07, 0.35, 0.69 and 1.00 A cm^{-2} on the reference EWII benchmark cell, Cell 0.

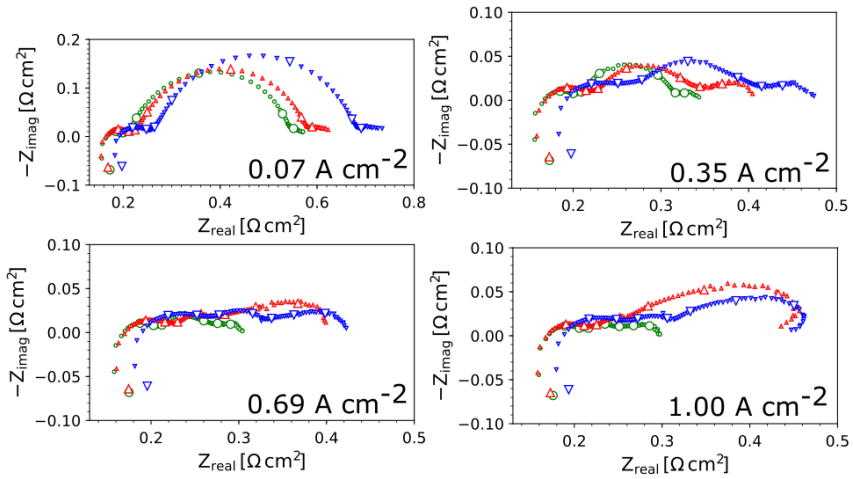

Figure 5.3.1.26 EIS measured at 55-56 °C (blue circles), 63 °C (green triangles) and 70-71 °C (red triangles) and at 0.07, 0.35, 0.69 and 1.00 A cm^{-2} on the EWII benchmark cell, ALIP.

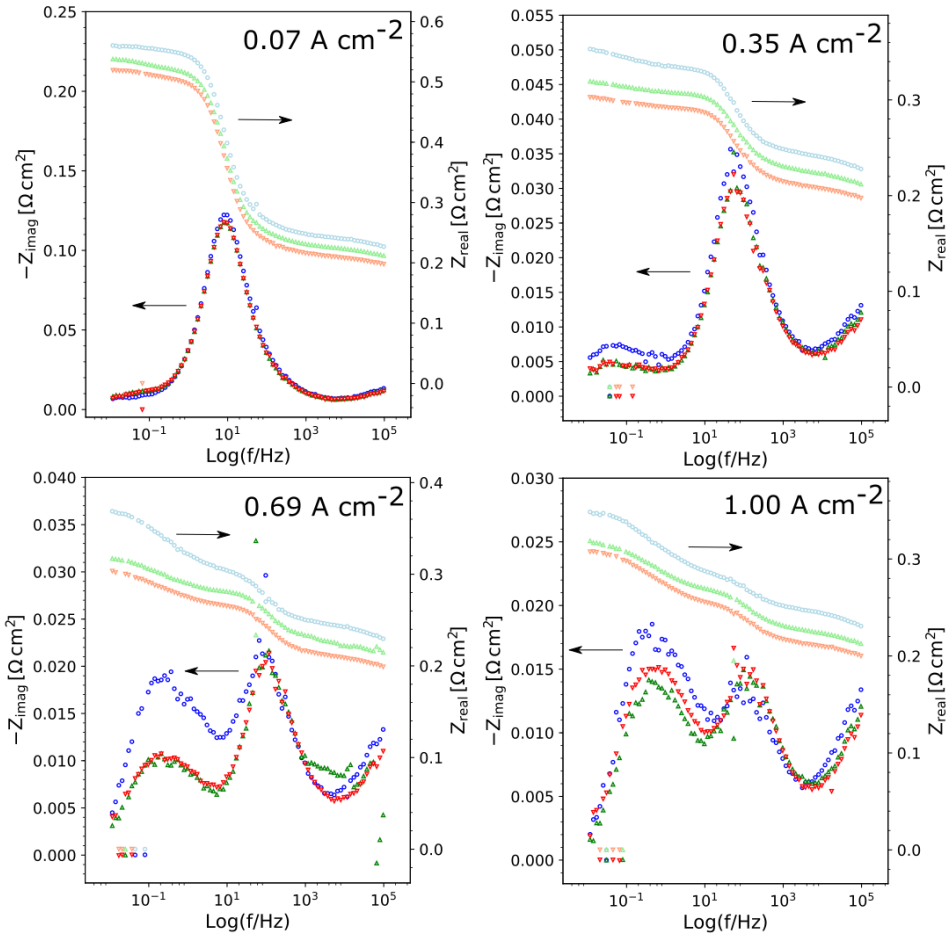

Figure 5.3.1.27 EIS shown in Bode plots measured at 53 °C (blue / light blue circles), 61 °C (green / light green triangles) and 69 °C (red/ light red triangles) and at 0.07, 0.35, 0.69 and 1.00 A cm^{-2} on the reference EWII benchmark cell, cell 0. The imaginary part of the impedance are shown with dark colours and y-axis to the left, while real part of the impedance is shown with light colours and y-axis to the right.

Bode plots of the EIS of the two EWII benchmark cells can be found in figure 5.3.1.27 for the reference EWII benchmark cell, cell 0, and in figure 5.3.1.28 for the EWII benchmark cell, ALIP. The Bode plots in this thesis is shown with the imaginary and real part of the impedance versus frequency instead of phase and modulus versus frequency, as this representation form easily show capacitive and resistive contributions to the overall impedance. Furthermore, this representation form ease the reading of summit frequencies (read off as the frequency at the summit of the imaginary part of the impedance in the Bode plot), which are used for the fitting of the measured EIS to an EIS model described in another subsection. Summit frequencies are important for the interpretation of EIS, since the summit frequency of an arc is the inverse of the time constant of the electrochemical process causing the arc, and the time constant characterizes the process type (46).

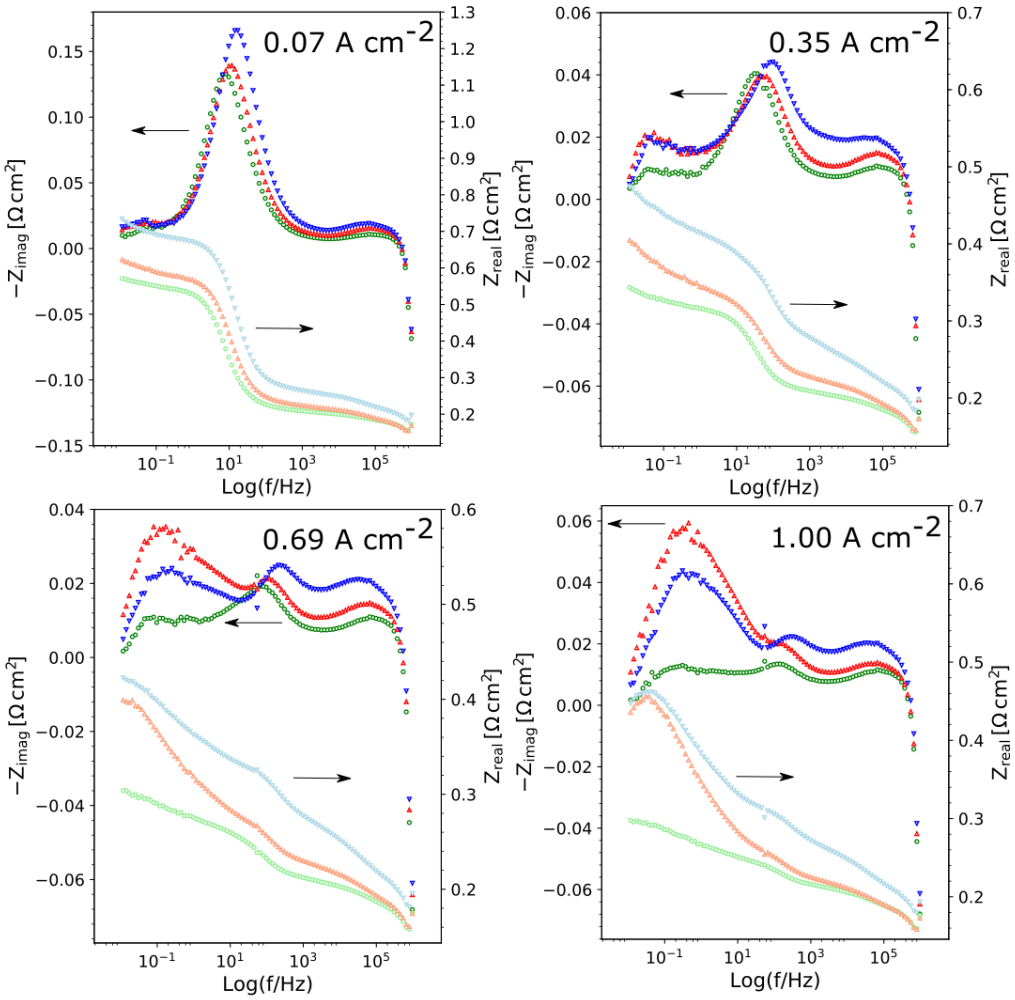

Figure 5.3.1.28 EIS shown in Bode plots measured at 55-56 °C (blue / light blue circles), 63 °C (green / light green triangles) and 70-71 °C (red/ light red triangles) and at 0.07, 0.35, 0.69 and 1.00 A cm^{-2} on the reference EWII benchmark cell, ALIP. The imaginary part of the impedance are shown with dark colours and y-axis to the left, while real part of the impedance is shown with light colours and y-axis to the right.

In the Nyquist plot of the EIS measured for the reference EWII benchmark cell in figure 5.3.1.25, and for the EWII benchmark cell, ALIP, in figure 5.3.1.26, a high frequency local minimum of $-Z_{im}$ is observed, as described in article 1. The real part of the impedance at this local minimum has been denoted $Z_{re,\ HF\ min}$ and are listed in table C.39 together with summit frequencies determined from the Bode plots. $Z_{re,\ HF\ min}$ is almost constant above 0.35 A cm^{-2}, when operating in the linear region of the iV-curve, and averages of $Z_{re,\ HF\ min}$ at each operating temperature measured at 0.35, 0.69 and 1.00 are given in table C.42 for all the PEMECs in this thesis and for the EWII benchmark cells in table 5.3.1.11. The total resistance of a PEMEC can be determined from EIS measurements, and is the DC impedance given by the real part of the impedance at the lowest frequency measured. In this thesis the total cell resistance determined from EIS measurements is named $Z_{re,LF}$ and it is given for all the PEMECs reported in this thesis in table C.39 in appendix C. $Z_{re,LF}$ is almost constant in the linear region of the iV-curve, and averages of $Z_{re,LF}$ with standard deviations are given in table C.42 the appendix C for all the PEMECs in this thesis and for the EWII benchmark cells in table 5.3.1.11. The total resistance of the middle and low frequency arcs in figure 5.3.1.25 and 5.3.1.26 is determined from the difference between $Z_{re,LF}$ and $Z_{re,\ HF\ min}$ and is denoted $Z_{re,\ LF\ -\ HF\ min}$. $Z_{re,\ LF\ -\ HF\ min}$ is almost constant in the linear region of the iV-curve and the average value is given for the EWII benchmark cells in table 5.3.1.11, whereas $Z_{re,\ LF\ -\ HF\ min}$ for each EIS spectrum of the PEMECs are given in table C.39 in appendix C. As described in article 1, the electrolyte resistance of the Nafion 117 membrane should be 0.159 Ω cm^2 at 53 °C, 0.148 Ω cm^2 at 61 °C and 0.138 Ω cm^2 at 69 °C according to Malis et al., who have determined the resistance of a wetted Nafion 117 membrane after testing in an electrolysis cell (47). However, comparing $Z_{re,\ HF\ min}$ measured at 53, 61 and 69 °C for the reference EWII benchmark cell, cell 0, to the resistances of the Nafion electrolyte reported by Malis et al. at the same temperatures, show an incongruence between the two numbers. In addition the Nyquist plots of the EIS measured on the reference EWII benchmark cell, cell 0, in figure 5.3.1.25 show an increase in capacitive impedance, $-Z_{im}$, at very high frequencies, which suggest that a third arc is partly seen at vary high frequencies, and that $Z_{re,\ HF\ min}$ is a sum of the electrolyte resistance and the resistance of the high frequency arc. Therefore, the difference between $Z_{re,\ HF\ min}$ and the electrolyte resistance calculated for the particular temperature from literature values by Malis et al. (47), denoted $Z_{re,HF\ min\ -\ Rs(Malis)}$, is listed in table C.39 for all PEMECs in this thesis, where it was possible to read off $Z_{re,\ HF\ min}$, and an average value of $Z_{re,HF\ min\ -\ Rs(Malis)}$ above 0.35 A cm^{-2} is given for the two EWII benchmark cells, cell 0 and ALIP, in table 5.3.1.11. It is noted in table 5.3.1.11 that the standard deviations on $Z_{re,LF}$ is small for the reference EWII benchmark cell, cell 0, meaning that the total cell resistance is constant above 0.35 A cm^{-2}, whereas the standard deviations of $Z_{re,LF}$ for the other EWII benchmark cell, ALIP, is bigger meaning that the total cell resistance of the ALIP is less constant above 0.35 A cm^{-2}, which is consistent with the iV-curves in figure 5.3.1.21, where the iV-curve of the EWII benchmark cell ALIP is less linear than the other EWII benchmark cells.

Table 5.3.1.11 EIS Overview Table showing averages of the total cell resistance, $Z_{re,LF}$, from 0.35 A cm^{-2} to 1.00 A cm^{-2} (the linear part of the iV-curves), averages of $Z_{re,HF}$ min up to 1.00 A cm^{-2}, averages of the resistance of the middle and low frequency arcs, $Z_{re,\ LF\ -\ HF\ min}$ from 0.35 A cm^{-2} to 1.00 A cm^{-2} and averages of $Z_{re,HF\ min\ –\ Rs(Malis)}$ up to 1.00 A cm^{-2}.

Cell	Cell Temperature, T	Average $Z_{re,LF}$ from 0.35 to 1.00 A cm^{-2}	Average $Z_{re,HF\ min.}$ up to 1.00 A cm^{-2}	Average $Z_{re,\ LF\ -\ HF\ min}$ denoted Z_{MF+LF} from 0.35 to 1.00 A cm^{-2}	Average $Z_{re,HF\ min\ –\ Rs(Malis)}$ denoted Z_{HF} up to 1 A cm^{-2}
Cell 0 EWII reference	**53 °C**	0.357 ± 0.009 Ω cm^2	0.244 ± 0.002 Ω cm^2	0.112 ± 0.009 Ω cm^2	0.085 ± 0.002 Ω cm^2
	61 °C	0.318 ± 0.001 Ω cm^2	0.224 ± 0.001 Ω cm^2	0.095 ± 0.000 Ω cm^2	0.076 ± 0.001 Ω cm^2
	69 °C	0.304 ± 0.002 Ω cm^2	0.210 ± 0.001 Ω cm^2	0.095 ± 0.001 Ω cm^2	0.072 ± 0.001 Ω cm^2
ALIP EWII	**55-56 °C**	0.448 ± 0.025 Ω cm^2	0.261 ± 0.006 Ω cm^2	0.159 ± 0.055 Ω cm^2	0.105 ± 0.006 Ω cm^2
	63 °C	0.315 ± 0.024 Ω cm^2	0.207 ± 0.005 Ω cm^2	0.101 ± 0.036 Ω cm^2	0.062 ± 0.005 Ω cm^2
	70-71 °C	0.413 ± 0.020 Ω cm^2	0.221 ± 0.003 Ω cm^2	0.147 ± 0.055 Ω cm^2	0.085 ± 0.003 Ω cm^2

In table 5.3.1.12 the average total cell resistance determined from the EIS measurements, $Z_{re,LF}$, is compared to the total cell resistance determined from the slope of the linear iV-curve above 0.35 A cm^{-2} for the and two EWII benchmark cells, cell 0 and ALIP. It is seen that there is a very good accordance between the total cell resistance determined with EIS and with iV-curves for the reference EWII benchmark cell, cell 0, and a less good accordance between the total cell resistance determined with EIS contra iV-curves for the other EWII benchmark cell, ALIP, however, there is still a fairly good accordance.

Table 5.3.1.12 Total differential cell resistance given by the slope of linear regressions from 0.35-0.98 A cm^{-2} of iV-curves measured before and after EIS measurements on EWII benchmark cells shown in figure 5.3.1.21. The total cell resistances are compared to average total cell resistances above 0.35 A cm^{-2} determined by DC impedance, $Z_{re,LF}$, at the same EWII benchmark cells.

Cell	Cell Temperature, T	Linear slope of iV-curve before EIS at the given T [Ω cm^{-2}]	Linear slope of iV-curve after EIS at the given T [Ω cm^{-2}]	Average $Z_{re,LF}$ from 0.35 to 1.00 A cm^{-2}
Cell 0 EWII reference	**53 °C**	0.366	0.365	0.357 ± 0.009 Ω cm^2
	61 °C	0.311	0.321	0.318 ± 0.001 Ω cm^2
	69 °C	0.301	0.309	0.304 ± 0.002 Ω cm^2
ALIP EWII	**55-56 °C**	0.458	0.389	0.448 ± 0.025 Ω cm^2

63 °C	0.308	0.314	0.315 ± 0.024 Ω cm^2
70-71 °C	0.377	0.362	0.413 ± 0.020 Ω cm^2

It was noted from the standard deviations in table 5.3.1.11 that the total cell resistance, $Z_{re,\ HF\ min}$, the sum of the resistances of the middle frequency arc and the low frequency arc denoted Z_{MF+LF} and the resistance of the high frequency arc denoted Z_{HF} clearly do not change with changes in current density, when the cell is operated in the linear region of the iV-curve above 0.35 A cm^{-2} for the reference EWII benchmark cell, and likewise, but less clearly, do not change with changes in current density for the other EWII benchmark cell, ALIP (slightly higher standard deviations were observed). In figure 5.3.1.29 the dependence of operating temperature on the total cell resistance, $Z_{re,\ HF\ min}$, Z_{MF+LF} and Z_{HF} is shown for the reference EWII benchmark cell in figure 5.3.1.29 a) and for the other EWII benchmark cell, ALIP, in figure 5.3.1.29 b). This comparison for the reference EWII benchmark cell is also shown in figure 8 in article 1. In figure 5.3.1.29 a) it is noted that the total cell resistance, $Z_{re,\ HF\ min}$, Z_{MF+LF} and Z_{HF} of the reference EWII benchmark cell show the same order of magnitude decrease with increasing operating temperature as reported by Malis et al. (47) for a hydrated and operated Nafion 117 membrane. The linear regressions of the total cell resistance, $Z_{re,\ HF\ min}$, Z_{MF+LF} and Z_{HF} as function of temperature for the other EWII benchmark cell, ALIP, is less good as the regressions for the reference EWII benchmark cell, cell 0, but the regressions still show the same order of magnitude dependence between total cell resistance, $Z_{re,\ HF\ min}$, Z_{MF+LF} and Z_{HF} and operating temperature as was reported by Malis et al. (47). This imply that the resistive impedance contributions in the EWII benchmark PEMECs originate from Nafion in the electrolyte, and from Nafion connected in parallel with capacitive processes giving rise to the high frequency, middle frequency and low frequency arcs.

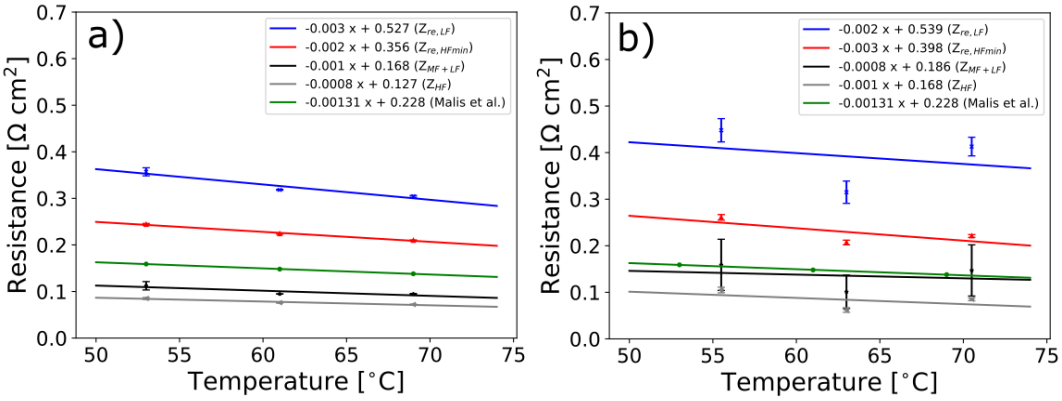

Figure 5.3.1.29 $Z_{re,LF}$ (blue crosses), $Z_{re,\ HF\ min}$ (red triangles), Z_{MF+LF} (black stars) and Z_{HF} (gray triangles) shown as function of operating temperature for the reference EWII benchmark cell, cell 0, in a) and for the other EWII benchmark cell, ALIP, in b) and compared to in-plane resistance measurements of operated Nafion 117 membranes reported by Malis et al. (47) (green circles).

5.3.1.1.5 EIS Model

As described earlier and in article 1, an increase in capacitive impedance is observed at very high frequencies at all four current densities and all three temperatures in figure 5.3.1.25. This, in combination with the fact that the local minimum at the high current densities before the increase in capacitive impedance, does not correlate with the resistance of the Nafion 117 membrane reported by Malis et al. (47), suggests a third arc to be partly seen in the EIS spectrum at very high frequencies. Lettenmeier et al. (22) have reported EIS showing three impedance arcs as well. In figure 5.3.1.30. the EIS measured at 61 °C and in the linear region of the iV-curve (at 0.35, 0.69 and 1.00 A cm^{-2}) on the reference EWII benchmark cell, cell0, have been modelled with three arcs and a serial resistance of the Nafion electrolyte fixed to 0.148 Ω cm^2, which is the value reported by Malis et al. (47) at 61 °C. It can be seen that the EIS spectra modelled with three arcs and a serial resistance (R-RQ-RQ-RQ) (black lines) fits very well with the measured EIS spectra (black triangles). The EIS fits are shown together with Kramers-Kronig compliance tests for the EIS data measured at each of the current densities. The relative residuals of the Kramers-Kronig compliance test is small (less than 1.0 %), which means that the measured EIS obey the four Kramers-Kronig relations, which means that it is reasonable to fit the EIS data to an equivalent circuit.

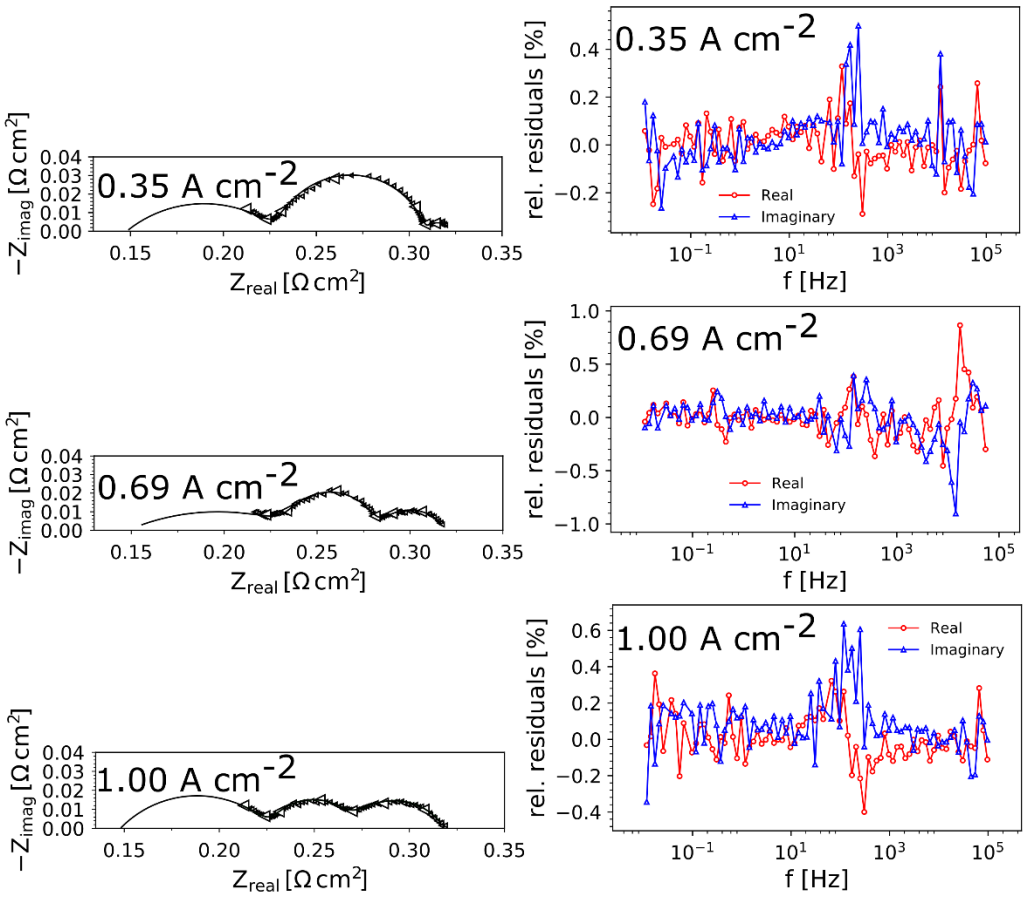

Figure 5.3.1.30 Nyquist plots and Kramers-Kronig compliance tests of EIS measured at 61 °C and at 0.07, 0.35, 0.69 and 1.00 A cm^{-2} on the reference EWII benchmark cell, cell 0. Fits of the measured EIS to the equivalent circuit R-RQ-RQ-RQ is also shown in the plots. The serial resistance was kept constant at the literature value reported by Malis et al. (47) during fitting (0.148 Ω cm^2 at 61 °C). EIS measured at 50-60 Hz and with Z_{re} below 0.01 Ω cm^2 were excluded from the fits. At 0.69 A cm^2 EIS measured at frequencies above 55 kHz was also excluded due to outliers.

In order to measure a bigger fraction of the high frequency impedance arc, EIS was measured up to 1 MHz instead of up to 100 kHz, however as earlier described inductive impedance contributions were observed in these EIS spectra cf. figure 5.3.1.26. When comparing Z_{re} at the high frequency x-axis intercept in figure 5.3.1.26 with resistances of the pure Nafion electrolyte reported by Malis et al. (47) at the various temperatures, it is noticed that the resistances obtained from the high frequency intercept still are slightly higher than the literature values (e.g. 0.17 Ω cm^2 compared to 0.145 Ω cm^2 according to Malis at 63 °C). This is due to phase errors introduced by the Solartron, when measuring at these high frequencies. Other EIS analysers may have been able to measure up to 1 MHz EIS such as e.g. a Zahner EIS analyser, however it was not possible to use such an instrument for the experiments. The phase error phenomenon has been described by Shin et al. (48). In figure 3, 4 and 5 in the article by Shin et al. (48) it is shown, how an inductive impedance contribution in parallel with a resistance, is influencing the high frequency intercept of the x-axis and leading to higher Z_{re} at the high frequency x-axis intercept than the serial resistance. They show how the high frequency arc is suppressed by the phase error contribution from the EIS analyser. In figure 5.3.1.26, where EIS has been measured up to 1 MHz, it is seen that the EIS data point measured at the highest frequency has a higher Z_{re} than the data points measured at slightly lower frequencies. However, the data points measured at slightly lower frequencies has decreasing Z_{re} with increasing frequency, and therefore it may be assumed that the data point at the highest frequency is an artefact and therefore may be excluded from the fitting. This means that EIS measured on PEMECs up to 1 MHz should be modelled with the equivalent circuit R-L-RQ-RQ-RQ, since the high frequency inductance is not parallel connected to a resistor as is the case in the article by Shin et al. (48). In figure 5.3.1.31 EIS measured on the EWII benchmark cell ALIP at 63 °C have been fitted to the R-L-RQ-RQ-RQ equivalent circuit. In this figure it is noticed how well the third arc is fitting to the EIS measurements, when modelling to the equivalent circuit R-L-RQ-RQ-RQ and keeping the serial resistance constant at the literature values for Nafion at 63 °C reported by Malis et al. (47), which is 0.145 Ω cm^2. The measured EIS data is shown as black triangles, and the EIS fit is shown as a black line. Kramers-Kronig compliance tests are given in the figure for each EIS spectrum, and low relative residuals (less than 1.0 %) is observed for all three EIS spectra at frequencies below approximately 80 kHz. At frequencies above 80 kHz, higher Kramers-Kronig relative residuals up to approximately 4 % is observed, which complies with the EIS fits shown in figure 5.3.1.31, which fits less good at very high frequencies compared to the rest of the EIS spectra.

In figure 5.3.1.32 the total EIS fit from figure 5.3.1.31 is shown together with each of the three arcs and the inductance from the equivalent circuit. From this figure it can be seen, how the phase error from the Solartron is influencing the x-axis intercept, even when the phase error is due to an inductor and not an inductor in parallel with a resistor as reported by Shin et al. (48), making the high frequency x-axis intercept different from the electrolyte resistance, when the EIS includes high frequency inductance.

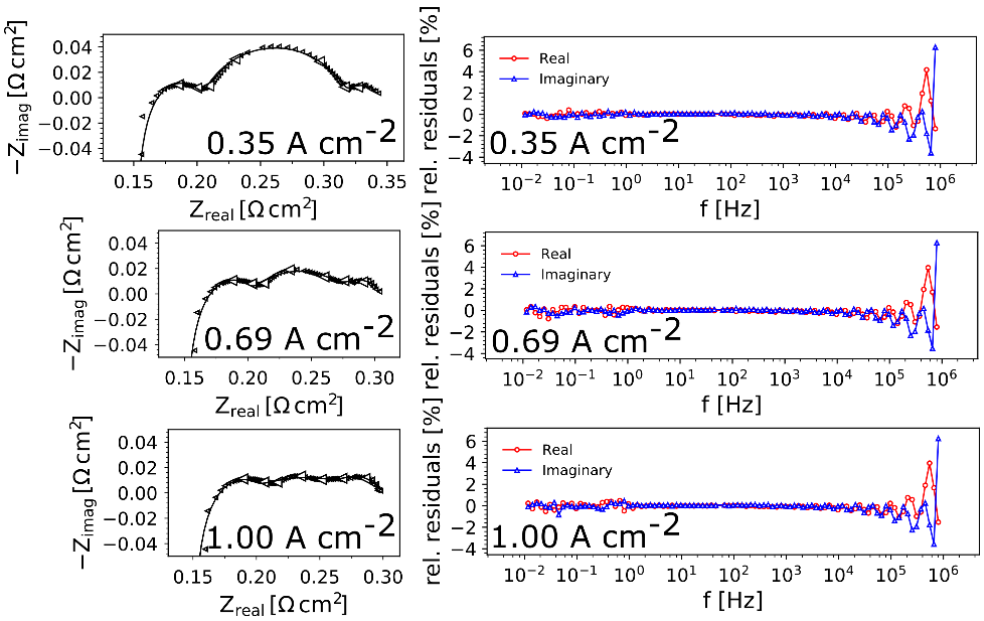

Figure 5.3.1.31 Nyquist plots and Kramers-Kronig compliance tests of EIS measured at 63 °C and at 0.07, 0.35, 0.69 and 1.00 A cm^{-2} on an EWII benchmark cell, ALIP. Fits of the measured EIS to the equivalent circuit R-L-RQ-RQ-RQ is also shown in the plots. The serial resistance was kept constant at the literature value reported by Malis et al. (47) during fitting (0.145 Ω cm^2 at 63 °C). EIS measured at 50-60 Hz and above 800 kHz was excluded from the fits.

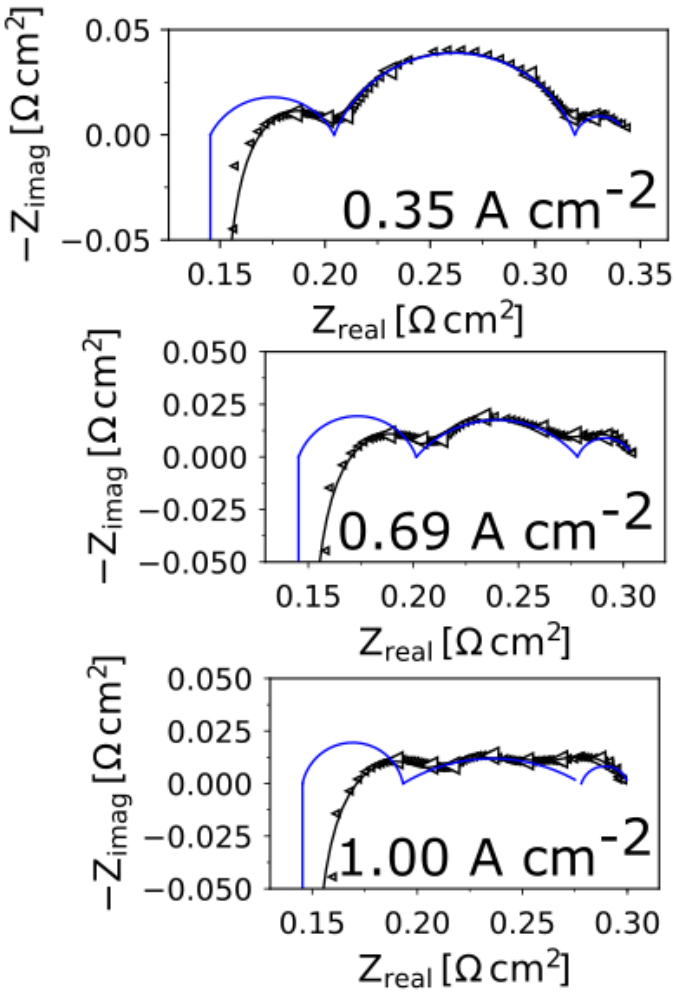

Figure 5.3.1.32 Nyquist plots of EIS measured at 63 °C and at 0.07, 0.35, 0.69 and 1.00 A cm^{-2} on an EWII benchmark cell, ALIP. Fits of the measured EIS to the equivalent circuit R-L-RQ-RQ-RQ is also shown in the plots. The serial resistance was kept constant at the literature value reported by Malis et al. (47) during fitting (0.145 Ω cm^2 at 63 °C). The three arcs of the equivalent circuit (blue) is shown together with the data points and the total fit (black). EIS measured at 50-60 Hz and above 800 kHz was excluded from the fits.

5.3.1.1.6 EIS Model Explained with Physical Processes

Based on the findings in figure 5.3.1.29 it was suggested that the resistive impedance contributions in the EWII benchmark PEMECs originate from Nafion in the electrolyte, and from Nafion connected in parallel with capacitive processes giving rise to the high frequency, middle frequency and low frequency arcs. In this section, it will be examined, which processes that could contribute with the capacitive impedances observed in the EIS spectra of the benchmark PEMECs.

According to the microstructures of the various PEMECs examined in this PhD study depicted in figure 4.2.7, the electrodes of the PEMECs are porous in nature. This porous nature of the electrodes implies that the capacitance is not purely capacitive, and a distribution of time constants will arise throughout the electrode. A constant phase element is used to describe the distributed capacitance. (34)

The equivalent or effective capacitance of the constant phase element, Q, of each of the three arcs in the EIS spectra is calculated by applying equation (27), which is used by e.g. Hirschorn et al. (49) and originally described by Hsu et al. (50).

$$C_{eff} = Q^{1/n} R^{(1-n)/n} \tag{27}$$

In equation (27) C_{eff} is the equivalent or effective capacitance of the constant phase element, which is the average capacitance of the constant phase element (34), R is the resistance of the arc, n is the constant phase exponent, related to the deviation from pure capacitive behaviour (1 if pure capacitor, and smaller the more deviation from capacitive behaviour) and Q represents the differential capacity of the interface, when n is 1. The equivalent capacitance of the three arcs in the EIS spectra measured on the two EWII benchmark cells, cell 0 and ALIP, have been calculated based on the parameters resulting from the fits shown in figure 5.3.1.30 and 5.3.1.31. The fit programme Ravdav returns R, n and the summit frequency, f, for each of the arcs, and equation (28) is applied to calculate Q, which is then used to calculate the equivalent capacitance cf. equation (27). (34)

$$\omega = \left(\frac{1}{RQ}\right)^{\frac{1}{n}} \Leftrightarrow 2\pi f = \left(\frac{1}{RQ}\right)^{\frac{1}{n}} \Leftrightarrow Q = \frac{1}{R(2\pi f)^n} \tag{28}$$

In table 5.3.1.13 and 5.3.1.14 the fit parameters for the fits of EIS measured on the two EWII benchmark cells, cell 0 and ALIP, at 0.35, 0.69 and 1.00 A cm^{-2} is shown together with the equivalent capacitance of the tree arcs in each of the measured EIS spectra. The equivalent capacitances are in table 5.3.1.13 and 5.3.1.14 given as total values and not area-specific values. It is noticed that n is very small for all three arcs in all the EIS spectra (between 0.26 and 0.89), which means that the time constants are distributed for the three processes. This supports that the electrodes are porous composites. The EIS of porous composite structures, which contains multiple time constants, can both be modelled with a transmission line and with a constant phase element in parallel with a resistor, since the constant phase element take the distribution of time constants into account by the exponent n. In this work it has been chosen to model the porous structure with a constant element in parallel with a resistor due to the simplicity of this circuit compared to transmission lines in general.

Table 5.3.1.13 Fit parameters for the fits of EIS measured on the reference EWII benchmark cell, cell0, at 61 °C and 0.35, 0.69 and 1.00 A cm^{-2}. Q and the equivalent capacitance, Ceff, are calculated based on equation (27) and (28), and listed in the table for each of the three arcs in the measured EIS spectra.

	High Frequency Arc			**Middle Frequency Arc**			**Low Frequency Arc**		
	R [Ω cm^2]	**n**	**C_{eff} [µF]**	**R [Ω cm^2]**	**n**	**C_{eff} [mF]**	**R [Ω cm^2]**	**n**	**C_{eff} [F]**
0.35 A cm^{-2}	0.08	0.44	5.1	0.08	0.82	88	0.01	0.74	690
0.69 A cm^{-2}	0.10	0.26	4.4	0.04	0.89	103	0.03	0.67	65
1.00 A cm^{-2}	0.08	0.51	5.8	0.04	0.75	81	0.05	0.66	20

Table 5.3.1.14 Fit parameters for the fits of EIS measured on the EWII benchmark cell, ALIP, at 63 °C and 0.35, 0.69 and 1.00 A cm^{-2}. Q and the equivalent capacitance, Ceff, are calculated based on equation (27) and (28), and listed in the table for each of the three arcs in the measured EIS spectra.

	High Frequency Arc			**Middle Frequency Arc**			**Low Frequency Arc**		
	R [Ω cm^2]	**n**	**C_{eff} [µF]**	**R [Ω cm^2]**	**n**	**C_{eff} [mF]**	**R [Ω cm^2]**	**n**	**C_{eff} [F]**
0.35 A cm^{-2}	0.06	0.70	35.2	0.11	0.76	121	0.02	0.80	344
0.69 A cm^{-2}	0.06	0.77	28.5	0.08	0.55	108	0.03	0.76	163
1.00 A cm^{-2}	0.05	0.87	28.4	0.08	0.35	72	0.02	0.81	107

In order to examine the processes of the three EIS arcs, we first consider them as normal plate capacitors. The capacitance of a plate capacitor is given by equation (29) in which ε' is the permittivity of the medium between the plates, ε^0 is the permittivity of free space, which is 8.854 · 10^{-14} F cm^{-1}, A is the area of the capacitor and l is the distance between the plates (51).

$$C = \varepsilon' \varepsilon^0 \frac{A}{l} \tag{29}$$

Let us now consider the biggest possible area specific capacity for a plate capacitor in a PEMEC. ε^0 is constant, the smallest possible l is the size of an atom, which is 1 Å (52) and ε' is typically 10. (51) The calculation is shown in (30).

$$\frac{C}{A} = \frac{\varepsilon' \varepsilon^0}{l} = \frac{10 \cdot 8.854 \cdot 10^{-14} F cm^{-1}}{10^{-8} cm} = 8.85 \cdot 10^{-5}\ F\ cm^{-2} \tag{30}$$

Calculation (30) show that the biggest possible capacitance for a plate capacitor in the PEMEC is in the 10^{-5} F cm^{-2} range.

Now consider the equivalent capacitances of the three arcs of the EIS spectra of the EWII benchmark cells listed in table 5.3.1.13 and 5.3.1.14. In order to be able to determine the processes causing the three arcs, the equivalent capacitances have to be normalized by area. Table 5.3.1.15 compares the equivalent capacitances normalised by the geometrical electrode area, 2.89 cm^2, and normalised by ECSA calculated from the CVs recorded after initiation of the cells (given in table 5.1.5.6). It is assumed that the ECSA determined from CV after initiation of the cells is a good approximation to the ECSA of the cells during the EIS measurements, though the ECSA may be a bit higher during the EIS measurements than during the CV measurement. This may be the case, since the CVs are measured up to 1.4 V and the EIS measurements were done at higher potentials above 1.5 V, which means that a bigger fraction of the iridium metal particles may be oxidized and electrochemically available.

When considering the two area-specific capacitances of the high frequency arc, it is noticed that the capacitance normalized to the geometrical electrode area is in the same order of magnitude or one order of magnitude different from the area specific capacitance calculated in (30) for the maximum plate capacitor in a PEMEC. On the other hand the area-specific capacitance of the high frequency arc normalised to ECSA determined from the CVs are three to four orders of magnitudes lower than the plate capacitance given in equation (30). This implies that the processes giving rise to the high frequency arc is a two dimensional process, which, when taking the finding from figure 5.3.1.29 that the resistance of all three arcs seem to be ascribable to Nafion binder and electrolyte into account, may suggest that the capacitance of the high frequency arc originates from current constrictions at the electrode-electrolyte interface as described by Fleigh et al. (53) and in article 1. Big catalyst agglomerates attached to the Nafion membrane and big Ir-metal particles, may cause areas with extended contact between electrode and electrolyte and other areas without contact. This will lead to an uneven proton conductivity in parts of the electrolyte surface increasing the resistance of the Nafion electrolyte close to the surface. The big catalyst agglomerates or Ir-metal particles may contribute with a capacitive impedance contribution, which in combination with the increased resistance of the surface layer of the membrane compared to the bulk Nafion membrane, will cause a very high frequent arc. (53) Fleig et al. (53) also reports a capacitance for the current constrictions phenomenon of 0.88 µF cm^{-2}, which is close to what is reported in table 5.3.1.15. The current constriction phenomenon can be considered two dimensional, since the phenomenon is taking place at the surface between the electrolyte and the electrode.

Table 5.3.1.15 Equivalent capacitances for the high, middle and low frequency arcs normalised by the geometrical electrode area, which is 2.89 cm^2, C_{eff} ($A_{geo.}$), and normalized by ECSA derived from CV measured after initiation given in table 5.1.5.6, $C_{eff}(A_{ECSA})$.

		High Frequency Arc		Middle Frequency Arc		Low Frequency Arc	
		$C_{eff}(A_{geo.})$ [F cm^{-2}]	$C_{eff}(A_{ECSA})$ [F cm^{-2}]	$C_{eff}(A_{geo.})$ [F cm^{-2}]	$C_{eff}(A_{ECSA})$ [F cm^{-2}]	$C_{eff}(A_{geo.})$ [F cm^{-2}]	$C_{eff}(A_{ECSA})$ [F cm^{-2}]
EWII benchmark (ALIO)	**0.35 A cm^{-2}**	$1.8 \cdot 10^{-6}$	$1.7 \cdot 10^{-9}$	$3.05 \cdot 10^{-2}$	$2.90 \cdot 10^{-5}$	238.8	$2.3 \cdot 10^{-1}$
	0.69 A cm^{-2}	$1.5 \cdot 10^{-6}$	$1.5 \cdot 10^{-9}$	$3.56 \cdot 10^{-2}$	$3.38 \cdot 10^{-5}$	22.5	$2 \cdot 10^{-2}$
	1.00 A cm^{-2}	$2.0 \cdot 10^{-6}$	$1.9 \cdot 10^{-9}$	$2.81 \cdot 10^{-2}$	$2.67 \cdot 10^{-5}$	6.8	$1 \cdot 10^{-2}$
EWII benchmark (ALIP)	**0.35 A cm^{-2}**	$1.21 \cdot 10^{-5}$	$1.2 \cdot 10^{-8}$	$4.19 \cdot 10^{-2}$	$3.98 \cdot 10^{-5}$	119.1	$1.1 \cdot 10^{-1}$
	0.69 A cm^{-2}	$9.9 \cdot 10^{-6}$	$9.4 \cdot 10^{-9}$	$3.75 \cdot 10^{-2}$	$3.56 \cdot 10^{-5}$	56.5	$5 \cdot 10^{-2}$
	1.00 A cm^{-2}	$9.8 \cdot 10^{-6}$	$9.3 \cdot 10^{-9}$	$2.49 \cdot 10^{-2}$	$2.37 \cdot 10^{-5}$	37.2	$4 \cdot 10^{-2}$

The area-specific capacitance in table 5.3.1.15 of the middle frequency arc normalised by ECSA determined from CVs after initiation of the cells, are in the same order of magnitude as the capacitance of the model plate capacitor cf. (30). On the other hand the capacitance of the middle frequency arc normalised by the geometrical area is three orders of magnitude too big compared to the capacitance of the model plate capacitor cf. (30). This suggest that the process explaining the middle frequency arc is somehow a three-dimensional process and can be ascribed to the Ir metal and IrO_x particles and is taking place at the electrochemically active surface of the Ir and IrOx particles. The resistance of the middle frequency arc was according to the findings from figure 5.3.1.29 ascribed to Nafion, which can be explained by the Nafion binder in the IrO_x and Ir metal layers.

The area-specific capacitance of the low frequency arc normalised to the geometrical area is five to seven orders of magnitude bigger than the capacitance of the model plate capacitor and normalised to the ECSA determined from the CVs measured after initiation is three to four orders of magnitude larger than the capacitance of the model plate capacitor cf. (30) and table 5.3.1.15. These very high capacitances suggest that the process causing the low frequency arc is a more three-dimensional process than the processes causing the middle frequency arc, which primarily takes place at the surface of the Ir metal and IrO_x particles. In order to investigate how three dimensional the process is, the charge associated with the unnormalised capacitances given in table 5.3.1.13 and 5.3.1.14 of the low frequency arc has been calculated. The general definition of a capacitor is given by equation (31), in which Q is charge in C, E is potential in V and C is capacitance in F.

$$C = \frac{Q}{E} \Leftrightarrow Q = C \cdot E \tag{31}$$

The potential associated with the capacitance of an EIS arc is the AC potential associated with the particular arc applied during the EIS measurements. The EIS measurements during OER in this thesis are measured galvanostatically, which means that the AC potential associated with the particular arc is calculated from the AC current and the modulus of the impedance of the particular arc cf. equation (32), in which i_{AC} is the amplitude of the AC current and |Z| is the modulus of the impedance of the particular EIS arc.

$$Q = C \cdot i_{AC} \cdot |Z| \tag{32}$$

Modulus of the impedance of an arc consisting of a resistance and a capacitor connected in parallel is given by equation (33), which means that the charge associated with the low frequency arc can be calculated from equation (34), which is resulting from equation (32) and (33).

$$|Z| = \sqrt{R^2 + \frac{1}{\omega \cdot C^2}} = \sqrt{R^2 + \frac{1}{2\pi \cdot f \cdot C^2}} \tag{33}$$

$$Q = C \cdot i_{AC} \cdot \sqrt{R^2 + \frac{1}{2\pi \cdot f \cdot C^2}} \tag{34}$$

Charges associated with the three EIS arcs calculated from equation (34) are given in table 5.3.1.16. By comparing the charges of the low frequency arc in table 5.3.1.16 to the charges given in table 5.1.5.8, which are the charges calculated from the Ir metal and IrO_x loading and the geometry of the particles according to SEM, it is realized that the charge associated with the low frequency arc is two orders of magnitude smaller than the charge associated with electrochemically accessibility of all the Ir metal atoms in the EWII benchmark PEMECs. This suggests that though the process associated with the low frequency arc is more three-dimensional than the process associated with the middle frequency arc, not all the iridium is electrochemically active, and only approximately 1 % of the total amount of iridium in the EWII benchmark cells is causing the low frequency arc, if it assumed that the low frequency arc can be ascribed to the catalyst and Ir metal layers. The findings from figure 5.3.1.29 ascribed the resistance of the low frequency arc to Nafion, which may be explained by Nafion binder in the catalyst and Ir metal layers and support the assumption that the low frequency arc can be ascribed to the catalyst and Ir metal layers. This is further supported by the very small n for the middle and low frequency arcs in table 5.3.1.13 and 5.3.1.14, which is below 0.9 and down to 0.35, suggesting a distribution of relaxation times of the two arcs, probably due to a porous composite structure such as the Ir metal and IrO_x porous layers.

Table 5.3.1.16 Charges calculated from the unnormalised equivalent capacitances given in table 5.3.1.13 and 5.3.1.14 for the high, middle and low frequency arcs. The charges have been calculated from the AC potential, $Q(E_{AC})$, according to equation (34).

		High Frequency Arc	**Middle Frequency Arc**	**Low Frequency Arc**
		$Q(E_{AC})$ [mC]	**$Q(E_{AC})$ [mC]**	**$Q(E_{AC})$ [mC]**
EWII benchmark (ALIO)	**0.35 A cm^{-2}**	$9.37 \cdot 10^{-3}$	1.20	89
	0.69 A cm^{-2}	$9.44 \cdot 10^{-3}$	0.93	28.8
	1.00 A cm^{-2}	$9.87 \cdot 10^{-3}$	0.83	16.5
EWII benchmark (ALIP)	**0.35 A cm^{-2}**	$2.48 \cdot 10^{-2}$	2.04	98.6
	0.69 A cm^{-2}	$2.18 \cdot 10^{-2}$	1.57	56.2
	1.00 A cm^{-2}	$2.01 \cdot 10^{-2}$	1.35	36.1

Based on the above findings the middle frequency arc is ascribed to oxidation of Ir^{4+} to Ir^{5+} in the catalyst and Ir metal layers of the EWII benchmark, and the low frequency arc is ascribed to the oxidation of Ir^{5+} to Ir^{6+} in the catalyst and Ir metal layers of the EWII benchmark cells.

Fits of iV-curves Based on EIS Findings

The iV-curves measured on the EWII benchmark cells, cell 0 and ALIP, have been fitted to the iV-curve model given in equation (35), and the Tafel parameters have been determined.

$$E(i) = E_{Onset} + E_{Ohmic}(i) + E_{Tafel}(i) = E_{Onset} + R_{Ohmic} \cdot i + a + b \cdot \log(i) \qquad (35)$$

According to the EIS findings explained above, the resistance of all the processes contributing to the total differential cell resistance is ascribed to Nafion in the electrolyte and in the catalyst and the iridium metal layers, when operating the PEMEC in the linear part of the iV-curve above 0.35 A cm^{-2}. This means that the total differential cell resistance, which is the slope of the iV-curve, in the linear part of the iV-curve of the EWII benchmark cells is ohmic in nature. This implies that the ohmic resistance, R_{Ohmic}, is given by the slope of the iV-curves or the low frequency intercept of the measured impedance, and not by the high frequency intercept as is often used in the literature for ohmic resistance correction of iV-curves of PEMECs (20). In equation (35) I is current density, E(i) is the cell potential as function of i, E_{Tafel}(i) is the Tafel potential associated with the electrode reactions as function of i, a and b is the Tafel parameters and E_{Onset} is the onset potential. The onset potential is the potential, where OER cause an abrupt increase in current density, which is at 1.4 V as can be seen in figure E.1.73 and all other iV-curves in the thesis and of PEMECs in general.

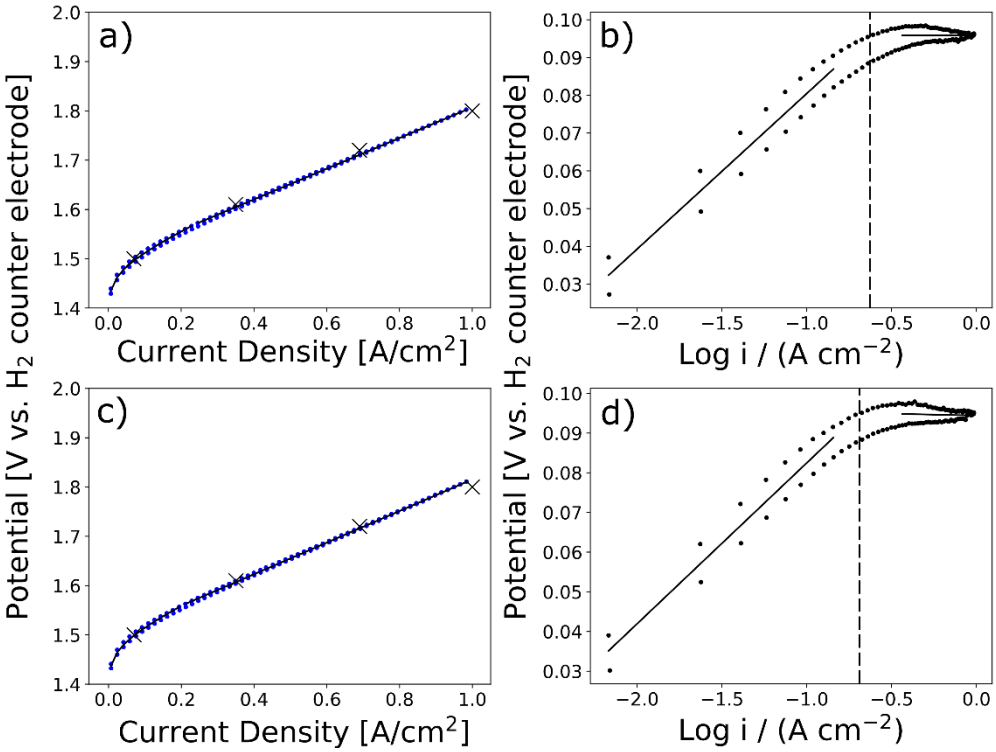

Figure 5.3.1.33 iV-curve measured at 61 °C, before EIS measurements on the reference EWII benchmark cell, cell 0, shown with fit to the model $E(i) = E_{onset} + E_{ohmic}(i) + E_{Tafel}(i) = E_{Onset} + R_{ohmic} \cdot i + a + b \cdot log(i)$ *(a).* $E_{Onset} = 1.4\,V$ *and* R_{ohmic} *was set to the slope of the iV-curve in the linear region at current densities above 0.35 A cm^{-2}. The Tafel parameters were determined from linear regression of the Tafel plot of* E_{Tafel}*, shown in (b). Two regions with different Tafel parameter were distinguished, and linear regression of the Tafel plot was made at the current density range 0.0173 – 0.15 A cm^{-2} and at 0.35-0.9 A cm^{-2}. (c) shows iV-curve with fit measured at 61 °C after EIS measurements on the same reference EWII benchmark cell, cell 0, and (d) shows Tafel plot of* E_{Tafel} *from the iV-curve shown in (d). Tafel parameters for the low and high current density region of the two iV-curves can be found in table 5.3.1.17. (i,E) measured during the EIS measurements are shown together with the iV-curves with fits as big black crosses.*

The onset potential is different from EMF, which is 1.23 V for splitting of water into hydrogen and oxygen. The difference between EMF and the onset potential is explained by Rossmeisl et al. (39), who ascribe the potential difference between EMF and the onset potential to intermediates on the catalyst surface during OER. Rossmeisl et al. (39) ascribe intermediates on the IrO_x catalyst surface to an overpotential of 0.56 V at 25 °C, which is bigger than the overpotential of 0.17 V of intermediates associated with an onset potential of 1.4 V is slightly smaller than the overpotential of intermediates described by Rossmeisl et al., which may be explained by the increased operating temperature of the PEMECs (50-70 °C) compared to the temperature at which the DFT calculations by Rossmeisl et al. is performed (25 °C). Beside that the increase in current density of the iV-curves takes of at 1.4 V, an OCV of 1.4 V has been observed for the PEMECs just after electrolysis (1.39 V was observed for the EWII benchmark cell, ALIP and 1.37 and 1.45 V was observed for two of the PSI benchmark cells). The potential then decrease over time, when the cell is kept at open circuit cf. figure 5.3.1.34.

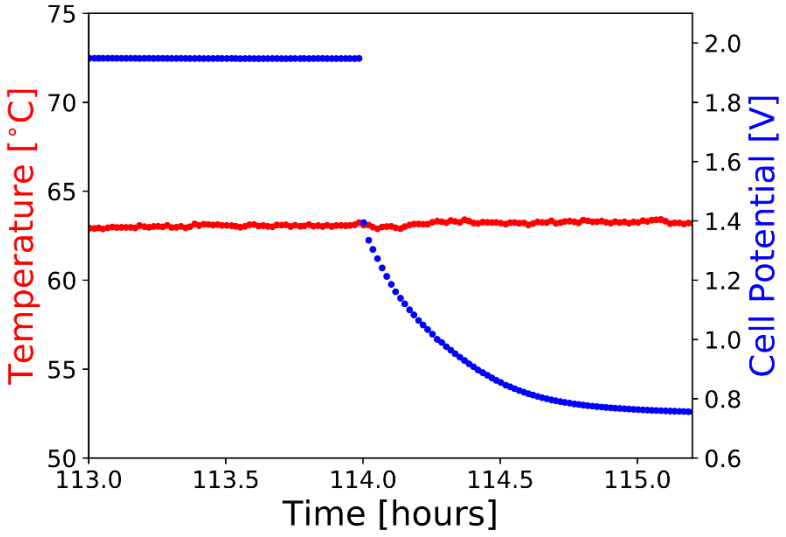

Figure 5.3.1.34 Potential decay after electrolysis operation of the EWII benchmark cell, ALIP, while flushing the cathode with humidified hydrogen and supplying oxygen saturated water to the anode. The potential drops to 1.4 V, when the cell is put at open circuit, where after the potential decays to 0.76 V.

The Tafel parameters, a and b, are determined from Tafel plots of E_{Tafel} from equation (35), in which E_{Onset} = 1.4 V and R_{Ohmic} is determined as the linear part of the iV-curve. Figure 5.3.1.33 shows iV-curves measured at 61 °C on the reference EWII benchmark cell, cell 0, before and after EIS measurements (blue dots) and Tafel plots of E_{Tafel} for the two iV-curves. The Tafel parameters, a and b, are determined as a average of the anodic and cathodic scan of the iV-curves. Two Tafel regions are observed in the two Tafel plots in figure 5.3.1.33; one at 0.017 – 0.15 A cm^{-2} and one at 0.35 – 0.9 A cm^{-2}. Tafel parameters are determined from each of these regions and listed in table 5.3.1.17 together with Tafel parameters determined from iV-curves measured on the same reference EWII benchmark cell, cell 0, at 53 and 69 °C. R_{Ohmic} determined as the slope of the iV-curves at 0.35 – 0.98 A cm^{-2} is additionally given in table 5.3.1.17 together with the total cell resistance determined from the real part of the impedance at low frequency, which according to the EIS findings should correspond to R_{Ohmic}, which it according to table 5.3.1.17 does. The current density, at which the linear regressions of the two regions of the Tafel plots cross, denoted $i_{cross\ of\ Tafel\ regressions}$, is also given in the table. The iV-curves, Tafel regressions and iV-curve fits at 53 and 69 °C can be found in appendix E. It should be noted that the fits of the full iV-curves shown in figure 5.3.1.33 and in appendix E consists of two regions; one low current density fit region from 0 A cm^{-2} to $i_{cross\ of\ Tafel\ regressions}$ in which a_{low} and b_{low} is used ad Tafel parameters in the total fit given in equation (35), and one high current density region from $i_{cross\ of\ Tafel\ regressions}$ to 1.00 A cm^{-2} in which a_{high} and b_{high} is used ad Tafel parameters in the total fit given in equation (35). The reason for the two fit regions are, that according to the Tafel plots e.g. shown in figure 5.3.1.33, the iV-curve contains two quasi linear regions.

Table 5.3.1.17 Reference EWII benchmark cell, cell0. The Tafel fit in the low current density region was done at 0.0173 – 0.15 A cm^{-2}, while the Tafel fit in the high current density region was done at 0.35-0.9 A cm^{-2}.

	Average $Z_{re,LF}$ from 0.35 to 1.00 A cm^{-2} [Ω cm^2]	R_{ohmic} [Ω cm^2]	a_{low} (Tafel intercept) [mV]	b_{low} (Tafel slope) [mV/dec.]	a_{high} (Tafel intercept) [mV]	b_{high} (Tafel slope) [mV/dec.]	$i_{cross\ of\ Tafel\ regressions}$ [A cm^{-2}]
53 °C start	0.357 ± 0.009	0.366	138	39	108	1	0.16
53 °C end		0.365	139	39	109	1	0.16
61 °C start	0.318 ± 0.001	0.311	122	41	96	0.03	0.24
61 °C end		0.321	123	41	94	-1	0.20
69 °C start	0.304 ± 0.002	0.301	104	41	78	-1	0.23
69 °C end		0.309	106	39	76	-2	0.20

iV-curves measured on the other EWII benchmark cell, ALIP, at 55-56, 63 and 70-71 °C is shown with Tafel plots and iV-curve fits in appendix D. R_{Ohmic}, Tafel parameters for the two Tafel regions, $i_{cross\ of\ Tafel\ regressions}$ determined from the iV-curves measured on the EWII benchmark cell, ALIP, and the real part of the impedance at low frequency measured at ALIP is shown in table 5.3.1.18. It has been chosen to fit the anodic and cathodic scan of the iV-curves of the EWII benchmark cell, ALIP, in one fit meaning that the fit value is an average of the anodic and cathodic scan of the iV-curves. This is done even though the hysteresis of the iV-curves of the EWII benchmark cell, ALIP, is bigger than the hysteresis of the reference EWII benchmark cell, cell 0, in order to apply the same fitting routines on the data for both cells. From table 5.3.1.17 it can be seen that the Tafel slopes determined for the low current density range, b_{low}, is 39 - 41 mV dec^{-1}, whereas the Tafel slopes determined for the high current density range, b_{high}, is -2 – 1 mV $dec.^{-1}$, which is approximately 0 mV dec^{-1}, and the Tafel slopes does not seem dependent on temperature. On the other hand the Tafel intercept, a, seems to decrease with increasing operating temperature, ad was determined to vary from 139 mV to 104 mV for the low current density range, and from 109 mV to 76 mV for the high current density range. In table 5.3.1.18 much higher deviation are observed in the table compared to table 5.3.1.17, which is consistent with the fact that the fits to the iV-curves measured on the reference EWII benchmark cell, cell 0, is better than the fits to the iV-curves measured on the other EWII benchmark cell, ALIP. The Tafel intercepts, a, measured for the EWII benchmark cell, ALIP, is likewise the reference EWII benchmark cell, cell 0, dependent on operating temperature, and vary from 233 mV to 122 mV for the low current density region and from 208 mV to 109 mV for the high current density region. The Tafel slope for the EWII benchmark cell, ALIP, was for the low current density range, b_{low}, found to be 48 – 77 mV $dec.^{-1}$ and for the high current density range, b_{high}, -9 – 15 mV $dec.^{-1}$. In this regard it should be noted that the Tafel parameters given in table 5.3.1.17 and 5.3.1.18 are apparent Tafel parameters and an average between the Tafel parameters for the two electrodes.

Table 5.3.1.18 EWII benchmark cell, ALIP. The Tafel fit in the low current density region was done at 0.0173 – 0.15 A cm^{-2}, while the Tafel fit in the high current density region was done at 0.35-0.9 A cm^{-2}.

	Average $Z_{re,LF}$ from 0.35 to 1.00 A cm^{-2} [Ω cm^2]	R_{ohmic} [Ω cm^2]	a_{low} (Tafel inter-cept) [mV]	b_{low} (Tafel slope) [mV/dec.]	a_{high} (Tafel inter-cept) [mV]	b_{high} (Tafel slope) [mV/dec.]	$i_{cross\ of\ Tafel\ re-gressions}$ [A cm^{-2}]
55-56 °C start	0.448 ± 0.025	0.458	208	66	170	-9	0.32
55-56 °C end		0.389	233	77	208	8	0.43
63 °C start	0.315 ± 0.024	0.308	143	54	125	7	0.42
63 °C end		0.314	150	54	130	6	0.38
70-71 °C start	0.413 ± 0.020	0.377	122	48	114	15	0.54
70-71 °C end		0.362	138	52	109	-3	0.30

A Tafel slope close to zero, as observed for the two EWII benchmark cells at current densities above 0.35 A cm^{-2} cf. table 5.3.1.17 and 5.3.1.18, implies that the faradaic processes are not rate limiting in this current density interval, and the primary process contributing to the cell resistance is the ohmic resistance (32). However the Tafel parameter a, is still influencing the iV-curve cf. 5.3.1.17 and 5.3.1.18. The Tafel slopes of 39-77 mV $dec.^{-1}$ in the low current density region is similar to Tafel slopes reported for the OER on IrO_2 elsewhere (55-68 mV $dec.^{-1}$ by De Pauli et al. (54) and 40 mV $dec.^{-1}$ by Owe et al. (55) and 58 mV $dec.^{-1}$ by Kötz et al. (56), 45-50 mV $dec.^{-1}$ by Bernt et al. (19) and 60 mV $dec.^{-1}$ by Angelinetta et al. (57)). The change in Tafel slope with increasing potentials may be explained by the change in oxidation state of the iridium in the IrO_x catalyst to very high oxidation states up to Ir^{6+} according to the EIS findings, which changes the catalytic properties of the iridium catalyst and increase the catalytic activity and the faradaic processes is therefore not performance limiting.

5.3.1.1.7 Theoretical Considerations

Now it is considered how the different terms in the fit model given in equation (35) is affecting the shape of the iV-curve. In figure 5.3.1.35 the fit given in the fit model in equation (35) is shown with Tafel parameters determined from the low current density region from 0.017 to 0.15 A cm^{-2} in the green graph and with Tafel parameters determined in the high current density region from 0.35 to 0.9 A cm^{-2} in the red graph. It is seen that neither of the two fits are fitting the measured iV-curve, which mean that the iV-curve has to be fitted in two regions with different Tafel slopes.

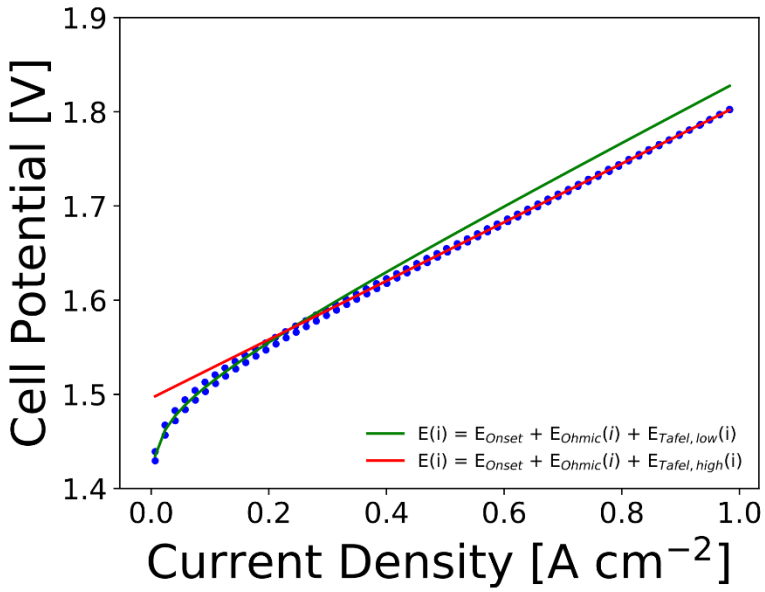

Figure 5.3.1.35 iV-curve measured at 61 °C, before EIS measurements on the reference EWII benchmark cell, cell 0, shown with fit to the model $E(i) = E_{onset} + E_{ohmic}(i) + E_{Tafel}(i) = E_{Onset} + R_{ohmic} \cdot i + a + b \cdot log(i)$ *with* $E_{Onset} = 1.4$, R_{ohmic} *was set to the slope of the iV-curve in the linear region at current densities above 0.35 A cm^{-2} and the Tafel parameters, a and b, were for the green graph set to parameter values determined from Tafel plots at the low current density range (0.017 – 0.15 A cm^{-2}) and for the red graph set to parameter values determined from Tafel plots at the high current density range (0.35-0.9 A cm^{-2}).*

In figure 5.3.1.36 the influence of the various terms in the fit model in equation (35) on the shape of the iV-curve is shown. It is seen in figure 5.3.1.36 a) that an increase in E_{onset} translates the iV-curve to higher potentials, from figure 5.3.1.36 b) it is seen that R_{Ohmic} determines the slope of the linear part of the iV-curve and from figure 5.3.1.36 c) and d) it is seen that the Tafel parameters, a and b, translates the iV-curve to higher or lower potentials and changes the bending of the iV-curve at low current densities, respectively. It is noted that the effect of the two parameters E_{onset} and the Tafel parameter a is the same; they translate the iV-curve to higher or lower potentials. However, the two parameters are originating from two different processes, though their influence on the iV-curve is the same. While E_{onset} is EMF and the overpotentials of intermediates adsorbed on the catalyst surface, the Tafel parameter a may originate from changes in the IrO_x structure during the OER.

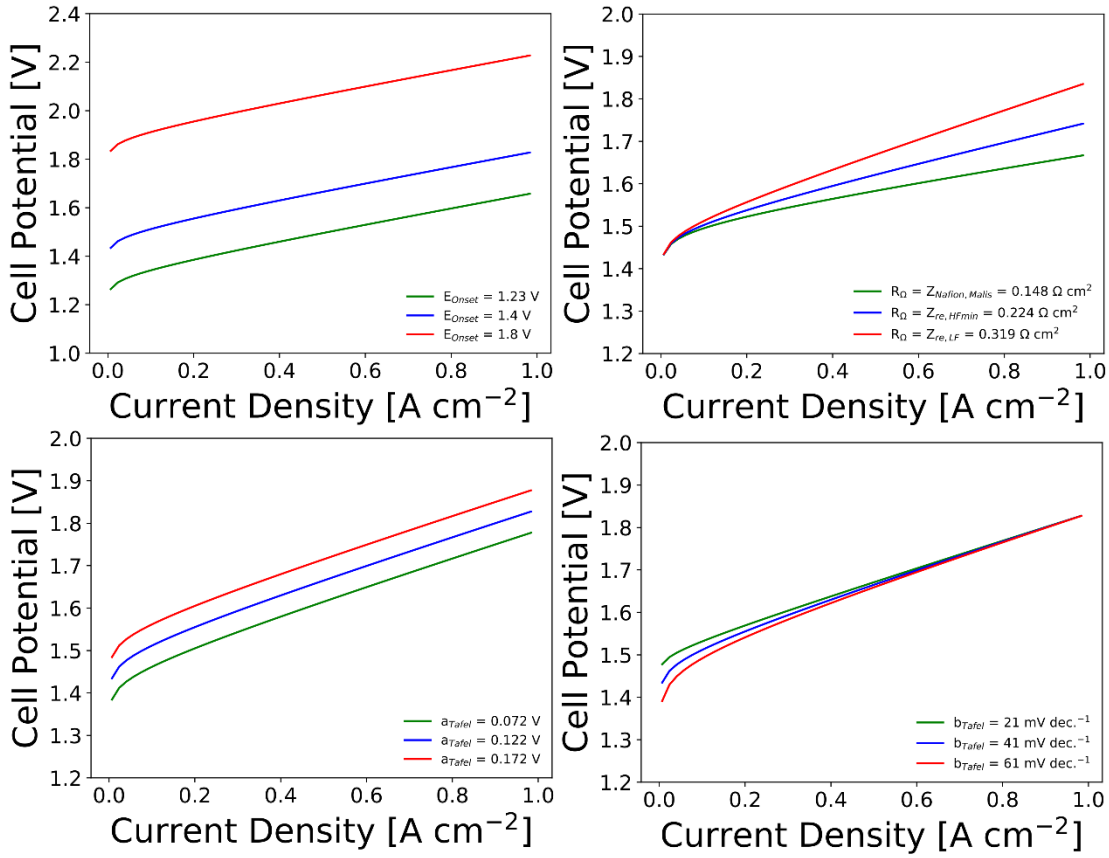

Figure 5.3.1.36 Potential decay after electrolysis operation of the EWII benchmark cell, ALIP, while flushing the cathode with humidified hydrogen and supplying oxygen saturated water to the anode. The potential drops to 1.4 V, when the cell is put at open circuit, where after the potential decays to 0.76 V.

5.3.2 EWII Cells without IrO_x Catalyst

IV-curves

5.3.2.1.1 Linearity and Hysteresis

iV-curves measured on an EWII cell without IrO_x anode catalyst, but with the Ir-metal current collector layer, is compared to iV-curves of the reference EWII benchmark cell in figure 5.3.2.37. More hysteresis is observed in the iV-curves of the EWII cell without IrO_x anode catalyst compared to the iV-curves of the reference EWII benchmark cell, and the performance of the EWII cell without IrO_x is not as good as the performance of the reference EWII benchmark cell.

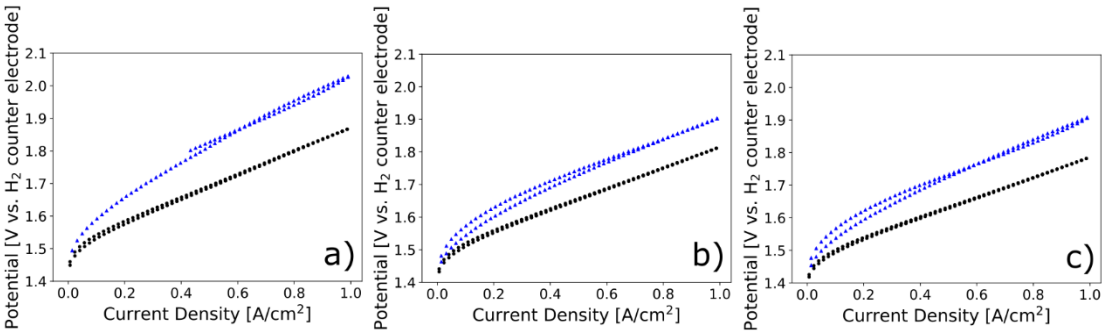

Figure 5.3.2.37 iV-curves measured after EIS measurements at 56 °C (a), 64 °C (b) and 70-71 °C (c) on an EWII cell, ATMJ, without IrO_x, but with the Ir-metal layer (blue triangles) and compared with similar measurements on the reference EWII benchmark cell, Cell 0. It is noticed that the cell without IrO_x catalyst is performing worse than the reference EWII benchmark cell, however it is possible to draw current with the cell without IrO_x, which suggests that the Ir-metal layer is electrochemically active.

It is seen from figure 5.3.2.37 that the slope of the cathodic and anodic scan of the iV-curves are different due to hysteresis, however the iV-curves measured on the EWII cell without IrO_x is fairly linear. iV-curves and temperatures measured on the EWII cell without IrO_x, ATMJ, before EIS measurements (a, b and c) and after EIS measurements (d, e and f) at 56 °C (a and d), 64 °C (b and e) and 70-71 °C (c and f) is shown in figure 5.3.2.38. From this figure it can be seen that the slope of the anodic scan is bigger than the slope of the cathodic scan of the iV-curves. This means that the cathodic scan of the iV-curves of the EWII cell without IrO_x, ATMJ, is more similar to the iV-curves measured on the reference EWII benchmark cell than the anodic scan of the iV-curves measured on the EWII cell without IrO_x. The constant differential cell resistances for the EWII cell without IrO_x, ATMJ, given by the slope of the iV-curves measured before and after EIS measurements at three different water temperatures are listed for the cathodic scan of the iV-curve in table 5.3.2.19. Similar to the EWII benchmark cells cf. section 5.3.1 the differential cell resistance of the EWII cell without IrO_x seem to decrease with increasing operating current density, however the trend is less clear than for the EWII benchmark cells. When comparing the differential cell resistances obtained for the cathodic scan of the EWII cell without IrO_x in table 5.3.2.19 to the differential cell resistance of the EWII benchmark cells given in table 5.3.1.10, it is noticed that the obtained values are fairly similar, ranging from 0.278 to 0.458 Ω cm^{-2} for the EWII benchmark cells and from 0.310-0.429 Ω cm^{-2} for the EWII cell without IrO_x.

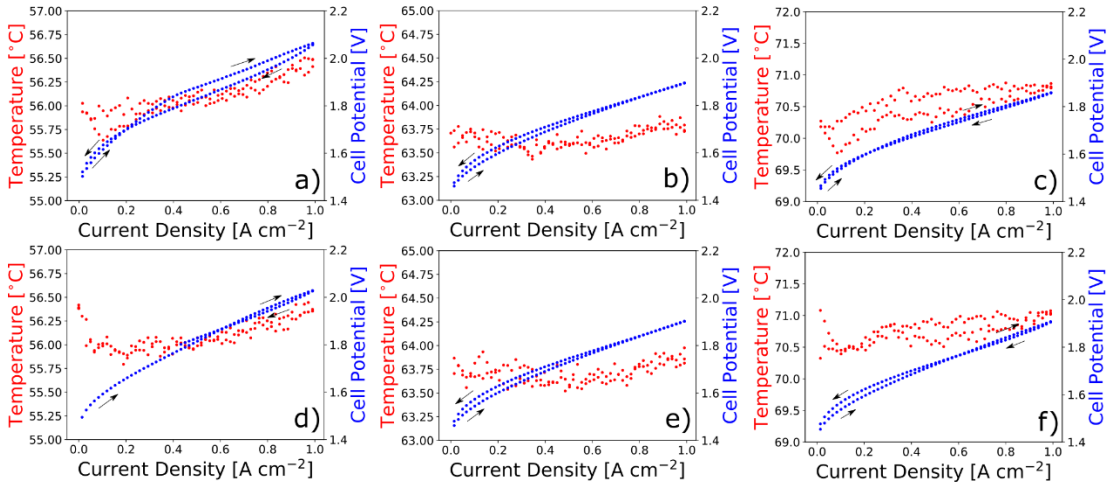

Figure 5.3.2.38 iV-curves with temperature measured on the EWII cell without IrOx anode catalyst, ATMJ, at 56 °C (a), 64 °C (b) and 70-71 °C (c) before EIS and at 56 °C (d), 64 °C (e) and 71 °C (f) after EIS measurements. The arrows express the current density scan direction.

Table 5.3.2.19 Linear regressions from 0.35-0.98 A cm^{-2} of the cathodic scan of iV-curves measured on EWII cells without IrO_x, ATMJ shown in figure 5.3.1.21.

Cell	Cell Temperature, T	Linear slope of iV-curve before EIS at the given T [Ω cm^{-2}]	Linear slope of iV-curve after EIS at the given T [Ω cm^{-2}]
ATMJ	**56 °C**	0.429	0.391
	64 °C	0.312	0.321
	70-71 °C	0.310	0.335

5.3.2.1.2 Stability during EIS Measurements – Comparison of iV-curves Measured Before and After EIS.

Figure 5.3.2.39 compares iV-curves measured before (blue dots) and after (black triangles) EIS measurements at the three operating temperatures for the EWII cell without IrO_x, ATMJ. The iV-curves are identical at 64 °C shown in b), but it is noticed that the cell potential have not been totally stable during the EIS measurements at 56 and 70-71 °C.

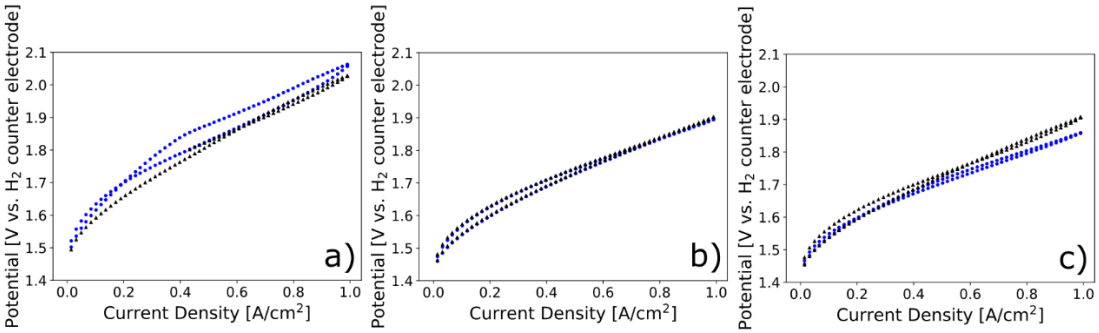

Figure 5.3.2.39 iV-curves measured before (blue dots) and after (black triangles) EIS measurements at 56 °C (a), 64 °C (b) and 70-71 °C (c) on an EWII cell, ATMJ, without IrO_x catalyst, but with the Ir-metal layer only. The iV-curves measured before and after the EIS measurement at each temperature is hardly distinguishable at 64 °C, but differs at 70-71 °C and 56 °C, which suggests that the cell changes state during the EIS measurements at 70-71 °C and 56 °C.

Electrochemical Impedance Spectroscopy

5.3.2.1.3 Nyquist and Bode Plots of EIS Measured on EWII Cells without IrO_x Catalyst

Nyquist plots of EIS measures on the EWII cell without IrO_x, ATMJ, at various current densities (0.07, 0.35, 0.69 and 1.00 A cm^{-2}) and at cell temperatures of 56, 64 and 70-71 °C is shown in figure 5.3.2.40. Similar to the EWII benchmark cells in section 5.3.1, the low frequency arc of the EIS spectra is increasing with increasing current density and the middle frequency arc is decreasing with increasing current density.

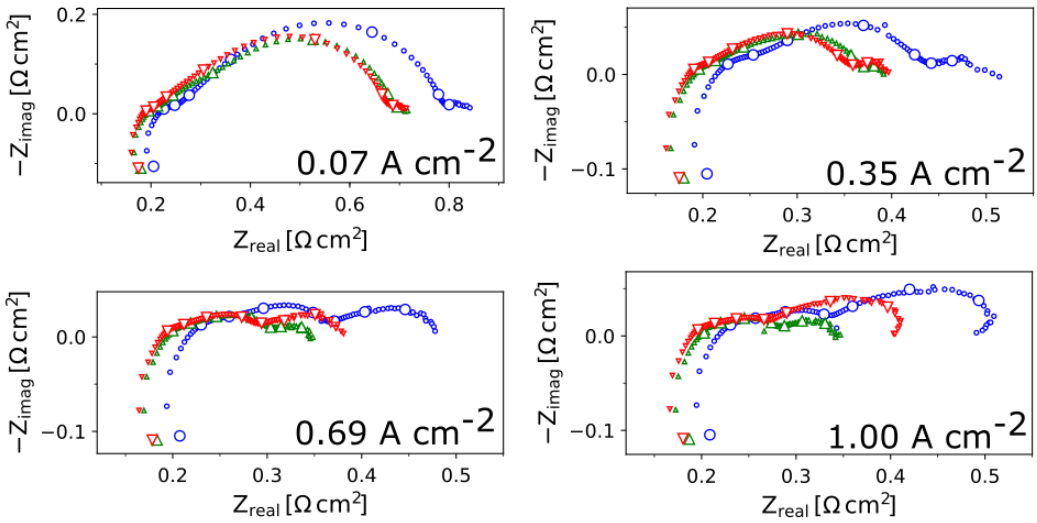

Figure 5.3.2.40 EIS measured at 56 °C (blue circles), 64 °C (green triangles) and 70-71 °C (red triangles) and at 0.07, 0.35, 0.69 and 1.00 A cm^{-2} on an EWII cell without IrO_x catalyst, ATMJ, but with the Ir-metal layer only.

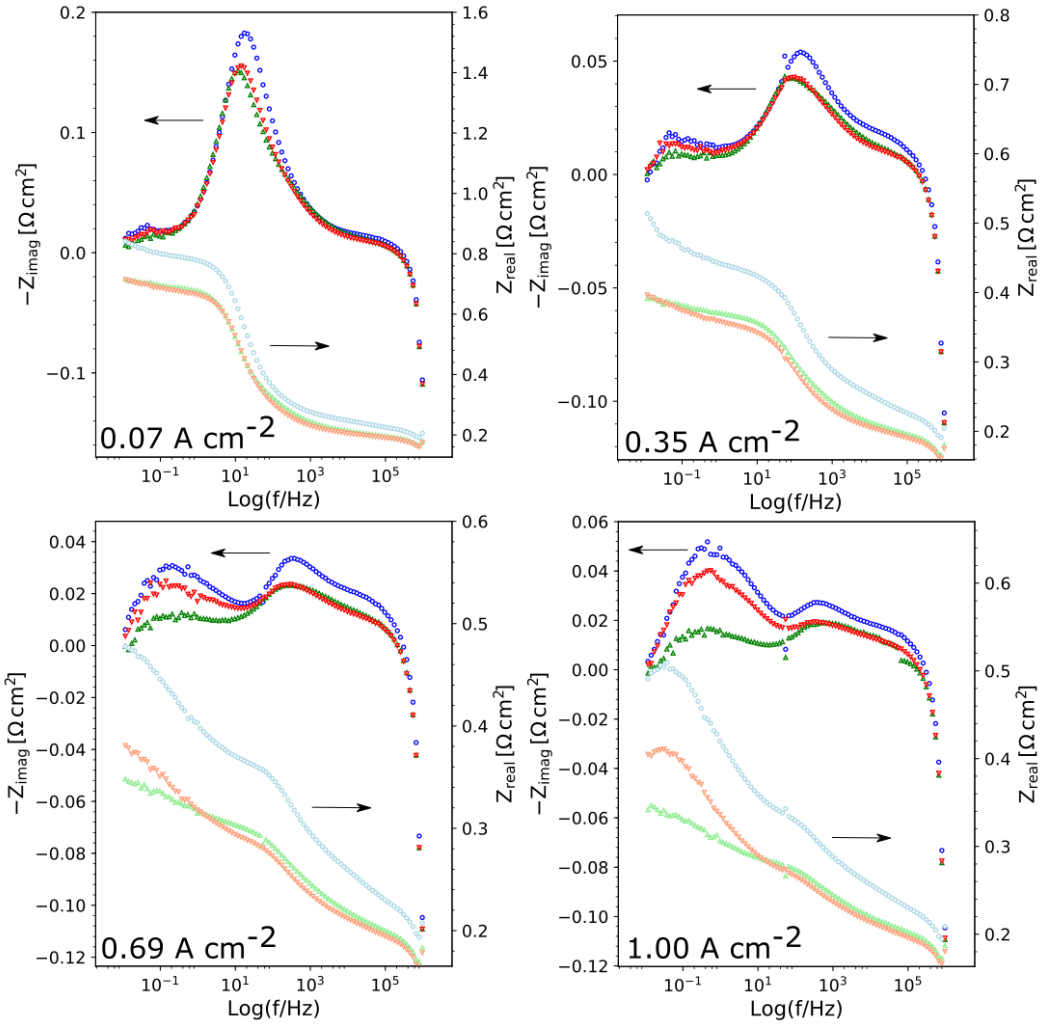

Figure 5.3.2.41 EIS shown in Bode plots measured at 56 °C (blue / light blue circles), 64 °C (green / light green triangles) and 70-71 °C (red/ light red triangles) and at 0.07, 0.35, 0.69 and 1.00 A cm^{-2} on the EWII cell without IrO$_x$, ATMJ. The imaginary part of the impedance are shown with dark colours and y-axis to the left, while real part of the impedance is shown with light colours and y-axis to the right.

Bode plots of the EIS data measured on the EWII cell without IrO_x, ATMJ, are depicted in figure 5.3.2.41. Summit frequencies read off from the Bode plots and $Z_{re,LF}$ for the EWII cell without IrO_x, ATMJ, is given in table C.39 in the appendix C, and averages of $Z_{re,LF}$ measured above 0.35 A cm^{-2} for each operating temperature is given in table 5.3.2.20. It is noticed that values for $Z_{re,HF\ min}$, $Z_{re,LF\text{-}HF\ min}$ and $Z_{re,HF\ min\text{-}Rs(Malis)}$ is not given in table 5.3.2.20, which they are for the EWII benchmark cells in table 5.3.1.11, due to difficulties with reading off these values. It is furthermore noted that the deviation of the average $Z_{re,LF}$ is higher for the EWII cell without IrO_x compared to the EWII benchmark cells, implying that the differential cell resistance determined from the EIS measurements for the EWII cell without IrO_x is not as constant with current density even in the linear region of the iV-curve as the EWII benchmark cells. This in combination with the fairly linear iV-curves implying a constant differential cell resistance above 0.35 A cm^{-2}, may imply that the cell have not been as steady during the EIS measurements as the EWII benchmark cells.

Table 5.3.2.20 Averages of the total cell resistance, $Z_{re,LF}$, from 0.35 A cm^{-2} to 1.00 A cm^{-2} (the linear part of the iV-curves), averages of $Z_{re,HF}$ min up to 1.00 A cm^{-2}, averages of the resistance of the middle and low frequency arcs, $Z_{re,\ LF\ -\ HF\ min}$ from 0.35 A cm^{-2} to 1.00 A cm^{-2} and averages of $Z_{re,HF\ min\ -\ Rs(Malis)}$ up to 1.00 A cm^{-2}.

	Cell Temperature, T	Average $Z_{re,LF}$ from 0.35 to 1.00 A cm^{-2}	Average $Z_{re,HF\ min.}$ up to 1.00 A cm^{-2}	Average $Z_{re,\ LF\ -\ HF\ min}$ from 0.35 to 1.00 A cm^{-2}	Average $Z_{re,HF\ min\ -\ Rs(Malis)}$ up to 1 A cm^{-2}
ATMJ Without IrO_x	**56 °C**	0.494 ± 0.018 Ω cm^2	-	-	-
	64 °C	0.360 ± 0.027 Ω cm^2	-	-	-
	70-71 °C	0.394 ± 0.012 Ω cm^2	-	-	-

In table 5.3.2.21 the average differential cell resistance determined from EIS measurements, $Z_{re,LF}$, is compared to the differential cell resistance of the linear part of the iV-curves above 0.35 A cm^{-2} measured before and after the EIS measurements. It is noted from table 5.3.2.21 that the differential cell resistance determined from the EIS measurements are higher than the differential cell resistances determined from the iV-curves even when taking the deviation into account.

Table 5.3.2.21 Total differential cell resistance given by the slope of linear regressions from 0.35-0.98 A cm^{-2} of iV-curves measured before and after EIS measurements on EWII benchmark cells shown in figure 5.3.1.21. The total cell resistances are compared to average total cell resistances above 0.35 A cm^{-2} determined by DC impedance, $Z_{re,LF}$, at the same EWII benchmark cells.

Cell	Cell Temperature, T	Linear slope of iV-curve before EIS at the given T [Ω cm^{-2}]	Linear slope of iV-curve after EIS at the given T [Ω cm^{-2}]	Average $Z_{re,LF}$ from 0.35 to 1.00 A cm^{-2} [Ω cm^{-2}]
EWII cell without IrO_x, ATMJ	**56 °C**	0.429	0.391	0.494 ± 0.018
	64 °C	0.312	0.321	0.360 ± 0.027
	70-71 °C	0.310	0.335	0.394 ± 0.012

The dependence of operating temperature on the differential cell resistances of the EWII cell without IrO_x is in figure 5.3.2.42 shown and compared to the temperature dependence of the Nafion membrane reported by Malis et al. (47). The linear regression of $Z_{re,LF}$ as function of operating temperature is less good as for the reference EWII benchmark cell shown in figure 5.3.1.29, but from the regression of $Z_{re,LF}$ in figure 5.3.2.42 it is determined that the differential cell resistance of the EWII cell without IrO_x decrease with 7 mΩ cm^2 per degree increase in operating temperature, which is a dependence of the same order of magnitude as reported by Malis et al. (47) for the Nafion membrane and observed for the EWII benchmark cells cf. figure 5.3.1.29. This supports that Nafion in the electrolyte and the electrodes cause all the resistance of the PEMEC during OER.

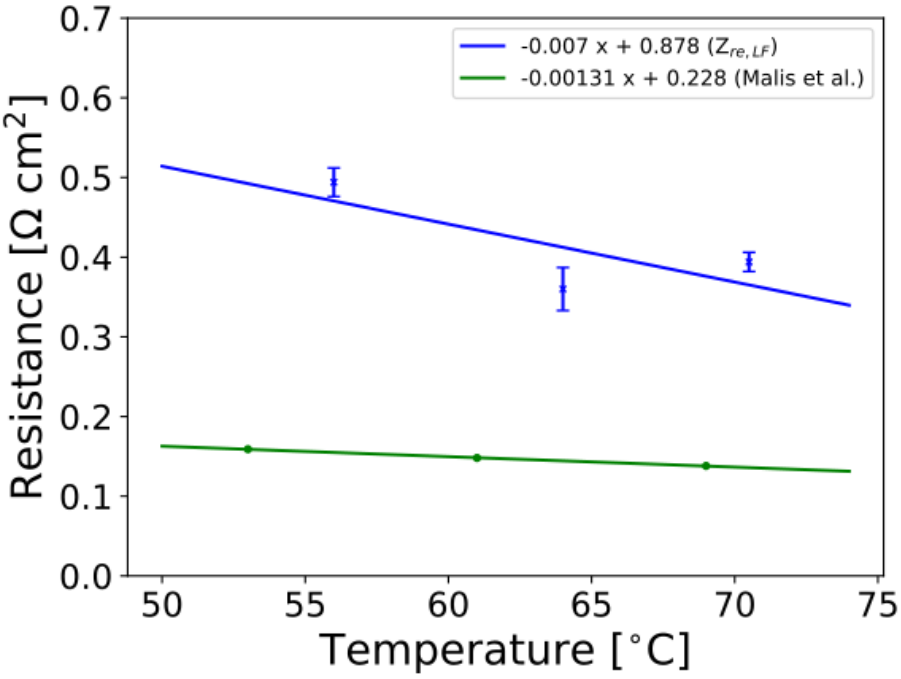

Figure 5.3.2.42 $Z_{re,LF}$ (blue crosses) shown as function of operating temperature for the EWII cell without IrO_x, ATMJ, compared to in-plane resistance measurements of operated Nafion 117 membranes reported by Malis et al. (47) (green circles).

5.3.2.1.4 EIS Model

Since the EIS spectra of the EWII cell without IrO_x are measured up to 1 MHz, high frequency inductance is observed in all the EIS spectra. As described in section 5.3.1, the EIS spectra of the PEMECs with high frequency inductance are fitted to the equivalent circuit R-L-RQ-RQ-RQ. These fits can be found in figure 5.3.2.43 for EIS measured on the EWII cell without IrO_x at 64 °C and at 0.35, 0.69 and 1.00 A cm^{-2}. Kramers-Kronig plots are depicted in figure 5.3.2.43 along with the fits and show a very good Kramers-Kronig compliance up to 100 kHz. The EIS data and fits in figure 5.3.2.43 are shown with each of the three arcs and the inductance from the equivalent circuit in figure 5.3.2.44.

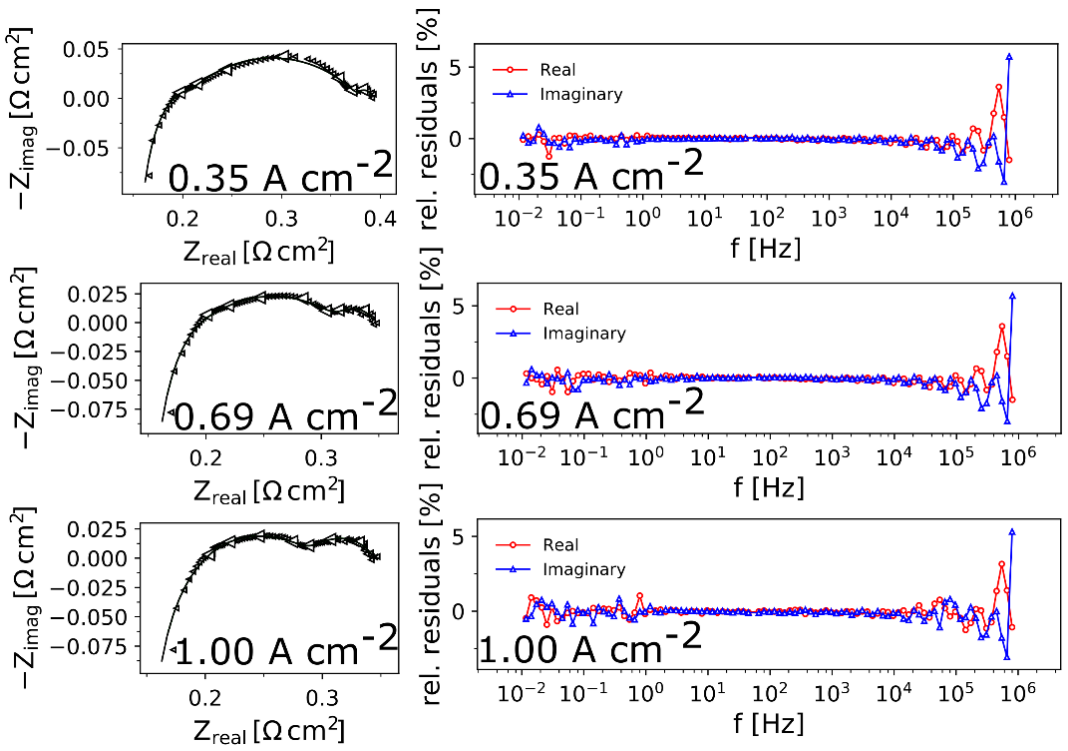

Figure 5.3.2.43 Nyquist plots and Kramers-Kronig compliance tests of EIS measured at 64 °C and at 0.07, 0.35, 0.69 and 1.00 A cm^{-2} on an EWII cell without IrO_x, ATMJ. Fits of the measured EIS to the equivalent circuit R-L-RQ-RQ-RQ is also shown in the plots. The serial resistance was kept constant at the literature value reported by Malis et al. (47) during fitting (0.144 Ω cm^2 at 64 °C). EIS measured at 50-60 Hz and above 800 kHz was excluded from the fits.

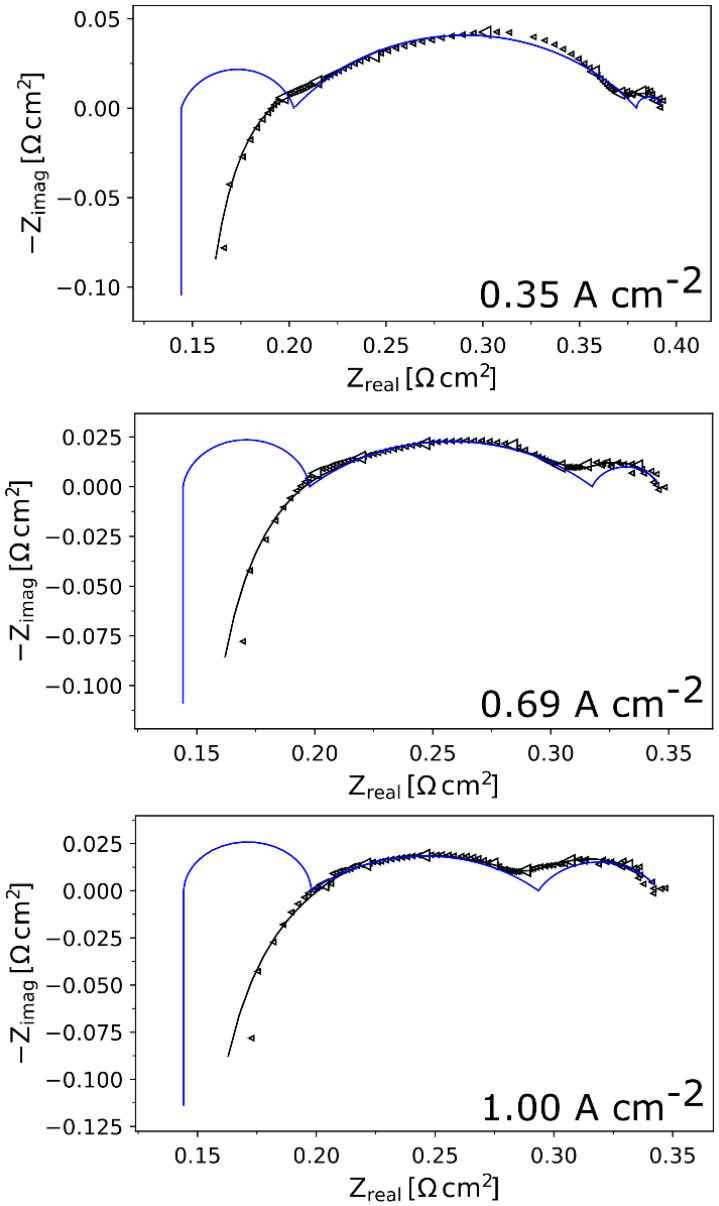

Figure 5.3.2.44 Nyquist plots of EIS measured at 64 °C and at 0.07, 0.35, 0.69 and 1.00 A cm^{-2} on an EWII cell without IrO_x, ATMJ. Fits of the measured EIS to the equivalent circuit R-L-RQ-RQ-RQ is also shown in the plots. The serial resistance was kept constant at the literature value reported by Malis et al. (47) during fitting (0.144 Ω cm^2 at 64 °C). The three arcs of the equivalent circuit (blue) is shown together with the data points and the total fit (black). EIS measured at 50-60 Hz and above 800 kHz was excluded from the fits.

5.3.2.1.5 EIS Model Explained with Physical Processes

The fit parameters for the fits of EIS measured on the EWII cell without IrO_x at 64 °C and 0.35, 0.69 and 1.00 A cm^{-2} shown in figure 5.3.2.44 are listed in table 5.3.2.22 together with equivalent capacitances for each of the three subarcs. When comparing table 5.3.2.22 to table 5.3.1.13 and 5.3.1.14 it is seen that the equivalent capacitance of the high and low frequency arcs are in the same order of magnitude for the EWII benchmark cells and the EWII cell without IrO_x, whereas the equivalent capacitance of the middle frequency arc is one order of magnitude small for the EWII cell without IrO_x than the EWII benchmark cells.

Table 5.3.2.22 Fit parameters for the fits of EIS measured on the EWII cell without IrO_x, ATMJ, at 64 °C and 0.35, 0.69 and 1.00 A cm^{-2}. Q and the equivalent capacitance, C_{eff}, are calculated based on equation (27) and (28), and listed in the table for each of the three arcs in the measured EIS spectra.

	High Frequency Arc			**Middle Frequency Arc**			**Low Frequency Arc**		
	R [Ω cm^2]	**n**	**C_{eff} [µF]**	**R [Ω cm^2]**	**n**	**C_{eff} [mF]**	**R [Ω cm^2]**	**n**	**C_{eff} [F]**
0.35 A cm^{-2}	0.06	0.82	16.0	0.18	0.55	17	0.01	1.00	590
0.69 A cm^{-2}	0.05	0.92	15.2	0.12	0.46	8	0.03	0.77	83
1.00 A cm^{-2}	0.05	0.98	13.5	0.10	0.47	5	0.05	0.69	23

In table 5.3.2.23 the equivalent capacitance from table 5.3.2.22 of the three subarcs are normalised by the geometrical electrode area, which was 2.89 cm^2 and by the ECSA given in table 5.1.5.6 determined from CVs shown in figure 5.1.5.19. The area specific equivalent capacitances in table 5.3.2.23 are for the high and low frequency arc in the same order of magnitude as observed for the EWII benchmark cells, whereas the area-specific equivalent capacitance of the middle frequency arc is one order of magnitude smaller than observed for the EWII benchmark cells, which also follows from the findings from table 5.3.2.22.

Table 5.3.2.23 Equivalent capacitances for the high, middle and low frequency arcs normalised by the geometrical electrode area, which is 2.89 cm^2, C_{eff} ($A_{geo.}$), and normalized by ECSA derived from CV measured after initiation given in table 5.1.5.6, $C_{eff}(A_{ECSA})$.

		High Frequency Arc		**Middle Frequency Arc**		**Low Frequency Arc**	
		C_{eff} ($A_{geo.}$) [F cm^{-2}]	**$C_{eff}(A_{ECSA})$ [F cm^{-2}]**	**C_{eff} ($A_{geo.}$) [F cm^{-2}]**	**$C_{eff}(A_{ECSA})$ [F cm^{-2}]**	**C_{eff} ($A_{geo.}$) [F cm^{-2}]**	**$C_{eff}(A_{ECSA})$ [F cm^{-2}]**
EWII without IrOx (ATMJ)	**0.35 A cm^{-2}**	$5.6 \cdot 10^{-6}$	$5.7 \cdot 10^{-9}$	$6.0 \cdot 10^{-3}$	$6.2 \cdot 10^{-6}$	204.2	$2.1 \cdot 10^{-1}$
	0.69 A cm^{-2}	$5.3 \cdot 10^{-6}$	$5.4 \cdot 10^{-9}$	$2.7 \cdot 10^{-3}$	$2.7 \cdot 10^{-6}$	28.6	$3 \cdot 10^{-2}$
	1.00 A cm^{-2}	$4.7 \cdot 10^{-6}$	$4.8 \cdot 10^{-9}$	$1.6 \cdot 10^{-3}$	$1.7 \cdot 10^{-6}$	7.8	$1 \cdot 10^{-2}$

The charge associated with the unnormalised capacitances of the EIS arcs of the EWII cell without IrO_x given in table 5.3.2.22 are calculated according to equation (34) and given in table 5.3.2.24. When comparing table 5.3.2.24 to table 5.3.1.16 it is seen that the charges for the three arcs of the EWII cell without IrO_x is in the same order of magnitude as the charges of the three arcs of the EWII benchmark cells. The findings from table 5.3.2.23 and 5.3.2.24 is equivalent to the findings in section 5.3.1 that the high frequency arc originates from a two dimensional

process such as current constrictions, the middle frequency arc originates from a three-dimensional process at the surface of the Ir metal and IrO_x particles and the low frequency arc originates from the process more three dimensional than the middle frequency arc, which could be oxidation of the iridium to very high oxidation states, which will collapse the oxide structure and increase the ECSA of the catalyst.

Table 5.3.2.24 Charges calculated from the unnormalised equivalent capacitances for the high, middle and low frequency arcs. The charges have been calculated from the DC potential, $Q(E_{DC})$, and from the AC potential, $Q(E_{AC})$.

		High Frequency Arc	**Middle Frequency Arc**	**Low Frequency Arc**
		$Q(E_{AC})$ [C]	**$Q(E_{AC})$ [C]**	**$Q(E_{AC})$ [C]**
EWII without IrOx (ATMJ)	**0.35 A cm^{-2}**	$1.67 \cdot 10^{-5}$	$9.54 \cdot 10^{-4}$	$9.08 \cdot 10^{-2}$
	0.69 A cm^{-2}	$1.56 \cdot 10^{-5}$	$5.22 \cdot 10^{-4}$	$3.58 \cdot 10^{-2}$
	1.00 A cm^{-2}	$1.47 \cdot 10^{-5}$	$3.67 \cdot 10^{-4}$	$2.19 \cdot 10^{-2}$

Fits of iV-curves Based on EIS Findings

Since the EIS findings for the EWII cell without IrO_x, ATMJ, is similar to the EIS findings for the EWII benchmark cells, the iV-curves measured on the EWII cell without IrO_x, ATMJ, have been fitted to the same iV-curve model as the EWII benchmark cells, and which is given in equation (35). The cathodic scan of the iV-curves were fitted. E_{Onset} was set to 1.4 V as for the EWII benchmark cells, R_{Ohmic} was set to the slope of the iV-curve from 0.35 to 0.98 A cm^{-2} and the Tafel parameters, a and b, were determined from Tafel plots of E_{Tafel}.

iV-curves measured at 64 °C on the EWII cell without IrO_x, ATMJ, before and after EIS measurements (blue dots) and Tafel plots of E_{Tafel} for the two iV-curves are shown in figure 5.3.2.45. The black crosses shown with the iV-curves denotes (i,E) points of the EIS measurements. It is noticed that the (i,E) points of the EIS measurements lies slightly below the iV-curves. The Tafel parameters for the low current density region were determined at 0.017 – 0.15 A cm^{-2}, whereas Tafel parameters for the high current density region were determined at 0.35 – 0.90 A cm^{-2}, which is equivalent to the Tafel parameter determination procedure for the EWII benchmark cells. The Tafel parameters are together with the total cell resistance determined from the real part of the impedance at low frequency, R_{Ohmic} and $i_{cross\ of\ Tafel\ regressions}$ given in table 5.3.2.25 for the EWII cell without IrO_x, ATMJ. The iV-curves, Tafel regressions and iV-curve fits at 56 and 70-71 °C can be found in appendix E.

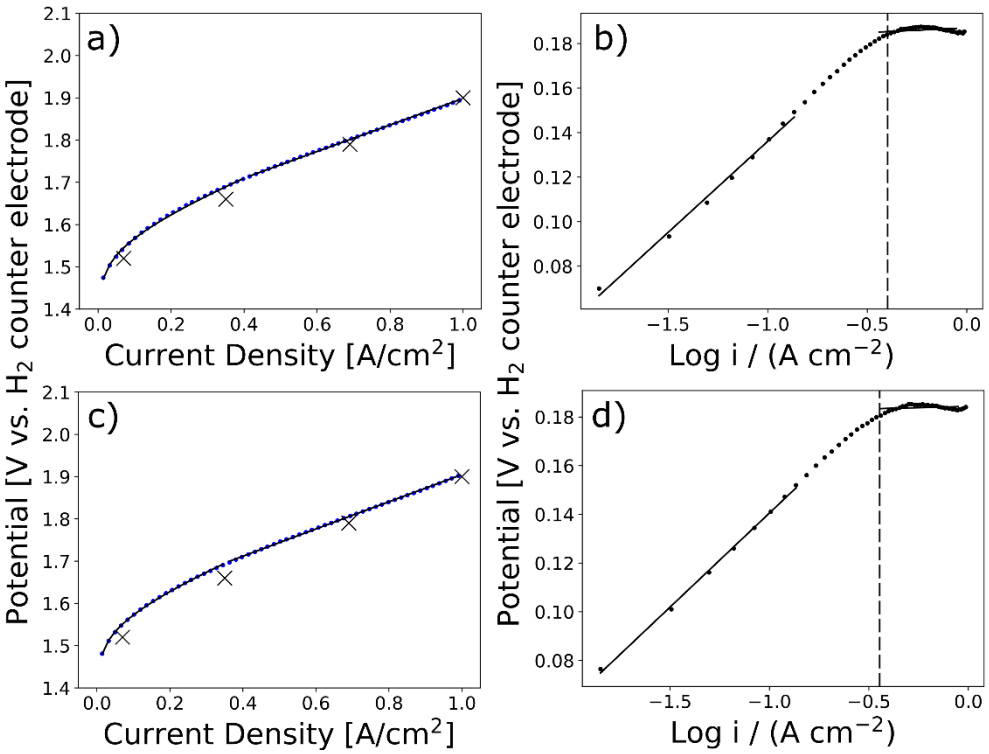

Figure 5.3.2.45 iV-curve measured at 64 °C, before EIS measurements on the EWII cell without IrO_x, ATMJ, shown with fit to the model $E(i) = E_{onset} + E_{ohmic}(i) + E_{Tafel}(i) = E_{Onset} + R_{ohmic} \cdot i + a + b \cdot log(i)$ (a). $E_{Onset} = 1.4$ and R_{ohmic} was set to the slope of the iV-curve in the linear region at current densities above 0.35 A cm^{-2}. The Tafel parameters were determined from linear regression of the Tafel plot of E_{Tafel}, shown in (b). Two regions with different Tafel parameters were distinguished, and linear regression of the Tafel plot was made at the current density range 0.0173 – 0.15 A cm^{-2} and at 0.35-0.9 A cm^{-2}. (c) shows iV-curve with fit measured at 64 °C after EIS measurements on the same EWII cell without IrO_x, ATMJ, and (d) shows Tafel plot of E_{Tafel} from the iV-curve shown in (d). Tafel parameters for the low and high current density region of the two iV-curves can be found in table 5.3.1.17. (i,E) measured during the EIS measurements are shown together with the iV-curves with fits as big black crosses.

By comparing table 5.3.2.25 with table 5.3.1.17 and 5.3.1.18 it is noticed that the Tafel slope of at current densities below 0.35 A cm^{-2} are 67-90 mV dec.$^{-1}$ for the EWII cell without IrO_x, which is slightly higher than for the EWII benchmark cells, which were 39-77 mV dec.$^{-1}$. The Tafel slope of the high current density region above 0.35 A cm^{-2} is ranging from -24 – 0 mV dec.$^{-1}$ for the EWII cell without IrO_x, meaning that it is varying around 0 mV dec.$^{-1}$ like the EWII benchmark cells, though the variations are biggest for the EWII cell without IrO_x. The similar Tafel slope of the high current density region above 0.35 A cm^{-2} of approximately 0 mV dec.$^{-1}$ for both types of EWII cells support the hypothesis that faradaic processes are not limiting above 0.35 A cm^{-2}, but only ohmic processes are limiting the performance of the PEMEC at these high current densities. The slightly higher Tafel slope of the low current density region below 0.35 A cm^{-2} (where the faradaic processes are performance limiting) for the EWII cell without IrO_x compared to the EWII benchmark cells implies that the catalytic activity of the IrO_x are smaller for the EWII cell without IrO_x compared to the EWII benchmark cells, which may be explained by the anode structure of the cells. Cf. figure 4.2.7 and ECSA from the CV measurements given in table 5.1.5.6 the ECSA is smaller for the EWII cell without IrO_x than the ECSA of the EWII benchmark cells leading to a higher Tafel slope.

Table 5.3.2.25 EWII cell without IrOx, ATMJ. The Tafel fit in the low current density region was done at 0.0173 – 0.15 A cm^{-2}, while the Tafel fit in the high current density region was done at 0.35-0.9 A cm^{-2}.

	Average $Z_{re,LF}$ from 0.35 to 1.00 A cm^{-2} [Ω cm^2]	R_{ohmic} [Ω cm^2]	a_{low} (Tafel inter-cept) [mV]	b_{low} (Tafel slope) [mV/dec.]	a_{high} (Tafel inter-cept) [mV]	b_{high} (Tafel slope) [mV/dec.]	$i_{cross\ of\ Tafel\ re-gressions}$ [A cm^{-2}]
55-56 °C start	0.494 ± 0.018	0.429	279	90	207	-24	0.229
55-56 °C end		-	-	-	-	-	-
63 °C start	0.360 ± 0.027	0.312	218	82	187	4	0.401
63 °C end		0.321	218	77	184	2	0.359
70-71 °C start	0.394 ± 0.012	0.310	184	67	148	-1	0.297
70-71 °C end		0.335	206	73	162	-10	0.298

5.3.3 PSI Cells

IV-curves

5.3.3.1.1 Linearity and Hysteresis

Hysteresis have been measured in all iV-curves of PSI benchmark cells, as e.g. seen in figure 5.3.3.46 and 5.3.3.47. Figure 5.3.3.46 depicts iV-curves measured before (a, b and c) EIS measurements and after (d, e and f) EIS measurements at 58 °C (a and d), 66 °C (b and e) and 74 °C (c and f) on the benchmark PSI cell on which the CV measurements on section 5.1.5 have been measured, PSI_s5_3. More significant hysteresis are observed in these iV-curves compared to the iV-curves measured on the EWII benchmark cell shown in figure 5.3.1.22, though the iV-curves are measured up to the same current density (1 A cm^{-2}) and the temperature variations during the measurement of each iV-curve is the same (0.5 °C), which suggests that the increased hysteresis cannot be ascribed to a temperature effect. Furthermore, one would expect an increase in temperature to lower the differential cell resistance, but the differential cell resistance is increasing and then decreasing during the increase in current density during the anodic scans, which then furthermore disprove the hysteresis to be a temperature effect. An explanation of the cause of hysteresis in the iV-curves measured of the PSI benchmark cells could be bed contacting of the catalyst material on the Nafion membrane. The contact between the IrO_x catalyst and the Nafion membrane may be better for the EWII benchmark cells, due to the Ir metal layer, which is applied on top of the IrO_x layer by the decal method and due to hotpressing of the MEAs after application of the IrO_x catalyst and Ir metal layers, which may

increase the contact between the catalyst layer and the Nafion membrane and prevent hysteresis in the iV-curves measured on the EWII benchmark cells.

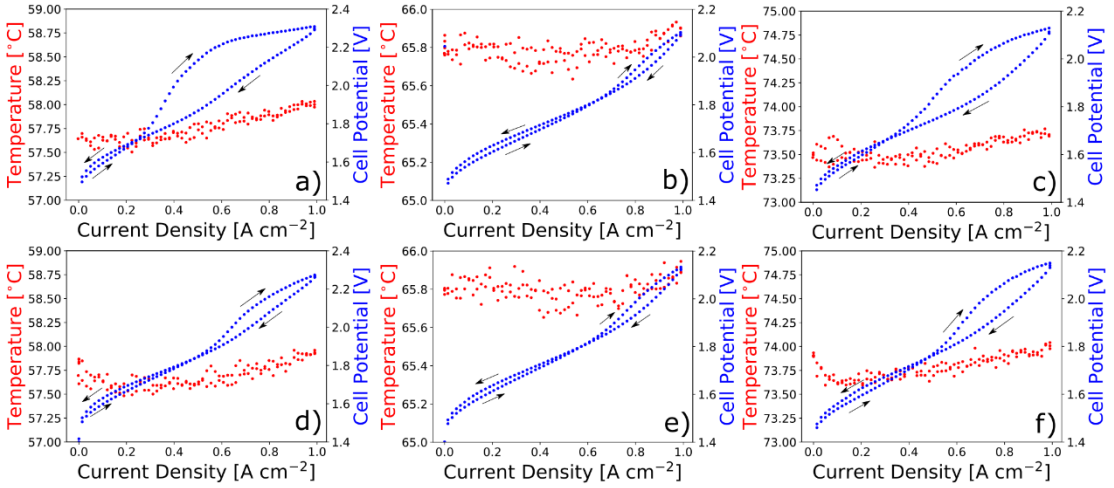

Figure 5.3.3.46 iV-curves with temperature measured on the PSI cell, PSI_s5_3, at 58 °C (a), 66 °C (b) and 74 °C(c) before EIS and at 58 °C (d), 66 °C (e) and 74 °C (f) after EIS measurements. The arrows express the current density scan direction.

Figure 5.3.3.47 shows iV-curves measured before (a, b and c) EIS measurements and after (d, e and f) EIS measurements at 57-60 °C (a and d), 66-68 °C (b and e) and 73-76 °C (c and f) on the benchmark PSI cell, PSI_s5_2. The current density range of these iV-curves are larger than the current density range for the PSI benchmark cell, PSI_s5_3, shown in figure 5.3.3.46. The hysteresis of the iV-curves measured on PSI_s5_2 in figure 5.3.3.47 is significant, especially at high current densities, and higher potentials are measured during the anodic scan than potentials measured at similar current densities during the cathodic scan. From the temperature plots it can be seen that the cell temperature is increasing at high current densities approximately from 1 A cm^{-2}.

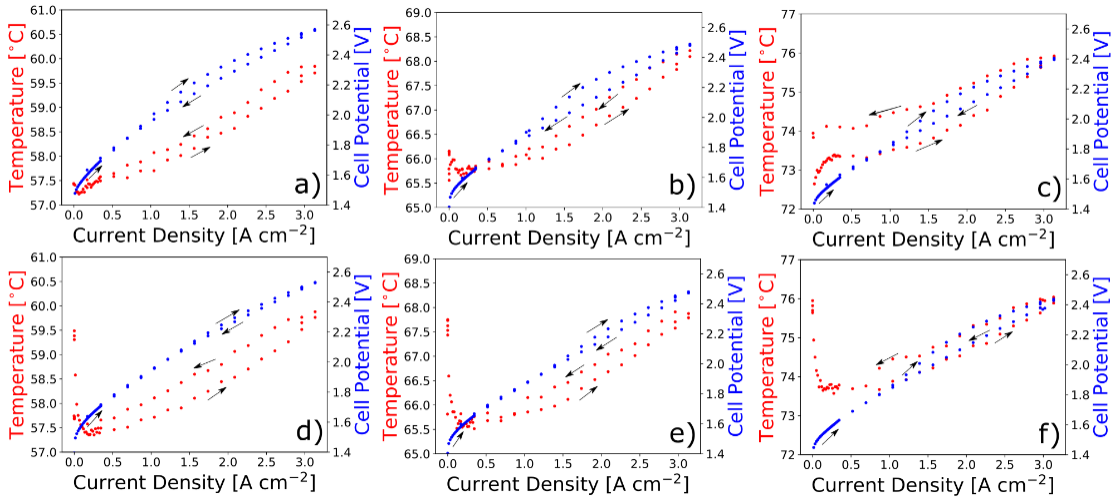

Figure 5.3.3.47 iV-curves with temperature measured on the PSI cell, PSI_s5_2, at 57-60 °C (a), 66-68 °C (b) and 73-76 °C (c) before EIS and at 57-60 °C (d), 66-68 °C (e) and 73-76 °C (f) after EIS measurements. The arrows express the current density scan direction.

Due to the significant hysteresis of the iV-curves measured on PSI cells seen in figure 5.3.3.46 and 5.3.3.47, it may easily be confusing to compare iV-curves of various PSI cells. For this reason, it has been decided to compare the cathodic scan and the anodic scan of the iV-curves measured on the PSI cells separately. These are shown together with the anodic and cathodic scan of the reference EWII benchmark cell, cell0, in figure 5.3.3.48 and 5.3.3.49. iV-curves obtained from Ugljesa Babic from PSI (green crosses), which have been measured at 50, 60 and 70 °C on PSI benchmark cells by Ugljesa Babic at PSI are also shown in figure 5.3.3.48 and 5.3.3.49 for comparison. In figure 5.3.3.48 it is seen that the anodic scans of the iV-curves for the PSI cells are non-linear, whereas the iV-curve of the EWII reference cell, is very linear at current densities above 0.35 A cm^{-2}. On the other hand, the cathodic scans of the iV-curves of the PSI cells, shown in figure 5.3.3.49 is a lot more linear than the anodic scans of the iV-curves. In figure 5.3.3.49 it can be seen that the iV-curve for the PSI benchmark cell, PSI_s5_2 (blue squares), becomes non-linear above 1.50 or 2.00 A cm^{-2}, and the iV-curve is bending down compared to the linear relation between potential and current density meaning that lower potentials are measure compared to the linear regression. The lower potential values imply that the non-linearity at these high current densities are not due to mass transport limitations, but the increase in operating temperature due to the high current densities cf. figure 5.3.3.43 can explain the non-linear behavior of the anodic scan at these very high current densities.

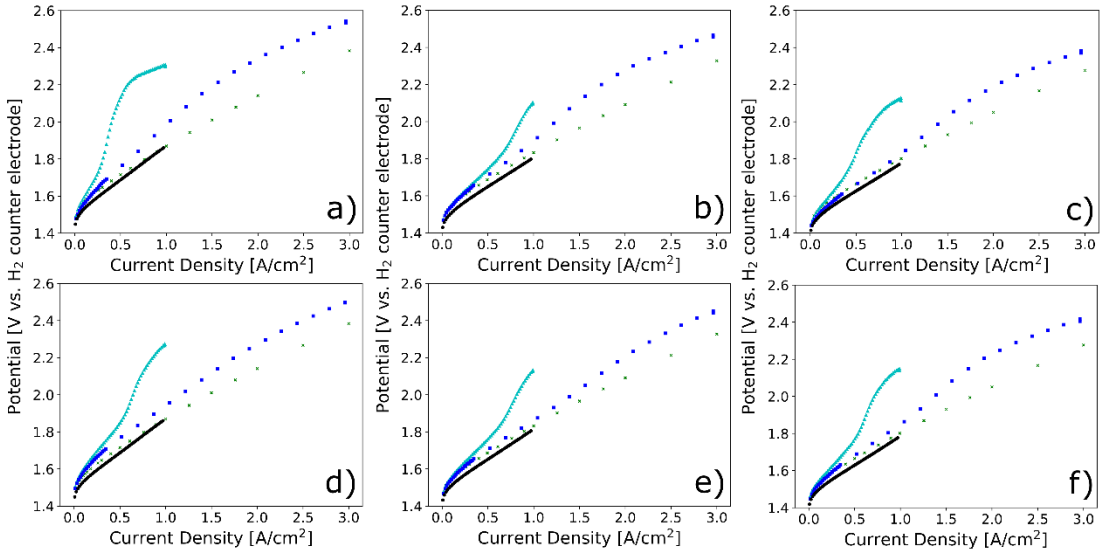

Figure 5.3.3.48 Anodic scans of iV-curves measured on two different PSI cells, PSI_s5_3 (cyan triangles), PSI_s5_2 (blue squares) and the reference EWII benchmark cell, cell 0 (black circles) shown with iV-curves obtained from Ugljesa Babic (58) measured on PSI benchmark cells at PSI (green crosses) at 50-60 °C (a), 60-68 °C (b) and 69-76 °C (c) before EIS and at 50-60 °C (d), 60-68 °C (e) and 69-76 °C (f) after EIS measurements.

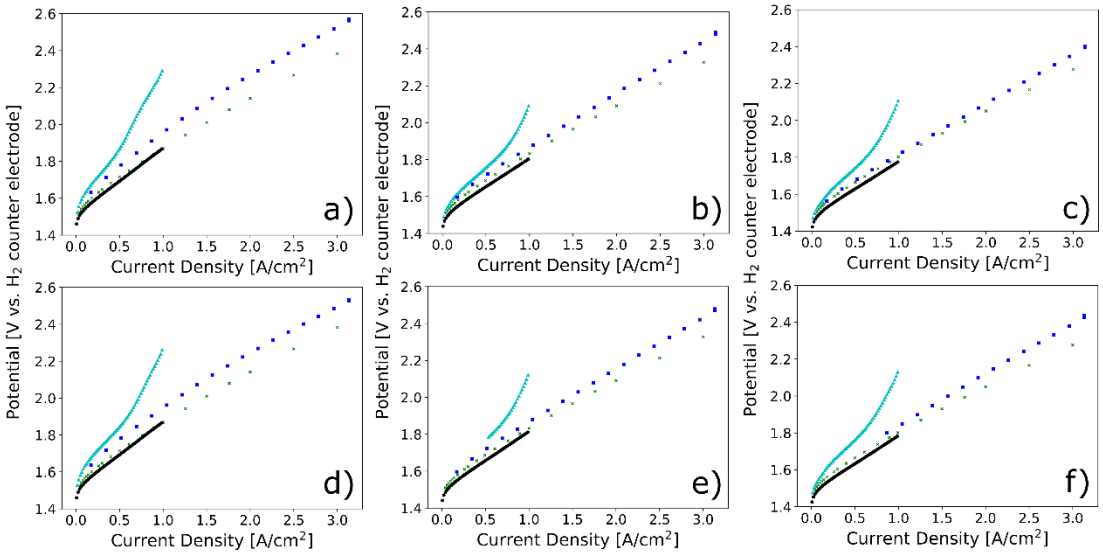

Figure 5.3.3.49 Cathodic scans of iV-curves measured on two different PSI cells, PSI_s5_3 (cyan triangles), PSI_s5_2 (blue squares) and the reference EWII benchmark cell, cell 0 (black circles) shown with iV-curves obtained from Ugljesa Babic (58) measured on PSI benchmark cells at PSI (green crosses) at 50-60 °C (a), 60-68 °C (b) and 69-76 °C (c) before EIS and at 50-60 °C (d), 60-68 °C (e) and 69-76 °C (f) after EIS measurements. It is observed that the cathodic scan is more linear than the anodic scan.

In figure 5.3.3.49 it is seen that slightly higher potentials are measured for the cathodic scan of the PSI benchmark cell, PSI_s5_2, compared to the PSI measurements obtained from Ugljesa Babic and the reference EWII cell, Cell 0, in figure 5.3.3.49 b), 5.3.3.49 c), 5.3.3.49 e) and 5.3.3.49 f), and the difference between the PSI benchmark cell, PSI_s5_2, and the reference EWII benchmark cell end the iV-curve reported by Babic Ugljesa of a PSI benchmark cell is bigger at 50-60 °C. It is furthermore noted in figure 5.3.3.49 that even the cathodic scan of the iV-curve measured on the PSI benchmark cell, PSI_5s_3 (cyan triangles), have a shape different from the iV-curves of the PSI benchmark cell, PSI_s5_2, the reference EWII benchmark cell and the iV-curve reported by Ugljesa Babic on PSI benchmark cell measured at PSI. For this reason it has been chosen to investigate the EIS and fit the iV-curves measured on the PSI benchmark cell, PSI_s5_2. However, CV results measured on the PSI benchmark cell, PSI_S5_3, is reported in section 5.1.5, since CV was only measured on this PSI cell.

The constant differential cell resistance for the PSI benchmark cell, PSI_s5_2, given by the slope of the cathodic scans of the iV-curves of PSI_s5_2 shown in figure 5.3.3.49 (blue squares) determined from linear regression in the current density range 0.35-0.98 A cm^{-2}, are listed in table 5.3.3.26. The reason for the limited current density range of the linear regression is, that a temperature effect is influencing the iV-curve above approximately 1.5 A cm^{-2}, and it has therefor been chosen to determine the slope of the iV-curve in the same current density interval as the EWII benchmark cells. It is noted in table 5.3.3.26 that the differential cell resistance is decreasing with increasing current density for the iV-curves measured before the EIS measurements, which was also observed for the EWII benchmark cells. Furthermore, it is noticed by comparison of table 5.3.3.26 with table 5.3.1.10 that the differential cell resistance above 0.35 A cm^{-2} determined from the slope of the iV-curves of the PSI benchmark cell, PSI_s5_2, is very similar to the differential cell resistance determined above 0.35 A cm^{-2} from the slope of the iV-curves of the EWII benchmark cells.

Table 5.3.3.26 Linear regressions from 0.35-0.98 A cm^{-2} of the cathodic scan of iV-curves measured on the PSI benchmark cell, PSI_s5_2.

Cell	Cell Temperature, T	Linear slope of iV-curve before EIS at the given T [Ω cm^{-2}]	Linear slope of iV-curve after EIS at the given T [Ω cm^{-2}]
PSI_s5_2	**57-60 °C**	0.411	0.351
	66-68 °C	0.328	0.305
	73-76 °C	0.305	0.321

5.3.3.1.2 Stability during EIS Measurements – Comparison of iV-curves Measured Before and After EIS.

Figure 5.3.3.50 compares iV-curves measured before (blue dots) and after (black triangles) EIS measurements at three different operating temperatures of the PSI benchmark cell, PSI_s5_2. Since the two iV-curves measured before and after EIS are fairly similar, the cell seem to have been stable during the EIS measurements at all three temperatures.

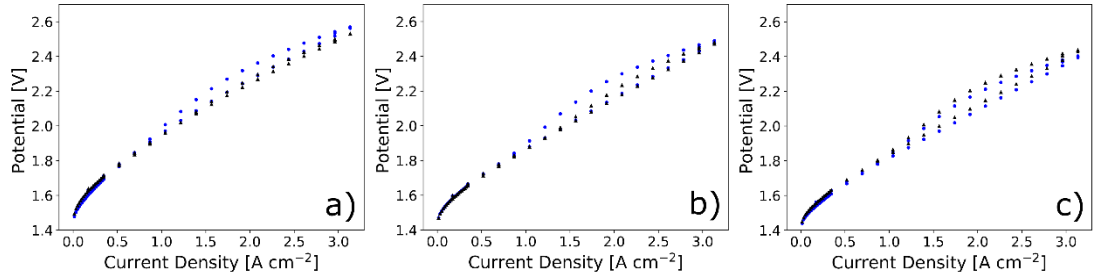

Figure 5.3.3.50 iV-curves measured before (blue dots) and after (black triangles) EIS measurements at 57-60 °C (a), 66-68 °C (b) and 73-76 °C (c) on a benchmark PSI cell, PSI_s5_2. The iV-curves measured before and after the EIS measurement at each temperature is fairly similar in each of the three plots meaning that the cell seem to be in the same state before and after the EIS measurements at each temperature.

Electrochemical Impedance Spectroscopy

5.3.3.1.3 Nyquist and Bode Plots of EIS Measured on PSI Benchmark Cells

EIS measured on the PSI benchmark cell, PSI_s5_2, during operation at 57-60 °C, 66-68 °C and 73-76 °C and at 0.07, 0.35, 0.69, 1.00, 2.00 and 3.00 A cm^{-2} are shown in Nyquist plots in figure 5.3.3.51 and in Bode plots in figure 5.3.3.52. The trend observed for the EWII benchmark cells and the EWII cell without IrO_x that the middle frequency arc is decreasing with increasing current density and the low frequency arc is increasing with increasing current density, is also observed in the EIS measured on the PSI benchmark cell, PSI_s5_2, though it is more difficult to realise due to a bigger extend of overlap between the three arcs in the EIS spectra of the PSI benchmark cell. The more pronounced overlap of the three EIS arcs in the PSI cells may be explained by the more porous composite structure of the anode in the PSI benchmark cells due to

the small size of the IrO_x particles mixed with Nafion binder cf. figure 4.2.7. Nyquist plots of EIS measured on other PSI cells can be found in appendix F, and look similar.

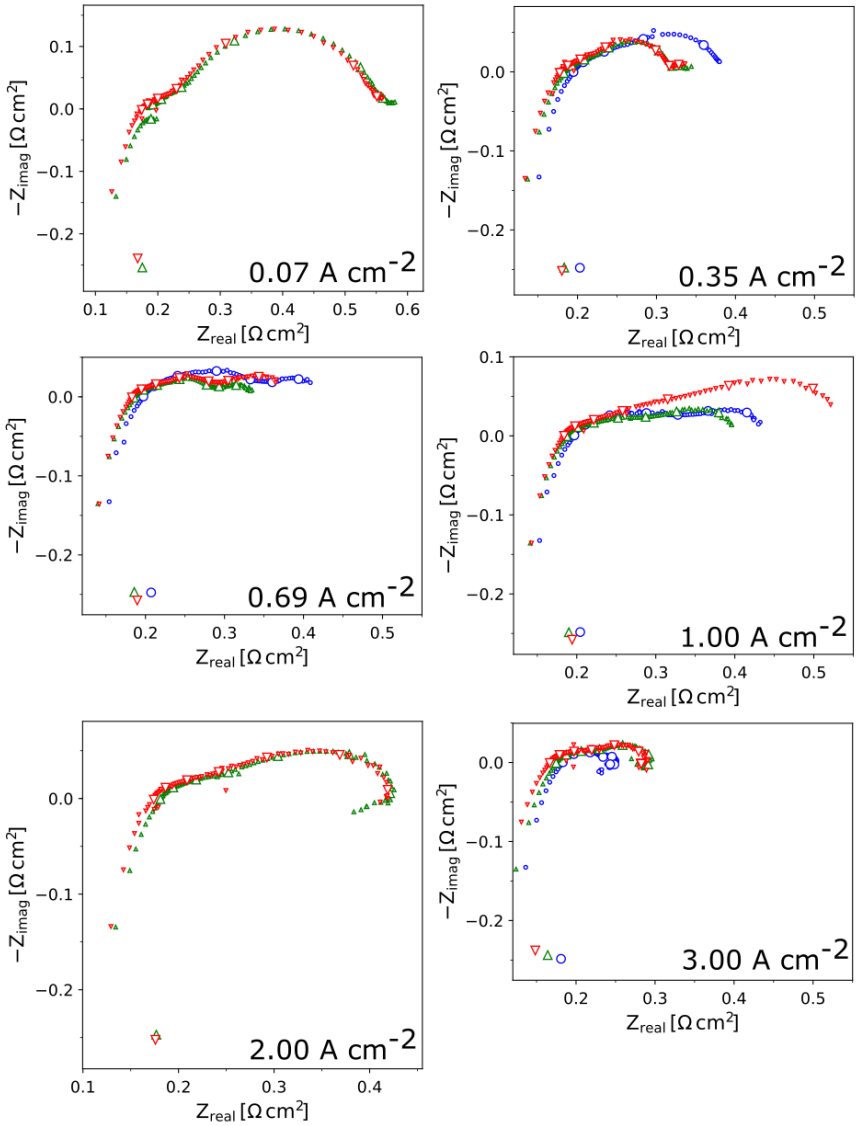

Figure 5.3.3.51 EIS measured at 57-60 °C (blue circles), 66-68 °C (green triangles) and 73-76 °C (red triangles) and at 0.07, 0.35, 0.69, 1.00, 2.00 and 3.00 A cm^{-2} on the benchmark PSI cell, PSI_s5_2.

In figure 5.3.3.51, low frequency inductance loops are observed at 2.00 and 3.00 A cm^{-2}, which may arise from adsorption and desorption processes of oxygen species on the catalyst surface (59). Due to the high overlap of the EIS arcs for the PSI benchmark cell, PSI_s5_2, it has not been possible to determine $Z_{re,HF\ min}$, $Z_{re,LF\text{-}HF\ min}$ and $Z_{re,HF\ min\text{-}Rs(Malis)}$, but $Z_{re,LF}$ have been determined for all the EIS spectra and are listed in table C.39 and C.41 in appendix C, and average values for $Z_{re,LF}$ in the linear region of the cathodic scan of the iV-curves with no temperature effect at current densities from 0.35 A cm^{-2} to 1.00 A cm^{-2} are listed in table 5.3.3.27.

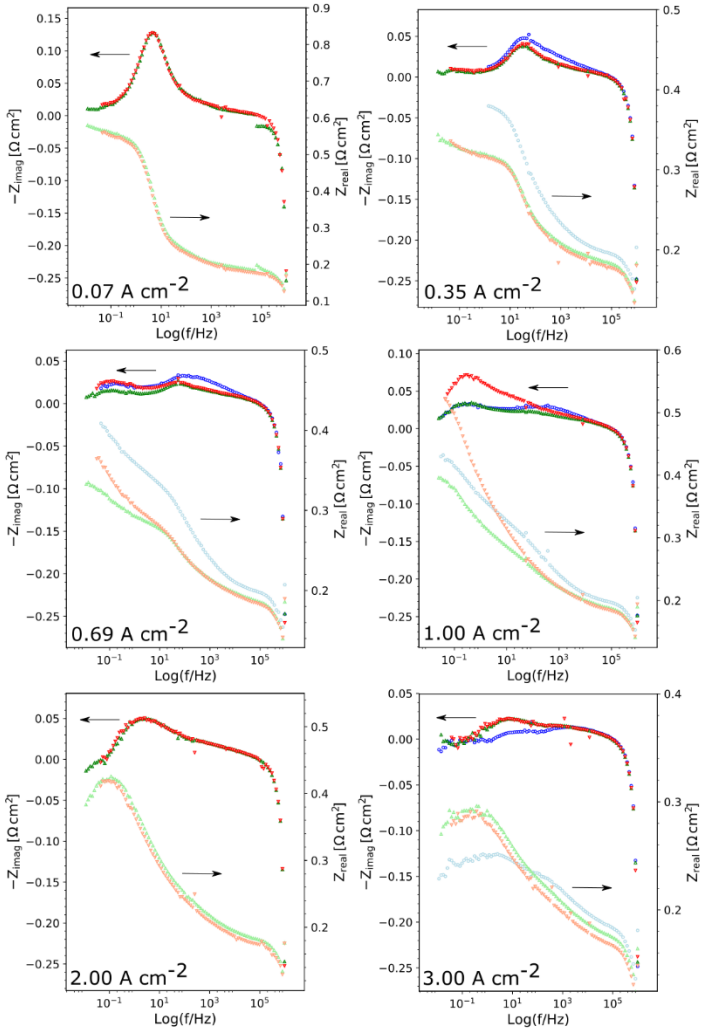

Figure 5.3.3.52 EIS shown in Bode plots measured at 57-60 °C (blue / light blue circles), 66-68 °C (green / light green triangles) and 73-76 °C (red/ light red triangles) and at 0.07, 0.35, 0.69, 1.00, 2.00 and 3.00 A cm^{-2} on the PSI benchmark cell, PSI_s5_2. The imaginary part of the impedance are shown with dark colours and y-axis to the left, while real part of the impedance is shown with light colours and y-axis to the right.

Table 5.3.3.27 EIS Overview Table showing averages of the total cell resistance, $Z_{re,LF}$, from 0.35 A cm^{-2} to 1.00 A cm^{-2} (the linear part of the iV-curves), averages of $Z_{re,HF}$ min up to 1.00 A cm^{-2}, averages of the resistance of the middle and low frequency arcs, $Z_{re,\ LF\ -\ HF\ min}$ from 0.35 A cm^{-2} to 1.00 A cm^{-2} and averages of $Z_{re,HF\ min\ -\ Rs(Malis)}$ up to 1.00 A cm^{-2}.

Cell	Cell Temperature, T	Average $Z_{re,LF}$ from 0.35 to 1.00 A cm^{-2}	Average $Z_{re,HF\ min.}$ up to 1.00 A cm^{-2}	Average $Z_{re,\ LF\ -\ HF\ min}$ from 0.35 to 1.00 A cm^{-2}	Average $Z_{re,HF\ min\ -\ Rs(Malis)}$ up to 1 A cm^{-2}
PSI_s5_2	**57-60 °C**	0.406 ± 0.026 Ω cm^2	-	-	-
	66-68 °C	0.357 ± 0.034 Ω cm^2	-	-	-
	73-76 °C	0.406 ± 0.100 Ω cm^2	-	-	-

In table 5.3.3.28 the differential cell resistance determined from the EIS measurements, $Z_{re,LF}$, are compared to the differential cell resistance determined from the slope of the cathodic scan of the iV-curves between 0.35 and 1.00 A cm^{-2} of the PSI benchmark cell, PSI_s5_2. A very high deviation is observed for $Z_{re,LF}$ at 73-76 °C, which means that the differential cell resistances of the PSI benchmark cell, PSI_s5_2, determined from the EIS measurements are similar to the differential cell resistances determined from the cathodic scan of the iV-curves measured before the EIS measurements.

Table 5.3.3.28 Total differential cell resistance given by the slope of linear regressions from 0.35-0.98 A cm^{-2} of iV-curves measured before and after EIS measurements on EWII benchmark cells shown in figure 5.3.1.21. The total cell resistances are compared to average total cell resistances above 0.35 A cm^{-2} determined by DC impedance, $Z_{re,LF}$, at the same EWII benchmark cells.

	Cell Temperature, T	**Linear slope of iV-curve before EIS at the given T [Ω cm^{-2}]**	**Linear slope of iV-curve after EIS at the given T [Ω cm^{-2}]**	**Average $Z_{re,LF}$ from 0.35 to 1.00 A cm^{-2}**
PSI_s5_2	**57-60 °C**	0.411	0.351	0.406 ± 0.026 Ω cm^2
	66-68 °C	0.328	0.305	0.357 ± 0.034 Ω cm^2
	73-76 °C	0.305	0.321	0.406 ± 0.100 Ω cm^2

The dependence of operating temperature on the differential cell resistances, $Z_{re,LF}$, of the PSI benchmark cell, PSI_s5_2, is shown in figure 5.3.3.53, in which it is also compared to the temperature dependence of the Nafion membrane reported by Malis et al. (47). The linear regression of $Z_{re,LF}$ as function of operating temperature indicate that the differential cell resistance decrease with 0.1 Ω cm^2 per degree increase in operating temperature, which is one order of magnitude smaller than reported by Malis et al. (47) and observed for the EWII benchmark cells and the EWII cell without IrO_x. However, due to the big deviation of the average $Z_{re,LF}$ at 73-76 °C, a slope in the same order of magnitude as the EWII benchmark cells and the EWII cell without IrO_x is within the uncertainty. This does not reject that Nafion in the electrolyte and the electrodes cause all the resistance of the PEMEC during OER, as was concluded for the EWII benchmark cells and the EWII cell without IrO_x layer.

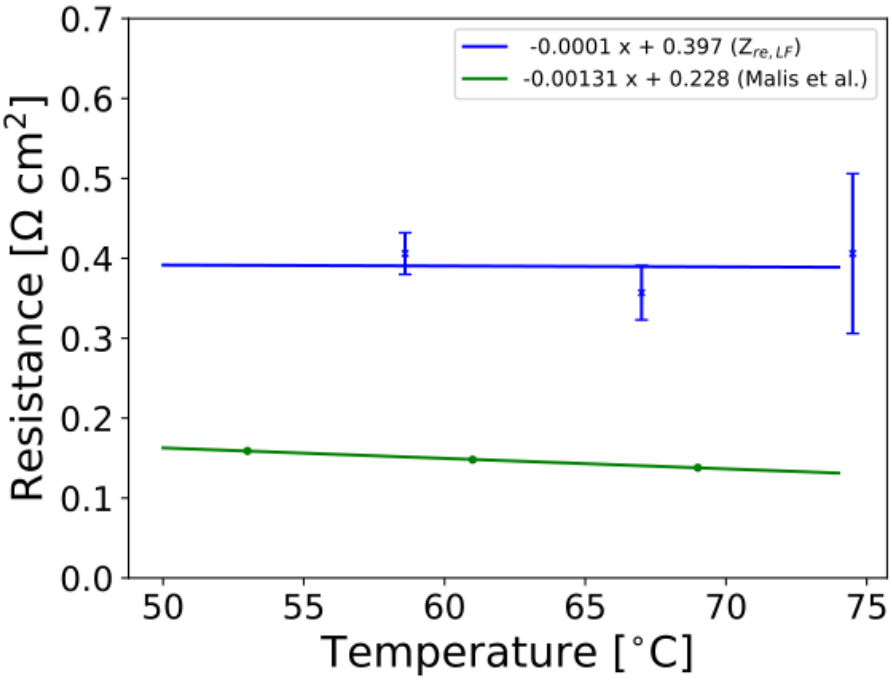

Figure 5.3.3.53 $Z_{re,LF}$ (blue crosses) shown as function of operating temperature for the PSI benchmark cell, PSI_s5_2, compared to in-plane resistance measurements of operated Nafion 117 membranes reported by Malis et al. (47) (green circles).

5.3.3.1.4 EIS Model

The EIS spectra measured on the PSI benchmark cell, PSI_s5_2, is measured up to 1 MHz, and EIS measured at 66-68 °C in the linear part of the iV-curve without temperature effects at 0.35 to 1.00 A cm^{-2} is therefore fitted to the equivalent circuit R-L-RQ-RQ-RQ similar to the EWII benchmark cell, ALIP, and the EWII cell without IrO_x, ATMJ. These fits are shown in figure 5.3.3.54 together with Kramers-Kronig plots of the fitted EIS spectra. In figure 5.3.3.55 the EIS fits from figure 5.3.3.54 are shown with each of the three arcs and the inductance from the equivalent circuit.

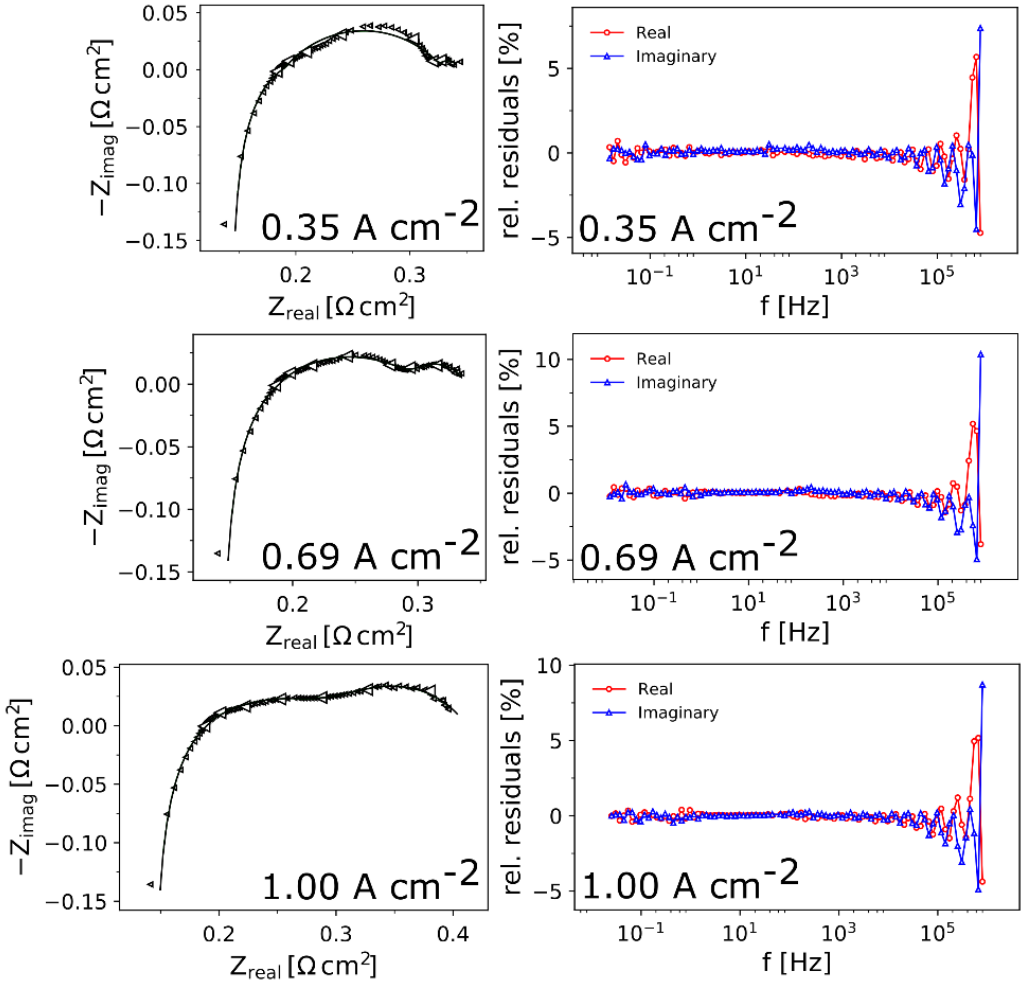

Figure 5.3.3.54 Nyquist plots and Kramers-Kronig compliance tests of EIS measured at 66 °C and at 0.07, 0.35, 0.69 and 1.00 A cm^{-2} on a PSI benchmark cell, PSI_s5_2. Fits of the measured EIS to the equivalent circuit R-L-RQ-RQ-RQ is also shown in the plots. The serial resistance was kept constant at the literature value reported by Malis et al. (47) during fitting (0.142 Ω cm^2 at 66 °C). EIS measured at 50-60 Hz and above 800 kHz was excluded from the fits.

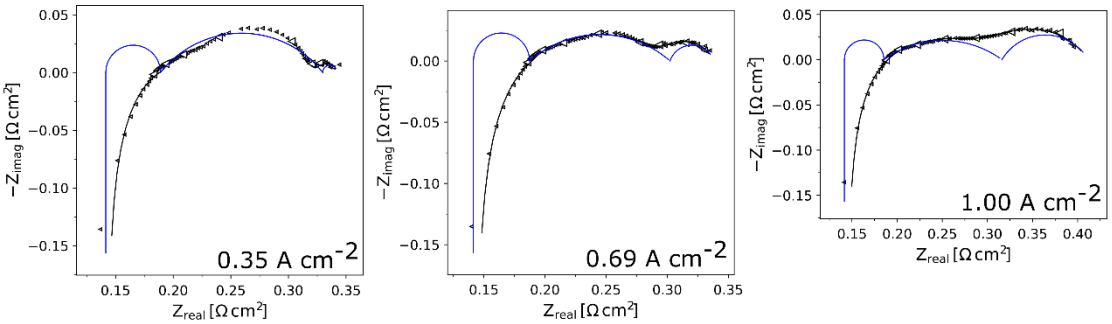

Figure 5.3.3.55 Nyquist plots of EIS measured at 66 °C and at 0.07, 0.35, 0.69 and 1.00 A cm^{-2} on an PSI benchmark cell, PSI_s5_2. Fits of the measured EIS to the equivalent circuit R-L-RQ-RQ-RQ is also shown in the plots. The serial resistance was kept constant at the literature value reported by Malis et al. (47) during fitting (0.142 Ω cm^2

at 66 °C). The three arcs of the equivalent circuit (blue) is shown together with the data points and the total fit (black). EIS measured at 50-60 Hz and above 800 kHz was excluded from the fits.

5.3.3.1.5 EIS Model Explained with Physical Processes

Fit parameters determined from the fits in figure 5.3.3.54 measured on the PSI benchmark cell, PSI_s5_2, at 66-68 °C and 0.35, 0.69 and 1.00 A cm^{-2} are given in table 5.3.3.29. By comparing table 5.3.3.29 with table 5.3.2.22, 5.3.1.13 and 5.3.1.14 it is observed that the equivalent capacitance of the high frequency arc of EIS measured on the PSI benchmark cell, PSI_s5_2, is one magnitude larger than the equivalent capacitances of the high frequency arcs determined for the EWII benchmark cells and the EWII cell without IrO_x. The equivalent capacitances of the middle frequency arc of EIS measured on the PSI benchmark cell, PSI_s5_2, is in the same order of magnitude as the EWII benchmark cells, but one order of magnitude bigger than measured on the EWII cell without IrO_x. The equivalent capacitance of the low frequency arc of the EIS spectra is approximately twice as large for the PSI benchmark cell, PSI_s5_2, than the EWII benchmark cells and the EWII cell without IrO_x.

Table 5.3.3.29 Fit parameters for the fits of EIS measured on the PSI benchmark cell, PSI_s5_2, at 66 °C and 0.35, 0.69 and 1.00 A cm^{-2}. Q and the equivalent capacitance, Ceff, are calculated based on equation (27) and (28), and listed in the table for each of the three arcs in the measured EIS spectra.

	High Frequency Arc			**Middle Frequency Arc**			**Low Frequency Arc**		
	R [Ω cm^2]	**n**	**C_{eff} [µF]**	**R [Ω cm^2]**	**n**	**C_{eff} [mF]**	**R [Ω cm^2]**	**n**	**C_{eff} [F]**
0.35 A cm^{-2}	0.05	1	28.6	0.14	0.57	63	0.01	1.00	1114
0.69 A cm^{-2}	0.05	1	26.9	0.11	0.46	41	0.04	0.80	148
1.00 A cm^{-2}	0.04	1	27.6	0.13	0.40	34	0.10	0.66	18

In table 5.3.3.30 the equivalent capacitances in table 5.3.3.29 have been normalised to the geometrical electrode area of 2.89 cm^2 and by the ECSA given in table 5.1.5.6 determined from CVs shown in figure 5.1.5.19. Both the area specific equivalent capacitances of the high and low frequency arcs and the area specific equivalent capacitance of the middle frequency arc normalised by the geometrical area were on the same order of magnitude as observed for the EWII benchmark cells. The area specific equivalent capacitance of the middle frequency arcs normalised by ECSA were one order of magnitude smaller than observed for the EWII benchmark cells and in the same order of magnitude as the EWII cell without IrO_x layer.

The charge associated with the unnormalised capacitances of the EIS arcs of the PSI benchmark cell, PSI_s5_2, are calculated according to equation (34) and given in table 5.3.3.30. By comparing table 5.3.3.30 to table 5.3.1.16 it is noted that the charges associated with the three arcs in the EIS spectra of the PSI benchmark cell, PSI_s5_2, is in the same order of magnitudes as the charges of the three EIS arcs of the EWII benchmark cells. This in combination

with the findings from table 5.3.3.30 implies that the high frequency arc originates from a two dimensional process such as current constrictions, the middle frequency arc originates from a three-dimensional process at the surface of the Ir metal and IrO_x particles and the low frequency arc originates from the process more three dimensional than the middle frequency arc, which could be oxidation of the iridium to very high oxidation states, just as described for the EWII benchmark cells.

Table 5.3.3.30 Equivalent capacitances for the high, middle and low frequency arcs normalised by the geometrical electrode area, which is 2.89 cm^2, C_{eff} ($A_{geo.}$), and normalized by ECSA derived from CV measured after initiation given in table 5.1.5.6, C_{eff}(A_{ECSA}).

		High Frequency Arc		**Middle Frequency Arc**		**Low Frequency Arc**	
		C_{eff} [F cm^{-2}] ($A_{geometrisk}$)	**C_{eff} [F cm^{-2}] ($ECSA_{CV\ after\ init}$)**	**C_{eff} [F cm^{-2}] ($A_{geometrisk}$)**	**C_{eff} [F cm^{-2}] ($ECSA_{CV\ after\ init}$)**	**C_{eff} [F cm^{-2}] ($A_{geometrisk}$)**	**C_{eff} [F cm^{-2}] ($ECSA_{CV\ after\ init}$)**
PSI benchmark, PSI_s5_2	**0.35 A cm^{-2}**	$9.9 \cdot 10^{-6}$	$3.5 \cdot 10^{-9}$	$2.19 \cdot 10^{-2}$	$7.7 \cdot 10^{-6}$	385.4	$1.4 \cdot 10^{-1}$
	0.69 A cm^{-2}	$9.3 \cdot 10^{-6}$	$3.3 \cdot 10^{-9}$	$1.41 \cdot 10^{-2}$	$5.0 \cdot 10^{-6}$	51.1	$2 \cdot 10^{-2}$
	1.00 A cm^{-2}	$9.6 \cdot 10^{-6}$	$3.4 \cdot 10^{-9}$	$1.17 \cdot 10^{-2}$	$4.1 \cdot 10^{-6}$	6.2	0.00

Table 5.3.3.31 Overview of charges calculated from the unnormalised equivalent capacitances for the high, middle and low frequency arcs. The charges have been calculated from the DC potential, $Q(E_{DC})$, and from the AC potential, $Q(E_{AC})$.

		High Frequency Arc	**Middle Frequency Arc**	**Low Frequency Arc**
		$Q(E_{AC})$ [C]	**$Q(E_{AC})$ [C]**	**$Q(E_{AC})$ [C]**
PSI benchmark, PSI_s5_2	**0.35 A cm^{-2}**	$2.01 \cdot 10^{-5}$	$1.63 \cdot 10^{-3}$	$1.56 \cdot 10^{-1}$
	0.69 A cm^{-2}	$1.91 \cdot 10^{-5}$	$1.18 \cdot 10^{-3}$	$6.66 \cdot 10^{-2}$
	1.00 A cm^{-2}	$1.90 \cdot 10^{-5}$	$1.15 \cdot 10^{-3}$	$2.85 \cdot 10^{-2}$

Fits of iV-curves Based on EIS Findings

Since the cathodic scan of the iV-curves measured on the PSI benchmark cell, PSI_s5_2, is too few for fitting, the iV-curve fit have been done on both the anodic and cathodic scan up to 1 A cm^{-2} before temperature and activation processes changes the slope of the iV-curves. The iV-curves were fitted to the same iV-curve model as the EWII benchmark cells, and which is given in equation (35). E_{Onset} was set to 1.4 V as for the EWII benchmark cells, R_{Ohmic} was set to the slope of the iV-curve from 0.35 to 0.98 A cm^{-2} and the Tafel parameters, a and b, were determined from Tafel plots of E_{Tafel}.

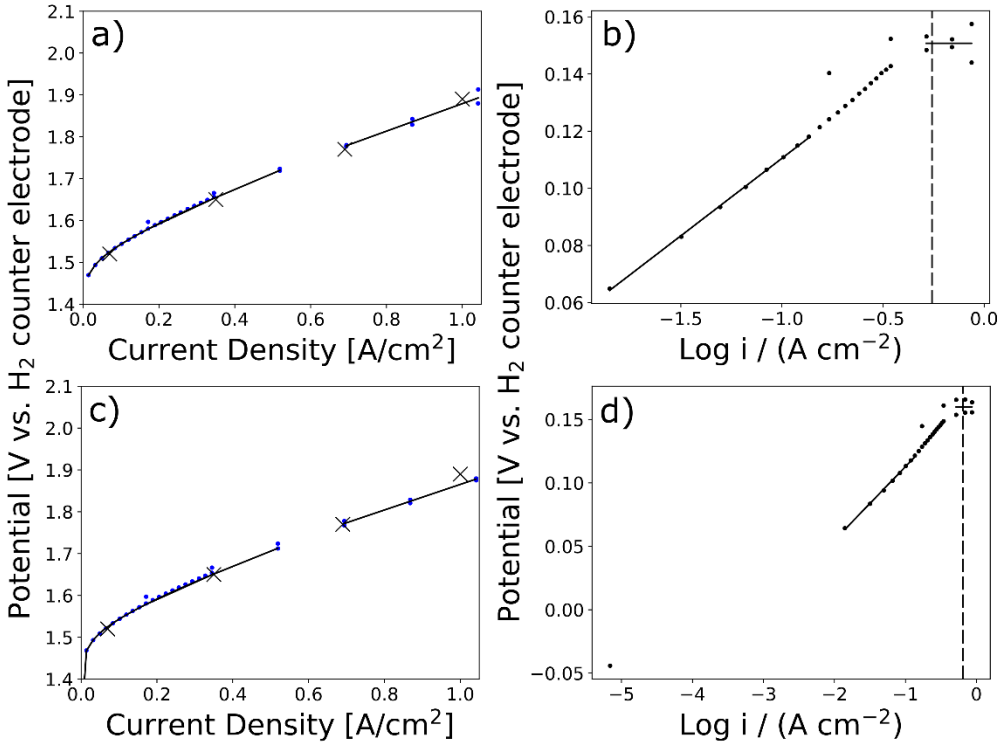

Figure 5.3.3.56 iV-curve measured at 66-68 °C, before EIS measurements on the PSI benchmark cell, PSI_s5_2, shown with fit to the model $E(i) = E_{onset} + E_{ohmic}(i) + E_{Tafel}(i) = E_{Onset} + R_{ohmic} \cdot i + a + b \cdot log(i)$ *(a).* $E_{Onset} = 1.4$ *and* R_{ohmic} *was set to the slope of the iV-curve in the linear region at current densities above 0.35 A cm^{-2}. The Tafel parameters were determined from linear regression of the Tafel plot of* E_{Tafel}*, shown in (b). Two regions with different Tafel parameters were distinguished, and linear regression of the Tafel plot was made at the current density range 0.0173 – 0.15 A cm^{-2} and at 0.35-0.9 A cm^{-2}. (c) shows iV-curve with fit measured at 66-68 °C after EIS measurements on the same PSI benchmark cell, PSI_s5_2, and (d) shows Tafel plot of* E_{Tafel} *from the iV-curve shown in (d). Tafel parameters for the low and high current density region of the two iV-curves can be found in table 5.3.1.17. (i,E) measured during the EIS measurements are shown together with the iV-curves with fits as big black crosses.*

Figure 5.3.3.56 depicts iV-curves measured at 66-68 °C on the PSI benchmark cell, PSI_s5_2, before and after EIS measurements (blue dots) and Tafel plots of E_{Tafel} for the two iV-curves. The black crosses shown with the iV-curves denotes (i,E) points of the EIS measurements. It is noticed that the (i,E) points of the EIS measurements in most cases lies on the iV-curves. The Tafel parameters for the low current density region were determined at 0.017 – 0.15 A cm^{-2}, whereas Tafel parameters for the high current density region were determined at 0.35 – 0.90 A cm^{-2}, which is equivalent to the Tafel parameter determination procedure for the EWII benchmark cells. The iV-curves, Tafel regressions and iV-curve fits at 60-70 °C and 73-76 °C can be found in appendix E. In table 5.3.3.32 is Tafel parameters given together with the total cell resistance determined from the real part of the impedance at low frequency, R_{Ohmic} and $i_{cross\ of\ Tafel\ regressions}$ for the PSI benchmark cell, PSI_s5_2.

Table 5.3.3.32 PSI benchmark cell, PSI_s5_2. The Tafel fit in the low current density region was done at 0.0173 – 0.15 A cm^{-2}, while the Tafel fit in the high current density region was done at 0.35-0.9 A cm^{-2}.

	Average $Z_{re,LF}$ from 0.35 to 1.00 A cm^{-2} [Ω cm^2]	R_{ohmic} [Ω cm^2]	a_{low} (Tafel inter-cept) [mV]	b_{low} (Tafel slope) [mV/dec.]	a_{high} (Tafel inter-cept) [mV]	b_{high} (Tafel slope) [mV/dec.]	$i_{cross\ of\ Tafel\ re-gressions}$ [A cm^{-2}]
55-56 °C start	0.406 ± 0.026 Ω cm^2	0.411	170	53	160	0	0.633
55-56 °C end		0.351	215	69	196	0	0.525
63 °C start	0.357 ± 0.034 Ω cm^2	0.328	165	54	151	0	0.552
63 °C end		0.305	171	58	160	0	0.649
70-71 °C start	0.406 ± 0.100 Ω cm^2	0.305	121	47	117	0	0.794
70-71 °C end		0.321	140	52	123	0	0.469

The Tafel slope at current densities above 0.35 A cm^{-2} for the PSI benchmark cell, PSI_s5_2, is 0 mV $dec.^{-1}$ at all operating temperatures, which is similar to what was observed for the EWII benchmark cells and the EWII cell without IrO_x cf. table 5.3.1.17, 5.3.1.18 and 5.3.2.25, which support that no faradaic processes are limiting the performance of the PEMEC at current densities above 0.35 A cm^{-2}. The Tafel slope at current densities below 0.35 A cm^{-2} were 47-69 mV $dec.^{-1}$ for the PSI benchmark cell, PSI_s5_2, which is similar to what was observed for the EWII benchmark cells (39-77 mV $dec.^{-1}$) and which is smaller than what was observed for the EWII cell without IrO_x (67-90 mV $dec.^{-1}$).

5.3.4 EWII Benchmark Cells with Pt Coated Ti Felt as Current Collector

IV-curves

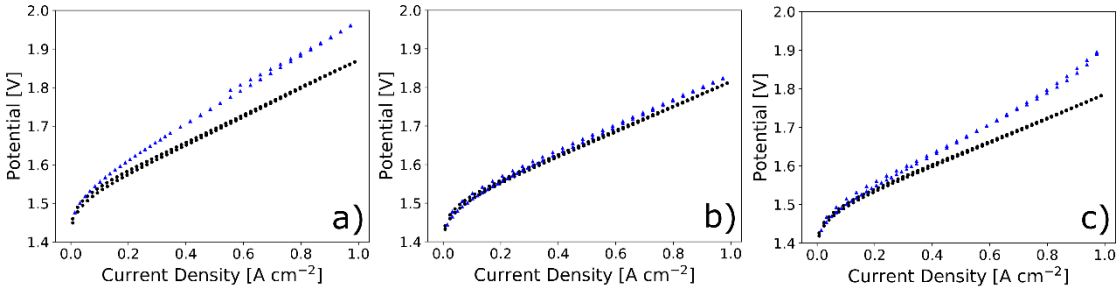

Figure 5.3.4.57 iV-curves measured after EIS measurements at 54-55 °C (a), 62 °C (b) and 69 °C (c) on an EWII benchmark cell with Pt coated Ti felt as current collector (blue triangles) and compared with similar measurements on the reference EWII benchmark cell, Cell 0.

iV-curves measured after EIS at 54-55 °C, 62 °C and 69 °C of the EWII benchmark cell with platinized titanium current collector is shown in figure 5.3.4.57 together with iV-curves measured

at 53 °C, 61 °C and 69 °C on the reference EWII benchmark cell, cell 0. Almost similar iV-curves are observed at 61-62 °C, whereas the iV-curve of the EWII benchmark cell with platinized Ti felt measured at 69 °C has a larger slope at current densities above approximately 0.3 A cm^{-2} compared to the reference EWII benchmark cell and at 53-55 °C is the slope larger for the EWII benchmark cell with platinized Ti felt than the reference EWII cell. These results imply that platinizing the Ti felt does not improve the cell performance. It was considered, if the EWII benchmark cell with platinized Ti felt was degrading during the experiments, since the results at 62 °C was obtained before the results at 69 °C, which again were obtained before the results at 54-55 °C, but according to figure 5.3.4.58, which compares iV-curves measured before and after EIS measurements at each of the three operating temperatures (54-55, 62 and 69 °C), the cell does not seem to degrade significantly during the EIS measurements.

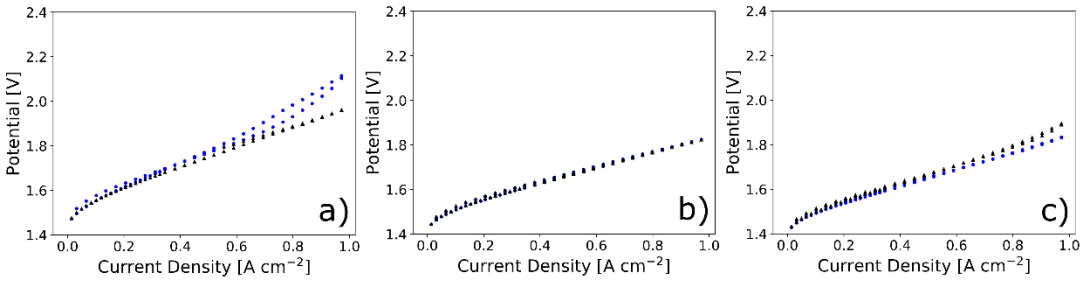

Figure 5.3.4.58 iV-curves measured before (blue dots) and after (black triangles) EIS measurements at 57-60 °C (a), 66-68 °C (b) and 73-76 °C (c) on a benchmark PSI cell, PSI_s5_2. The iV-curves measured before and after the EIS measurement at each temperature is fairly similar in each of the three plots meaning that the cell seem to be in the same state before and after the EIS measurements at each temperature.

Electrochemical Impedance Spectroscopy

EIS measured at various current densities (0.07, 0.35, 0.69 and 1.00 A cm^{-2}) and temperatures (54-55, 62 and 69 °C) on the EWII benchmark cell with platinised Ti felt is shown in Nyquist plots in figure 5.3.4.59 and in Bode plots in figure 5.3.4.60. Low frequency inductive loops are observed at 1.00 A cm^{-2} and 54-55 °C and 69 °C. This correspond to the iV-curves given in figure 5.3.4.57 and 5.3.4.58, in which some of the iV-curves measured at 54-55 and 69 °C is bending upwards (the differential cell resistance is increasing) at 1.00 A cm^{-2}. The arcs observed in the EIS spectra in figure 5.3.4.59 just as for the other PEMECs. Furthermore, is the same trend of the EIS arcs with increasing current density observed as what was observed for all the other PEMECs in this thesis; the high frequency arc is constant with increasing current density, the middle frequency arcs is decreasing with increasing current density, and the low frequency arc is increasing with increasing current density. These EIS results implies that the performance limiting processes of the PEMECs are not prevented by platinising the Ti felt. It should be noted that the platinum probably does not cover the full surface of the Ti felt, but areas without platinum coating may be observed. However if the platinum has an effect on the resistance of the cell, it should still be possible to observe, since most of the surface of the Ti felt is platinised.

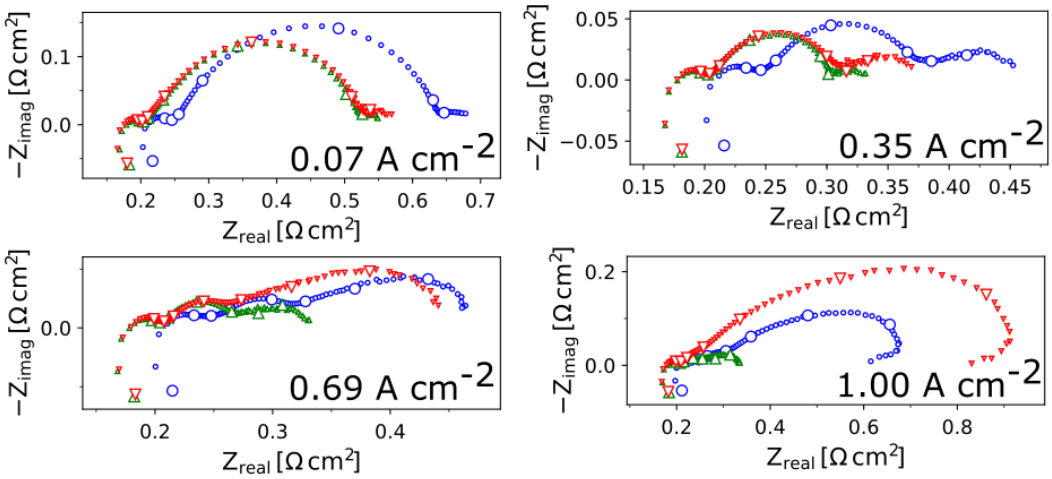

Figure 5.3.4.59 EIS measured at 54-55 °C (blue circles), 62 °C (green triangles) and 69 °C (red triangles) and at 0.07, 0.35, 0.69 and 1.00 A cm^{-2} on an EWII benchmark cell with Pt coated TI felt as anode current collector. (New Pt coated cell)

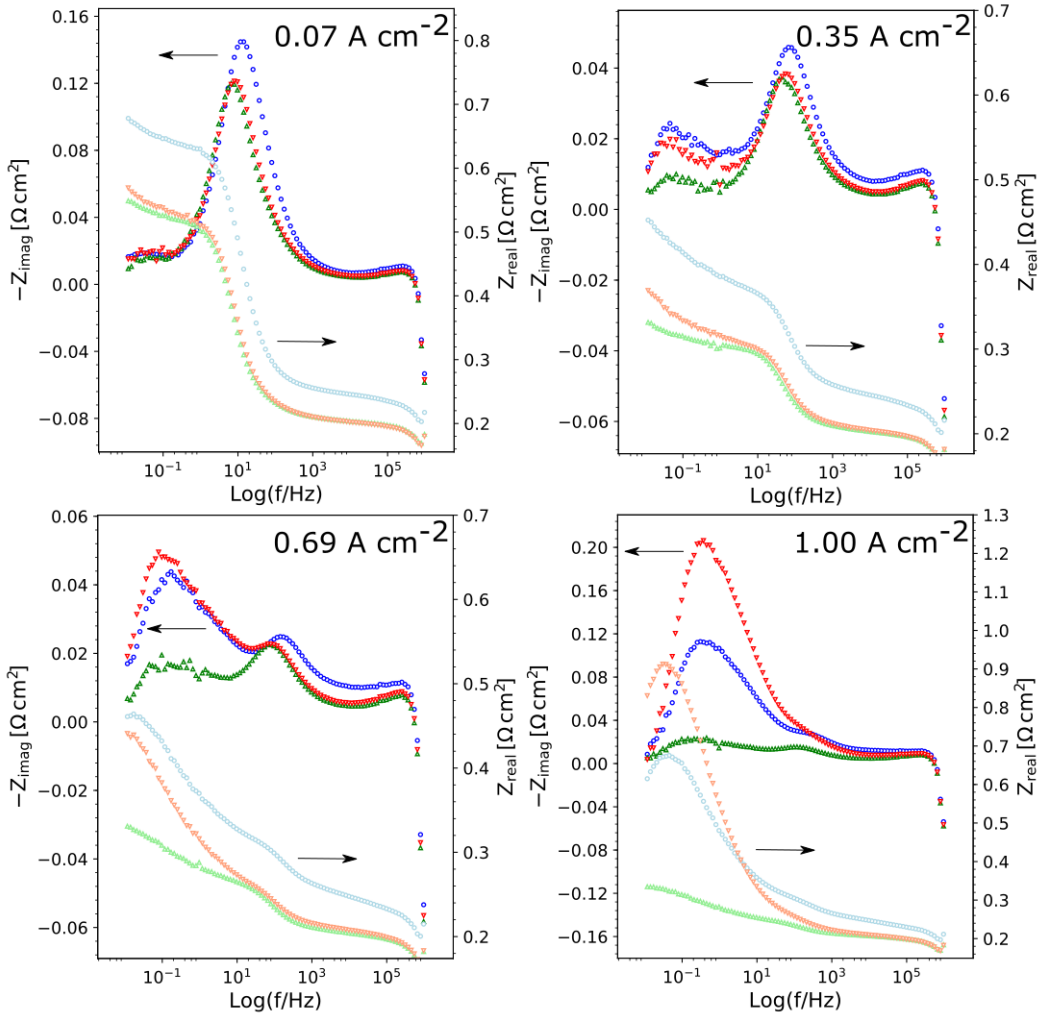

Figure 5.3.4.60 EIS shown in Bode plots measured at 54-55 °C (blue / light blue circles), 62 °C (green / light green triangles) and 69 °C (red/ light red triangles) and at 0.07, 0.35, 0.69 and 1.00 A cm^{-2} on the EWII benchmark cell with Pt coated TI felt as anode current collector (New Pt coated cell). The imaginary part of the impedance are shown with dark colours and y-axis to the left, while real part of the impedance is shown with light colours and y-axis to the right.

The surface of the Ti felt is oxidized to TiO_2 upon exposure to air, and TiO_2 is non-conducting. The current collector in a PEMEC have to be electronic conducting, so one would expect un-coated Ti felt not to be able to function as current collector and therefore many researchers coat the anodic Ti current collector with gold or platinum. However, these results show that it is not necessary to coat the Ti felt, which is being conducting in the EWII test setup. Filippo Fenini (60) have shown that the TiO_2 layer is very thin (2-5 nm) and it therefore may be broken through upon assembling the PEMEC, which is done by applying a uniaxial pressure of 60 kg. This maybe the reason why platinizing the Ti felt does not seem to improve the PEMEC performance or change the nature of the EIS measured on the PEMECs.

5.4 EIS Noise Phenomena

As described in article 2, EIS spectra of operating PEMECs sometimes contain noise (21) (17) (26) and sometimes do not contain noise (29) (22) (28). Figure 5.4.61 shows EIS spectra measured on six different PEMECs with various amounts of noise. This phenomenon is investigated in article 2 and a hypothesis has been suggested.

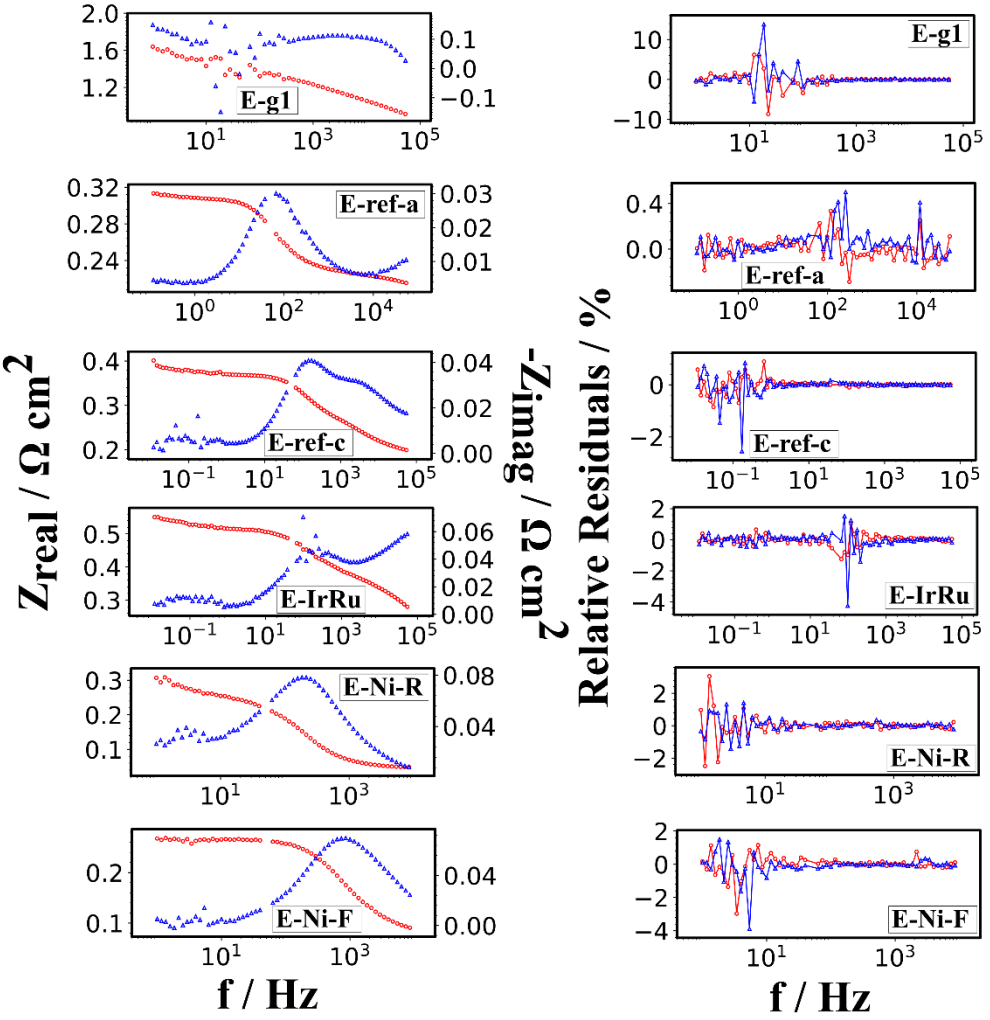

Figure 5.4.61 EIS measured on six different PEMEC types; (E-g1) early generation acidic PEMEC from EWII at 0.35 A cm^{-2}, (E-ref-a) EWII benchmark PEMEC at 0.35 A cm^{-2}, (E-ref-c) another EWII benchmark PEMEC at 0.35 A cm^{-2}, (E-IrRu) EWII IrRuO$_x$ PEMEC at 0.35 A cm^{-2}, (E-Ni-R) Raney Ni alkaline PEMEC at 0.4 A cm^{-2} and (E-Ni-F) Ni foam alkaline PEMEC at 0.4 A cm^{-2}. Bode plots of the EIS data are shown in the left column and relative residuals of Kramers-Kronig compliance tests of the EIS data are shown in the right column. The real part of the impedance is shown with red circles, and the imaginary part of the impedance is shown with blue triangles. Adapted from article 2.

EIS noise have been quantified by calculating relative residuals of Kramers-Kronig compliance test cf. equation (15) in section 3.2.2. Relative residuals of Kramers-Kronig compliance tests are shown together with the Bode plots of the EIS data for the six PEMECs in figure 5.4.61. The noise was further quantified in order to be able to compare the overall noise level of the cells. This was done by applying equation (36), which sums the square of the relative residuals of the Kramers-Kronig compliance test of the real and the imaginary part of the impedance. In equation (36) δ is the overall noiselevel in %^{2}, $\Delta_{re,i}$ is the Kramers-Kronig relative residuals of the real part of the impedance at frequency i in %, $\Delta_{im,i}$ is the Kramers-Kronig relative residuals of the imaginary part of the impedance at frequency i in % and n is the maximum frequency measured.

$$\delta = \sum_{i=0}^{n} {\Delta_{re,i}}^2 + {\Delta_{im,i}}^2 \quad (36)$$

In article 2 it was found that the noise varied between different types of PEMECs and between different cells of the same PEMEC type. It was furthermore found that the EIS noise did not originate from the water pumps, no noise was observed during DC operation without applying an AC signal, that the noise was dependent on amplitude, but not on integration time, which suggest that the noise originate from a physical process associated with the operation of the PEMECs.

Based on the findings described above, a hypothesis explaining the origin of the noise observed in EIS spectra of PEMECs from gas bubbles partly covering the electrodes during operation was proposed in article 2. During DC operation the bubble coverage of the electrodes will be in a quasi-steady-state and will be released from the electrode surface at a constant average release rate. When applying an AC signal on top of the DC signal, the bubble coverage will no longer be in a quasi-steady-state, but will fluctuate with the AC signal leading to a non-constant/unstable average release rate of the bubbles from the electrodes. The release of bubbles from the electrode surface may be synchronized by the AC perturbation applied during the EIS measurements. The AC signal may cause the bubble release rate to take place in an unstable manner at particular resonance frequency ranges for some bubble sizes, which may depend on the microstructure of the particular PEMEC.

6. Overall Discussion

A hypothesis have been presented in article 1, that above a current density in the range of 0.35 A cm^{-2} the total differential cell resistance in the investigated cells can be ascribed to the resistance of the Nafion membrane, current constriction at the electrode/electrolyte interface and Nafion binder in the electrodes. The hypothesis was supported by the electrochemical measurements on all the different PEMEC types. In section 5.3.1, 5.3.2 and 5.3.3 it was found that all three PEMEC types tested (EWII benchmark cells, EWII cell without IrO_x catalyst layer and PSI benchmark cells) show linear iV-curves from 0.35 A cm^{-2} to 1.00 or approximately 1.5 A cm^{-2} (at high current densities the high power is influencing the cell temperature and thereby the iV-curve). This is in accordance with the literature, where linear iV-curves in general are reported for PEMECs (23) (29) (31) (28) (22) (26) (24) (21) (30) (61) (27). They also showed a temperature dependence of the total differential cell resistance determined from EIS measurements in the same order of magnitude as the temperature dependence of the resistance of a Nafion membrane, which was tested in a PEMEC prior to the conductivity measurements, reported by Malis et al. (47). The EWII benchmark cells showed the same temperature dependence of $Z_{HF,min}$ and the sum of the resistances of the middle and low frequency arcs as the reported by Malis et al. (47) for the tested Nafion membrane. These results implied that the total differential cell resistance can be ascribed to Nafion.

Three arcs were observed in the EIS spectra measured on all three cell types. The area specific capacitances of the three arcs of the EIS spectra measured on the three PEMECs and modelled to the EIS model R-RQ-RQ-RQ or L-R-RQ-RQ-RQ was in the same order of magnitudes for the high and low frequency arc for all four PEMECs cf. table 5.3.1.15, 5.3.2.23, 5.3.3.30 and C.43. The area specific capacitance of the middle frequency arc was similar within two orders of magnitude for all four PEMECs. This indicates that it is the same performance limiting processes for all three PEMECs. It was added to the hypothesis, that the high frequency arc can be ascribed to current constrictions in the anode catalyst layer for all PEMEC types and in the Nafion in the Ir metal layer for the EWII cell types. The capacitance of the middle frequency arc was ascribed to the redox reaction $Ir^{4+} \rightleftharpoons Ir^{5+}$ in the anode catalyst layers and at the surface of the Ir metal layer, and the capacitance of low frequency arc was ascribed to the redox reaction $Ir^{5+} \rightleftharpoons Ir^{6+}$ in the anode catalyst layers and at the surface of the Ir metal layer. Lettenmeier et al. (16) examined the oxidation states of the IrO_x catalyst during OER up to 1.4 V, and measured iridium in oxidation states up to Ir^{4+}, but concluded that the iridium may be present at higher oxidation states at higher operating current densities or at a very short timescale even at 1.4 V. The suggested hypothesis are supported by findings by Bernt et al. (19) and Xu et al. (62), who found performance limitations of PEMECs to originate from ionomer (Nafion binder) in the electrodes and contact resistances (current constrictions) at the electrolyte/electrode interfaces without the use of EIS.

The hypothesis described above based on findings from iV-curve measurements and EIS measurements is supported by the CV measurements combined with the iV-curve measurements for all three PEMEC types. In the CV measurements in section 5.1.5 it was found that the IrO_x catalyst was most electrochemical active in the PSI benchmark cell compared to the EWII benchmark cell and the EWII cell without IrO_x, which catalysts were equally electrochemical active after initiation of the cells over-night at 1 A cm^{-2}. When comparing the cell performance of

the three cells on which CVs were measured as shown in figure 6.62, it is seen that the cell with the best performance at all three cell temperatures (55-58 °C, 63-66 °C and 70-74 °C) were the EWII benchmark cell, ALIP, whereas the cell with the lowest performance was the PSI benchmark cell, PSI_s5_3, which according to the CV measurements contained the most active electrocatalyst. This supports the hypothesis that when operating the PEMEC in the linear part of the iV-curve above 0.35 A cm^{-2}, ohmic processes are performance limiting and the contributions of the faradaic electrode processes to the differential impedance are insignificant.

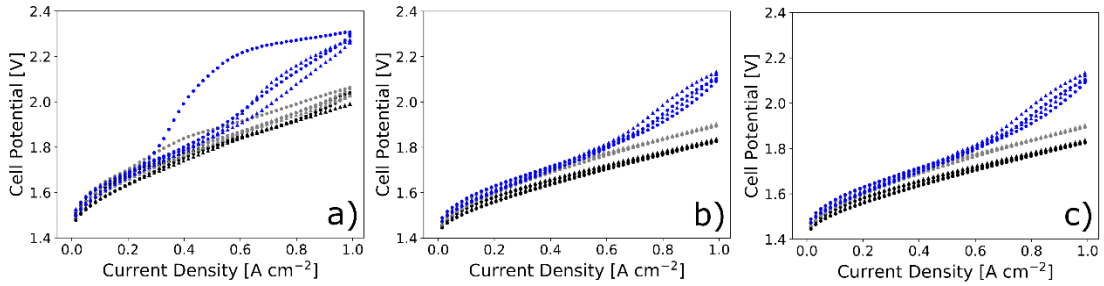

Figure 6.62 iV-curves measured at the three cells, which were examined with CV prior to iV-curve and EIS testing; the EWII benchmark cell, ALIP (black), the PSI benchmark cell, PSI_S5_3 (blue) and the EWII cell without IrO_x layer, ATMJ (gray). The iV-curves in a) are measured at 55-58 °C, the iV-curve in b) are measured at 63-66 °C and the iV-curves at c) are measured at 70-74 °C.

The iV-curves of the four PEMECs of three different PEMEC types, were fitted to the iV-curve model in equation (35). Two Tafel regions were assumed in order to simplify the iV-curve fitting. At high current densities above 0.35 A cm^{-2}, all four cells had a Tafel slope of 0.0 mV $dec.^{-1}$, suggesting that the faradaic processes are not performance limiting at these high current densities, as suggested by the hypothesis. The Tafel slope at low current densities up to 0.15 A cm^{-2} was determined to be 39-77 mV $dec.^{-1}$ for the EWII benchmark cells, 67-90 mV $dec.^{-1}$ for the EWII cells without IrO_x catalyst layer and 47-69 mV $dec.^{-1}$ for the PSI benchmark cells. The low current density Tafel slopes of the PSI and the EWII benchmark cells are very similar, whereas the low current density Tafel slopes measured for the EWII cells without IrO_x layer are larger than the low current density Tafel slopes of the PSI and EWII benchmark cells. This may suggest that the reaction mechanism is similar for the PSI and EWII benchmark cells, and slightly different for the EWII cell without IrO_x layer. In literature, Tafel slopes varying from 40 mV $dec.^{-1}$ to 68 mV $dec.^{-1}$ have been reported for OER on IrO_x in PEMECs and for OER on IrO_x model electrodes. The Tafel slopes determined for the low current density region of the PSI and EWII benchmark cells are similar to what was found in literature (55-68 mV $dec.^{-1}$ by De Pauli et al. (54) and 40 mV $dec.^{-1}$ by Owe et al. (55) and 58 mV $dec.^{-1}$ by Kötz et al. (56), 45-50 mV $dec.^{-1}$ by Bernt et al. (19) and 60 mV $dec.^{-1}$ by Angelinetta et al. (57)), whereas the Tafel slope determined for the low current density range for the EWII cell without IrO_x is a bit larger.

On the basis of the hypothesis explained above, an optimized structure of the PEMEC can be proposed, which according to the hypothesis would allow for better PEMEC performance and less performance limiting processes. A thinner Nafion membrane would decrease the serial resistance of the PEMEC and decrease the differential cell resistance in total. However, a thinner membrane will increase the risk of hydrogen cross over through the membrane and increase the risk of explosion. Another way of limiting the total differential cell resistance according to the

hypothesis, would be to apply as small IrO_x catalyst particles as possible to avoid big pores and thereby avoid current constrictions, while still having a very porous structure, but with small pores. By applying small IrO_x particles, the anode catalyst layer would be thinner though the same amount of Nafion binder was applied to ensure sufficient proton conductivity in the anode catalyst layer, and the lower thickness of the anode catalyst layer would decrease the total differential cell resistance of the PEMECs. The size of the IrO_x particles and the Nafion loading should be optimized in order still to obtain as many triple phase boundaries as possible. Furthermore contact between the current collector and all the IrO_x particles should still be ensured in order for all the IrO_x particles to be electrochemically active. The PSI benchmark cell already contains small IrO_x particles, but still current constrictions are observed, which may be due to the large pores of the Ti felt cf. figure 5.1.4.16 in section 5.1.5, which means that the current distribution is very uneven in the IrO_x layer and therefore current constrictions are observed at the electrode/electrolyte interface. This is diminished in the EWII benchmark cells due to the Ir metal layer, which increase the electron conductivity along the surface of the IrO_x catalyst and the current collector. This suggest that the current collector, which is now made of Ti felt, should be replaced by another electron conducting material stable at potentials up to approximately 2.0 V with a structure with finer pores than the Ti felt currently applied. In figure 6.63 the present structure of an EWII benchmark PEMEC is compared to the ideal microstructure of a PEMEC according to the presented hypothesis, and this ideal PEMEC microstructure is suggested as a basis for future PEMEC development.

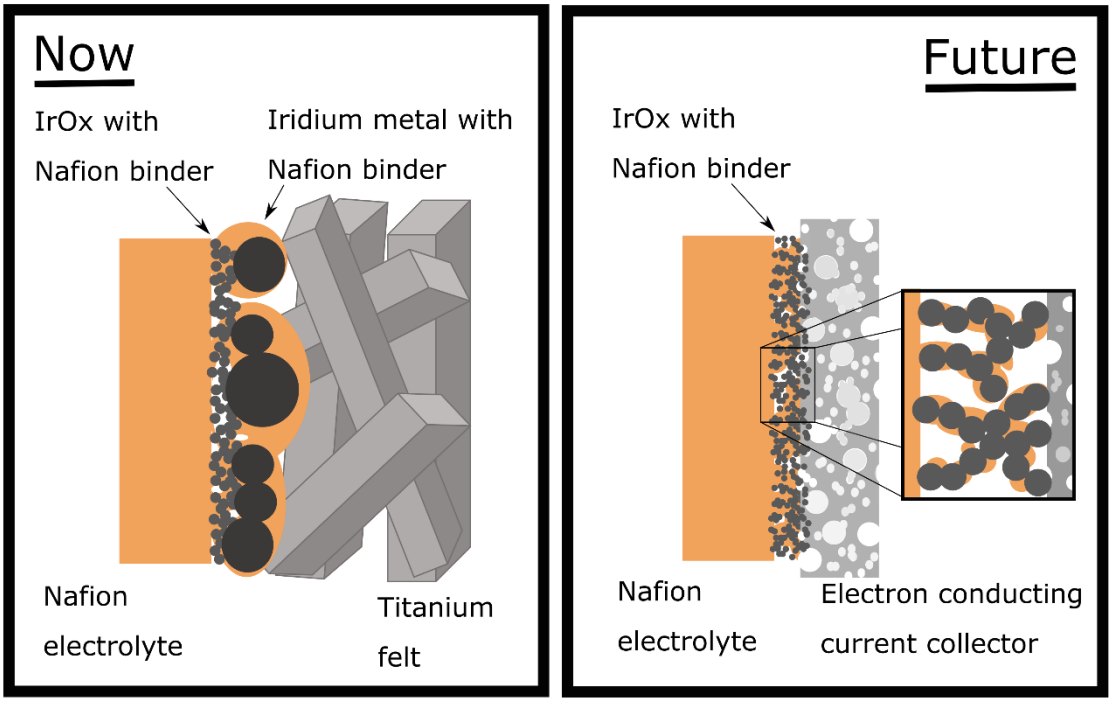

Figure 6.63 Comparison of schematic drawings of the present microstructure of an EWII benchmark PEMEC (left) and a schematic drawing of the ideal microstructure of a PEMEC according to the hypothesis presented in this thesis (right).

7. Concluding Remarks and Outlook

iV-curves measured on different types of PEMECs reported in this thesis showed linear iV-curves above 0.35 A cm^{-2} up to 1.5 A cm^{-2}, where temperature effect start to influence the measurements. This was in accordance with the literature in general. CV measurements and EIS measurements in combination with the linear iV-curves above 0.35 A cm^{-2} led to the following hypothesis, which is new in PEMEC research: The total differential cell resistance of PEMECs originates from proton conduction resistance in Nafion in the membrane, in the Nafion binder in the anode catalyst layer and from current constrictions at the electrode/electrolyte interface. It has been proposed to manufacture PEMECs with as thin a Nafion membrane as possible, which still avoids hydrogen crossover, with smaller IrO_x particles in the anode catalyst layer, to decrease current constrictions and to decrease the amount of Nafion binder in the anode catalyst layer. Additionally it was suggested to use a current collector with smaller pores likewise to decrease current constrictions. With this optimized PEMEC microstructure based on the new hypothesis, it should be possible to obtain better performing PEMECs in the future.

References

1. Energikommisionen. *Energikommisionens anbefalinger til fremtidens energipolitik.* Denmark, 2017.
2. *Parking the power: Strategies and physical limitations for bulk energy storage in supply–demand matching on a grid whose input power is provided by intermittent sources.* W. F. Pickard, A. Q. Shen, N. J. Hansing. s.l. : Renew. Sust. Energ. Rev., 2009, 13. 1934–1945.
3. *A comprehensive review on PEM water electrolysis.* M. Carmo, D. L. Fritz, J. Mergel, D. Stolten. 2013, Int. J. Hydrogen Energ., 4901-4934.
4. *Review - Identifying Critical Gaps for Polymer Electrolyte Water Electrolysis Development.* U. Babic, M. Suermann, F. N. Büchi, L. Gubler, T. J. Schmidt. 4, J. Electrochem. Soc., 2017, 164. F387-F399.
5. *Developments and perspectives of oxide-based catalysts for the oxygen evolution reaction.* E. Fabbri, A. Habereder, K. Walter, R. Kötz, T. J. Schmidt. Catal. Sci. Technol., 2014, 4. 3800-3821.
6. Mosbæk, R. R. *Solid Oxide Fuel Cell Stack Diagnostics.* Technical University of Denmark, 2014.
7. *Nafion Perfluorinated Membranes in Fuel Cells.* S. Banerjee, D. E. Curtin. s.l. : J. Fluorine Chem., 2004, 125. 1211–1216.
8. *Hydrogen Generation by Solid Polymer Electrolyte Water Electrolysis.* J. H. Russell, L. J. Nuttall, A. P. Fickett. 3, American Chemical Society Division of Fuel Chemistry Preprints, 1973, 18. 24-40.
9. *Pure Hydrogen Production by PEM Electrolysis for Hydrogen Energy.* S. A. Grigoriev, V. I. Porembsky, V. N. Fateev. Int. J. Hydrogen Energ., 2006, 31. 171 – 175.
10. *Bipolar plates for PEM fuel cells: A review.* A. Hermann, T. Chaudhuri, P. Spagnol. 2005, Int. J. Hydrogen Energ., 1297-1302.
11. *Metal bipolar plates for PEM fuel cell - A review.* H. Tawfik, Y. Hung, D. Mahajan. 2007, J. Power Sources, 755-767.
12. *Stabilization of RuO2 by IrO2 for Anodic Oxygen Evolution in Acid Media.* R. Kötz, S. Stucki. 10, Electrochim. Acta, 1986, 31. 1311-1316.
13. *Addressing the Terawatt Challenge: Scalability in the Supply of Chemical Elements for Renewable Energy.* P. C. K. Vesborg, T. F. Jaramillo. RSC Advances, 2012, 2. 7933-7947.
14. *The Stability Challenges of Oxygen Evolving Catalysts: Towards a Common Fundamental Understanding and Mitigation of Catalyst Degradation.* C. Spöri, J. T. H. Kwan, A. Bonakdarpour, D. P. Wilkinson, P. Strasser. Angew. Chem. Int. Ed., 2017, 56. 5994–6021.
15. *Anodic Iridium Oxide Films.* R. Kötz, H. Neff, S. Stucki. 1, J. Electrochem. Soc., 1984, 131. 72-77.
16. *Highly active nano-sized iridium catalysts: synthesis and operando spectroscopy in a proton exchange membrane electrolyzer.* P. Lettenmeier, J. Majchel, L. Wang, V. A. Saveleva, S. Zafeiratos, E. R. Savinova, J.-J. Gallet, F. Bournel, A. S. Gago, K. A. Friedrich. Chem. Sci., 2018, 9. 3570–3579.
17. *An analysis of degradation phenomena in polymer electrolyte membrane water electrolysis.* C. Rakousky, U. Reimer, K. Wippermann, M. Carmo, W. Lueke, D. Stolten. 2016, J. Power Sources, 120-128.
18. *Electrochemical impedance studies of IrO2 catalysts for oxygen evolution.* A. Papaderakis, D. Tsiplakides, S. Balomenou, S. Sotiropoulos. 2015, J. Electroanal. Chem., 216–224.

19. *Influence of Ionomer Content in IrO2/TiO2 Electrodes on PEM Water Electrolyzer Performance.* M. Bernt, H. A. Gasteiger. 11, J. Electrochem. Soc., 2016, 163. F3179-F3189.
20. *High Pressure Polymer Electrolyte Water Electrolysis: Test Bench Development and Electrochemical Analysis.* M. Suermann, A. Patru, T. J. Schmidt, F. N. Büchi. Int. J. Hydrogen Energ., 2017, 42. 12076-12086.
21. *In situ diagnostic techniques for characterisation of polymer electrolyte membrane water electrolysers e Flow visualisation and electrochemical impedance spectroscopy.* I. Dedigama, P. Angeli, K. Ayers, J. B. Robinson, P. R. Shearing, D. Tsaoulidis, D. J. L. Brett. 2014, Int. J. Hydrogen Energy, 4468-4482.
22. *Towards Developing a Backing Layer for Proton Exchange Mambrane Electrolyzers.* P. Lettenmeier, S. Kolb, F. Burggraf, A. S. Gago, K. A. Friedrich. 2016, J. Power Sources, 153-158.
23. *Electrochemical Characterization of Single Cell and Short Stack PEM Electrolyzers based on a Nanosized IrO2 Anode Electrocatalyst.* S. Siracusano, V. Baglio, A. Di Blasi, N. Briguglio, A. Stassi, R. Ornelas, E. Trifoni, V. Antonucci, A. S. Aricò. Int. J. Hydrogen Energ., 2010, 35. 5558-5568.
24. *Investigations on Degradation of the Long-Term Proton Exchange Membrane Water Electrolysis Stack.* S. Sun, Z. Shao, H. Yu, G. Li, B. Yi. J. Power Sources, 2014, 267. 515-520.
25. *Energy Dispersive X-Ray and Electrochemical Impedance Spectroscopies for Performance and Corrosion Analysis of PEMWEs.* S. M. Steen, F.-Y. Zhang. J. Phys. Conf. Ser., 2014, 548.
26. *Electrochemical characterization of Polymer Electrolyte Membrane Water Electrolysis Cells.* C. Rozain, P. Millet. 2014, Electrochim. Acta, 160-167.
27. *Influence of iridium oxide loadings on the performance of PEM water electrolysis cells: Part II – Advanced oxygen electrodes.* C. Rozain, E. Mayoussea, N. Guilleta, P. Millet. Appl. Catal. B - Environ., 2016, Appl. catal. B - Environ., 182, 123–131. 123-131.
28. *Durable Membrane Electrode Assemblies for Proton Exchange Membrane Electrolyzer Systems Operating at High Current Densities.* P. Lettenmeier, R. Wang, R. Abouatallah, S. Helmly, T. Morawietz, R. Hiesgen, S. Kolb, F. Burggraf, J. Kallo, A. S. Gago, K. A. Friedrich. 2016, Electrochim. Acta, 502-511.
29. *Electrochemical characterization of a PEM water electrolyzer based on a sulfonated polysulfone membrane.* S. Siracusano, V. Baglio, F. Lufrano, P. Staiti, A. S. Aricò. 2013, J. Membr. Sci., 209-214.
30. *Characterisation Tools Development for PEM Electrolysers.* J. van der Merwe, K. Uren, G. van Schoor, D. Bessarabov. Int. J. Hydrogen Energ., 2014, 39. 14212-14221.
31. *Electrochemical Performances of PEM Water Electrolysis Cells and Perspectives.* P. Millet, N. Mbemba, S. A. Grigoriev, V. N. Fateev, A. Aukauloo, C. Etiévant. Int. J. Hydrogen Energ., 2011, 36. 4134-4142.
32. R. Greef, R. Peat, L. M. Peter, D. Pletcher, J. Robinson. *Instrumental Methods in Electrochemistry.* Chichester : Ellis Horwood Limited, 1985.
33. A. J. Bard, L. R. Faulkner. *Electrochemical Methods - Fundamentals and Applications.* Hoboken : John Wiley and Sons, 2001.
34. Lasia, A. *Electrochemical Impedance Spectroscopy and its Applications.* London : Springer, 2014.
35. E. Barsoukov, J. R. Macdonald. *Impedance Spectroscopy Theory, Experiment, and Applications.* Hoboken : John Wiley & Sons, 2005. Second edition.
36. M. E. Orazem, B. Tribollet. *Electrochemical Impedance Spectroscopy.* Hoboken : John Wiley & Sons, 2008.

37. *A Linear Kronig-Kramers Transform Test for Immittance Data Validation.* Boukamp, B. A. 6, J. Electrochem. Soc., 1995, 142. 1885-1894.
38. Analytical, Solartron. SI1287 Electrochemical Interface. *User Guide.* Hampshire : Solartron, 1999.
39. *Electrolysis of water on oxide surfaces.* J. Rossmeisl, Z. –W. Qu, H. Zhu, G. –J. Kroes, J. K. Nørskov. 2007, J. Electroanal. Chem., 83-89.
40. *Hydrogen Oxidation and Evolution Reaction Kinetics on Platinum: Acid vs Alkaline Electrolytes.* W. Sheng, H. A. Gasteiger, Y. Shao-Horn. 2010, J. Electrochem. Soc., B1529-B1536.
41. *A Perovskite Oxide Optimized for Oxygen Evolution Catalysis from Molecular Orbital Principles.* J. Suntivich, K. J. May, H. A. Gasteiger, J. B. Goodenough, Y. Shao-Horn. 2011, Science, 1383-1385.
42. Graves, C. RAVDAV data analysis software, version 0.9.7. 2012.
43. *Electrochemical comparison of IrO2 prepared by anodic oxidation of pure iridium and IrO2 prepared by thermal decomposition of H2IrCl6 precursor solution.* L. Ouattara, S. Fierro, O. Frey, M. Koudelka, C. Comninellis. 2009, J. Appl. Electrochem., 1361–1367.
44. *Investigation of the electrical and optical properties of iridium oxide by reflectance FTIR spectroscopy and density functional theory calculations.* S. H. Brewer, D. Wicaksana, J.-P. Maria, A. I. Kingon, S. Franzen. 2005, Chem. Phys., 25-31.
45. *Electrochemical Characterization of a PEMEC Using Impedance Spectroscopy.* K. Elsøe, L. Grahl-Madsen, G. G. Scherer, J. Hjelm, M. B. Mogensen. 2017, J. Electrochem. Soc., F1419-F1426.
46. Definition of Impedance and Impedance of Electrical Circuits. *Electrochemical Impedance Spectroscopy and its Applications.* New York Heidelberg Dordrecht London : Springer, 2014, 7-67.
47. *Nafion 117 Stability under Conditions of PEM Water Electrolysis at Elevated Temperature and Pressure.* J. Malis, P. Mazur, M. Paidar, T. Bystron, K. Bouzek. 2016, Int. J. Hydrogen Energy, 2177-2188.
48. *Polarization Mechanism of High Temperature Electrolysis in a Ni-YSZ/YSZ/LSM Solid Oxide Cell by Parametric Impedance Analysis.* E.-C. Shin, P.-A. Ahn, H.-H. Seo, J.-M. Jo, S.-D. Kim, S.-K. Woo, J. H. Yu, J. Mizusaki, J.-S. Lee. 2013, Solid State Ionics, 80-96.
49. *Determination of effective capacitance and film thickness from constant-phase-element parameters.* B. Hirshorn, M. E. Orazem, B. Tribollet, V. Vivier, I. Frateur, M. Musiani. 2010, Electrochim. Acta, 6218–6227.
50. *Technical Note: Concerning the Conversion of the Constant Phase Element Parameter Y0 into a Capacitance.* C. H. Hsu, F. Mansfeld. 2001, Corrosion, 747-748.
51. *Electroceramics: Characterization by Impedance Spectroscopy.* J. T. S. Irvine, D. C. Sinclair, A. R. West. 1990, Adv. Mater., 132-138.
52. P. Atkins, J. De Paula. *Atkins' Physical Chemistry.* Oxford : Oxford University Press, 2010.
53. *The Influence of Current Constriction on the Impedance of Polarizable Electrodes.* J. Fleig, J. Maier. 1997, J. Electrochem. Soc., L302-L305.
54. *Composite materials for electrocatalysis of O2 evolution: IrO2 + SnO2 in acid solution.* C. P. De Pauli, S. Trasatti. 2002, J. Electroanal. Chem., 538-539.
55. *Iridium–ruthenium single phase mixed oxides for oxygen evolution: Composition dependence of electrocatalytic activity.* L.-E. Owe, M. Tsypkin, K. S. Wallwork, R. G. Haverkamp, S. Sunde. 2012, Electrochim. Acta, 158-164.

56. *Stabilization of RuO2 by IrO2 for anodic oxygen evolution in acid media.* R. Kötz, S. Stucki. 1986, Electrochim. Acta, 1311-1316.
57. *Effect of preparation on the surface and electrocatalytic properties of RuO2 + IrO2 mixed oxide electrodes.* C. Angelinetta, S. Trasatti, L. D. Atanasoka, Z. S. Minevski, R. T. Atanasoski. 1989, Mater. Chem. Phys., 231-247.
58. Babic, U. Unpublished results.
59. *Nano-structured (La, Sr)(Co, Fe)O3 + YSZ composite cathodes for intermediate temperature solid oxide fuel cells.* J. Chen, F. Liang, L. Liu, S. Jiang, B. Chi, J. Pu, J. Li. 2008, J. Power Sources, 586-589.
60. Fenini, F. Unpublished results.
61. *Performance of a PEM water electrolysis cell using IrxRuyTazO2 electrocatalysts for the oxygen evolution electrode.* A. T. Marshall, S. Sunde, M. Tsypkin, R. Tunold. Int. J. Hydrogen Energ., 2007, 32. 2320–2324.
62. *The effects of ionomer content on PEM water electrolyser membrane electrode assembly performance.* W. Xu, K. Scott. Int. J. Hydrogen Energy, 2010, 35. 12029-12037.
63. *Stolten, M. Carmo and D. L. Fritz and J. Mergel and D. 2013, International Journal of Hydrogen Energy 38 (1) , 4901–4934.*
64. Schmidt, E. Fabbri and A. Habereder and K. Waltar and R. Kötz and T. J. 2014, Catal. Sci. Technol. 4 (11), 3800–3821.
65. The AC Impedance Response of the Physical Interface Between Yttria-Stabilized Zirconia and YBa2Cu3O7-x. J. G. Fletcher, A. R. West, J. T. S. Irvine. 1995, J. Electrochem. Soc., 2650-2654.
66. Rumble, J. Handbook of Chemistry and Physics. CRC Press, 2017.

A. Experimental EIS Parameters

A.1 EWII Benchmark Cell, ALIP.

Potential measured for the EWII benchmark cell, ALIP, during galvanostatic EIS measurements at three different temperatures and four different current densities are given in table A.1.33. The potential change the last five minutes before each EIS measurements at 63 °C of the EWII benchmark cell, ALIP, are given in table A.1.34.

Table A.1.33 Potentials measured during EIS measurements at four different current densities and at three different temperatures on the EWII benchmark cell, ALIP.

		Current density [A cm^{-2}]			
		0.07	**0.35**	**0.69**	**1.00**
Temperature [°C]	**55-56**	1.55 V	1.72 V	1.88 V	2.00 V
	63	1.50 V	1.62 V	1.74 V	1.84 V
	70-71	1.49 V	1.63 V	1.76 V	1.87 V

Table A.1.34 Potential change the last 5 minutes before EIS measurements at four different current densities and three different temperatures on the EWII benchmark cell, ALIP.

		Current density [A cm^{-2}]			
		0.07	**0.35**	**0.69**	**1.00**
Temperature [°C]	**63**	0.2 mV min^{-1}	0.2 mV min^{-1}	0.0 mV min^{-1}	0.2 mV min^{-1}

A.2 EWII Cell Without IrO_x Layer.

Potential measured for the EWII cell without IrO_x layer, ATMJ, during galvanostatic EIS measurements at three different temperatures and four different current densities are given in table A.2.35. The potential change the last five minutes before each EIS measurements at 64 °C of the EWII cell without IrO_x layer, ATMJ, are given in table A.2.36.

Table A.2.35 Potentials measured during EIS measurements at four different current densities and at three different temperatures on the EWII cell without IrO_x, ATMJ.

		Current density [A cm^{-2}]			
		0.07	**0.35**	**0.69**	**1.00**
Temperature [°C]	**56**	1.57 V	1.75 V	1.91 V	2.04 V
	64	1.52 V	1.66 V	1.79 V	1.90 V
	70-71	1.51 V	1.65 V	1.78 V	1.89 V

Table A.2.36 Potential change the last 5 minutes before EIS measurements at four different current densities and three different temperatures on the EWII cell without IrO_x, ATMJ.

		Current density [A cm^{-2}]			
		0.07	**0.35**	**0.69**	**1.00**
Temperature [°C]	**64**	0.2 mV min^{-1}	0.2 mV min^{-1}	0.0 mV min^{-1}	0.2 mV min^{-1}

A.3 PSI Benchmark Cell, PSI_s5_2.

Potential measured for the PSI benchmark cell, PSI_s5_2, during galvanostatic EIS measurements at three different temperatures and six different current densities are given in table A.3.37. The potential change the last five minutes before each EIS measurements at 66-68 °C of the PSI benchmark cell, PSI_s5_2, are given in table A.3.38.

Table A.3.37 Potentials measured during EIS measurements at four different current densities and at three different temperatures on the PSI benchmark cell, PSI_s5_2.

		Current density [A cm^{-2}]					
		0.07	**0.35**	**0.69**	**1.00**	**2.00**	**3.00**
Temperature [°C]	**57-60**	1.55 V	1.70 V	1.86 V	2.00 V	2.31 V	2.51 V
	66-68	1.52 V	1.65 V	1.77 V	1.89 V	2.24 V	2.43 V
	73-76	1.50 V	1.62 V	1.76 V	1.90 V	2.19 V	2.39 V

Table A.3.38 Potential change the last 5 minutes before EIS measurements at four different current densities and three different temperatures on the PSI benchmark cell, PSI_s5_2.

		Current density [A cm^{-2}]					
		0.07	**0.35**	**0.69**	**1.00**	**2.00**	**3.00**
Temperature [°C]	**66-68**	0.2 mV min^{-1}	0.2 mV min^{-1}	0.2 mV min^{-1}	0.0 mV min^{-1}	-1.2 mV min^{-1}	-1.2 mV min^{-1}

B. Cell Histories

In this section, the cell histories of the tested PEMECs are shown. Figure B.64 and B.65 show the cell history of the reference EWII benchmark cell, cell 0, during cell testing and figure B.66 and B.67 show the cell history of the other EWII benchmark cell, cell y. Figure B.68 and B.69 show the cell history of the PSI benchmark cell, PSI_s5_3, during cell testing and figure B.70 and B.71 show the cell history of the EWII benchmark without IrO_x layer, ATMJ.

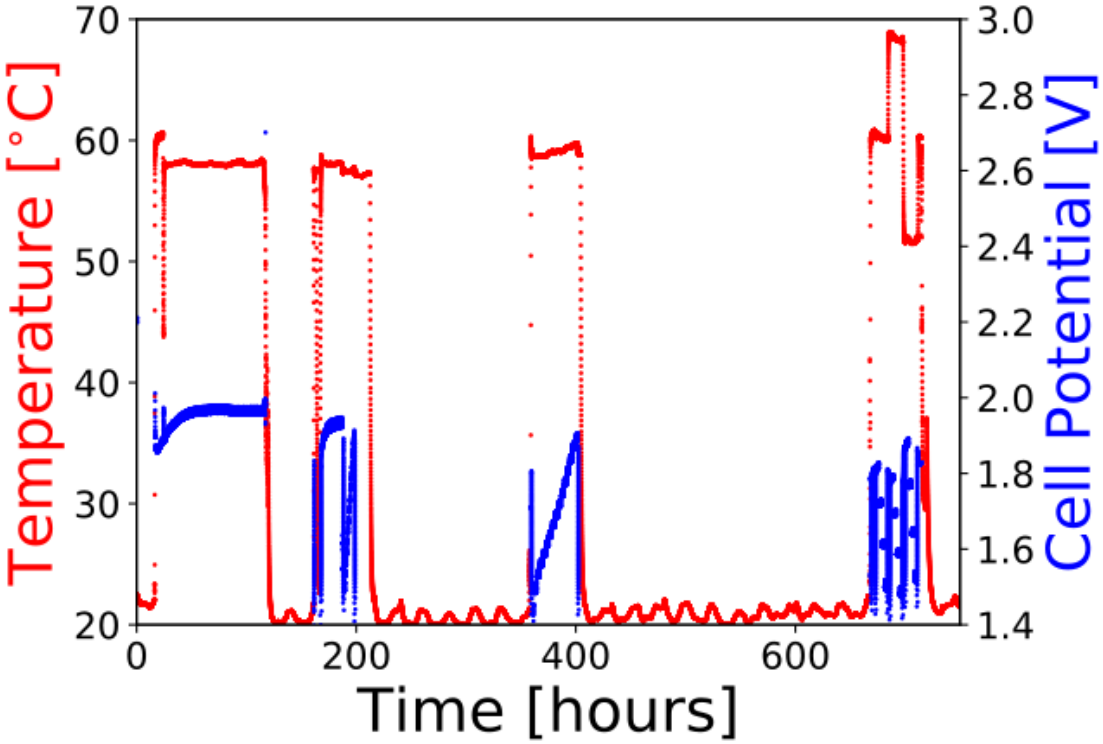

Figure B.64 Temperature and cell potential measured during test of the benchmark EWII cell, Cell 0.

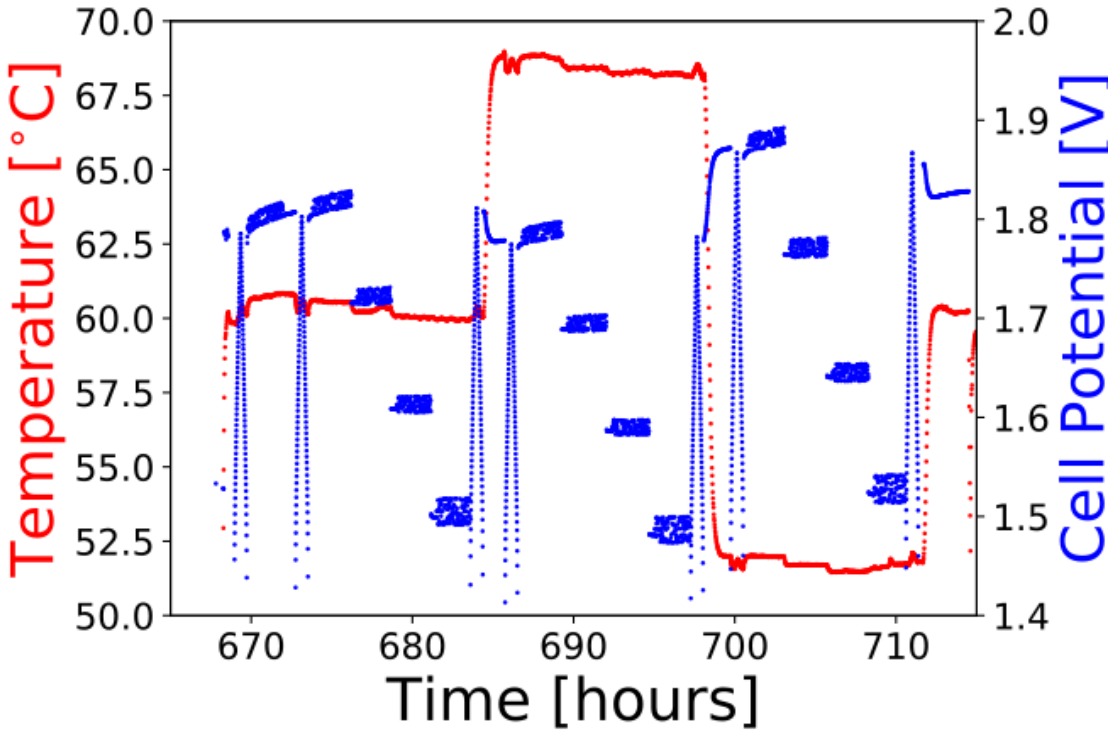

Figure B.65 Temperature and cell potential measured during standard EIS test of the benchmark EWII cell, Cell 0. During the standard EIS test, EIS is measured at four different current densities (0.07, 0.35, 0.69 and 1.00 A cm^{-2}) at three different temperatures (53, 61 and 69 ˚C).

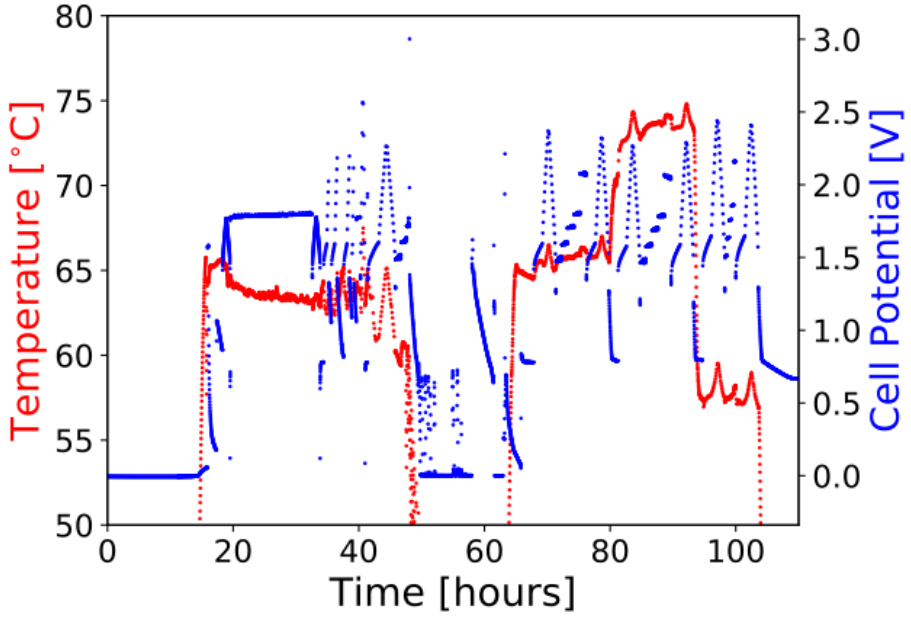

Figure B.66 Temperature and cell potential measured during test of cell Y.

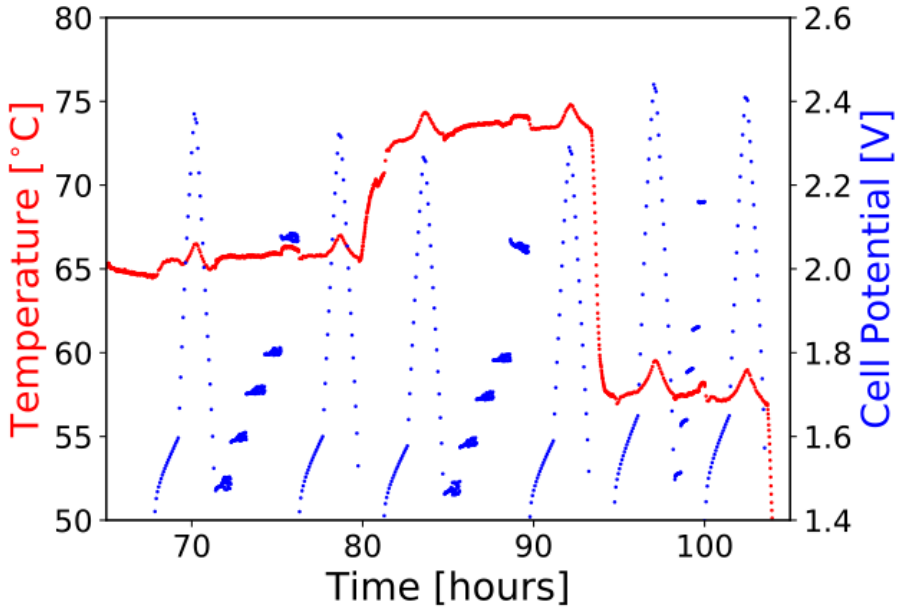

Figure B.67 Temperature and cell potential measured during standard EIS test of the EWII benchmark cell, cell Y. During the standard EIS test, EIS is measured at five different current densities (0.07, 0.35, 0.69, 1.00 and 2.00 A cm^{-2}) at three different temperatures.

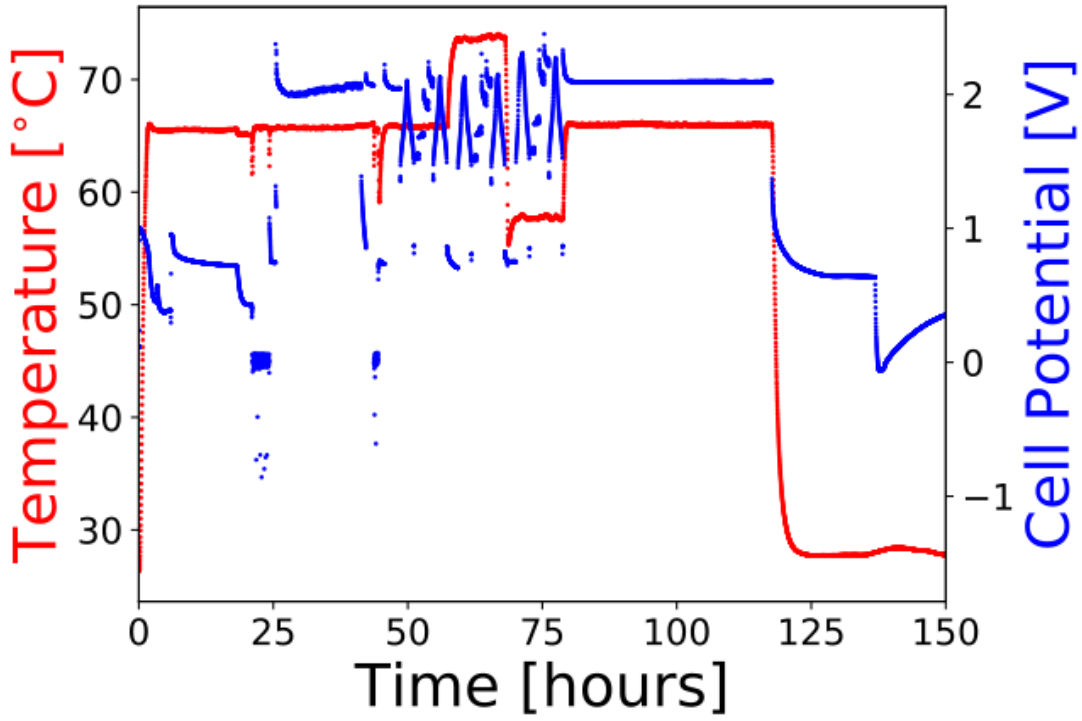

Figure B.68 Temperature and cell potential measured during test of the PSI cell, PSI_s5_3.

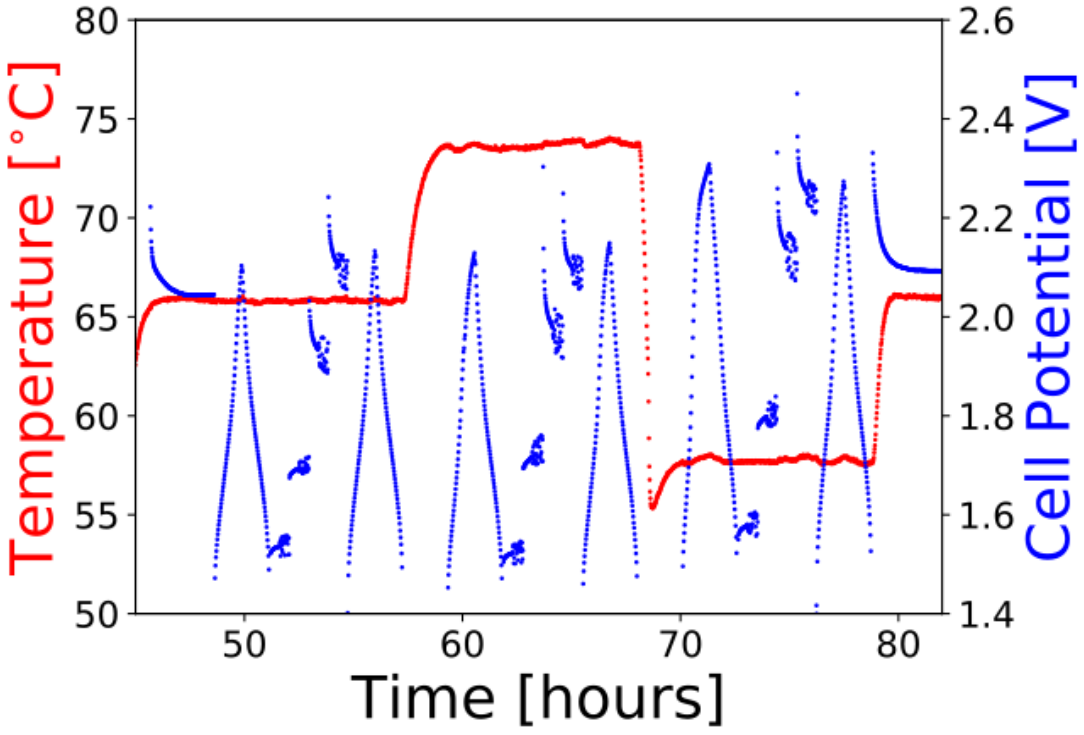

Figure B.69 Temperature and cell potential measured during standard EIS test of the PSI cell, PSI_s5_3. During the standard EIS test, EIS is measured at four different current densities (0.07, 0.35, 0.69 and 1.00 A cm^{-2}) at three different temperatures (58, 66 and 74 ˚C).

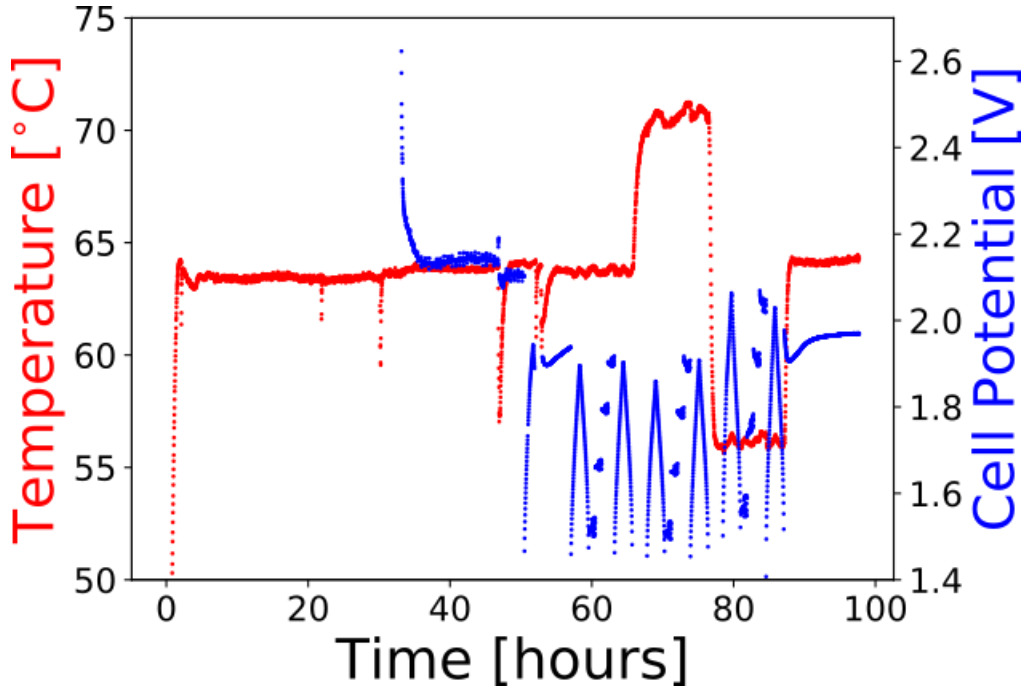

Figure B.70 Temperature and cell potential measured during test of the EWII cell without IrOx layer, ATMJ.

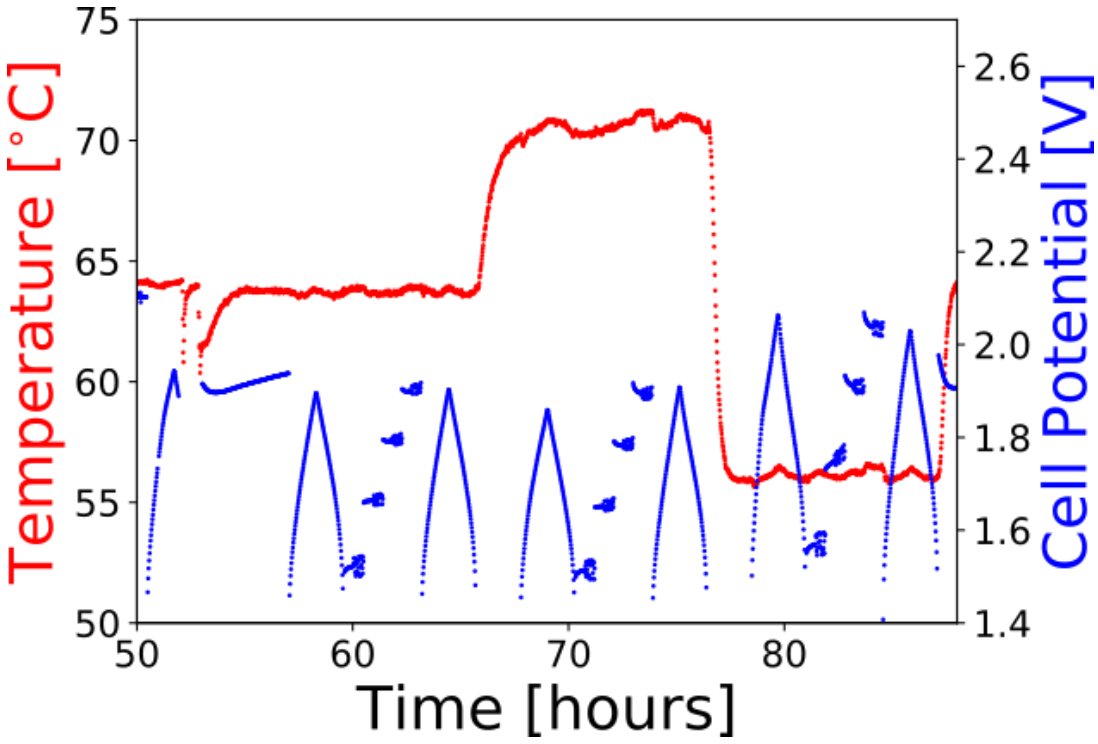

Figure B.71 Temperature and cell potential measured during standard EIS test of the EWII cell without IrOx, ATMJ. During the standard EIS test, EIS is measured at four different current densities (0.07, 0.35, 0.69 and 1.00 A cm^{-2}) at three different temperatures (56, 64 and 70-71 ˚C).

C. EIS Overview Tables

The values in table C.39 and C.40 are reading values from Nyquist plots and Bode plots of the EIS measured on the various PEMECs reported in this thesis. The lowest measured frequency, at which $Z_{re,LF}$ has been read off, is given in parenthesis next to the reading value in table C.39 and C.40 . For some of the cells, it was not possible to determine $Z_{re,HF\ min}$ due to high frequency inductance. Therefore it was also not possible to determine the resistance of the middle and low frequency arcs of these cells.

For some of the cells EIS was measured up to 3.00 A cm^{-2}. EIS values measured above 1.00 A cm^{-2} is shown in table C.41.

Table C.42 lists averages of the total cell resistance, $Z_{re,LF}$, from 0.35 A cm^{-2} to 1 A cm^{-2} (the linear part of the iV-curves), averages of $Z_{re,HF}$ min up to 1 A cm^{-2} and averages of the resistance of the middle and low frequency arcs, ΔZ_{re} from 0.35 A cm^{-2} to 1 A cm^{-2}. The average values are given with ± the deviation of the values. The lower the deviation the more linear the iV-curve.

In table C.43 is equivalent capacitances determined from fits of the three different PEMEC types (EWII benchmark cell, PSI benchmark cell, EWII cell without IrO_x layer) shown. The equivalent capacitances are both normalized to the geometrical electrode area (2.9 cm^2) and to the ECSA determined from CVs shown in section 5.2.

Charges for the high, middle and low frequency arcs determined from fitting of EIS data measured on the three different PEMEC types (EWII benchmark cell, PSI benchmark cell, EWII cell without IrO_x layer) are given in table C.44.

Table C.39 EIS Overview Table showing $Z_{re,\ LF}$, $Z_{re,HF\ minimum}$, $Z_{re,\ LF\ -\ HF\ min}$, $f_{summit,\ MF}$, $f_{summit,\ LF}$, T_{cell}, $R_{s,\ Malis}$, measured at current densities up to 1.00 A cm^{-2}. The lowest measured frequency, at which $Z_{re,LF}$ has been read off, is higher than 0.01 Hz, it is given in parenthesis next to the reading value. LFIL stands for low frequency inductive loop. $Z_{re,LF}$ read off in EIS spectra, where the EIS measured at the lowest frequency has a capacitive contribution and is not purely resistive, is marked with a *. Und. stands for undefinable.

Cell	Cell Temperature, T	Rs @ T (47)	0.07 A cm^{-2}						0.35 A cm^{-2}					
			$Z_{re,LF}$	$Z_{re,HF\ min.}$	$Z_{re,\ LF\ -\ HF\ min}$	$f_{MF\ summit}$	$f_{LF\ summit}$	$Z_{re,HF\ min.}$-R_s(Malis)	$Z_{re,LF}$	$Z_{re,HF\ min.}$	$Z_{re,\ LF\ -\ HF\ min}$	$f_{MF\ summit}$	$f_{LF\ summit}$	$Z_{re,HF\ min.}$-R_s(Malis)
Cell 0 EWII reference	**53 °C**	**0.159 Ω cm^2**	0.560	0.242	0.318	9 Hz	-	0.083	0.353	0.242	0.111	60 Hz	0.05 Hz	0.083
	61 °C	**0.148 Ω cm^2**	0.538	0.225	0.313	9 Hz	-	0.077	0.319	0.224	0.095	60 Hz	0.05 Hz	0.076
	69 °C	**0.138 Ω cm^2**	0.519	0.210	0.309	9 Hz	-	0.072	0.303	0.208	0.095	60 Hz	0.05 Hz	0.070
ALIP EWII	**55-56 °C**	**0.156-0.155 Ω cm^2**	0.734	0.254	0.480	16 Hz	-	0.098	0.474	0.259	0.215	93 Hz	0.07 Hz	0.103
	63 °C	**0.145 Ω cm^2**	0.571	0.202	0.369	8 Hz	-	0.057	0.343	0.203	0.140	35 Hz	0.04 Hz	0.058
	70-71 °C	**0.136-0.135 Ω cm^2**	0.623	0.217	0.406	11 Hz	-	0.081	0.404	0.221	0.183	54 Hz	0.05 Hz	0.085
ATMJ Without IrOx	**56 °C**	**0.155 Ω cm^2**	0.842	Und.	Und.	17 Hz	0.04 Hz	-	0.514	Und.	Und.	145 Hz	0.06 Hz	-
	64 °C	**0.144 Ω cm^2**	0.717	Und.	Und.	12 Hz	0.06 Hz	-	0.391	Und.	Und.	92 Hz	0.06 Hz	-
	70-71 °C	**0.136-0.135 Ω cm^2**	0.714	Und.	Und.	15 Hz	0.06 Hz	-	0.397	Und.	Und.	93 Hz	0.06 Hz	-
Pt on Ti felt EWII	**54-55 °C**	**0.157-0.156 Ω cm^2**	0.678	0.246	0.432	13 Hz	0.05 Hz	0.089	0.452	0.245	0.207	71 Hz	0.05 Hz	0.088
	62 °C	**0.147 Ω cm^2**	0.549	0.203	0.346	7 Hz	0.06 Hz	0.056	0.332	0.202	0.130	47 Hz	0.05 Hz	0.055
	69 °C	**0.138 Ω cm^2**	0.569	0.201	0.368	8 Hz	0.05 Hz	0.063	0.369	0.203	0.166	57 Hz	0.07 Hz	0.065
PSI_s5_2	**57-60 °C**	**0.153-0.149 Ω cm^2**	-	-	-	-	-	-	0.379* (1.422 Hz)	Und.	Und.	32 Hz	-	-
	66-68 °C	**0.142-0.139 Ω cm^2**	0.581	Und.	Und.	4.5 Hz	-	-	0.344	Und.	Und.	32 Hz	0.07 Hz	-

73-76 °C	**0.132-0.128 Ω cm^2**	0.558 (0.045 Hz)	Und.	Und.	4.5 Hz	-	-	0.335 (0.045 Hz)	Und.	Und.	32 Hz	-	-

Table C.40 EIS Overview Table showing $Z_{re,\ LF}$, $Z_{re,HF\ minimum}$, $Z_{re,\ LF\ -\ HF\ min}$, $f_{summit,\ MF}$, $f_{summit,\ LF}$, T_{cell}, $R_{s,\ Malis}$, measured at current densities up to 1.00 A cm^{-2}. The lowest measured frequency, at which $Z_{re,LF}$ has been read off, is higher than 0.01 Hz, it is given in parenthesis next to the reading value. LFIL stands for low frequency inductive loop. $Z_{re,LF}$ read off in EIS spectra, where the EIS measured at the lowest frequency has a capacitive contribution and is not purely resistive, is marked with a *. Und. stands for undefinable.

Cell	Cell Temperature, T	Rs @ T (47)	0.69 A cm^{-2} $Z_{re,LF}$	$Z_{re,HF\ min.}$	$Z_{re,\ LF\ -\ HF\ min}$	$f_{MF\ summit}$	$f_{LF\ summit}$	$Z_{re,HF\ min.}$-R_s(Malis)	1.00 A cm^{-2} $Z_{re,LF}$	$Z_{re,HF\ min.}$	$Z_{re,\ LF\ -\ HF\ min}$	$f_{MF\ summit}$	$f_{LF\ summit}$	$Z_{re,HF\ min.}$-R_s(Malis)
Cell 0 EWII reference	**53 °C**	**0.159 Ω cm^2**	0.369	0.245	0.124	96 Hz	0.3 Hz	0.086	0.349	0.247	0.102	105 Hz	0.4 Hz	0.088
	61 °C	**0.148 Ω cm^2**	0.317	0.222	0.095	96 Hz	0.3 Hz	0.074	0.319	0.225	0.094	125 Hz	0.5 Hz	0.077
	69 °C	**0.138 Ω cm^2**	0.303	0.210	0.093	96 Hz	0.3 Hz	0.072	0.307	0.211	0.096	125 Hz	0.5 Hz	0.073
ALIP EWII	**55-56 °C**	**0.156-0.155 Ω cm^2**	0.423	0.268	0.155	240 Hz	0.2 Hz	0.112	0.447 LFIL	0.262	0.185	322 Hz	0.4 Hz	0.106
	63 °C	**0.145 Ω cm^2**	0.304	0.208	0.096	78 Hz	0.13 Hz	0.063	0.298	0.213	0.085	145 Hz	0.3 Hz	0.068
	70-71 °C	**0.136-0.135 Ω cm^2**	0.399	0.225	0.174	115 Hz	0.14 Hz	0.089	0.436 LFIL	0.220	0.216	145 Hz	0.4 Hz	0.084
ATMJ Without IrOx	**56 °C**	**0.155 Ω cm^2**	0.478	Und.	Und.	344 Hz	0.21 Hz	-	0.491 LFIL	Und.	Und.	398 Hz	0.34 Hz	-
	64 °C	**0.144 Ω cm^2**	0.348	Und.	Und.	287 Hz	0.25 Hz	-	0.342	Und.	Und.	618 Hz	0.45 Hz	-
	70-71 °C	**0.136-0.135 Ω cm^2**	0.381	Und.	Und.	261 Hz	0.20 Hz	-	0.405 LFIL	Und.	Und.	317 Hz	0.53 Hz	-
Pt on Ti felt EWII	**54-55 °C**	**0.157-0.156 Ω cm^2**	0.461	0.244	0.217	152 Hz	0.18 Hz	0.087	0.615	0.243	0.372	171 Hz	0.39 Hz	0.086
	62 °C	**0.147 Ω cm^2**	0.331	0.204	0.127	74 Hz	0.17 Hz	0.057	0.335	0.209	0.126	117 Hz	0.25 Hz	0.062
	69 °C	**0.138 Ω cm^2**	0.441	0.208	0.233	78 Hz	0.10 Hz	0.070	0.831	0.209	0.622	-	0.36 Hz	0.071
PSI_s5_2	**57-60 °C**	**0.153-0.149 Ω cm^2**	0.407* (0.045 Hz)	Und.	Und.	134 Hz	0.19 Hz	-	0.431 (0.0306 Hz)	Und.	Und.	297 Hz	0.33 Hz	-

66-68 °C	**0.142-0.139 Ω cm²**	0.332	Und.	Und.	59 Hz	0.11 Hz	-	0.396 (0.0253 Hz)	Und.	Und.	65 Hz	0.33 Hz	-
73-76 °C	**0.132-0.128 Ω cm²**	0.364* (0.0306 Hz)	Und.	Und.	56 Hz	0.12 Hz	-	0.520* (0.045Hz)	Und.	Und.	-	0.30 Hz	-

Table C.41 EIS Overview Table showing $Z_{re,\ LF}$, $Z_{re,HF\ minimum}$, $Z_{re,\ LF\ -\ HF\ min}$, $f_{summit,\ MF}$, $f_{summit,\ LF}$, T_{cell}, $R_{s,\ Malis}$, measured above 1.00 A cm^{-2}.

Cell	**Cell Temperature**	**2.00 A cm^{-2}**					**3.00 A cm^{-2}**				
		$Z_{re,LF}$	**$Z_{re,HF}$ min.**	**$Z_{re,\ LF\ -}$ HF min**	**f_{MF} summit**	**f_{LF} summit**	**$Z_{re,LF}$**	**$Z_{re,HF}$ min.**	**$Z_{re,\ LF\ -}$ HF min**	**f_{MF} summit**	**f_{LF} summit**
PSI_s5_2	**57-60 °C**	-	-	-	-	-	0.229 LFIL	Und.	Und.	2094 Hz	22 Hz
	66-68 °C	0.383 LFIL	Und.	Und.	-	2.4 Hz	0.270 (0.0142 Hz) LFIL	Und.	Und.	439 Hz	8 Hz
	73-76 °C	0.411 (0.045 Hz)	Und.	Und.	-	2.4 Hz	0.279 (0.0371 Hz) LFIL	Und.	Und.	588 Hz	7 Hz

Table C.42 Averages of the total cell resistance, $Z_{re,LF}$, from 0.35 A cm^{-2} to 1.00 A cm^{-2} (the linear part of the iV-curves), averages of $Z_{re,HF}$ min up to 1.00 A cm^{-2}, averages of the resistance of the middle and low frequency arcs, $Z_{re,\ LF\ -\ HF\ min}$ from 0.35 A cm^{-2} to 1.00 A cm^{-2} and averages of $\Delta Z_{re,HF\ min\ -\ Rs(Malis)}$ up to 1.00 A cm^{-2}.

Cell	Cell Temperature, T	Average $Z_{re,LF}$ from 0.35 to 1.00 A cm^{-2}	Average $Z_{re,HF\ min.}$ up to 1.00 A cm^{-2}	Average $Z_{re,\ LF\ -\ HF\ min}$ from 0.35 to 1.00 A cm^{-2}	Average $Z_{re,HF\ min\ -\ Rs(Malis)}$ up to 1 A cm^{-2}
Cell 0 EWII reference	**53 °C**	0.357 ± 0.009 Ω cm^2	0.244 ± 0.002 Ω cm^2	0.112 ± 0.009 Ω cm^2	0.085 ± 0.002 Ω cm^2
	61 °C	0.318 ± 0.001 Ω cm^2	0.224 ± 0.001 Ω cm^2	0.095 ± 0.000 Ω cm^2	0.076 ± 0.001 Ω cm^2
	69 °C	0.304 ± 0.002 Ω cm^2	0.210 ± 0.001 Ω cm^2	0.095 ± 0.001 Ω cm^2	0.072 ± 0.001 Ω cm^2
ALIP EWII	**55-56 °C**	0.448 ± 0.025 Ω cm^2	0.261 ± 0.006 Ω cm^2	0.159 ± 0.055 Ω cm^2	0.105 ± 0.006 Ω cm^2
	63 °C	0.315 ± 0.024 Ω cm^2	0.207 ± 0.005 Ω cm^2	0.101 ± 0.036 Ω cm^2	0.062 ± 0.005 Ω cm^2
	70-71 °C	0.413 ± 0.020 Ω cm^2	0.221 ± 0.003 Ω cm^2	0.147 ± 0.055 Ω cm^2	0.085 ± 0.003 Ω cm^2
ATMJ Without IrOx	**56 °C**	0.494 ± 0.018 Ω cm^2	-	-	-
	64 °C	0.360 ± 0.027 Ω cm^2	-	-	-
	70-71 °C	0.394 ± 0.012 Ω cm^2	-	-	-
Pt on Ti felt EWII	**54-55 °C**	0.509 ± 0.092 Ω cm^2	0.245 ± 0.001 Ω cm^2	0.170 ± 0.073 Ω cm^2	0.088 ± 0.001 Ω cm^2
	62 °C	0.333 ± 0.002 Ω cm^2	0.205 ± 0.003 Ω cm^2	0.106 ± 0.038 Ω cm^2	0.058 ± 0.003 Ω cm^2
	69 °C	0.547 ± 0.249 Ω cm^2	0.205 ± 0.004 Ω cm^2	0.157 ± 0.081 Ω cm^2	0.067 ± 0.004 Ω cm^2
PSI_s5_2	**57-60 °C**	0.406 ± 0.026 Ω cm^2	-	-	-
	66-68 °C	0.357 ± 0.034 Ω cm^2	-	-	-
	73-76 °C	0.406 ± 0.100 Ω cm^2	-	-	-

Table C.43 Equivalent capacitances for the high, middle and low frequency arcs normalised by the geometrical electrode area, which is 2.89 cm^2, C_{eff} ($A_{geo.}$), and normalized by ECSA derived from CV measured after initiation given in table 5.1.5.6, $C_{eff}(A_{ECSA})$.

		High Frequency Arc		**Middle Frequency Arc**		**Low Frequency Arc**	
		C_{eff} ($A_{geo.}$) [F cm^{-2}]	**$C_{eff}(A_{ECSA})$ [F cm^{-2}]**	**C_{eff} ($A_{geo.}$) [F cm^{-2}]**	**$C_{eff}(A_{ECSA})$ [F cm^{-2}]**	**C_{eff} ($A_{geo.}$) [F cm^{-2}]**	**$C_{eff}(A_{ECSA})$ [F cm^{-2}]**
EWII benchmark (ALIO)	**0.35 A cm^{-2}**	$1.8 \cdot 10^{-6}$	$1.7 \cdot 10^{-9}$	$3.05 \cdot 10^{-2}$	$2.90 \cdot 10^{-5}$	238.8	$2.3 \cdot 10^{-1}$
	0.69 A cm^{-2}	$1.5 \cdot 10^{-6}$	$1.5 \cdot 10^{-9}$	$3.56 \cdot 10^{-2}$	$3.38 \cdot 10^{-5}$	22.5	$2 \cdot 10^{-2}$
	1.00 A cm^{-2}	$2.0 \cdot 10^{-6}$	$1.9 \cdot 10^{-9}$	$2.81 \cdot 10^{-2}$	$2.67 \cdot 10^{-5}$	6.8	$1 \cdot 10^{-2}$
EWII benchmark (ALIP)	**0.35 A cm^{-2}**	$1.21 \cdot 10^{-5}$	$1.2 \cdot 10^{-8}$	$4.19 \cdot 10^{-2}$	$3.98 \cdot 10^{-5}$	119.1	$1.1 \cdot 10^{-1}$
	0.69 A cm^{-2}	$9.9 \cdot 10^{-6}$	$9.4 \cdot 10^{-9}$	$3.75 \cdot 10^{-2}$	$3.56 \cdot 10^{-5}$	56.5	$5 \cdot 10^{-2}$
	1.00 A cm^{-2}	$9.8 \cdot 10^{-6}$	$9.3 \cdot 10^{-9}$	$2.49 \cdot 10^{-2}$	$2.37 \cdot 10^{-5}$	37.2	$4 \cdot 10^{-2}$
EWII with-out IrOx (ATMJ)	**0.35 A cm^{-2}**	$5.6 \cdot 10^{-6}$	$5.7 \cdot 10^{-9}$	$6.0 \cdot 10^{-3}$	$6.2 \cdot 10^{-6}$	204.2	$2.1 \cdot 10^{-1}$
	0.69 A cm^{-2}	$5.3 \cdot 10^{-6}$	$5.4 \cdot 10^{-9}$	$2.7 \cdot 10^{-3}$	$2.7 \cdot 10^{-6}$	28.6	$3 \cdot 10^{-2}$
	1.00 A cm^{-2}	$4.7 \cdot 10^{-6}$	$4.8 \cdot 10^{-9}$	$1.6 \cdot 10^{-3}$	$1.7 \cdot 10^{-6}$	7.8	$1 \cdot 10^{-2}$
PSI benchmark, PSI_s5_2	**0.35 A cm^{-2}**	$9.9 \cdot 10^{-6}$	$3.5 \cdot 10^{-9}$	$2.19 \cdot 10^{-2}$	$7.7 \cdot 10^{-6}$	385.4	$1.4 \cdot 10^{-1}$
	0.69 A cm^{-2}	$9.3 \cdot 10^{-6}$	$3.3 \cdot 10^{-9}$	$1.41 \cdot 10^{-2}$	$5.0 \cdot 10^{-6}$	51.1	$2 \cdot 10^{-2}$
	1.00 A cm^{-2}	$9.6 \cdot 10^{-6}$	$3.4 \cdot 10^{-9}$	$1.17 \cdot 10^{-2}$	$4.1 \cdot 10^{-6}$	6.2	0.00

Table C.44 Overview of charges calculated from the unnormalised equivalent capacitances for the high, middle and low frequency arcs. The charges have been calculated from the AC potential, $Q(E_{AC})$.

		High Frequency Arc	**Middle Frequency Arc**	**Low Frequency Arc**
		$Q(E_{AC})$ [C]	**$Q(E_{AC})$ [C]**	**$Q(E_{AC})$ [C]**
EWII benchmark (ALIO)	**0.35 A cm^{-2}**	$9.37 \cdot 10^{-6}$	$1.20 \cdot 10^{-3}$	$8.90 \cdot 10^{-2}$ $2.88 \cdot 10^{-2}$
	0.69 A cm^{-2}	$9.44 \cdot 10^{-6}$	$9.33 \cdot 10^{-4}$	$1.65 \cdot 10^{-2}$
	1.00 A cm^{-2}	$9.87 \cdot 10^{-6}$	$8.26 \cdot 10^{-4}$	
EWII benchmark (ALIP)	**0.35 A cm^{-2}**	$2.48 \cdot 10^{-5}$	$2.04 \cdot 10^{-3}$	$9.86 \cdot 10^{-2}$
	0.69 A cm^{-2}	$2.18 \cdot 10^{-5}$	$1.57 \cdot 10^{-3}$	$5.62 \cdot 10^{-2}$
	1.00 A cm^{-2}	$2.01 \cdot 10^{-5}$	$1.35 \cdot 10^{-3}$	$3.61 \cdot 10^{-2}$
EWII without IrOx (ATMJ)	**0.35 A cm^{-2}**	$1.67 \cdot 10^{-5}$	$9.54 \cdot 10^{-4}$	$9.08 \cdot 10^{-2}$
	0.69 A cm^{-2}	$1.56 \cdot 10^{-5}$	$5.22 \cdot 10^{-4}$	$3.58 \cdot 10^{-2}$
	1.00 A cm^{-2}	$1.47 \cdot 10^{-5}$	$3.67 \cdot 10^{-4}$	$2.19 \cdot 10^{-2}$
PSI benchmark, PSI_s5_2	**0.35 A cm^{-2}**	$2.01 \cdot 10^{-5}$	$1.63 \cdot 10^{-3}$	$1.56 \cdot 10^{-1}$
	0.69 A cm^{-2}	$1.91 \cdot 10^{-5}$	$1.18 \cdot 10^{-3}$	$6.66 \cdot 10^{-2}$
	1.00 A cm^{-2}	$1.90 \cdot 10^{-5}$	$1.15 \cdot 10^{-3}$	$2.85 \cdot 10^{-2}$

D. EIS Spectrum with Outlier

In figure D.72 the EIS spectrum measured on the reference EWII benchmark cell, cell 0, at 61 °C is shown with outlier, which is seen at low Z_{re}-values. A Kramers-Kronig plot of the data is shown together with the EIS spectrum, and show high relative residuals at low frequencies due to the outlier. In the thesis this EIS spectrum is shown without the outlier.

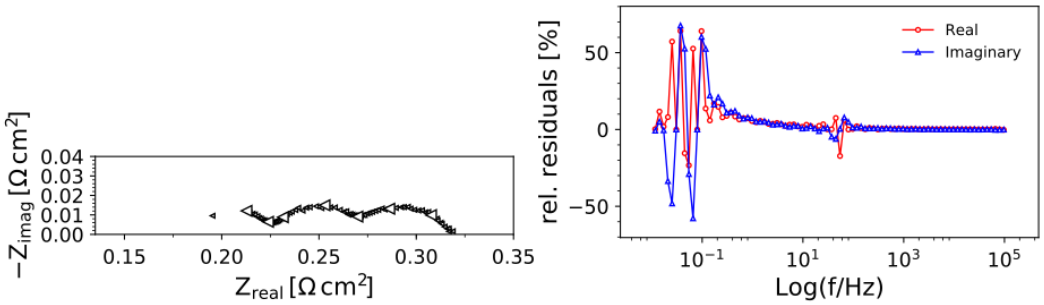

Figure D.72 EIS measured at 61 °C and at 1.00 A cm^{-2} on the reference EWII benchmark cell, cell 0, shown together with Kramers-Kronig residuals of the EIS shown in the Nyquist plot. All frequencies are shown.

E. Fit of iV-curves

E.1 Reference EWII Benchmark Cell, cell 0

Figure E.1.73 shows iV-curves measured at 53 °C on the reference EWII benchmark cell, cell 0, before and after EIS measurements (blue dots) and Tafel plots of E_{Tafel} for the two iV-curves. The Tafel parameters, a and b, are determined as described in section 5.3.1. Figure E.1.74 shows iV-curves measured at 69 °C on the reference EWII benchmark cell, cell 0, before and after EIS measurements (blue dots) and Tafel plots of E_{Tafel} for the two iV-curves.

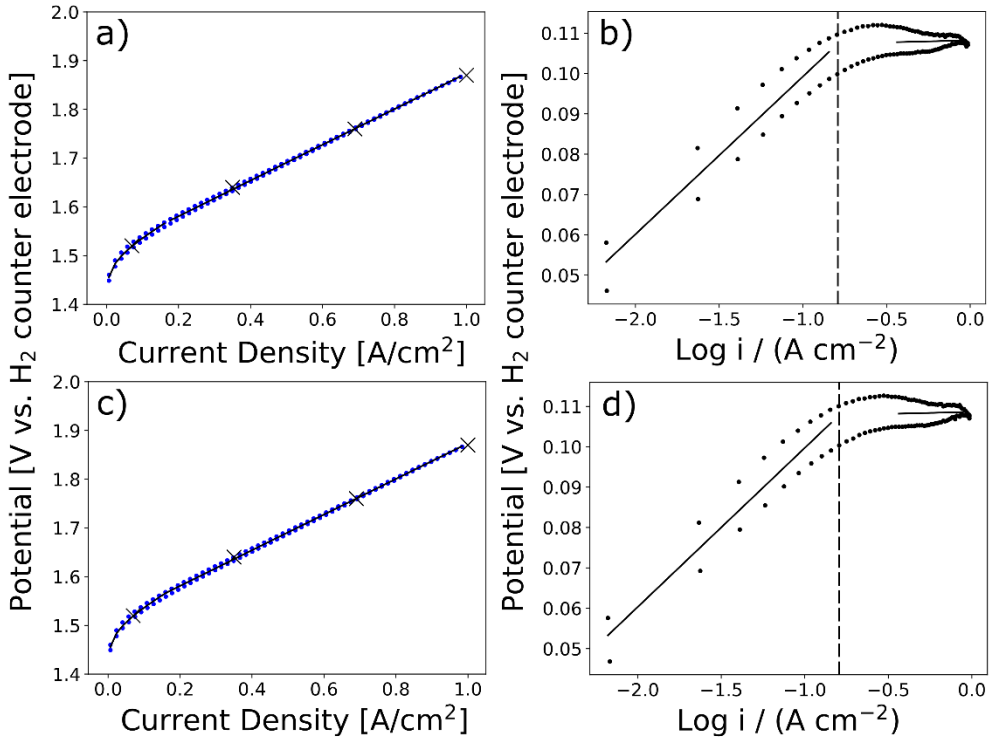

Figure E.1.73 iV-curve measured at 53 °C, before EIS measurements on the reference EWII benchmark cell, cell 0, shown with fit to the model $E(i) = E_{onset} + E_{ohmic}(i) + E_{Tafel}(i) = E_{Onset} + R_{ohmic} \cdot i + a + b \cdot log(i)$ *(a).* $E_{Onset} = 1.4$ *and* R_{ohmic} *was set to the slope of the iV-curve in the linear region at current densities above 0.35 A cm^{-2}. The Tafel parameters were determined from linear regression of the Tafel plot of* E_{Tafel}*, shown in (b). Two regions with different Tafel parameter were distinguished, and linear regression of the Tafel plot was made at the current density range 0.0173 – 0.15 A cm^{-2} and at 0.35-0.9 A cm^{-2}. (c) shows iV-curve with fit measured at 53 °C after EIS measurements on the same reference EWII benchmark cell, cell 0, and (d) shows Tafel plot of* E_{Tafel} *from the iV-curve shown in (d). Tafel parameters for the low and high current density region of the two iV-curves can be found in table 5.3.1.17. (i,E) measured during the EIS measurements are shown together with the iV-curves with fits as big black crosses.*

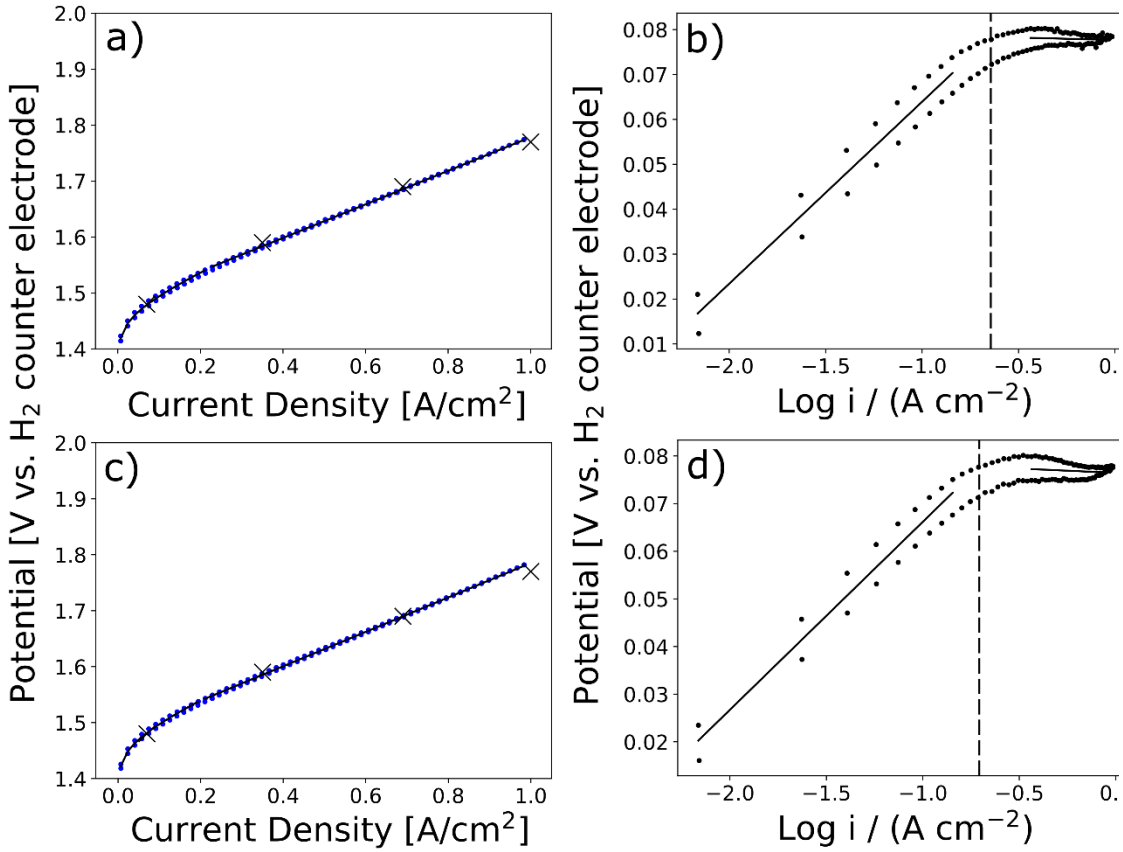

Figure E.1.74 iV-curve measured at 69 °C, before EIS measurements on the reference EWII benchmark cell, cell 0, shown with fit to the model $E(i) = E_{onset} + E_{ohmic}(i) + E_{Tafel}(i) = E_{Onset} + R_{ohmic} \cdot i + a + b \cdot log(i)$ *(a).* $E_{Onset} = 1.4$ *and* R_{ohmic} *was set to the slope of the iV-curve in the linear region at current densities above 0.35 A cm^{-2}. The Tafel parameters were determined from linear regression of the Tafel plot of* E_{Tafel}*, shown in (b). Two regions with different Tafel parameter were distinguished, and linear regression of the Tafel plot was made at the current density range 0.0173 – 0.15 A cm^{-2} and at 0.35-0.9 A cm^{-2}. (c) shows iV-curve with fit measured at 69 °C after EIS measurements on the same reference EWII benchmark cell, cell 0, and (d) shows Tafel plot of* E_{Tafel} *from the iV-curve shown in (d). Tafel parameters for the low and high current density region of the two iV-curves can be found in table 5.3.1.17. (i,E) measured during the EIS measurements are shown together with the iV-curves with fits as big black crosses.*

E.2 EWII Benchmark Cell, ALIP

Figure E.2.75, E.2.76 and E.2.77 show iV-curves measured at 55-56, 63 and 70-71 °C, respectively, on the EWII benchmark cell, ALIP, before and after EIS measurements (blue dots) and Tafel plots of E_{Tafel} for the iV-curves. The Tafel parameters, a and b, are determined as described in section 5.3.1.

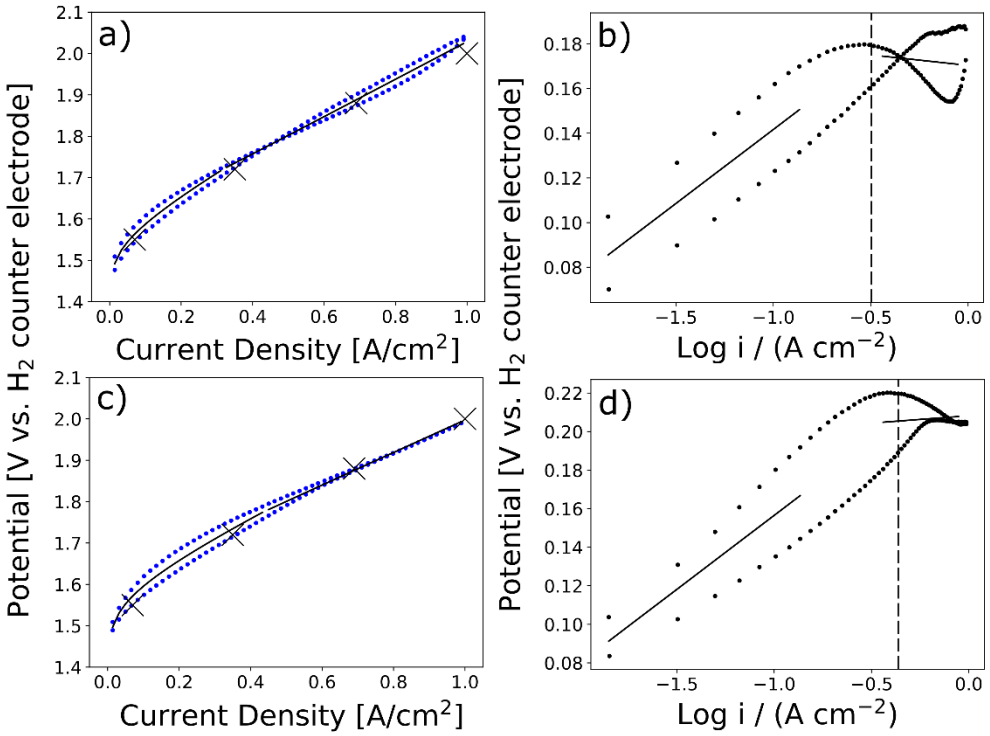

Figure E.2.75 iV-curve measured at 55-56 °C, before EIS measurements on the EWII benchmark cell, ALIP, shown with fit to the model $E(i) = E_{onset} + E_{ohmic}(i) + E_{Tafel}(i) = E_{Onset} + R_{ohmic} \cdot i + a + b \cdot log(i)$ *(a).* $E_{Onset} = 1.4$ *and* R_{ohmic} *was set to the slope of the iV-curve in the linear region at current densities above 0.35 A cm^{-2}. The Tafel parameters were determined from linear regression of the Tafel plot of* E_{Tafel}*, shown in (b). Two regions with different Tafel parameter were distinguished, and linear regression of the Tafel plot was made at the current density range 0.0173 – 0.15 A cm^{-2} and at 0.35-0.9 A cm^{-2}. (c) shows iV-curve with fit measured at 55-56 °C after EIS measurements on the same EWII benchmark cell, ALIP, and (d) shows Tafel plot of* E_{Tafel} *from the iV-curve shown in (d). Tafel parameters for the low and high current density region of the two iV-curves can be found in table 5.3.1.17. (i,E) measured during the EIS measurements are shown together with the iV-curves with fits as big black crosses.*

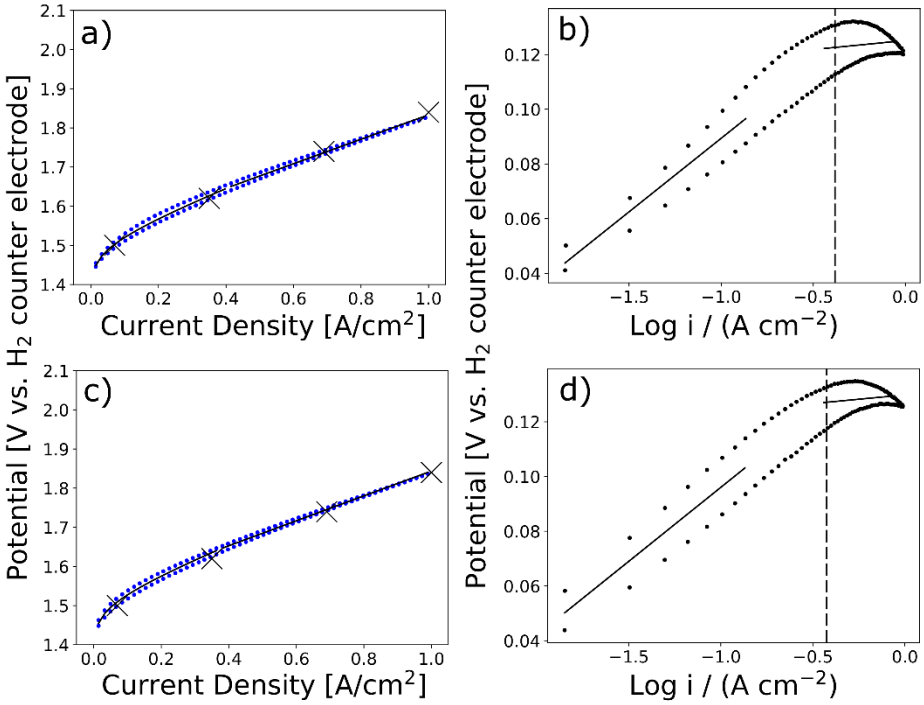

Figure E.2.76 iV-curve measured at 63 °C, before EIS measurements on the EWII benchmark cell, ALIP, shown with fit to the model $E(i) = E_{onset} + E_{ohmic}(i) + E_{Tafel}(i) = E_{Onset} + R_{ohmic} \cdot i + a + b \cdot log(i)$ *(a).* $E_{Onset} = 1.4$ *and* R_{ohmic} *was set to the slope of the iV-curve in the linear region at current densities above 0.35 A cm^{-2}. The Tafel parameters were determined from linear regression of the Tafel plot of E_{Tafel}, shown in (b). Two regions with different Tafel parameter were distinguished, and linear regression of the Tafel plot was made at the current density range 0.0173 – 0.15 A cm^{-2} and at 0.35-0.9 A cm^{-2}. (c) shows iV-curve with fit measured at 55-56 °C after EIS measurements on the same EWII benchmark cell, ALIP, and (d) shows Tafel plot of E_{Tafel} from the iV-curve shown in (d). Tafel parameters for the low and high current density region of the two iV-curves can be found in table 5.3.1.17. (i,E) measured during the EIS measurements are shown together with the iV-curves with fits as big black crosses.*

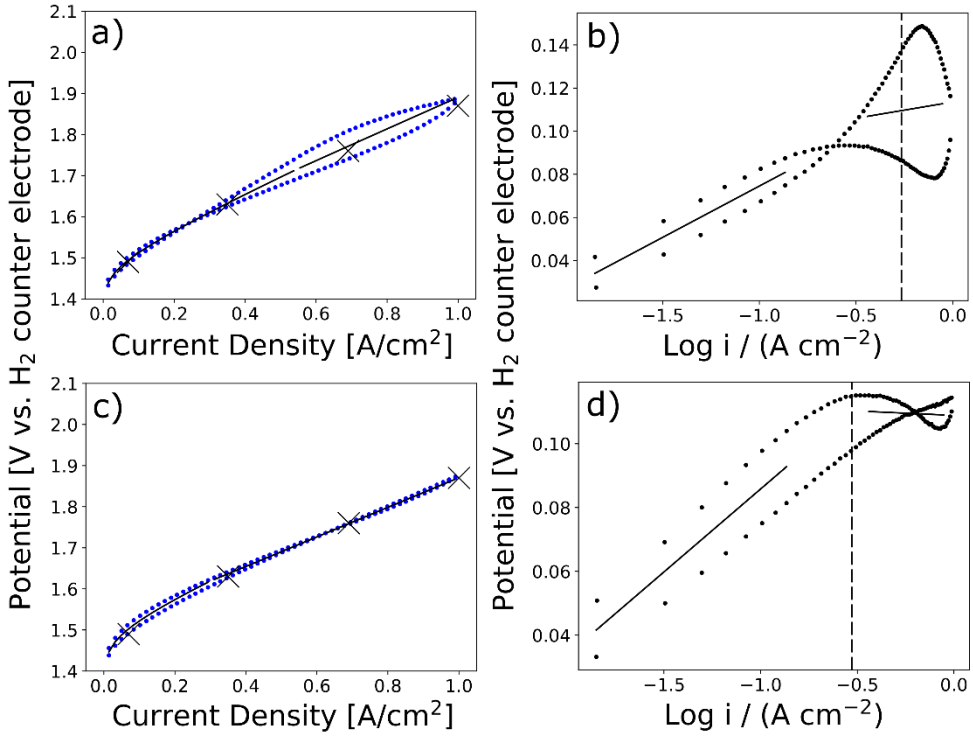

Figure E.2.77 iV-curve measured at 70-71 °C, before EIS measurements on the EWII benchmark cell, ALIP, shown with fit to the model $E(i) = E_{onset} + E_{ohmic}(i) + E_{Tafel}(i) = E_{Onset} + R_{ohmic} \cdot i + a + b \cdot log(i)$ *(a).* $E_{Onset} = 1.4$ *and* R_{ohmic} *was set to the slope of the iV-curve in the linear region at current densities above 0.35 A cm^{-2}. The Tafel parameters were determined from linear regression of the Tafel plot of* E_{Tafel}*, shown in (b). Two regions with different Tafel parameter were distinguished, and linear regression of the Tafel plot was made at the current density range 0.0173 – 0.15 A cm^{-2} and at 0.35-0.9 A cm^{-2}. (c) shows iV-curve with fit measured at 55-56 °C after EIS measurements on the same EWII benchmark cell, ALIP, and (d) shows Tafel plot of* E_{Tafel} *from the iV-curve shown in (d). Tafel parameters for the low and high current density region of the two iV-curves can be found in table 5.3.1.17. (i,E) measured during the EIS measurements are shown together with the iV-curves with fits as big black crosses.*

E.3 EWII Cell without IrO_x, ATMJ.

Figure E.3.78 and E.3.79 show iV-curves measured at 56 and 70-71 °C, respectively, on the EWII cell without IrO_x layer, ATMJ, before and after EIS measurements (blue dots) and Tafel plots of E_{Tafel} for the iV-curves. The Tafel parameters, a and b, are determined as described in section 5.3.1.

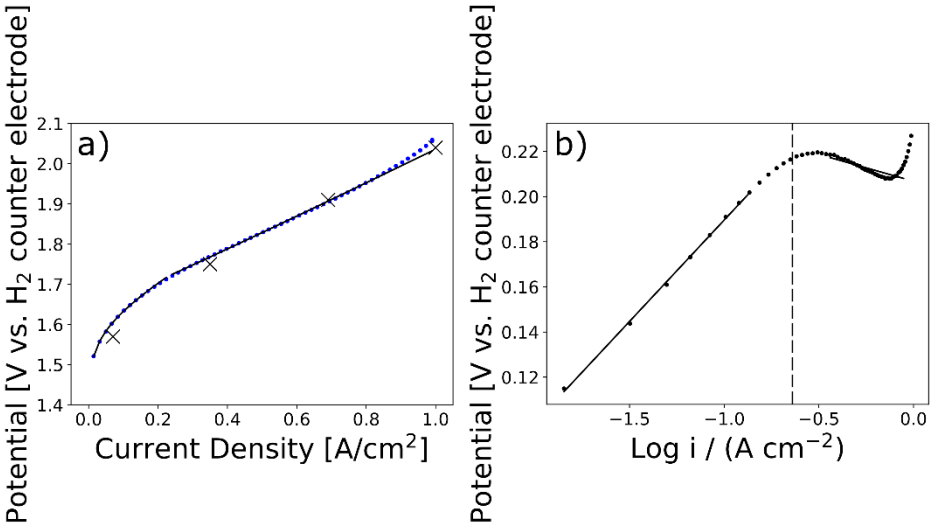

Figure E.3.78 iV-curve measured at 56 °C, before EIS measurements on the EWII cell without IrO_x, ATMJ, shown with fit to the model $E(i) = E_{onset} + E_{ohmic}(i) + E_{Tafel}(i) = E_{Onset} + R_{ohmic} \cdot i + a + b \cdot log(i)$ (a). $E_{Onset} = 1.4$ and R_{ohmic} was set to the slope of the iV-curve in the linear region at current densities above 0.35 A cm^{-2}. The Tafel parameters were determined from linear regression of the Tafel plot of E_{Tafel}, shown in (b). Two regions with different Tafel parameters were distinguished, and linear regression of the Tafel plot was made at the current density range 0.0173 – 0.15 A cm^{-2} and at 0.35-0.9 A cm^{-2}. (c) shows iV-curve with fit measured at 56 °C after EIS measurements on the same EWII cell without IrO_x, ATMJ, and (d) shows Tafel plot of E_{Tafel} from the iV-curve shown in (d). Tafel parameters for the low and high current density region of the two iV-curves can be found in table 5.3.1.17. (i,E) measured during the EIS measurements are shown together with the iV-curves with fits as big black crosses.

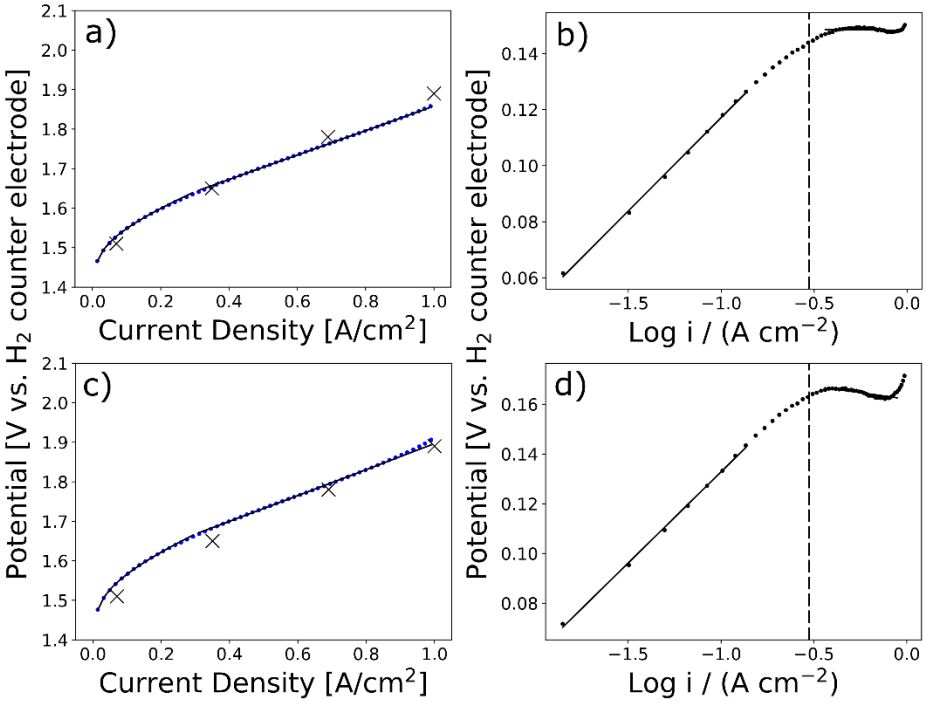

Figure E.3.79 iV-curve measured at 70-71 °C, before EIS measurements on the EWII cell without IrO_x, ATMJ, shown with fit to the model $E(i) = E_{onset} + E_{ohmic}(i) + E_{Tafel}(i) = E_{Onset} + R_{ohmic} \cdot i + a + b \cdot log(i)$ (a). $E_{Onset} = 1.4$ and R_{ohmic} was set to the slope of the iV-curve in the linear region at current densities above 0.35 A cm^{-2}. The Tafel parameters were determined from linear regression of the Tafel plot of E_{Tafel}, shown in (b). Two regions with different Tafel parameters were distinguished, and linear regression of the Tafel plot was made at the current density range 0.0173 – 0.15 A cm^{-2} and at 0.35-0.9 A cm^{-2}. (c) shows iV-curve with fit measured at 70-71 °C after EIS measurements on the same EWII cell without IrO_x, ATMJ, and (d) shows Tafel plot of E_{Tafel} from the iV-curve shown in (d). Tafel parameters for the low and high current density region of the two iV-curves can be found in table 5.3.1.17. (i,E) measured during the EIS measurements are shown together with the iV-curves with fits as big black crosses.

E.4 PSI Benchmark Cell, PSI_s5_2.

Figure E.4.80 and E.45.3.1.81 show iV-curves measured at 57-60 and 73-76 °C, respectively, on the PSI benchmark cell, PSI_s5_2, before and after EIS measurements (blue dots) and Tafel plots of E_{Tafel} for the iV-curves. The Tafel parameters, a and b, are determined as described in section 5.3.1. Only the part of the iV-curve, where the temperature is stable (below 1 A cm^{-2}) is shown in the figures. The same fit shown on the full iV-curves measured up to 3 A cm^{-2} are shown in figure E.4.82, E.4.83 and E.4.84.

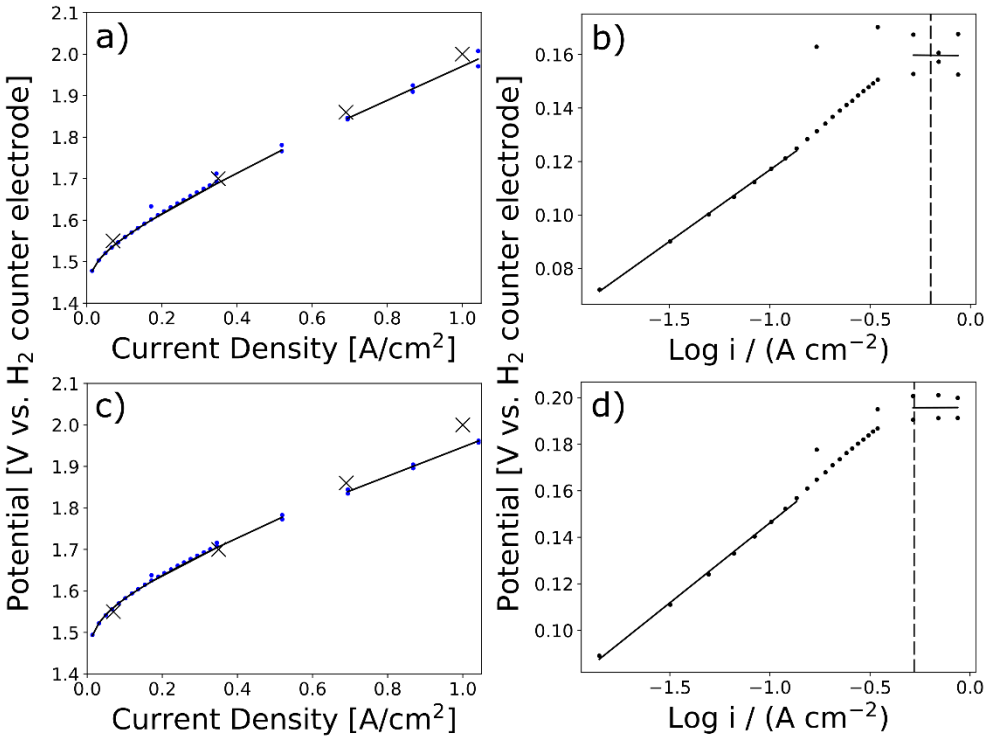

Figure E.4.80 iV-curve measured at 57-60 °C, before EIS measurements on the PSI benchmark cell, PSI_s5_2, shown with fit to the model $E(i) = E_{onset} + E_{ohmic}(i) + E_{Tafel}(i) = E_{Onset} + R_{ohmic} \cdot i + a + b \cdot log(i)$ *(a).* $E_{Onset} = 1.4$ *and* R_{ohmic} *was set to the slope of the iV-curve in the linear region at current densities above 0.35 A cm^{-2}. The Tafel parameters were determined from linear regression of the Tafel plot of* E_{Tafel}*, shown in (b). Two regions with different Tafel parameters were distinguished, and linear regression of the Tafel plot was made at the current density range 0.0173 – 0.15 A cm^{-2} and at 0.35-0.9 A cm^{-2}. (c) shows iV-curve with fit measured at 57-60 °C after EIS measurements on the same PSI benchmark cell, PSI_s5_2, and (d) shows Tafel plot of* E_{Tafel} *from the iV-curve shown in (d). Tafel parameters for the low and high current density region of the two iV-curves can be found in table 5.3.1.17. (i,E) measured during the EIS measurements are shown together with the iV-curves with fits as big black crosses.*

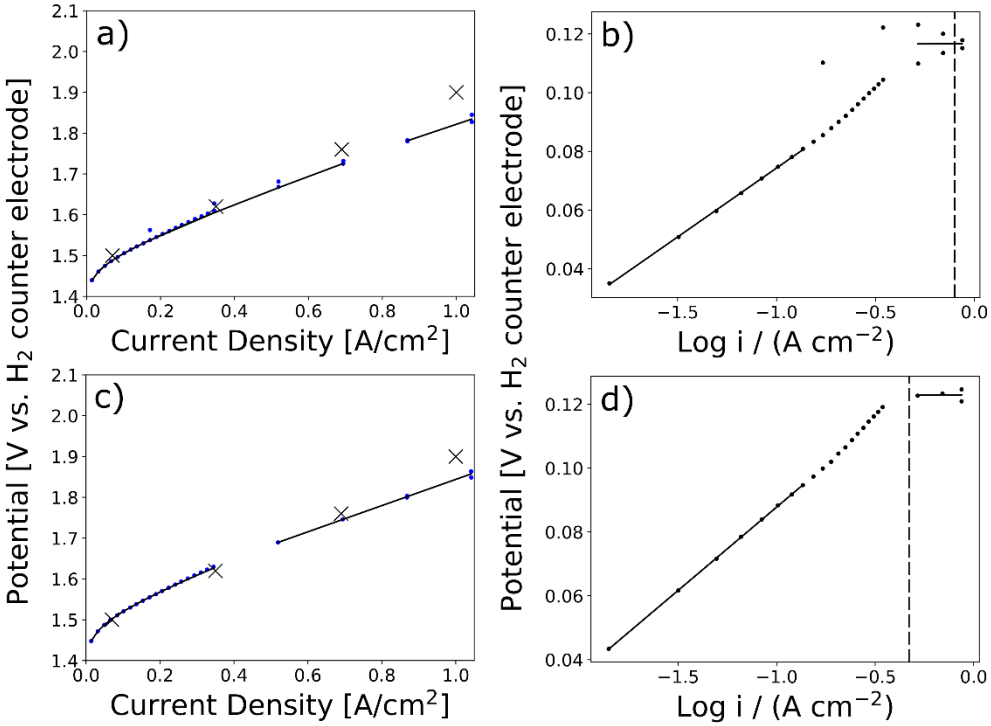

Figure E.45.3.1.81 iV-curve measured at 73-76 °C, before EIS measurements on the PSI benchmark cell, PSI_s5_2, shown with fit to the model $E(i) = E_{onset} + E_{ohmic}(i) + E_{Tafel}(i) = E_{Onset} + R_{ohmic} \cdot i + a + b \cdot log(i)$ *(a).* $E_{Onset} = 1.4$ *and* R_{ohmic} *was set to the slope of the iV-curve in the linear region at current densities above 0.35 A cm^{-2}. The Tafel parameters were determined from linear regression of the Tafel plot of E_{Tafel}, shown in (b). Two regions with different Tafel parameters were distinguished, and linear regression of the Tafel plot was made at the current density range 0.0173 – 0.15 A cm^{-2} and at 0.35-0.9 A cm^{-2}. (c) shows iV-curve with fit measured at 73-76 °C after EIS measurements on the same PSI benchmark cell, PSI_s5_2, and (d) shows Tafel plot of E_{Tafel} from the iV-curve shown in (d). Tafel parameters for the low and high current density region of the two iV-curves can be found in table 5.3.1.17. (i,E) measured during the EIS measurements are shown together with the iV-curves with fits as big black crosses.*

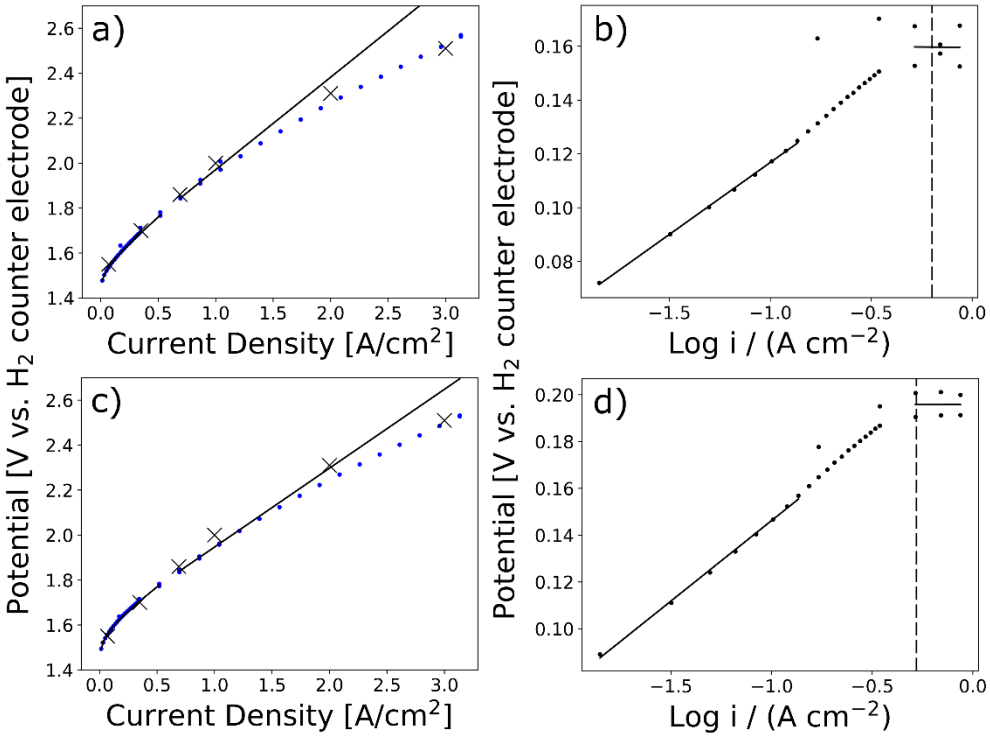

Figure E.4.82 iV-curve measured at 57-60 °C, before EIS measurements on the PSI benchmark cell, PSI_s5_2, shown with fit to the model $E(i) = E_{onset} + E_{ohmic}(i) + E_{Tafel}(i) = E_{Onset} + R_{ohmic} \cdot i + a + b \cdot log(i)$ *(a).* $E_{onset} = 1.4$ *and* R_{ohmic} *was set to the slope of the iV-curve in the linear region at current densities above 0.35 A cm^{-2}. The Tafel parameters were determined from linear regression of the Tafel plot of E_{Tafel}, shown in (b). Two regions with different Tafel parameters were distinguished, and linear regression of the Tafel plot was made at the current density range 0.0173 – 0.15 A cm^{-2} and at 0.35-0.9 A cm^{-2}. (c) shows iV-curve with fit measured at 57-60 °C after EIS measurements on the same PSI benchmark cell, PSI_s5_2, and (d) shows Tafel plot of E_{Tafel} from the iV-curve shown in (d). Tafel parameters for the low and high current density region of the two iV-curves can be found in table 5.3.1.17. (i,E) measured during the EIS measurements are shown together with the iV-curves with fits as big black crosses.*

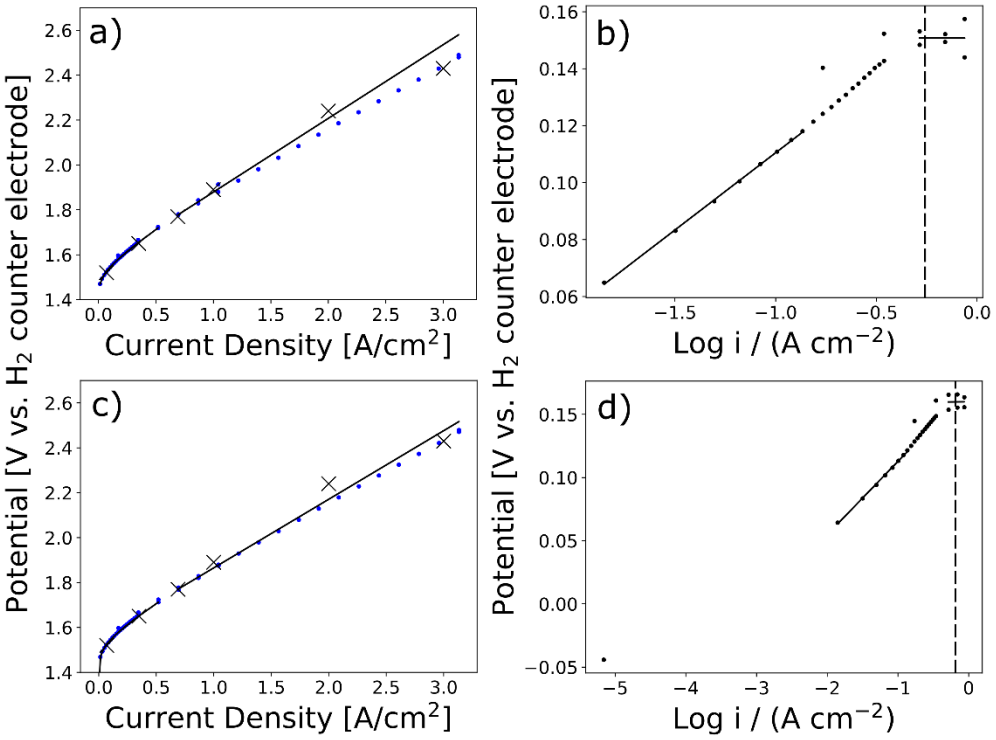

Figure E.4.83 iV-curve measured at 66-68 °C, before EIS measurements on the PSI benchmark cell, PSI_s5_2, shown with fit to the model $E(i) = E_{onset} + E_{ohmic}(i) + E_{Tafel}(i) = E_{Onset} + R_{ohmic} \cdot i + a + b \cdot log(i)$ *(a).* $E_{Onset} = 1.4$ *and* R_{ohmic} *was set to the slope of the iV-curve in the linear region at current densities above 0.35 A cm^{-2}. The Tafel parameters were determined from linear regression of the Tafel plot of* E_{Tafel}*, shown in (b). Two regions with different Tafel parameters were distinguished, and linear regression of the Tafel plot was made at the current density range 0.0173 – 0.15 A cm^{-2} and at 0.35-0.9 A cm^{-2}. (c) shows iV-curve with fit measured at 66-68 °C after EIS measurements on the same PSI benchmark cell, PSI_s5_2, and (d) shows Tafel plot of* E_{Tafel} *from the iV-curve shown in (d). Tafel parameters for the low and high current density region of the two iV-curves can be found in table 5.3.1.17. (i,E) measured during the EIS measurements are shown together with the iV-curves with fits as big black crosses.*

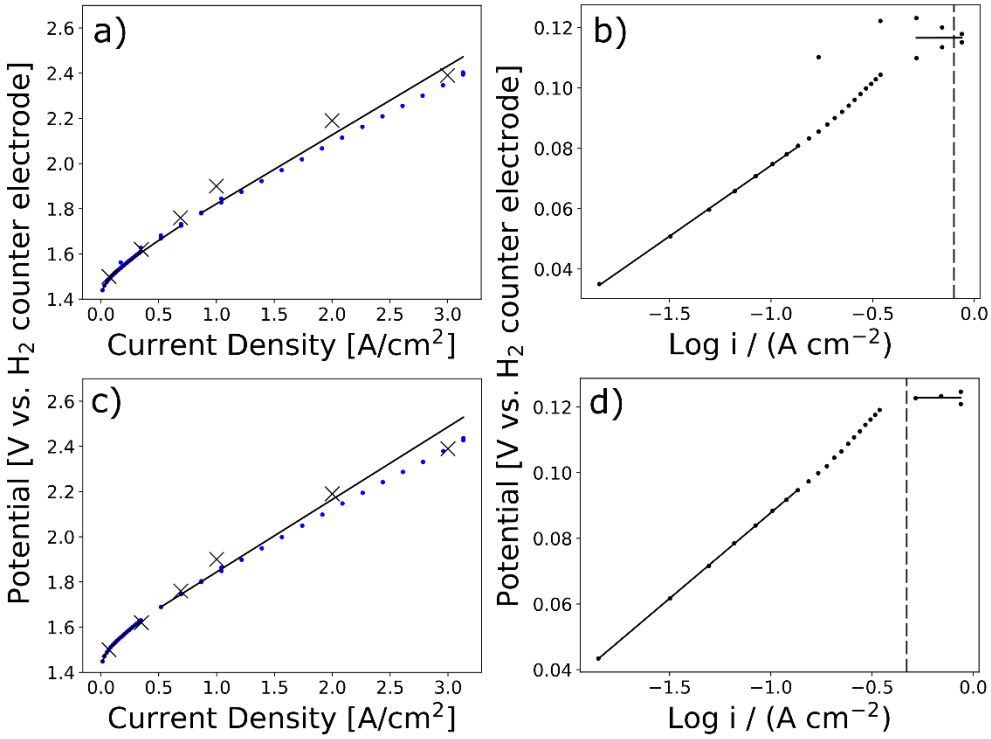

Figure E.4.84 iV-curve measured at 73-76 °C, before EIS measurements on the PSI benchmark cell, PSI_s5_2, shown with fit to the model $E(i) = E_{onset} + E_{ohmic}(i) + E_{Tafel}(i) = E_{Onset} + R_{ohmic} \cdot i + a + b \cdot log(i)$ *(a).* $E_{onset} = 1.4$ *and* R_{ohmic} *was set to the slope of the iV-curve in the linear region at current densities above 0.35 A cm^{-2}. The Tafel parameters were determined from linear regression of the Tafel plot of* E_{Tafel}*, shown in (b). Two regions with different Tafel parameters were distinguished, and linear regression of the Tafel plot was made at the current density range 0.0173 – 0.15 A cm^{-2} and at 0.35-0.9 A cm^{-2}. (c) shows iV-curve with fit measured at 73-76 °C after EIS measurements on the same PSI benchmark cell, PSI_s5_2, and (d) shows Tafel plot of* E_{Tafel} *from the iV-curve shown in (d). Tafel parameters for the low and high current density region of the two iV-curves can be found in table 5.3.1.17. (i,E) measured during the EIS measurements are shown together with the iV-curves with fits as big black crosses.*

F. EIS Measured on the PSI Benchmark Cells

In figure F.85 is Nyquist plots of EIS measured on the PSI benchmark cell, PSI_s5_3, shown. Figure F.86 depicts Nyquist plots of EIS measured on another PSI benchmark cell, PSI_s5, and figure F.87 show Nyquist plots of EIS measured on a PSI cell with half anode catalyst loading. It shall be noted that the trend of the arcs with changes in temperature and current density are the same.

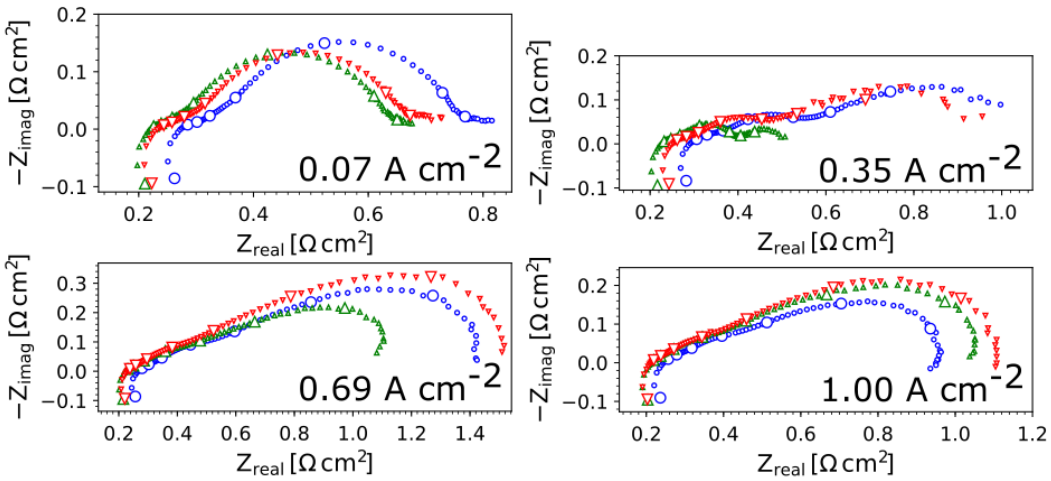

Figure F.85 EIS measured at 58 °C (blue circles), 66 °C (green triangles) and 74 °C (red triangles) and at 0.07, 0.35, 0.69 and 1.00 A cm^{-2} on PSI benchmark cell, PSI_s5_3.

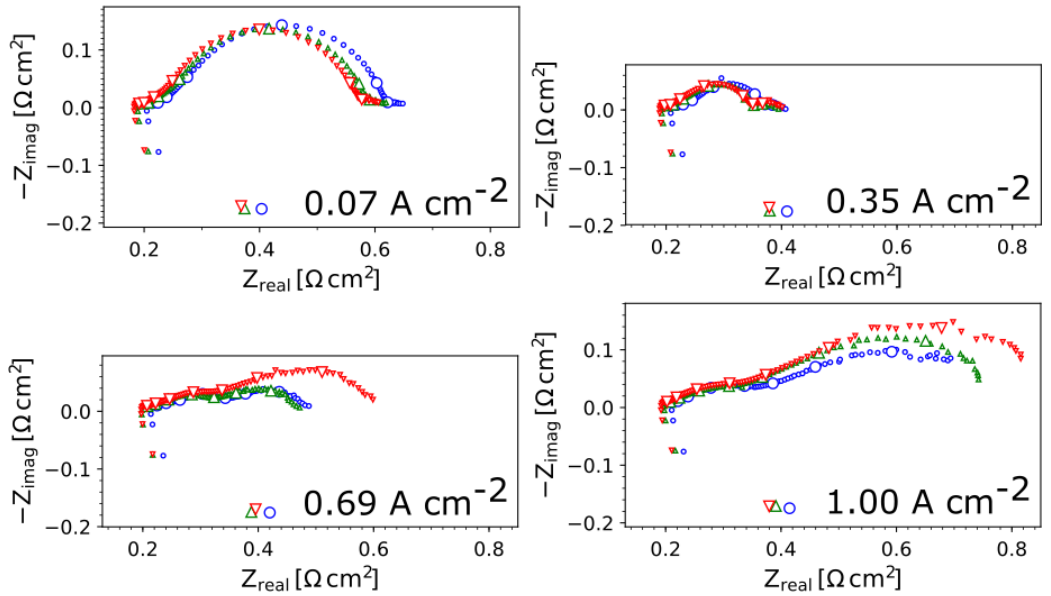

Figure F.86 EIS measured at 60 °C (blue circles), 70 °C (green triangles) and 80 °C (red triangles) and at 0.07, 0.35, 0.69 and 1.00 A cm^{-2} on PSI benchmark cell, PSI_s5.

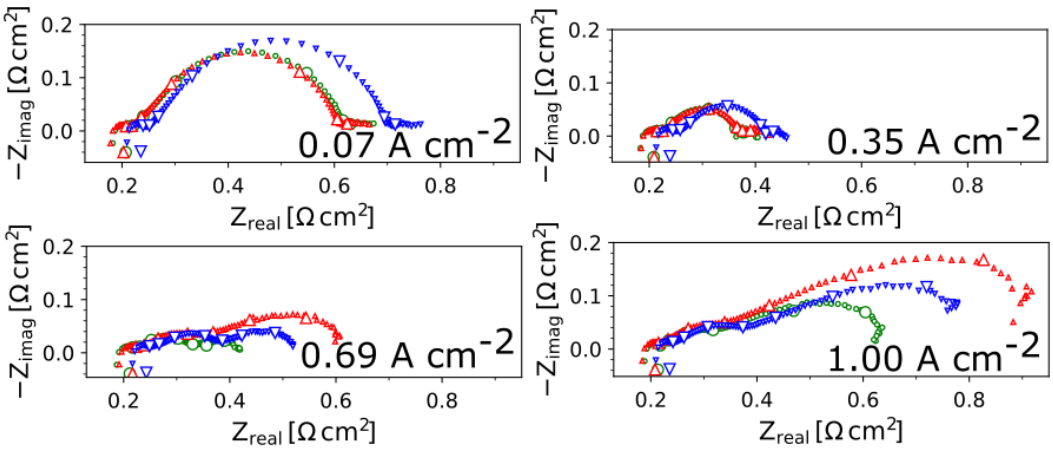

Figure F.87 EIS measured at 60 °C (blue circles), 70 °C (green triangles) and 80 °C (red triangles) and at 0.07, 0.35, 0.69 and 1.00 A cm^{-2} on PSI cell with half anode loading, PSI_s4_2.

G. Articles

Article 1

Electrochemical Characterization of a PEMEC Using Impedance Spectroscopy

K. Elsøe,[a,z] L. Grahl-Madsen,[b] G. G. Scherer,[c] J. Hjelm,[a,*] and M. B. Mogensen[a,]**

[a]*Department of Energy Conversion and Storage, Technical University of Denmark, 4000 Roskilde, Denmark*
[b]*EWII Fuel Cells A/S, 5220 Odense SE, Denmark*
[c]*5232 Hägglingen, Switzerland*

In this study, electrochemical impedance spectroscopy (EIS) is applied in combination with cyclic voltammetry (CV) and current density – cell voltage curves (iV-curves) to investigate the processes contributing to the total impedance of a polymer electrolyte membrane electrolysis cell (PEMEC). iV-curves were linear above 0.35 A cm^{-2} implying ohmic processes to be performance limiting, however the impedance spectra showed three arcs indicating three electrochemical reactions at these conditions not to be purely ohmic, but also to have capacitive properties. A hypothesis that the composite IrO_x/Nafion anode catalyst layer causes two of these arcs with a constant sum of resistance and current constrictions cause the third arc, is suggested. This hypothesis implies that the total differential cell resistance at current densities above 0.35 A cm^{-2} is purely ascribed to protonic resistance in Nafion in this type of PEMEC.
 [DOI: 10.1149/2.0651713jes]

Manuscript submitted May 11, 2017; revised manuscript received September 25, 2017. Published October 11, 2017.

The interest in renewable electrical energy obtained from e.g. wind turbines and solar cells have increased over the past years. However, the demand of electrical energy from society does not always correlate with the renewable electrical energy production, and a method to store the excess electrical energy for later use is needed. One such method is electrolysis of water into hydrogen and thus converts electrical energy into chemical energy bound in the hydrogen molecules, and thereby the energy can be stored. PEMECs have the ability to operate at high current densities, which reduces the operation costs.[1] The highest possible operation current density for a PEMEC at a given potential is i.a. depending on its internal resistance, i.e. a cell resistance as low as possible is preferred. The total cell resistance is given by the iV-curve, but multiple processes within the PEMEC may contribute to this. In order to resolve these processes, EIS should be applied, as this can resolve the time constants of the single processes.[2] It should be noted that the total cell resistance measured by EIS for a given point (i,V) is equal to the slope of the iV-curve in this point in case of steady state conditions. It should further be noted that a single EIS spectrum cannot be interpreted on its own, but has to be combined with either substantial pre-knowledge of the system, or with a series of experiments in which relevant physical and chemical parameters are varied systematically.[3] Furthermore, EIS has to be complemented by other methods; measurements of iV-curves and CV are such methods.

Within PEMEC research, EIS is so far primarily applied to determine the electrolyte resistance, which is frequently used for ohmic drop corrections of iV-curves.[4–12] However, some research groups such as Rozain et al.,[13,14] Lettenmeier et al.[15] and Siracusano et al.[5,16] among others have studied EIS of PEMECs in further detail, but most often at low current densities in the activation region of the iV-curve, where the oxygen evolution reaction (OER) current density is very low.[5–8,13,14,16,17] Only a few research groups have reported EIS measured at higher current densities in the linear region of the iV-curve during the OER.[6–8] The EIS data is often fitted to an empirical equivalent circuit consisting of a serial resistance and one or two arcs reported to originate from the anode, or from the cathode and the anode. Sometimes diffusion elements are added to the equivalent circuit as well.[7–8,14–16] Detailed impedance studies of the PEMEC anode catalyst material, IrO_x, by the application of model electrodes are also found in literature, e.g. as reported by Papaderakis et al.[4]

The work in this article is a technological unravelling investigating performance limitation in PEMECs operating at high current densities. It presents a hypothesis suggesting, which physical processes that are primarily contributing to the total cell impedance of a PEMEC based on findings from EIS measurements at various temperatures and current densities in combination with CV, iV-curves and scanning electron microscopy (SEM). The suggested hypothesis deviates from equivalent circuits reported in the literature so far.

Experimental

Materials and setup.—The PEMECs examined in this study are benchmark PEMECs from the Danish company EWII Fuel Cells A/S. The cells have an active electrode area of 2.89 cm^2 and contain a Nafion 117 membrane. A schematic drawing of the PEMEC mounted in a cell house, likewise provided by EWII Fuel Cells A/S, can be found in Figure 1. The anode is loaded with 0.3 mg cm^{-2} IrO_x catalyst with Nafion binder and 2.7 mg cm^{-2} Ir metal, likewise with Nafion binder, titanium felt is used as current collector and the anode flow plate is made of titanium. In this regard, it should be noted that the Ir metal layer functions as a current collector insuring electrical contact between the IrO_x catalyst layer and the titanium felt. The Ir metal layer is stated not to be electrochemical active by EWII Fuel Cells A/S. This is probably due to the low surface area of the Ir metal particles compared to the IrO_x particles c.f. the SEM images in Figure 7. The cathode contains 0.5 mg cm^{-2} platinum supported on carbon, carbon felt is used as current collector and the cathode flow plate is made of carbon. Gold coated copper current collectors are applied at both electrodes and the cell housing is made of stainless steel. The water inlet and the water outlet are sealed with nitrile O-rings at the current collectors and an EPDM O-ring is applied as sealing at the flow plate on the cathode. The cell temperature was measured with a Pt100 thermoresistor mounted in the stainless steel cell housing close to the water inlet.

Electrochemical characterization.—A PEMEC was characterized with CV at 61°C and ambient pressure while flushing the cathode with 10 mL min^{-1} hydrogen with 3 vol. % humidity (the temperature of the mQ water in the bubble flask was 26°C). The potential of the cathode is assumed to be close to 0 V vs. the standard hydrogen electrode (SHE) at open circuit voltage (OCV), since the cathode consists of platinum with pure hydrogen in an acidic environment due to the Nafion membrane. We are aware of the problem that the pH of Nafion in the H_2 electrode is not well-known.[1,18,19] It is known that the kinetics of this type of Pt/H_2 electrode are very fast compared to the kinetics of the IrO_x anode, meaning that the primary part of the total cell polarization resistance arise from the anode and not the Pt/H_2 electrode.[20–22] Approximately 400 mL min^{-1} nitrogen saturated mQ water was supplied to the anode. The cathode was counter and reference electrode, and the anode was the working electrode. CVs were recorded in the potential range 0.00–1.40 V and seven cycles

*Electrochemical Society Member.
**Electrochemical Society Fellow.
[z]E-mail: katel@dtu.dk

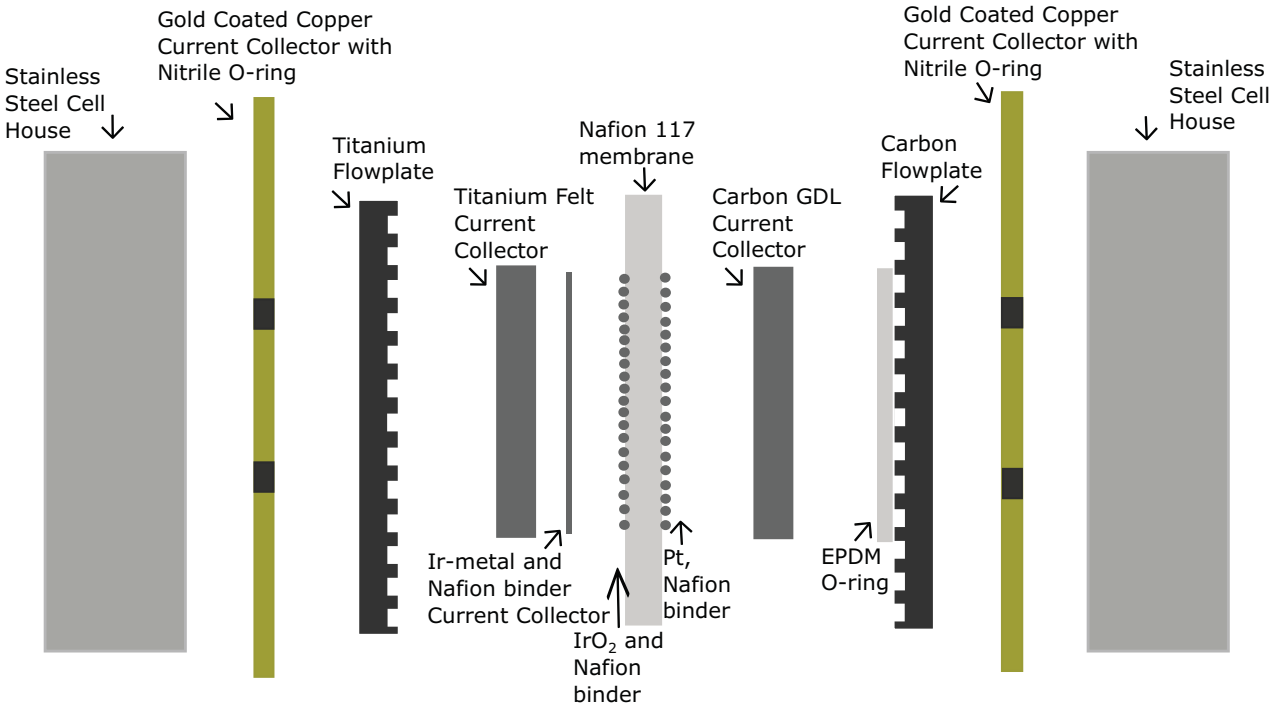

Figure 1. Schematic drawing of the PEMEC test setup provided by EWII Fuel Cells A/S.

were recorded with a sweep rate of 50 mV s^{-1}. The main purpose of the CV measurements was to use the position of the IrO_x redox peaks, which are known from the literature, to check if the assumption that the H_2/Pt/Nafion electrode potential is close to the SHE potential.

iV-curves and EIS were measured galvanostatically on another benchmark PEMEC from EWII Fuel Cells A/S similar to the PEMEC applied for the CV measurements. The measurements were conducted at potentials above the OER potential and at ambient pressure. No gases were supplied to the electrodes, and approximately 450 mL min^{-1} mQ water aerated with atmospheric air was supplied to the anode. A Delta Elektronika ES 015-10 power supply, with an accuracy of ±0.08 % in constant current mode on the potential and current measurements, respectively, was applied for cell polarization. A Solartron 1260 impedance analyzer was used for the impedance data acquisition, and a 50 mΩ shunt resistance was serially connected to the cell for exact DC current determination. iV-curves were measured at 53, 61 and 69°C from 0.050 A cm^{-2} to 1.000 A cm^{-2} with current steps of 50 mA and 20 seconds between each current step. Furthermore, the cell was operated at 0.07, 0.35, 0.69 and 1.00 A cm^{-2} at 53, 61 and 69°C while examined with EIS. The cell was conditioned for 20 minutes at each current step and for 1 hour at each temperature prior to EIS measurements. The frequency range was 100 kHz–0.01 Hz, the alternating current (AC) amplitude was 24.5 mA cm^{-2}, and 12 points were measured per decade.

All impedance data in this study has been analyzed and plotted using the impedance software Ravdav.[23]

Morphology of pristine and used PEMEC MEAs.—The microstructures of a pristine benchmark PEMEC from EWII Fuel Cells A/S and a used benchmark PEMEC from EWII Fuel Cells A/S tested at various temperatures and current densities as described above were examined with SEM. The microscope used for examination of the pristine PEMEC was a Zeiss Supra 35 with a field emission gun and a backscatter detector. An acceleration voltage of 10 kV was applied for imaging. A cross section of the pristine PEMEC was prepared for SEM examination by cutting the PEMEC with a scalpel followed by ion milling with argon atoms for 18 hours in an E-3500 ion milling system from Hitachi with an acceleration voltage of 6 kV. Cross sections of the used PEMEC were prepared by cutting the sample with a scalpel. The used PEMEC was examined with a Zeiss Merlin microscope with a field emission gun and a backscatter detector. An acceleration voltage of 15 kV was applied for imaging the used PEMEC. Both the SEM sample of the pristine and of the used PEMEC were coated with 10–20 nm carbon prior to SEM examination. Due to difficulties getting sharp SEM images at high magnification and being able to observe the microstructure of the anode, the ion milled pristine PEMEC was further studied using a focused ion beam (FIB) SEM CrossBeamTM 1540 XB (Carl Zeiss AG). A small cross section of the Ir metal layer, IrO_x anode catalyst layer and some Nafion membrane was cut with a 30 kV and 20 pA FIB, and an acceleration voltage of 2 kV was applied for imaging in order to avoid charging of the uncoated Nafion membrane during imaging.

Results

Redox properties of the oxygen evolution electrode.—Figure 2 depicts a CV of a PEMEC. Since the cathode is flushed with hydrogen, and only nitrogen saturated mQ water is supplied to the anode, only the redox properties of the anode should be displayed in the CV in Figure 2. The CV depicted in Figure 2 shows a redox peak at 0.77 V, a redox peak at 1.23 V and a sharp increase in the anodic current at 1.40 V, which is due to OER.[4,13,24] The CV does almost not have any slope at 0.07–0.40 V, which suggests that no faradaic reaction is taking place at these potentials. At 0.00 V to approximately 0.07 V negative currents that originate from hydrogen evolution on the Ir-electrode (the anode at higher potentials) are observed in the CV.

Cell performance.—iV-curves measured at 53, 61 and 69°C of a benchmark PEMEC are shown in Figure 3. It is seen that the cell has the better performance, the higher the operating temperature, and that all three iV-curves are linear above 0.35 A cm^{-2} implying constant total differential cell resistances above 0.35 A cm^{-2} at each temperature. The total differential cell resistances are determined to be 0.362 Ω cm^2 (R^2 = 0.9987) at 53°C, 0.318 Ω cm^2 (R^2 = 0.9992) at 61°C and 0.307 Ω cm^2 (R^2 = 0.9991) at 69°C from the slopes of the linear part of the three iV-curves.

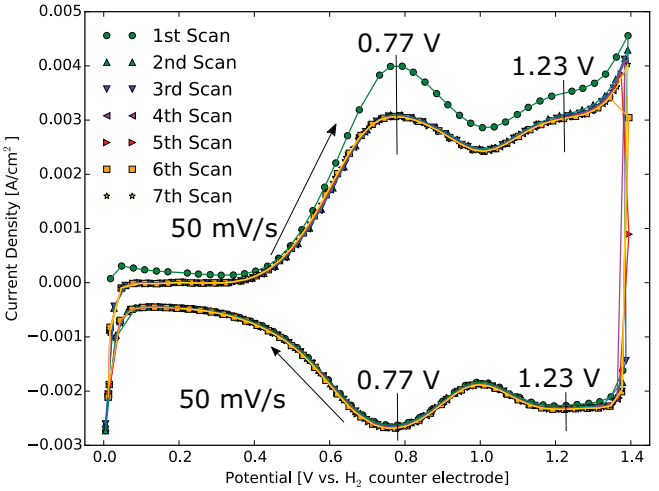

Figure 2. CV measured on a PEMEC showing seven cycles obtained with a sweep rate of 50 mV s^{-1} at 61°C and ambient pressure. The cathode consisted of platinum flushed with 10 mL min^{-1} moisturized hydrogen with 3 vol. % humidity. The anode was flushed with 400 mL min^{-1} nitrogen saturated mQ water. These experimental conditions imply that only the redox properties of the anode catalyst are displayed in the CV.

Influence of temperature and operating voltage / current density on cell impedance.—Nyquist plots of EIS measured on a PEMEC operated at 0.07, 0.35, 0.69 and 1.00 A cm^{-2} and at 53, 61 and 69°C are shown in Figure 4. EIS data at 50–80 Hz is left out due to noise from the electrical grid. It should be noted that $-Z_{im}$ is a positive number due to negative Z_{im} values. It is seen that the shape of the Nyquist plots at each current density is the same no matter the operating temperature. Figure 5 shows Nyquist plots of only the EIS data measured at 61°C at the four current densities. In this figure it might be easier to notice the changes in EIS with changes in current density, and the changes are representative for all three temperatures. The Nyquist plot of EIS measured at 0.07 A cm^{-2} shows a very significant arc, and a small arc at very low frequencies overlapped by the large arc. An increase in $-Z_{im}$ is observed at the highest frequencies. The real part of the

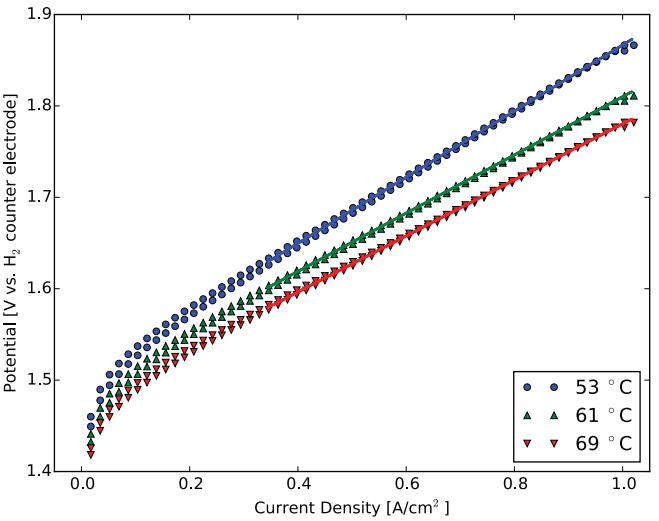

Figure 3. iV-curves for a PEMEC measured at 53, 61 and 69°C. The iV-curves are measured with ambient conditions at the cathode while flushing the anode with 450 mL min^{-1} aerated mQ water at ambient pressure. Linear regressions of the linear part of the iV-curves at current densities above 0.35 A cm^{-2} are depicted in the graphs, and total cell polarization resistances of 0.362 Ω cm^2 ($R^2 = 0.9987$), 0.318 Ω cm^2 ($R^2 = 0.9992$) and 0.307 Ω cm^2 ($R^2 = 0.9991$) are determined from the slopes of the iV-curves at 53, 61 and 69°C, respectively.

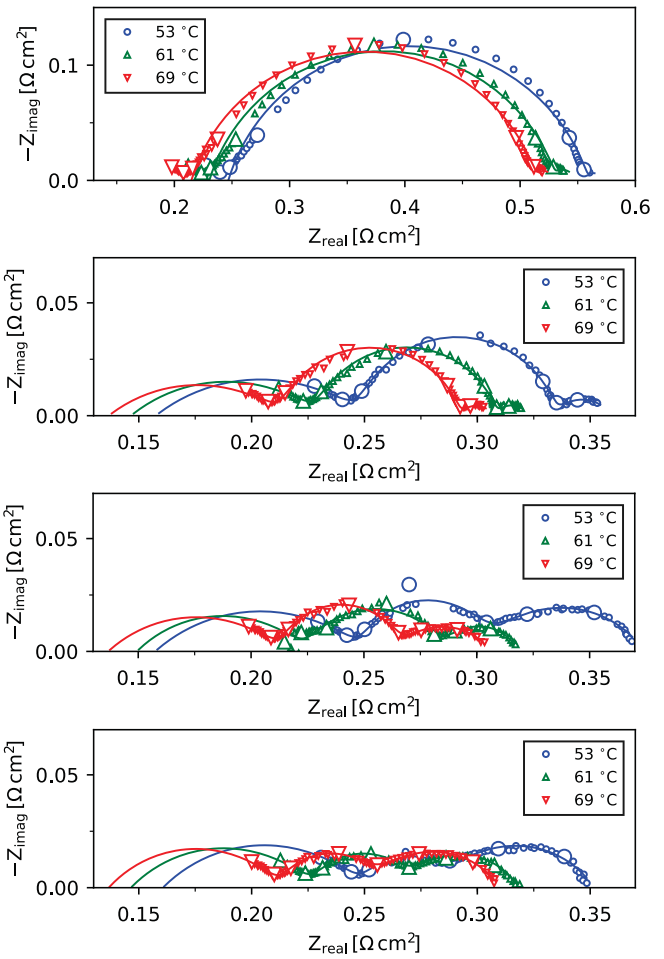

Figure 4. Nyquist representations of EIS and fits of a PEMEC operated at 53, 61 and 69°C at 0.07 (a), 0.35 (b), 0.69 (c) and 1.00 (d) A cm^{-2} and at ambient pressure. 450 mL min^{-1} aerated mQ water was supplied to the anode during operation with no gas supply to any of the electrodes as moisturized H_2 and O_2 are formed during electrolysis. EIS measured at 100 kHz, 10 kHz, 1 kHz, 100 Hz, 10 Hz, 1 Hz and 0.1 Hz are marked with bigger signs in each spectrum. An R-R_1Q_1-R_2Q_2 equivalent circuit was used to determine summit frequencies of the arcs at 0.07 A cm^{-2} above 5000 Hz, and an R-R_1Q_1-R_2Q_2-R_3Q_3 equivalent circuit was used to determine summit frequencies of arcs at 0.35-1.00 A cm^{-2}. The middle frequency arc had summit frequencies at 9.06-9.49 Hz, 63.2-67.2 Hz, 88.8-131.7 Hz and 118.6-143.9 Hz at 0.07, 0.35, 0.69 and 1.00 A cm^{-2}, respectively. The low frequency arc has summit frequencies of 0.010-0.017 Hz, 0.040-0.053 Hz, 0.179-0.273 Hz and 0.464-0.480 Hz at 0.07, 0.35, 0.69 and 1.00 A cm^{-2}, respectively. EIS data at 50–80 Hz is left out due to noise from the electrical grid.

impedance at the local minimum of $-Z_{im}$ at the high frequencies is denoted $Z_{re,\,HF\,min}$. In Figure 5 it can also be observed how the low frequency arc increases with increasing current density, and how the arc at the middle frequencies decreases with increasing current density, and the increase in $-Z_{im}$ at the highest frequencies are observed at all four current densities.

Morphology of pristine and used PEMEC MEAs.—Figure 6 and 7 show SEM images of cross sections of a pristine PEMEC, a used PEMEC and a zoom of the anode of the pristine PEMEC. A layer of IrO_x catalyst with Nafion binder is observed on the Nafion membrane in the images of the pristine PEMEC. Ir metal particles in Nafion binder are seen on top of the IrO_x catalyst layer in the pristine PEMEC, however in the SEM image of the used PEMEC it can be observed

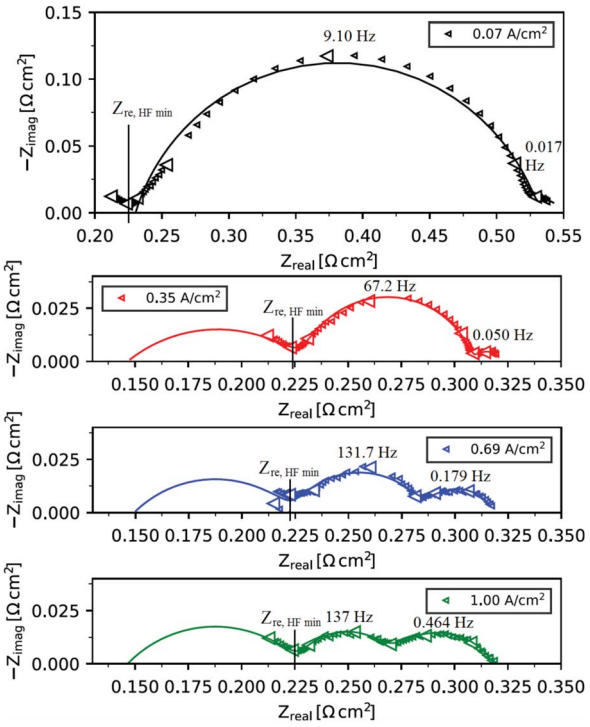

Figure 5. Nyquist representations and fits of EIS of a PEMEC operated at 0.07, 0.35, 0.69 and 1.00 A cm^{-2} at 61°C and ambient pressure. 450 mL min^{-1} aerated mQ water was supplied to the anode during operation with no gas supply to any of the electrodes as moisturized H_2 and O_2 are formed during electrolysis. EIS measured at 100 kHz, 10 kHz, 1 kHz, 100 Hz, 10 Hz, 1 Hz and 0.1 Hz are marked with bigger signs in each spectrum. An R-R_1Q_1-R_2Q_2 equivalent circuit was used to determine summit frequencies of the arcs at 0.07 A cm^{-2} above 5000 Hz, and an R-R_1Q_1-R_2Q_2-R_3Q_3 equivalent circuit was used to determine summit frequencies at 0.35-1.00 A cm^{-2}. EIS data at 50–80 Hz is left out due to noise at the electrical grid.

that the IrO_x and Ir metal layers have been peeled off the membrane in some areas during detachment of the titanium felt after cell operation.

Discussion

Cathode potential close to the SHE potential.—The redox peaks in the CV depicted in Figure 2 are in Table I compared to redox peaks in CVs of IrO_x model electrodes in PEMECs and in sulfuric acid media found in literature. From the comparison it can be seen that the redox peak potentials obtained from the CV in Figure 2 are very close to redox peak potentials reported for PEMECs at similar conditions and of the bare IrO_x, which imply that only the redox properties of the anode catalyst is seen in the CV. The redox peak at 0.77 V originates from the oxidation of Ir^{III} to Ir^{IV} and the redox peak at 1.23 V originates from the oxidation of Ir^{IV} to Ir^{V}.[4,13,24] This corroborates the assumption that the cathode potential - at least at low current density - is close to the SHE potential.

Ohmic resistances dominating above 0.35 A cm^{-2}.—At potentials below 0.40 V, the CV in Figure 2 has no slope and no current is flowing, meaning that at these low potentials, no faradaic reactions are taking place at the electrode, and the anode is said to be blocking. Only redox reactions in the IrO_x catalyst material take place at these low potentials. However, above 1.20 V vs. SHE (at 61°C) the electrode reaction rate increases (the polarization resistance decreases and oxygen evolves at the anode) fast with increasing potential, probably following the Butler-Volmer equation, until the current density reach a level, where the ohmic resistance becomes dominating. Ohmic resistances become totally dominating at current densities from 0.35 A cm^{-2}, which is seen from the constant total cell resistance from 0.35 A cm^{-2} given in Table II and seen in Figure 4 and 5. The total cell resistance is the DC impedance, here obtained as the impedance at the lowest frequency at 0.01 Hz. These findings are consistent with the iV-curves in Figure 3 measured at 53, 61 and 69°C, where ohmic resistances becomes dominating from 0.35 A cm^{-2} seen from the linear relation between the current density and the potential above 0.35 A cm^{-2}. In this regard, it should be noted that iV-curves of PEMECs in the literature generally are reported linear above 0.35 A cm^{-2}.[5–8,11,13–17,25] The constant total cell resistances measured above 0.35 A cm^{-2} found from the EIS data and from the slope of the iV-curves in this work are very similar, since at 53°C they are 0.357±0.009 Ω cm^2 and 0.362 Ω cm^2 ($R^2 = 0.9987$), respectively, at 61°C they are 0.318±0.001 Ω cm^2 and 0.318 Ω cm^2 ($R^2 = 0.9992$), respectively, and at 69°C they are 0.304±0.002 Ω cm^2 and 0.307 Ω cm^2 ($R^2 = 0.9991$), respectively. This constant total cell resistance means that above this 0.35 A cm^{-2}, the effect of the oxygen electrode catalyst is not seen, or in other words: adding a more active catalyst will not improve the performance of this cell.

Equivalent circuit for the PEMEC.—Local minima of $-Z_{im}$ at the high frequencies are observed in all the Nyquist plots in Figure 4

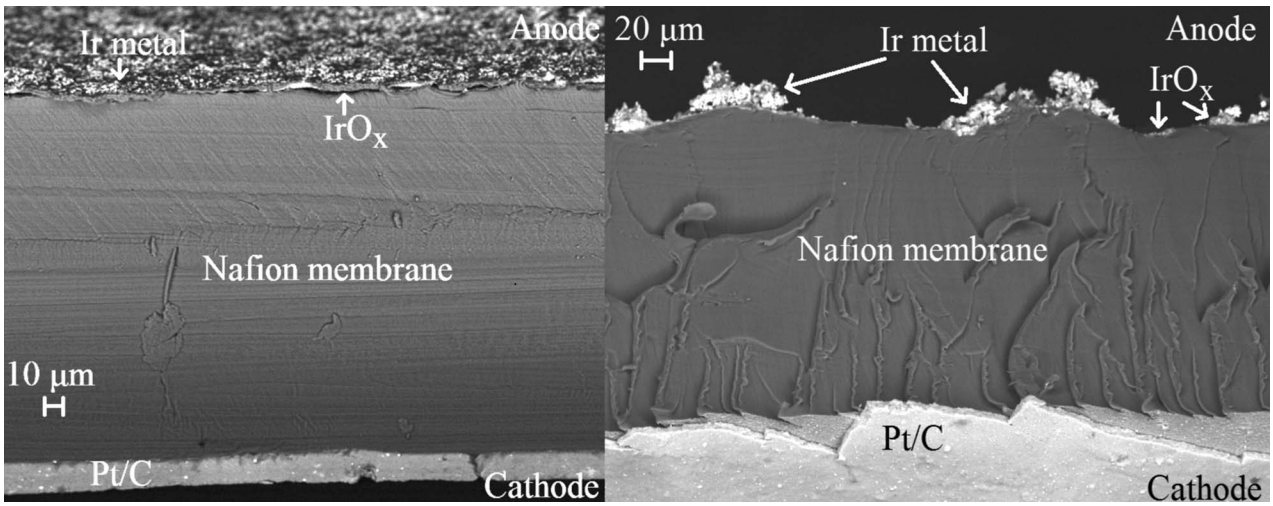

Figure 6. Backscattered electrons SEM images of cross sections of a pristine PEMEC (left) and a used PEMEC (right). A fine IrO_x catalyst layer is seen on the Nafion membrane of the pristine sample and the IrO_x layer is in contact with a well dispersed Ir metal current collector layer, whereas the IrO_x catalyst layer and the Ir metal current collector has been peeled off the used PEMEC during detachment of titanium felt after operation.

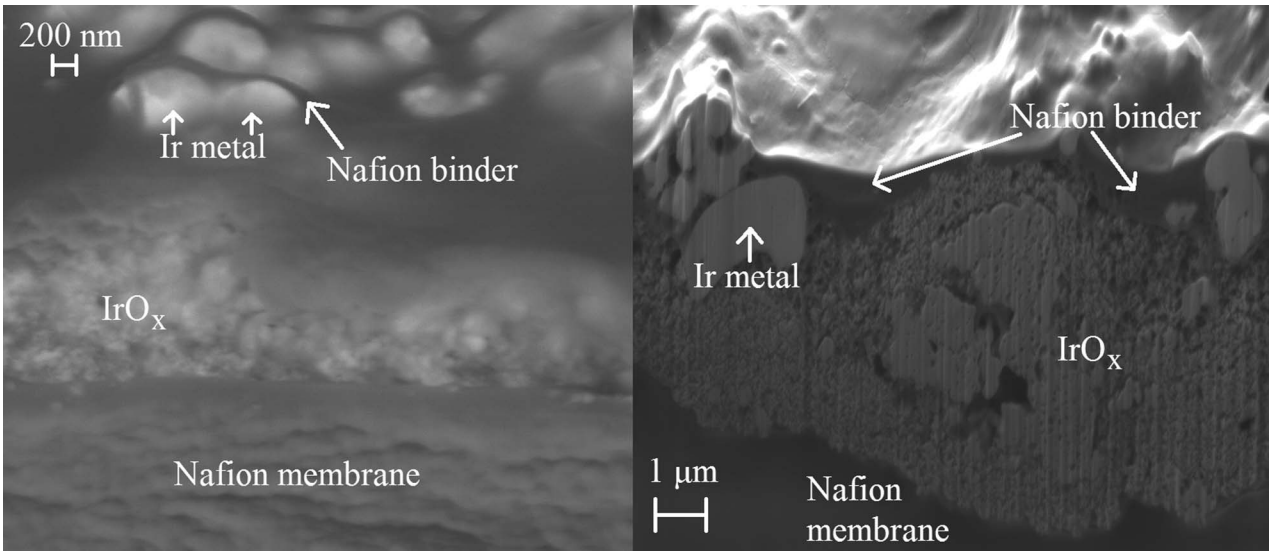

Figure 7. Backscattered electrons SEM image of a cross section of an ionmilled anode of a pristine PEMEC (left) and secondary electrons SEM image of a cross section of the anode of a pristine PEMEC cut with FIB (right). The IrO_x catalyst layer containing Nafion binder is observed on top of the Nafion membrane. Ir metal particles functioning as current collector are observed on top of the IrO_x layer. The Ir metal current collector layer does also contain Nafion binder, which is observed as black shadows between the Ir metal particles.

and 5. The real part of the impedance at these local minima are denoted $Z_{re,\,HF\,min}$ and are given in Table III for all three temperatures and four current densities. From Table III it can be seen that $Z_{re,\,HF\,min}$ is not dependent on current density, but dependent of temperature. One could think that $Z_{re,\,HF\,min}$ is the Nafion electrolyte resistance, but this is not the case, since the reported values for $Z_{re,\,HF\,min}$ is slightly higher than the pure electrolyte resistance reported by Malis et al.[26] They reported conductivity measurements on hydrated Nafion 117 membranes, which prior to EIS examination had been operated in PEMECs, and according to their findings, the membrane resistance should be 0.159 Ω cm^2 at 53°C, 0.148 Ω cm^2 at 61°C and 0.138 Ω cm^2 at 69°C (calculations can be found in the appendix), which are slightly lower than the $Z_{re,\,HF\,min}$ values found in this work. These findings in the combination with the fact that an increase in $-Z_{im}$ are observed at the highest frequencies in all the Nyquist plots, cause us to suggest that a third suppressed arc independent on current density is partly observed at the highest frequencies probably originating from current constrictions as described by Fleig et al.[27] Lettenmeier et al.[6] observed the same trend with a very high frequency EIS arc independent on current density. Porous nature of the anode or areas with extended electrolyte-electrode contact, causing two-phase boundaries instead of triple phase boundaries in the anode material, may prevent the proton conduction in parts of the electrolyte surface increasing the resistance of the electrolyte. If furthermore big catalyst agglomerates are attached to the electrolyte, these may contribute with a capacitive impedance contribution, which may account for the observed increase in capacitive impedance at the highest frequencies.[27] Figure 6 depicts SEM images of a pristine and a used PEMEC. A thin, even IrO_x catalyst layer is observed on the Nafion membrane at the anode of the pristine sample, and a coarse Ir metal current collector layer is observed on top of the IrO_x layer. The SEM image of the electrochemically tested sample shows a PEMEC with an uneven IrO_x catalyst layer and an uneven Ir metal layer. Both the IrO_x layer and the Ir metal layer contain Nafion binder, which can be observed in the Ir metal layer in Figure 7, where a SEM image of the anode of the pristine sample is depicted. In this image, big Ir metal particles

Table I. Comparison of redox peaks in the CV shown in Figure 2 with redox peaks of iridium oxide at similar conditions in the literature.

Reference	Experimental conditions	Redox peaks
This study	CV measured on a PEMEC consisting of a Nafion 117 membrane and 0.3 mg cm^{-2} IrO_2 and the anode and 0.5 mg cm^{-2} Pt at the cathode. The cathode was flushed with hydrogen.	0.77 and 1.23 V vs. H_2 counter electrode
Rozain et al.[13]	CV measured on a PEMEC consisting of a Nafion 115 membrane and 0.3 mg cm^{-2} IrO_2 and the anode and 0.25 mg cm^{-2} Pt at the cathode. The cathode was flushed with hydrogen.	0.48, 0.80 and 1.18 V vs. RHE
Papaderakis et al.[4]	CV of anodically grown IrO_2 on an iridium wire measured in deaerated 0.5 M H_2SO_4.	0.50-0.55 V (Pre ox.), 0.70-0.80 V (Ir^{III} to Ir^{IV}), 1.15 V (Ir^{IV} to Ir^{V}) vs. Ag/AgCl corresponding to 0.73-0.78 V (Pre ox.), 0.93-1.30 V (Ir^{III} to Ir^{IV}), 1.38 V (Ir^{IV} to Ir^{V}) vs. SHE
Papaderakis et al.[4]	CV of IrO_2/Nafion electrodes with a catalyst loading of 5–10 mg cm^{-2} on glassy carbon measured in deaerated 0.5 M H_2SO_4.	0.70 V (Ir^{III} to Ir^{IV}) and 1.07 V (Ir^{IV} to Ir^{V}) vs. Ag/AgCl corresponding to 0.93 V (Ir^{III} to Ir^{IV}) and 1.3 V (Ir^{IV} to Ir^{V}) vs. SHE
Ouattara et al.[24]	CV of anodically grown IrO_2 on a metallic iridium electrode in 1 M H_2SO_4.	0.65-0.70 V (Pre ox.), 0.90 V (Ir^{III} to Ir^{IV}) and 1.35 V (Ir^{IV} to Ir^{V}) vs. SHE
Ouattara et al.[24]	CV of an anodic iridium film electrode in 1 M H_2SO_4. The film was deposited on p-Si by sputtering.	0.70 V (Pre ox.), 0.90 V (Ir^{III} to Ir^{IV}) and 1.35 V (Ir^{IV} to Ir^{V}) vs. SHE

Table II. Total cell resistance measured at the lowest frequency (0.01 Hz) at 53, 61 and 69°C and at 0.07, 0.35, 0.69 and 1.00 A cm^{-2}.

Temperature [°C]	0.07 A cm^{-2} [Ω cm^2]	0.35 A cm^{-2} [Ω cm^2]	0.69 A cm^{-2} [Ω cm^2]	1.00 A cm^{-2} [Ω cm^2]	Average of numbers marked ∗ [Ω cm^2]
53	0.560	∗0.353	∗0.369	∗0.349	0.357±0.009
61	0.538	∗0.319	∗0.317	∗0.319	0.318±0.001
69	0.519	∗0.303	∗0.303	∗0.307	0.304±0.002

are observed on top of a very porous IrO_x layer. It is not possible to see the Nafion binder in the IrO_x layer, which may be ascribed to the very small particle size of approximately 9 nm of the IrO_x particles according to EWII Fuel Cells A/S. It should be noted that the titanium felt, which is used as current collector at the anode, is placed on top of the anode of the pristine sample prior to operation. After operation, the titanium felt detaches the PEMEC when disassembling the cell, and the SEM images in Figure 6 may suggest the IrO_x and Ir metal to be detached from the Nafion membrane by the titanium felt after operation. The easy detachment of the IrO_x and Ir metal layers may suggest bad contact between the Nafion membrane and the IrO_x layer and the Ir metal layer, which may cause current constrictions at the Nafion/IrO_x interface and support the assumption that the increase in $-Z_{im}$ at very high frequencies is due to current constrictions.

As earlier described, the Nyquist plots in Figure 4 and 5 show an increase of the low frequency arc and a decrease of the middle frequency arc with increasing current density. This trend is also seen in literature by Lettenmeier et al.[6] and Steen et al.[12] Furthermore we, as well as Lettenmeier et al.,[6] see no change in total cell impedance with increasing current density at current densities in the linear region of the iV-curve. This implies that the sum of resistances of the low and middle frequency arcs in the Nyquist plots of the impedance of the PEMEC during OER are constant at current densities from 0.35 A cm^{-2} to 1.00 A cm^{-2}. These findings imply that the low and middle frequency arcs originate from the composite IrO_x/Nafion anode causing two capacitive impedances dependent on current density, but with a total resistive impedance of the two processes independent on current density. The sum of the resistances of the low and middle frequency arcs are given by the difference between the total cell resistance and $Z_{re,\,HF\,min}$, and is given in Table IV. It is seen that the resistance of these two arcs, is approximately 1/3 of the total cell resistance.

Figure 8 depicts a graph of the average $Z_{re,\,HF\,min}$ and the average total cell resistance obtained from the EIS data as function of cell temperature including error bars of the standard deviations given in Table II and III and a linear regression of the points. From the graph it is found that $Z_{re,\,HF\,min}$ decreases 2.14 mΩ cm^2 per degree increase in temperature and that the total cell resistance decreases 3.29 mΩ cm^2 per degree increase in temperature. These results are in the Figure 8 compared to the decrease in in-plane Nafion 117 membrane resistance of 1.31 mΩ cm^2 per degree increase in temperature reported by Malis et al.[26] The decrease in resistance with temperature for the total cell resistance, $Z_{re,\,HF\,min}$ and the literature values for the in-plane Nafion 117 membrane resistance is in the same order of magnitude, and this may imply that all the resistive impedance contributions in the PEMEC originate from Nafion in the electrolyte and in the electrodes. When comparing the average values of the resistances of the low and middle frequency arcs in Table IV at 53 and 61°C, a decrease in resistance of 2.13 mΩ cm^2 per degree increase in cell temperature is found. This dependence is of the same order of magnitude as reported for the total cell resistance, $Z_{re,\,HF\,min}$ and for the literature values for the in-plane Nafion 117 membrane resistance in Figure 8. This indicates that the resistance of the low and middle frequency arcs originates from the Nafion binder in the anode catalyst material. The average resistance of the low and middle frequency arcs measured at 69°C does not show the same relation between temperature and resistance as the resistances of the two arcs at 53 and 61°C, and it is assumed that the measurements at 69°C are "outliers".

These findings cause us to suggest an equivalent circuit for the PEMEC consisting of a serial electrolyte resistance obtained from the literature values reported by Malis et al.,[26] a high frequency arc originating from current constrictions at the electrolyte and electrode interface and two low and middle frequency arcs originating from the composite IrO_x/Nafion anode. Therefore, the equivalent circuit is suggested to be $R\text{-}R_1Q_1\text{-}R_2Q_2\text{-}R_3Q_3$. Summit frequencies of the arcs in Figure 4 and 5 are obtained by fitting the EIS data measured from 0.35 A cm^{-2} to the equivalent circuit $R\text{-}R_1Q_1\text{-}R_2Q_2\text{-}R_3Q_3$. The EIS data obtained at 0.07 A cm^{-2} at frequencies above 5000 Hz have been fitted to a slightly different equivalent circuit, which was $R\text{-}R_1Q_1\text{-}R_2Q_2$, since the contribution of the high frequency arc was too small to fit at this low current density. A better fit was obtained, when excluding the very high frequency arc from the calculations, leading to more accurate summit frequency determinations of the middle and low frequency arcs. In this regard it should be noted that the equivalent circuits are only applied to determine summit frequencies, and no further quantifications are done from these fits. The summit frequencies of the middle frequency and low frequency data arcs were found to be 9.10 Hz and 0.017 Hz, respectively, at 0.07 A cm^{-2}, 67.2 Hz and 0.050 Hz, respectively, at 0.35 A cm^{-2}, 131.7 and 0.179 Hz, respectively, at 0.69 A cm^{-2} and 137 Hz and 0.464 Hz, respectively, at 1.00 A cm^{-2}.

Anode catalyst layer contributing to the total cell impedance – A hypothesis.—A hypothesis, which may explain the origin of the low and middle frequency arcs, is that the composite IrO_x/Nafion anode catalyst layer is causing these arcs. The resistive impedance of these two arcs, which is independent on current density, but dependent on temperature, is suggested to originate from the Nafion binder in the catalyst layer, while the capacitive contribution to the impedance of the two arcs is caused by the redox reactions of the IrO_x anode catalyst. Kötz et al.[28] have examined the reaction mechanism of the OER on an IrO_x catalyst in acidic media with X-ray photoelectron spectroscopy (XPS). They found the Ir in the oxidation states IV, V and VI during the catalytic reaction cycle. Based on their findings, the middle frequency arc is ascribed to oxidation of Ir^{IV} to Ir^{V} and the arc at the lowest frequencies is ascribed to the oxidation of Ir^{V} to Ir^{VI}, since the higher the potential the more likely the redox specie is in a higher oxidation state, and the low frequency arc is increasing with increasing current density/electrode potential, whereas the middle frequency arc is decreasing with increasing current density/electrode potential. Since the observed $Z_{re,\,HF\,min}$ is considered to arise from resistance of the Nafion membrane and from current constrictions at the Nafion

Table III. $Z_{re,\,HF\,min}$ at 53, 61 and 69°C and at 0.07, 0.35, 0.69 and 1.00 A cm^{-2}.

Temperature [°C]	0.07 A cm^{-2} [Ω cm^2]	0.35 A cm^{-2} [Ω cm^2]	0.69 A cm^{-2} [Ω cm^2]	1.00 A cm^{-2} [Ω cm^2]	Average [Ω cm^2]
53	0.242	0.242	0.245	0.247	0.244±0.002
61	0.225	0.224	0.222	0.225	0.224±0.001
69	0.210	0.208	0.210	0.211	0.210±0.001

Table IV. Resistance of the low and middle frequency arcs found as the difference between the total cell resistance and $Z_{re,\,HF\,min}$ at 53, 61 and 69°C and at 0.07, 0.35, 0.69 and 1.00 A cm^{-2}.

Temperature [°C]	0.07 A cm^{-2} [Ω cm^2]	0.35 A cm^{-2} [Ω cm^2]	0.69 A cm^{-2} [Ω cm^2]	1.00 A cm^{-2} [Ω cm^2]	Average of numbers marked ∗ [Ω cm^2]
53	0.318	∗0.111	∗0.124	∗0.102	0.112±0.009
61	0.313	∗0.095	∗0.095	∗0.094	0.095±0.000
69	0.309	∗0.095	∗0.093	∗0.096	0.095±0.001

membrane/electrode interface, this hypothesis implies that the total differential cell polarization resistance (which is equal to the Z_{re} intercept with the real axis, which again is equal to the slope of the linear part of the iV-curve) at current densities above 0.35 A cm^{-2} can be ascribed only to the proton resistance of Nafion in the electrolyte and in the electrodes. 44.5–46.5 % (resistance of a Nafion 117 membrane reported by Malis et al.[26] divided by the total cell resistance determined by EIS in this study) of the total cell resistance is ascribed to the proton resistance in the Nafion electrolyte and 53.5–55.5 % (the resistance of the three arcs in the Nyquist plots) is ascribed to the proton resistance in the anode catalyst layer and to current constriction at the electrode/electrolyte interface.

Conclusions

This study presents a hypothesis that the IrO_x anode catalyst layer, current constrictions in the Nafion membrane at the electrolyte/electrode interface and the electrolyte resistance of the Nafion membrane are accounting for the total PEMEC impedance above 0.35 A cm^{-2}, in the linear region of the iV-curve. Linear iV-curves were found at current densities above 0.35 A cm^{-2} at 53, 61 and 69°C implying the total differential cell resistance to be constant above 0.35 A cm^{-2}, which is consistent with EIS measurements. The total differential cell area specific resistance obtained from the iV-curves was found to vary from 0.362 Ω cm^2 at 53°C, to 0.307 Ω cm^2 at 69°C. 44.5–46.5 % of the total cell resistance has been ascribed to proton resistance in the Nafion electrolyte and 53.5–55.5 % of the total cell resistance has been ascribed to proton resistance in the IrO_x/Nafion composite anode catalyst layer and current constrictions associated with the electrodes. This hypothesis implies that the total differential cell resistance of the PEMEC is purely ascribed to Nafion at current densities above 0.35 A cm^{-2} for this type of PEMEC.

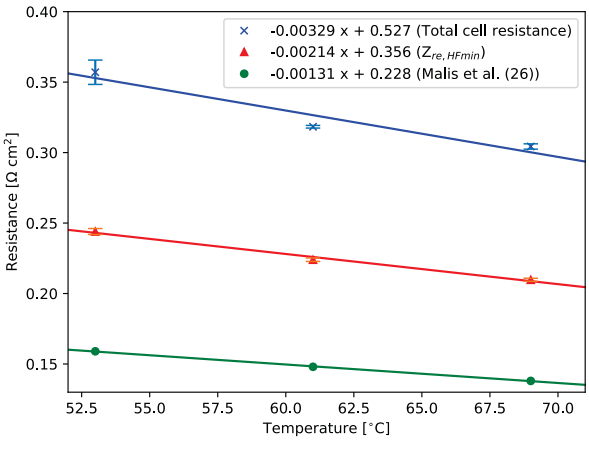

Figure 8. Total cell resistance (crosses) and $Z_{re,\,HF\,min}$ (triangles) are shown as function of operating temperature. The plotted data is deduced from the EIS data shown in Figure 4 and is also given in Table II and III, respectively. The plotted values are average values determined at 0.35, 0.69 and 1.00 A cm^{-2} and at ambient conditions at the cathode while flushing the anode with 450 mL min^{-1} aerated mQ water at ambient pressure. The results are compared to in-plane resistance measurements of operated Nafion 117 membranes reported by Malis at al.[26] (circles).

Acknowledgments

This work has been performed as part of a PhD project, which is part of the e-STORE project with contract no. 4106-00025B funded by the Innovation Fund Denmark.

Appendix: Calculations of the Area Specific Resistance of the Nafion 117 Membrane

The area specific resistance of the Nafion 117 membrane is calculated based on in-plane conductivity measurements of a Nafion 117 membrane used for electrolysis reported by Malis et al.[26]

First, the average thickness is calculated from the thicknesses reported in Table 1 in Reference 26.

$$Average\ \ thickness = \frac{(203 + 211 + 206 + 205 + 209 + 207)\,\mu m}{6} = 206.83\ \mu m$$

Conductivities of the membrane at the three temperatures are read off the graph in Figure 2 in Reference 26. The conductivities were 0.13 S cm^{-1} at 53°C, 0.14 S cm^{-1} at 61°C and 0.15 S cm^{-1} at 69°C. This gives the following values for the ohmic resistance of the Nafion membrane at the three temperatures using the average thickness for the calculations:

$$R_{53\,^\circ C} = \frac{0.020683\,cm}{0.13\,s\,cm^{-1}} = 0.159\,\Omega\,cm^2$$

$$R_{61^\circ C} = \frac{0.020683\,cm}{0.14\,s\,cm^{-1}} = 0.148\,\Omega\,cm^2$$

$$R_{69^\circ C} = \frac{0.020683\,cm}{0.15\,s\,cm^{-1}} = 0.138\,\Omega\,cm^2$$

ORCID

K. Elsøe https://orcid.org/0000-0002-7316-8053
J. Hjelm https://orcid.org/0000-0003-0072-5784
M. B. Mogensen https://orcid.org/0000-0002-0902-0580

References

1. M. Carmo, D. L. Fritz, J. Mergel, and D. Stolten, *Int. J. Hydrogen Energ.*, **38**, 4901 (2013).
2. A. Lasia, *Electrochemical Impedance Spectroscopy and its Applications*, chapter 9, Springer, London (2014).
3. S. H. Jensen, A. Hauch, P. V. Hendriksen, M. B. Mogensen, N. Bonanos, and T. Jacobsen, *J. Electrochem. Soc.*, **154**, B1325 (2007).
4. A. Papaderakis, D. Tsiplakides, S. Balomenou, and S. Sotiropoulos, *J. Electroanal. Chem.*, **757**, 216 (2015).
5. S. Siracusano, V. Baglio, A. Di Blasi, N. Briguglio, A. Stassi, R. Ornelas, E. Trifoni, V. Antonucci, and A. S. Arico, *Int. J. Hydrogen Energ.*, **35**, 5558 (2010).
6. P. Lettenmeier, S. Kolb, F. Burggraf, A. S. Gago, and K. A. Friedrich, *J. Power Sources*, **311**, 153 (2016).
7. I. Dedigama, P. Angeli, K. Ayers, J. B. Robinson, P. R. Shearing, D. Tsaoulidis, and D. J. L. Brett, *Int. J. Hydrogen Energ.*, **39**, 4468 (2014).
8. J. van der Merwe, K. Uren, G. van Schoor, and D. Bessarabov, *Int. J. Hydrogen Energ.*, **39**, 14212 (2014).
9. M. Bernt and H. A. Gasteiger, *J. Electrochem. Soc.*, **163**, F3179 (2016).
10. C. Rakousky, U. Reimer, K. Wippermann, M. Carmo, W. Lueke, and D. Stolten, *J. Power Sources*, **326**, 120 (2016).
11. S. Sun, Z. Shao, H. Yu, G. Li, and B. Yi, *J. Power Sources*, **267**, 515 (2014).

12. S. M. Steen and F. Y. Zhang, *J. Phys. Conf. Ser.*, **548**, (2014).
13. C. Rozain, E. Mayousse, N. Guillet, and P. Millet, *Appl. Catal. B- Environ.*, **182**, 123 (2016).
14. C. Rozain and P. Millet, *Electrochem. Acta*, **131**, 160 (2014).
15. P. Lettenmeier, R. Wang, R. Abouatallah, S. Helmly, T. Morawietz, R. Hiesgen, S. Kolb, F. Burggraf, J. Kallo, A. S. Gago, and K. A. Friedrich, *Electrochem. Acta*, **210**, 502 (2016).
16. S. Siracusano, V. Baglio, F. Lufrano, P. Staiti, and A. S. Aricò, *J. Memb. Sci.*, **448**, 209 (2013).
17. P. Millet, N. Mbemba, S. A. Grigoriev, V. N. Fateev, A. Aukauloo, and C. Etiévant, *Int. J. Hydrogen Energ.*, **36**, 4134 (2011).
18. H. Tawfik, Y. Hung, and D. Mahajan, *J. Power Sources*, **163**, 755 (2007).
19. A. Hermann, T. Chaudhuri, and P. Spagnol, *Int. J. Hydrogen Energ.*, **30**, 1297 (2005).
20. J. Rossmeisl, Z. –W. Qu, H. Zhu, G. –J. Kroes, and J. K. Nørskov, *J. Electroanal. Chem.*, **607**, 83 (2007).
21. W. Sheng, H. A. Gasteiger, and Y. Shao-Horn, *J. Electrochem. Soc.*, **157**, B1529 (2010).
22. J. Suntivich, K. J. May, H. A. Gasteiger, J. B. Goodenough, and Y. Shao-Horn, *Science*, **334**, 1383 (2011).
23. Graves, C. RAVDAV data analysis software, version 0.9.7, 2012.
24. L. Ouattara and S. Fierro, *J. Appl. Electrochem.*, **39**, 1361 (2009).
25. A. T. Marschall, S. Sunde, M. Tsypkin, and R. Tunold, *Int. J. Hydrogen Energ.*, **32**, 2320 (2007).
26. J. Malis, P. Mazur, M. Paidar, T. Bystron, and K. Bouzek, *Int. J. Hydrogen Energ.*, **41**, 2177 (2016).
27. J. Fleig and J. Maier, *J. Electrochem. Soc.*, **144**, L302 (1997).
28. R. Kötz, H. Neff, and S. Stucki, *J. Electrochem. Soc.*, **131**, 72 (1984).

Article 2

DOI: 10.1002/fuce.201800005

Fuel Cells

ORIGINAL RESEARCH PAPER

Noise Phenomena in Electrochemical Impedance Spectroscopy of Polymer Electrolyte Membrane Electrolysis Cells▲

K. Elsøe[1]*, M. R. Kraglund[1], L. Grahl-Madsen[2], G. G. Scherer[3], J. Hjelm[1], S. H. Jensen[1], T. Jacobsen[4], M. B. Mogensen[1]

[1] Department of Energy Conversion and Storage, Technical University of Denmark, 4000 Roskilde, Denmark
[2] EWII Fuel Cells A/S, 5220 Odense SE, Denmark
[3] 5607 Hägglingen, Switzerland
[4] Department of Chemistry, Technical University of Denmark, Kemitorvet Building 207, DK-2800 Kgs. Lyngby, Denmark

Received January 19, 2018; accepted May 29, 2018; published online ■■■

Abstract

In this study, the origin of noise in electrochemical impedance spectroscopy (EIS) spectra measured on a variety of polymer electrolyte membrane electrolysis cells (PEMECs) has been investigated. EIS was measured during operation at various current densities of seven different PEMECs divided in five different cell types including both acidic PEMECs and alkaline PEMECs. The noise pattern differed between various types of cells and between cells of the same cell type. Integration time had no influence on the EIS noise level, whereas the AC amplitude seems to influence the EIS noise level. Other electrical noise sources influencing the EIS measurements have been studied with oscilloscope. No noise was observed at DC. A hypothesis explaining the relation between bubble formation during electrolysis and EIS noise is proposed based on the experimental findings.

Keywords: EIS, EIS Noise, Electrochemical Impedance Spectroscopy, Gas Bubbles, Nafion 117, PEMEC, Polymer Electrolyte Membrane Electrolysis Cell

1 Introduction

The amount of research within the area of water electrolysis has increased a lot during recent years, in particular research on PEMEC that presently is commercially available for demonstration purposes, but still far too expensive to compete with hydrogen production from fossil fuels. [1, 2] Therefore, improving the electrolysis cells and stacks is still needed, and for this we need to improve our methods for characterizing the electrolysis cells, in order to give proper feedback to the cell developers.

EIS is a strong and popular electrochemical characterization technique in electrochemical research in general and in the areas of fuel cell and battery research in particular. [3] However, EIS has not been a preferred technique for investigation of PEMECs, and relatively few reports on systematic EIS studies can be found in literature. Among these studies some EIS data contains a limited amount of noise [4–6], whereas others do not contain any EIS noise [7–9]. The EIS noise phenomenon is to our knowledge never mentioned nor investigated. This article look into the EIS noise phenomenon, and experiments on both conventional acidic PEMECs and alkaline PEMECs with a KOH doped polybenzimidazole (PBI) membrane have been performed. We present a preliminary hypothesis on the mechanism of this noise as an AC perturbation interaction with gas bubbles adsorbed on the surface of the electrocatalyst.

[*] *Corresponding author: katel@dtu.dk*

▲ *Paper presented at the 6th EUROPEAN PEFC & ELECTROLYZER Forum (EFCF2017), July 4–7, 2017 held in Lucerne, Switzerland. Organized by the European Fuel Cells Forum – www.efcf.com*

2 Experimental

Various types of conventional acidic PEMECs and alkaline PEMECs have been studied with EIS during operation. All impedance data in this study has been analyzed using the impedance software Ravdav [10]. In this work, it has been chosen to report Bode plots showing the real part and the imaginary part of the EIS as functions of frequency, since these types of Bode plots very clearly show resistive and capacitive contributions to the total cell impedance, respectively, which is not the case for Bode plots depicting phase angle and modulus as functions of frequency.

2.1 Conventional Acidic Polymer Electrolyte Membrane Electrolysis Cells

Three types of PEMECs with Nafion 117 membranes produced by EWII Fuel Cells A/S (EWII) have been studied. All three cell types were of the same design with an active electrode area of 2.9 cm^2. Titanium felt was used as anode current collector, and the anode flow plate was interdigitated and made of titanium. The cathode catalyst loading was 0.5 mg cm^{-2} platinum (60 wt.% Pt/C), carbon felt was used as cathode current collector, and the cathode flow plate was made of carbon. Further information can be found elsewhere [11]. A schematic drawing of the cell and cell housing is shown in Figure 1. A more detailed schematic drawing of a benchmark PEMEC from EWII with scanning electron microscopy (SEM) images of the anode catalyst layer, the iridium metal current collector, the Ti-felt current collector and the carbon GDL can be seen in Figure 2.

The three conventional acidic PEMEC types studied differed in production generation and anode catalyst and were:

(i) A cell from an early generation production at EWII with 0.3 mg cm^{-2} IrO_x as anode catalyst and a 1.7 mg cm^{-2} iridium metal contact layer (E-g1);

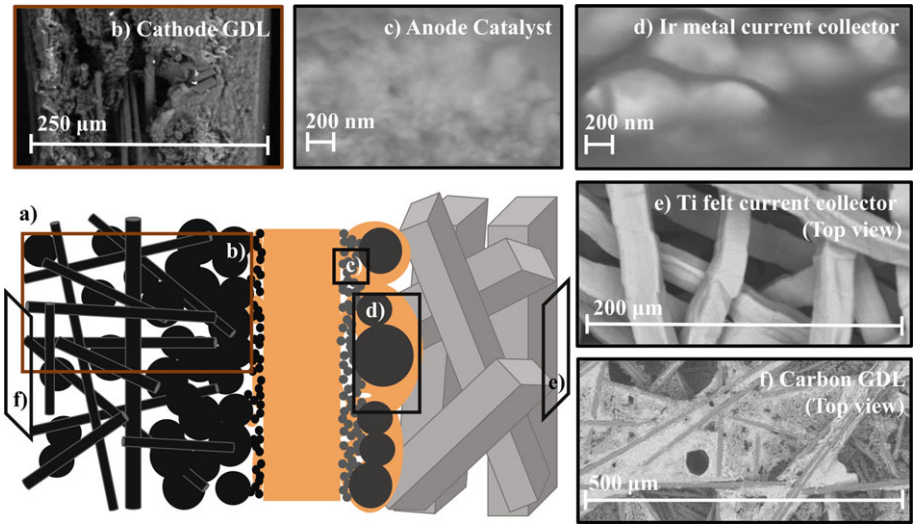

Fig. 2 Schematic drawing and SEM images of the microstructure of an EWII benchmark PEMEC (a). Image b, c and d are images of cross sections, whereas image e and f are images of the top of the anode Ti felt and the cathode carbon GDL, respectively.

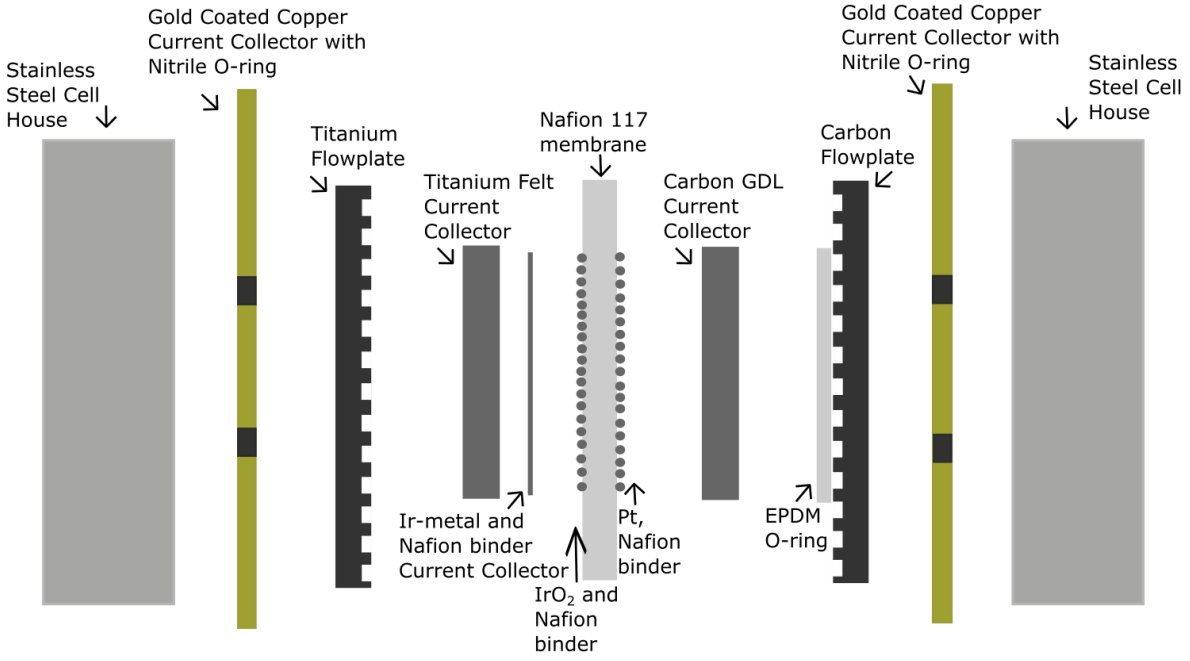

Fig. 1 Sketch of an expanded view of the PEMEC benchmark cell design of EWII cells [11].

(ii) A cell with 0.3 mg cm^{-2} anode catalyst consisting of 20 wt.% RuO_2 and 80 wt.% IrO_x and a 2.5 mg cm^{-2} iridium metal contact layer (E-IrRu);
(iii) The more mature EWII benchmark PEMEC with 0.3 mg cm^{-2} IrO_x as anode catalyst and a 2.7 mg cm^{-2} iridium metal contact layer. This is the cell that EWII uses as benchmark in the process of the further cell development. Three cells of the EWII benchmark type have been tested (E-ref-a, E-ref-b and E-ref-c).

2.1.1 Electrochemical Test Setup for Acidic PEMECs

All EIS measurements on conventional acidic PEMECs reported here were carried out at 61–65 °C. A Delta Elektronika ES 015-10 or a Delta Electronika SM 18-50 were applied for cell polarization. A 50 mΩ shunt resistance was serially connected to the cell for correct DC current determination. EIS was measured galvanostatically with a Solartron 1260 impedance analyzer, which was connected in parallel to the cell and shunt resistance. DC cancellation boxes were applied on the Solartron 1260 for improved AC signal resolution. 12 points were measured per frequency decade. The AC amplitude was 24.5–29.3 mA cm^{-2}, in most of the measurements, and in the few measurements, where other AC amplitudes have been applied on acidic PEMECs, it is given for the particular data in the corresponding text. The maximum frequency of EIS measured on acidic PEMECs shown in this article is 60 kHz, since above this frequency phase errors from the equipment, may influence the result. EIS measured at 45 and 54 Hz is left out of all the EIS plots, due to noise from the electrical grid. EIS measured on the EWII benchmark PEMEC named E-ref-a is only shown for frequencies above 0.10 Hz, due to an outlier in the measurements. The full EIS spectrum with outlier can be found in Figure A.1 in the Appendix. The anode of the acidic PEMECs were fed with Milli-DI water from Millipore at 300–500 mL min^{-1} during operation.

2.1.2 Oscilloscope Measurements

Electrochemical noise during DC operation of PEMECs was investigated, by measuring the cell potential of an operating benchmark PEMEC from EWII (E-ref-c) followed by fast Fourier transformation (FFT) of the signal with a digital differential oscilloscope from Picoscope. The oscilloscope was connected to the test setup *via* DC cancellation boxes, in order to increase the resolution of the noise signal. FFT of potential signals measured with the oscilloscope were generated by the oscilloscope software PicoScope6 using a Blackman filter. The measurements were done at a cell temperature of 64–66 °C and at two water flow rates.

2.2 Alkaline Polymer Electrolyte Membrane Electrolysis Cells

Two types of alkaline PEMECs have been studied with EIS and are schematically shown in Figure 3.

The two types were:
(i) A perforated nickel plate with a Raney-NiMo coating as cathode, a 40 µm m-PBI membrane and a perforated Ni plate as anode (R-NiMo | PBI | Ni), see Figure 3a (E-Ni-R).
(ii) A pressed Ni foam as cathode, a 40 µm m-PBI membrane and a perforated nickel plate as anode (Ni-foam | PBI | Ni) (E-Ni-F), see Figure 3b.

The used flow plates had a pin-type pattern and were made of Ni, PTFE was used as gasket material and the active electrode area was 25 cm^2.

Further details can be found elsewhere [12].

2.2.1 Electrochemical Test Setup for Alkaline PEMECs

The alkaline PEMECs were operated in partially separated mode in which 24 wt.% KOH (aq.) was circulated in independent electrolyte circuits. The anode flow was set to 50 mL min^{-1} for both alkaline PEMECs, whereas the cathode flow was depending on electrode geometry; 5 mL min^{-1} for the cathode of sample E-Ni-F, and 50 mL min^{-1} for the cathode of sample E-Ni-R. The electrolyte was flowed through a preheating cell prior to the electrolysis cell, to improve temperature stability at 80 °C. Heating was done by pairs of heating elements in the end-plates of both the pre-heating and the electrolysis cell.

EIS of the alkaline PEMECs was measured galvanostatically with a BioLogic Science Instruments HCP-1005 potentiostat in the frequency range 25 kHz – 0.1 Hz, however only EIS measured below 10 kHz is shown in this article due to outliers. EIS measured at 46 and 54 Hz is left out of all the EIS plots, due to noise from the electrical grid. The AC amplitude was 10% of the DC current applied to the cell and 15 points were measured per frequency decade.

3 Results and Discussion

3.1 EIS Noise Observed for Various PEMEC Types

The noise of the impedance spectra has been evaluated and quantified with a linear Kronig-Kramers transform compliance test, as reported by Boukamp [13]. The test gives an esti-

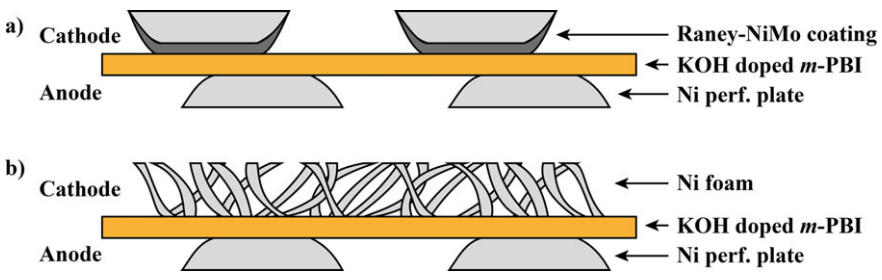

Fig. 3 Sketches of the two types of tested alkaline PEMECs.

mate on how well EIS data obey the four Kronig-Kramers relations; the system should show causality, be linear, stable and finite. In the linear Kronig-Kramers compliance test by Boukamp [13], measured EIS is fitted to multiple series connected Voigt elements (parallel R–C circuits) followed by calculating the relative Kramers-Kronig residuals as the difference between the fitted values and the measured impedance values at each frequency, according to Eq. (1)

$$\Delta_{re,i} = \frac{Z_{re,i} - Z_{re}(\omega_i)}{|Z(\omega_i)|} \quad and \quad \Delta_{im,i} = \frac{Z_{im,i} - Z_{im}(\omega_i)}{|Z(\omega_i)|} \tag{1}$$

with $Z_{re,i}$ and $Z_{im,i}$ being the real and imaginary parts of the ith data set impedance, and $Z_{re}(\omega_i)$ and $Z_{im}(\omega_i)$ being the fitted value of the real and the imaginary parts of the impedance for ω_i. $|Z(\omega_i)|$ is the absolute length of the modeling function [13]. Seven Voigt elements were applied per frequency decade for the calculations in this article. The Kramers-Kronig relative residuals can be used as a measure of the noise in the EIS spectra, as stochastic EIS noise would not obey the four Kramers-Kronig relations and therefore would increase the relative residuals in Boukamps Kramers-Kronig compliance test.

Figure 4 shows EIS measured on different PEMEC types shown in Bode plots and Kramers-Kronig relative residual plots, and EIS noise is observed in all the spectra. It should be noted that the operation current density is higher for the early generation EWII cell (E-g1) (1.00 A cm^{-2} compared to 0.35 or 0.40 A cm^{-2} for the other cells). However, since iV-curves of acidic PEMECs generally show a linear relation between current density and potential from current densities above approximately 0.35 A cm^{-2} [11], the differential cell resistance is constant for each PEMEC at current densities above 0.35 A cm^{-2}, and consequently the EIS of the various acidic PEMECs are comparable above this current density.

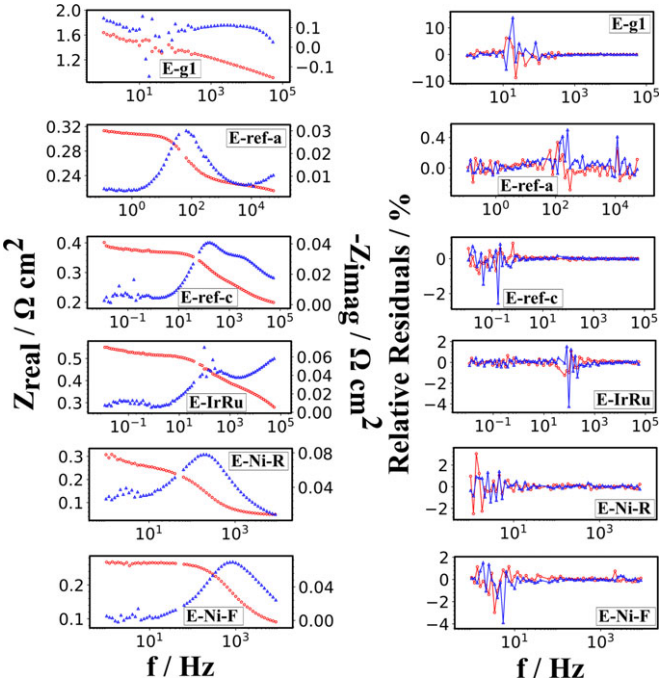

Fig. 4 EIS measured on six different PEMEC types: (E-g1) early generation acidic PEMEC from EWII at 0.35 A cm^{-2}, (E-ref-a) EWII benchmark PEMEC at 0.35 A cm^{-2}, (E-ref-c) another EWII benchmark PEMEC at 0.35 A cm^{-2}, (E-IrRu) EWII $IrRuO_x$ PEMEC at 0.35 A cm^{-2}, (E-Ni-R) Raney Ni alkaline PEMEC at 0.4 A cm^{-2} and (E-Ni-F) Ni foam alkaline PEMEC at 0.4 A cm^{-2}. Bode plots of the EIS data are shown in the left column and relative residuals of Kramers-Kronig compliance tests of the EIS data are shown in the right column. The real part of the impedance is shown with red circles, and the imaginary part of the impedance is shown with blue triangles.

The noise of the EIS spectra have been further quantified, in order to be able to compare the overall noise level of the cells, by summing the squares of the relative residuals (both of the real and of the imaginary part of the impedance) over all measured frequencies, cf. Eq. (2), where δ is the overall noise level in %^{2}, $\Delta_{re,i}$ is the Kramers-Kronig relative residual of the real part of the impedance at frequency i in %, $\Delta_{im,i}$ is the Kramers-Kronig relative residual of the imaginary part of the impedance at frequency i in % and n is the maximum frequency measured.

$$\delta = \sum_{i=0}^{n} {\Delta_{re,i}}^2 + {\Delta_{im,i}}^2 \tag{2}$$

Table 1 compares the cell performance determined as the differential cell resistance, which is the real part of the impedance at very low frequency and the overall noise level, δ, of EIS depicted in Figure 4 measured on different cell types. No relation is observed between the cell performance and overall noise level of the cells, but EIS noise is observed for all six PEMECs. However, in this regard it should be noted that the frequency range over which δ has been determined varies a bit between the cells in Table 1. Figure A.2 in the Appendix compares EIS measured at 0.35 A cm^{-2} on three different cells of the same cell type (EWII benchmark cells; E-ref-a, E-ref-b and E-ref-c) and the cell performance and overall EIS noise level of these cells can be found in Table 1. From these table values, it can be seen that the overall EIS noise level varies between cells of the same cell type and not only between cells of different cell types.

Table 1 Operating current density, cell performance ($Z_{re,LF}$) and the overall EIS noise level, δ, for various PEMEC types.

Cell	Current Density / A cm^{-2}	$Z_{re,LF}$ / Ω cm^2	δ / %^{2}
E-g1	1.00	1.639	522.089
E-ref-a	0.35	0.316	1.664
E-ref-c	0.35	0.388	16.525
E-ref-b	0.35	0.367	258.341
E-IrRu	0.35	0.551	35.693
E-Ni-R	0.40	0.307	40.868
E-Ni-F	0.40	0.267	44.412

3.2 Influence of DC Load, AC Amplitude and Integration Time on EIS Noise

EIS measured at various DC current densities on four different acidic PEMECs (E-IrRu, E-ref-a, E-ref-b and E-ref-c) can be found in Figures A.3–A.6 in the Appendix, respectively. Tables 2–5 summaries the cell performances and the overall noise level given by the Kramers-Kronig residuals, δ, for the four cells at the various current densities. Based on the four tables, no clear relation is observed between operating DC current density and the overall EIS noise level.

EIS measured at various AC amplitudes on two EWII benchmark PEMECs (E-ref-b and E-ref-c) can be found in Figures A.7 and A.8 in the Appendix, respectively. Tables 6 and 7 summaries the overall noise, δ, for the two cells at various AC amplitudes. The results indicate increasing overall EIS noise with decreasing AC amplitude.

Figure A.9 shows the influence of integration time applied when measuring EIS on the noise level of the EIS spectra measured at 0.35 A cm^{-2} on an EWII benchmark cell (E-ref-c). The integration time denotes the period over which the EIS analyzer is measuring the perturbation signal [14]. This means that white stochastic noise will be cancelled out the more the longer the integration time is. Table 8 lists the overall noise level at the various integration times.

Based on Table 8, the EIS noise level is not influenced by integration time.

Table 2 Cell performance ($Z_{re,LF}$) and the overall EIS noise level, δ, for the $IrRuO_x$ PEMEC from EWII (E-IrRu) measured at various current densities.

Current Density / A cm^{-2}	$Z_{re,LF}$ / Ω cm^2	δ / %^{2}
0.07	0.922	1.872
0.35	0.549	35.693
0.69	0.450	8.988
1.00	0.439	15.857

Table 3 Cell performance ($Z_{re,LF}$) and the overall EIS noise level, δ, for the EWII benchmark cell, E-ref-a, measured at various current densities.

Current Density / A cm^{-2}	$Z_{re,LF}$ / Ω cm^2	δ / %^{2}
0.07	0.531	1.619
0.35	0.316	1.664
0.69	0.311	5.434
1.00	0.311	2.829

Table 4 Cell performance ($Z_{re,LF}$) and the overall EIS noise level, δ, for the EWII benchmark cell, E-ref-b, measured at various current densities.

Current Density / A cm^{-2}	$Z_{re,LF}$ / Ω cm^2	δ / %^{2}
0.07	0.574	196.913
0.35	0.324	258.341
0.69	0.298	180.162
1.00	0.276	267.354
2.00	0.248	176.164

Table 5 Cell performance ($Z_{re,LF}$) and the overall EIS noise level, δ, for the EWII benchmark cell, E-ref-c, measured at various current densities.

Current Density / A cm^{-2}	$Z_{re,LF}$ / Ω cm^2	δ / %^{2}
0.35	0.313	16.525
1.00	0.402	14.779

Table 6 Overall EIS noise level, δ, for the EWII benchmark cell, E-ref-b, measured at various AC amplitudes and at 0.35 A cm^{-2}.

Amplitude / mA cm^{-2}	δ / %^{2}
29.3	298.919
14.6	660.659
4.9	5525.466

Table 7 Overall EIS noise level, δ, for the EWII benchmark cell, E-ref-c, measured at various AC amplitudes and at 0.35 A cm^{-2}.

Amplitude / mA cm^{-2}	δ / %^{2}
29.3	16.525
14.6	239.378

3.3 Investigations of Noise Sources with Oscilloscope

Sources of electrical noise have been investigated with oscilloscope by measuring the potential across an EWII benchmark PEMEC (E-ref-c) operated at 1.00 A cm^{-2} and with various water flow speed. Figure 5 shows the fast Fourier transform (FFT) of the potential measured across the PEMEC at various water flow speeds. Graph a in Figure 5 is measured at a high water flow speed, whereas graph b in Figure 5 is measured at a lower water flow. Clear changes in the magnitude and frequency of the noise peaks with changes in water flow speed is observed; the lower the water flow the lower the noise magnitude and the lower the frequency of the noise. At high water flow speed noise is observed slightly above 50 Hz, 100 Hz, 150 Hz, and 200 Hz, whereas at low water flow speed noise is observed at lower frequencies at approximately 20 Hz, 40 Hz, 60 Hz, and 80 Hz. These findings imply that the water pumps introduce electrical noise in the PEMEC system. However, the noise peak at 167 Hz does not change with the water flow speed.

It was speculated whether the noise introduced by the water pumps was caused by pressure changes in the gas

Table 8 Overall EIS noise level, δ, for the EWII benchmark cell, E-ref-b, measured at various integration times and at 0.35 A cm^{-2} and with an AC amplitude of 29.3 mA cm^{-2}.

Integration Cycles	δ / %^{2}
96	298.919
40	259.869
5	278.756
1	236.226

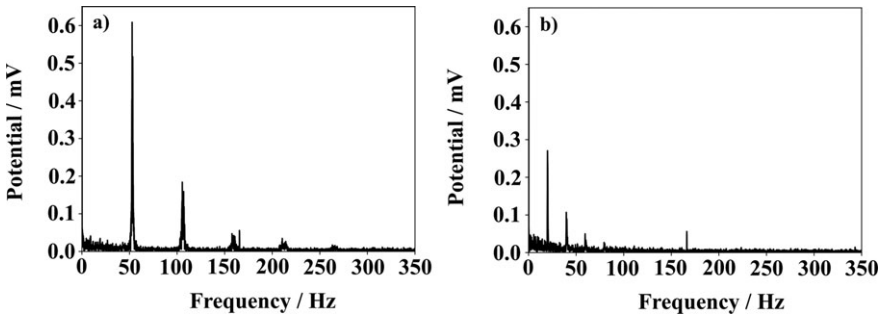

Fig. 5 FFT of potential measured with an oscilloscope across an EWII benchmark PEMEC (E-ref-c) during operation at 1.00 A cm^{-2} at with the pumps operating at high water flow speed (a) and with the pumps operating at low water flow speed (b). The two graphs show only the frequency range 0–350 Hz, since no peaks were observed above 350 Hz.

evolved at the electrodes in the PEMEC causing changes in the cell potential as function of the water flow changes, or whether the noise was introduced as electrical disturbances from the motor of the water pump. A cable applied as antenna able to record possible electrical interferences from the motor was held in the open air close to the water pump, and noise was recorded as can be seen in Figure 6. Graph b in Figure 6 is measured with the cable while operating the water pump at low water flow speed, and noise is observed at approximately 20 Hz, 40 Hz, 60 Hz, and 80 Hz. These frequencies correspond to the frequencies at which noise was observed in Figure 5 b for the PEMEC operated with at low water flow rate. This imply that the electrical noise observed during DC operation of the PEMEC is due to electrical disturbances from the motor of the water pump and not due to pressure changes in the PEMEC due to the water flowrate. Furthermore, the graphs in Figure 6 show potential peaks at 50 Hz, 100 Hz, and 150 Hz, which is expected to originate from electrical interferences from the 220 V electrical grid in the lab building.

3.4 EIS Noise Originating from Gas Bubbles – A Hypothesis

Our hypothesis explaining the noise observed in the EIS spectra recorded on various types of PEMECs is that the noise originates from gas bubbles partially covering the electrodes of the PEMECs during operation. The noise in the EIS spectra occurs at various frequencies depending on the particular cell, and not only at the frequencies, where noise from the water pumps was observed, according to the oscilloscope measurements reported in Figures 5 and 6. Therefore, it can be concluded that the EIS noise is not caused by electrical noise from the water pumps or any electrical noise from other sources than the cells. Since the noise is observed in many different PEMECs, it is expected that the EIS noise is caused by a physical process associated with the operation of a PEMEC. Another indication that the EIS noise is caused by a physical process is that the noise seems independent of integration time, cf. Table 8 and Figure A.9. If white electrical noise caused the EIS noise, an increase in integration time would decrease the noise level.

One may think that the suggested hypothesis imply the gas bubbles to be formed and released at a particular frequency depending on the DC magnitude and the microstructure of the cell. However, the FFT potential measurements in Figure 5, recorded during DC operation of a PEMEC with no AC perturbation, show only noise signals associated with the motor of the water pump. The lack of electrical noise from the cell during DC operation can be explained by a completely stochastic release of the gas bubbles across the electrode surface. During DC operation, the bubble coverage of the PEMEC electrodes will be in a quasi-steady-state where the average release rate of bubbles from the total electrode surface will be constant. When applying an AC potential on top of the DC operation potential, the bubble coverage of the PEMEC electrodes will no longer be in a quasi-steady-state, but will fluctuate with the AC signal leading to a non-constant (unstable) average release rate of the bubbles from the total electrode surface. The AC perturbation applied to the cell during EIS measurements may synchronize the release of bubbles across the electrode surface, causing the bubble release rate to preferably take place in an unstable manner at particular resonance frequency ranges for some bubble sizes dependent on the microstructure of the particular PEMEC. This will cause EIS noise in a narrow frequency range in the EIS spectrum dependent on the particular PEMEC. A schematic drawing and SEM images of the microstructure of a conventional acidic PEMEC from EWII is seen in Figure 2. Gas bubbles may be trapped in various locations on the active electrode in the microstructure such as in the anode catalyst layer blocking the current path and thereby locally increasing the potential, which is leading to EIS noise. These trapped bubbles will vibrate when the AC current is applied, due to fluctuations in the gas formation rate with the AC signal, and thereby the bubbles will be

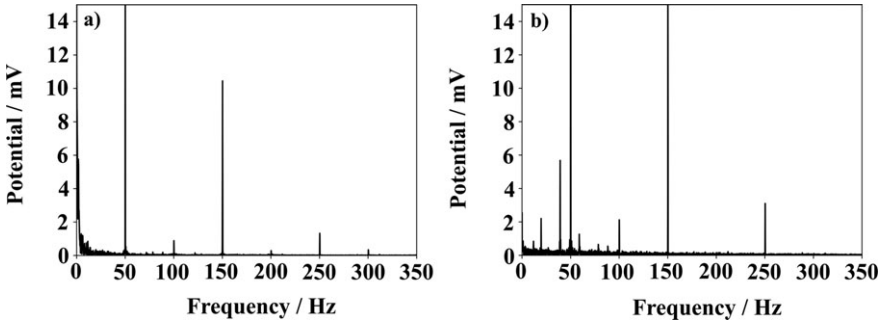

Fig. 6 FFT of potential measured on a cable applied as antenna in air close to the water pump supplying water to an operating EWII benchmark cell (cell 5) at high water flow speed (a) and at low water flow speed (b). The two graphs show only the frequency range 0–350 Hz, since no peaks were observed above 350 Hz.

released at certain frequencies. The optimal microstructure should have a sufficiently open structure, which enables gas bubble release from the electrocatalyst while the bubbles are small, leading to low or no noise in the EIS spectra. In this regard it shall be noted that the EIS noise reported in literature is not in conflict with this hypothesis [4–9].

4 Conclusions

A number of different PEMECs were investigated by EIS with respect to their noise pattern.

EIS noise from the electrodes was observed in one narrow frequency range for a number of different PEMECs. The EIS noise was found to be independent on cell internal resistance and EIS integration time. The EIS noise seems to increase with decreasing AC amplitude. A hypothesis has been presented, which suggests a constant bubble release rate from the electrocatalyst during DC operation leading to no electrochemical noise and a non-constant bubble release rate when an AC is overlaid the DC leading to electrical noise at resonance frequencies dependent on the particular microstructure of the PEMEC.

Acknowledgements

This work has been performed as part of a PhD project, which is part of the e-STORE project with contract no. 4106-00025B funded by the Innovation Fund Denmark.

Appendix

Figure A.1 shows the full EIS spectrum with outlier measured at 0.35 A cm^{-2} on the EWII benchmark cell, E-ref-a. EIS spectra measured on the same cell at other current densities showed identical outliers. Figure A.2 compares EIS measured at 0.35 A cm^{-2} on three different cells of the same cell type (EWII benchmark cells; E-ref-a, E-ref-b and E-ref-c).

EIS measured at various DC current densities on four different acidic PEMECs (E-IrRu, E-ref-a, E-ref-b and E-ref-c) are shown in Figures A.3–A.6, respectively. EIS measured at various AC amplitudes on two EWII benchmark PEMECs (E-ref-b and E-ref-c) can be found in Figures A.7 and A.8, respectively, and Figure A.9 shows the influence of integration time on the overall noise level of the EIS spectra measured at 0.35 A cm^{-2} on an EWII benchmark cell (E-ref-c).

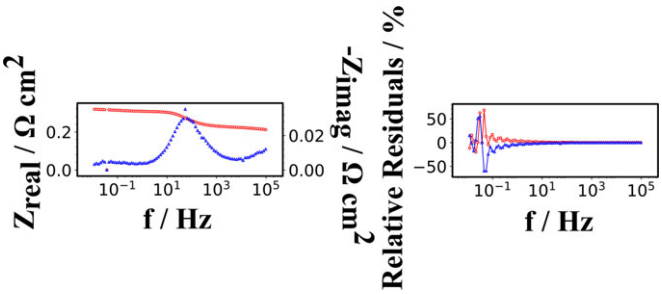

Fig. A.1 EIS spectrum measured at 0.35 A cm^{-2} on an EWII benchmark cell (E-ref-a). The full frequency range is shown with outliers. Bode plots of the EIS data are shown in the left column and relative residuals of Kramers-Kronig compliance tests of the EIS data are shown in the right column. The real part of the impedance is shown with red circles, and the imaginary part of the impedance is shown with blue triangles.

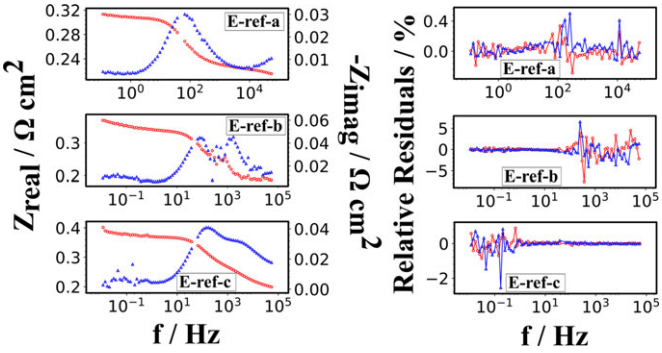

Fig. A.2 EIS measured on three different cells of the same EWII benchmark cell type at 0.35 A cm^{-2}: E-ref-a, E-ref-b, E-ref-c. An AC amplitude of 24.5 mA cm^{-2} was applied on E-ref-a, and an AC amplitude of 29.3 mA cm^{-2} was applied when measuring on E-ref-b and E-ref-c. Bode plots of the EIS data are shown in the left column and relative residuals of Kramers-Kronig compliance tests of the EIS data are shown in the right column. The real part of the impedance is shown with red circles, and the imaginary part of the impedance is shown with blue triangles.

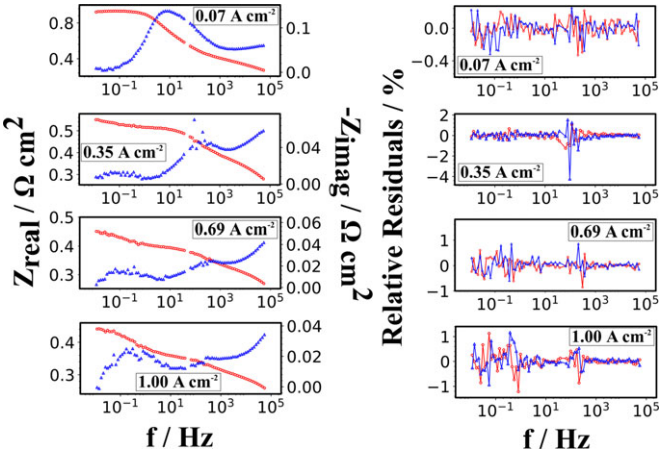

Fig. A.3 EIS measured at four different current densities (0.07, 0.35, 0.69, and 1.00 A cm^{-2}) on the IrRuOx PEMEC from EWII (E-IrRu). The AC amplitude was 24.5 mA cm^{-2}. Bode plots of the EIS data are shown in the left column and relative residuals of Kramers-Kronig compliance tests of the EIS data are shown in the right column. The real part of the impedance is shown with red circles, and the imaginary part of the impedance is shown with blue triangles.

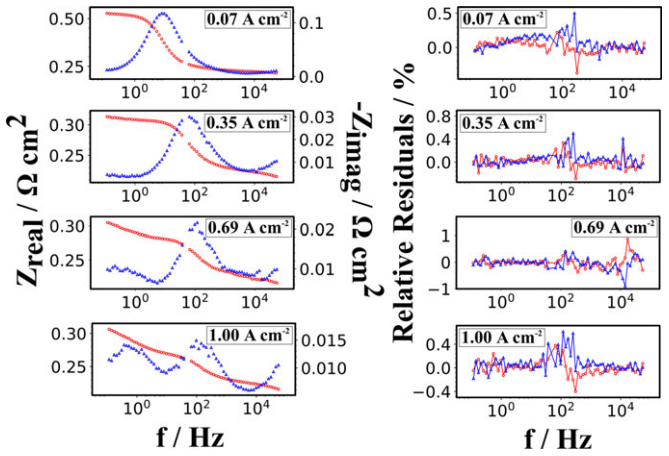

Fig. A.4 EIS measured at four different current densities (0.07, 0.35, 0.69, and 1.00 A cm^{-2}) on the EWII benchmark cell, E-ref-a. The AC amplitude was 24.5 mA cm^{-2}. Bode plots of the EIS data are shown in the left column and relative residuals of Kramers-Kronig compliance tests of the EIS data are shown in the right column. The real part of the impedance is shown with red circles, and the imaginary part of the impedance is shown with blue triangles.

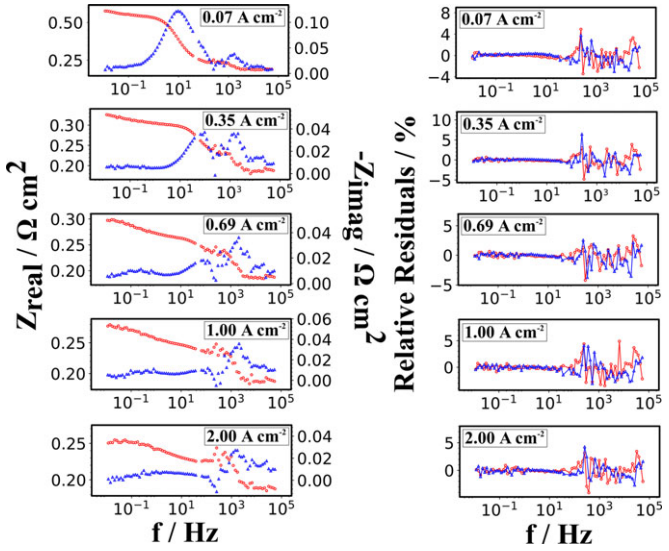

Fig. A.5 EIS measured at five different current densities (0.07, 0.35, 0.69, 1.00, and 2.00 A cm^{-2}) on the EWII benchmark cell, E-ref-b. The AC amplitude was 29.3 mA cm^{-2}. Bode plots of the EIS data are shown in the left column and relative residuals of Kramers-Kronig compliance tests of the EIS data are shown in the right column. The real part of the impedance is shown with red circles, and the imaginary part of the impedance is shown with blue triangles.

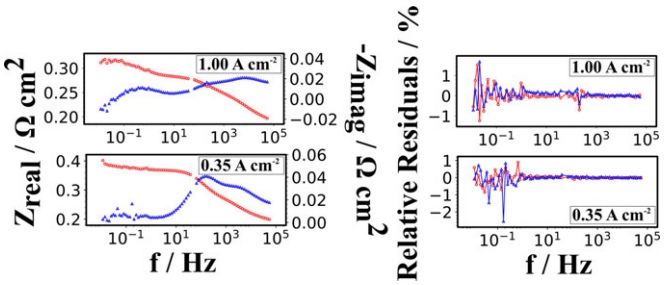

Fig. A.6 EIS measured at two different current densities (0.35 and 1.00 A cm^{-2}) on the EWII benchmark cell, E-ref-c. The AC amplitude was 29.3 mA cm^{-2}. Bode plots of the EIS data are shown in the left column and relative residuals of Kramers-Kronig compliance tests of the EIS data are shown in the right column. The real part of the impedance is shown with red circles, and the imaginary part of the impedance is shown with blue triangles.

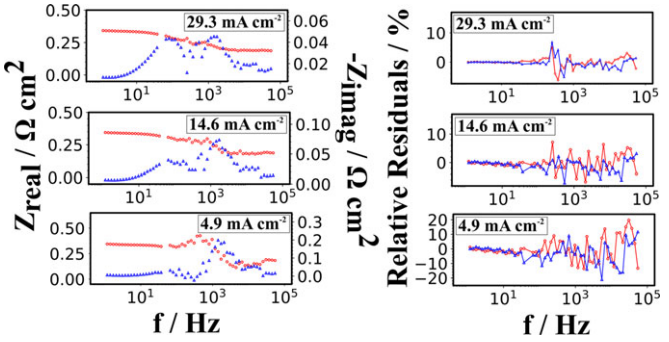

Fig. A.7 EIS measured at three different AC amplitudes (29.3, 14.6, and 4.9 mA cm^{-2}) on the EWII benchmark cell, E-ref-b, at 0.35 A cm^{-2}. Bode plots of the EIS data are shown in the left column and relative residuals of Kramers-Kronig compliance tests of the EIS data are shown in the right column. The real part of the impedance is shown with red circles, and the imaginary part of the impedance is shown with blue triangles.

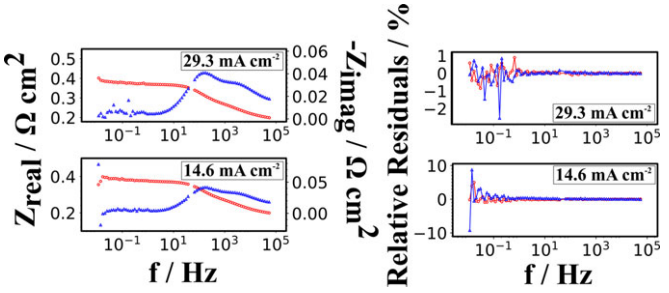

Fig. A.8 EIS measured at two different AC amplitudes (29.3 and 14.6 mA cm^{-2}) on the EWII benchmark cell, E-ref-c, at 0.35 A cm^{-2}. Bode plots of the EIS data are shown in the left column and relative residuals of Kramers-Kronig compliance tests of the EIS data are shown in the right column. The real part of the impedance is shown with red circles, and the imaginary part of the impedance is shown with blue triangles.

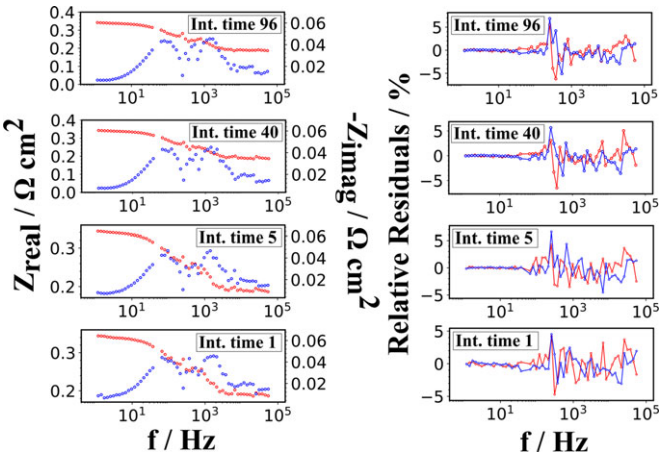

Fig. A.9 EIS measured at four different integration times (96, 40, 5, and 1) on the EWII benchmark cell, E-ref-b, at 0.35 A cm^{-2}. Bode plots of the EIS data are shown in the left column and relative residuals of Kramers-Kronig compliance tests of the EIS data are shown in the right column. The real part of the impedance is shown with red circles, and the imaginary part of the impedance is shown with blue triangles.

References

[1] M. Carmo, D. L. Fritz, J. Mergel, D. Stolten, *Int. J. Hydrogen Energy* **2013**, *38*, 4901.

[2] U. Babic, M. Suermann, F. N. Büchi, L. Gubler, T. J. Schmidt, *J. Electrochem. Soc.* **2017**, *164*, F387.

[3] E. Barsoukov, J. R. Macdonald, *Impedance Spectroscopy – Theory, Experiment, and Applications*, Second edition, John Wiley & Sons, Hoboken, New Jersey, **2005**.

[4] I. Dedigama, P. Angeli, K. Ayers, J. B. Robinson, P. R. Shearing, D. Tsaoulidis, D. J. L. Brett, *Int. J. Hydrogen Energy* **2014**, *39*, 4468.

[5] C. Rakousky, U. Reimer, K. Wippermann, M. Carmo, W. Lueke, D. Stolten, *J. Power Sources* **2016**, *326*, 120.

[6] C. Rozain, P. Millet, *Electrochim. Acta* **2014**, *131*, 160.

[7] S. Siracusano, V. Baglio, F. Lufrano, P. Staiti, A. S. Aricò, *J. Membr. Sci.* **2013**, *448*, 209.

[8] P. Lettenmeier, S. Kolb, F. Burggraf, A. S. Gago, K. A. Friedrich, *J. Power Sources* **2016**, *311*, 153.

[9] P. Lettenmeier, R. Wang, R. Abouatallah, S. Helmly, T. Morawietz, R. Hiesgen, S. Kolb, F. Burggraf, J. Kallo, A. S. Gago, K. A. Friedrich, *Electrochim. Acta* **2016**, *210*, 502.

[10] C. Graves, Ravdav data analysis software, version 0.9.7, **2012**.

[11] K. Elsøe, L. Grahl-Madsen, G. G. Scherer, J. Hjelm, M. B. Mogensen, *J. Electrochem. Soc.* **2017**, *164*, F1419.

[12] M. R. Kraglund, *PhD thesis*, DTU Energy, **2017**.

[13] B. A. Boukamp, *J. Electrochem. Soc.* **1995**, *142*, 1885.

[14] Solartron Analytical, 1260 Impedance/Gain-Phase Analyzer – Operating Manual, **1996**.

